Charles University in Prague
Faculty of Mathematics and Physics

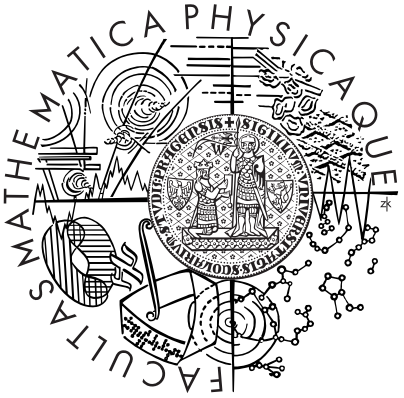

Institute of Particle and Nuclear Physics

Ondřej Chvála

Transverse Phenomena in Pion Production in Hadronic Collisions at SPS energy

Doctoral Thesis

Thesis Consultant:	Dr. Hans Gerhard Fischer
Thesis Supervisor:	Dr. Jiří Dolejší

Study program: Nuclear and Sub–nuclear Physics

Prague, November 2006

Abstract

A comparative study of pion production in hadronic collisions at SPS energies focusing on transverse phenomena is presented. Charged pion densities in p+p, p+C, p+Pb and Pb+Pb interactions, obtained at the CERN SPS with the NA49 detector setup, are discussed in the forward hemisphere covering ranges in Feynman x_F between 0 and 0.4 and in transverse momentum from 0 to 2.1 GeV/c. A detailed description of the data analysis, the corrections and centrality determination is given for p+Pb interactions using a sample of 2 M events. These data are compared to p+p collisions in order to extract those physics quantities which indicate deviations from the elementary reaction specific to the presence of the nucleus. The evolution of these quantities as a function of centrality is discussed. Their comparison to p+C and Pb+Pb collisions reveals a smooth dependence on the number of collisions per participant. In particular, the enhancement of pion yields at high transverse momentum is studied. It is shown to be governed by the superposition of the target and projectile contributions in asymmetric p+A collisions, as compared to symmetric p+p and A+A interactions. The extraction of the projectile component in p+A reactions leads to a new interpretation of the "anomalous nuclear enhancement" known as the "Cronin effect".

Contents

Chapter 1

Introduction

Contemporary understanding of the fundamental laws of the Universe is contained in the *Standard Model* [1]. It describes nature as composed of quantum fields of matter (fermions) interacting via fields of forces (bosons). There are four forces: gravitational, electromagnetic, strong and weak nuclear, and three families of matter particles (and antiparticles). Matter consists of leptons and hadrons. Hadrons are particles formed from quarks, like protons and neutrons. They interact via the strong interaction, while leptons do not.

The Standard Model is consistent with a large number of various measurements. Nevertheless, many particular aspects of our understanding of nature are as yet unclear. One example of such a "scientific frontier", where our understanding is in fact very limited, is the domain of high energy hadronic interactions.

This thesis aims to provide new and precise experimental data on pion production in p+Pb collisions as a part of the experimental program set up by the NA49 collaboration to investigate soft hadronic collisions at SPS energies. This program covers elementary as well as nuclear interactions with the same large acceptance detector, aiming to collect a high statistics event sample for each type of reaction, providing a self consistent basis of high precision and large acceptance measurements of hadron production in the soft sector. The study specifically addresses the question of the observed increase of pion production with increasing transverse momentum in nuclear as compared to elementary collisions.

1.1 Understanding the strong force

The strong force holds hadrons and nuclei together, drives the burning of stars, has been tamed by mankind to produce energy in nuclear power plants, and has found enormous use in nearly all areas of life in our industrial civilization.

Unlike electromagnetic and weak interactions, described well by theories which agree to a great and often unprecedented precision with the respective measurements on all experimentally accessible scales, the strong interaction poses a great theoretical and experimental challenge.

Modern understanding of the fundamental structure of matter started at the end of the 19th century with the discovery of X rays by Wilhelm Röntgen, "cathode rays" (electrons) by James John Thomson, and radioactivity by Henri Becquerel.

The first experiments with radioactivity by Ernst Rutherford, F. Soddy, the Curie family and others showed that there is a special force somehow connected with the atomic nucleus, different and much stronger than the electromagnetic force which drives chemistry and biology.

In the first decade of the 20th century Hans Geiger and Ernest Marsden performed famous experiments measuring the angular dependence of α and β particles scattered on a thin metal foil. Based on these experiments Rutherford proved in 1911 [2] that atoms have tiny positively charged centers, the nuclei. The nucleus carries over 99.9 % of the mass of an atom within a diameter smaller by five orders of magnitude than that of the atom itself.

In 1930 Wolfgang Pauli predicted the existence of neutrinos to explain the continuous spectrum of nuclear β decays, and they were discovered in 1956 by Frederick Reines and Clyde Cowan. The neutron was discovered by James Chadwick in 1932. Fission of uranium by neutrons was recognized in 1939 by Otto Hahn, Lise Meitner and Fritz Strassmann. The nuclear chain reaction was experimentally proven in a nuclear pile in 1942 by Enrico Fermi and his collaborators during the Manhattan Project. It was first used to produce electricity in 1951 in Experimental Breeder Reactor-I, Arco, Idaho.

Meanwhile, quantum theory was developed and used to describe the behavior of nature on the atomic scale: the photoelectric effect, Coulomb scattering, black body radiation, excitation spectra of atoms, etc. Further development led to relativistic quantum field theory, culminating in the formulation of quantum electrodynamics by Richard Feynman and others during 1940s.

Experimental research in high energy physics started with cosmic ray measurements in the beginning of the past century, and were pioneered by Theodor Wulf's measurements of elevation dependency of "atmospheric radiation" in 1910. Between the 1930's and the 1950's, new particles, the positron, pion, kaon and muon, were discovered by studying the cosmic rays. In the 1950's the first high energy accelerators and bubble chambers were invented. Soon more new particles were observed and their properties measured. Strangeness was understood as a quantum number conserved in strong interactions but not in the weak ones.

During the 1960's there were hundreds of new particles discovered, most of them very short lived ones decaying through the strong interaction within about 10^{-24} s, thus called the resonances.

Order in this "particle zoo" was established in the first half of the 1960s by Gell-Mann, Zweig, Neeman, Lipkin and others who formulated the additive quark model (AQM), in which hadrons were identified as bound and resonant states of quarks, of $q\bar{q}$ (mesons) and qqq (baryons). The AQM is based on isospin (SU(n) *flavor*) symmetry of the then hypothetical quarks. It was able to reproduce static properties of hadrons such as mass relations and magnetic moments. The discovery of the predicted Ω^- particle with an appropriate mass in 1964 was a great success of the quark hypothesis.

Despite the fact that baryons are fermions and therefore their wave function should be antisymmetric, the AQM assigns symmetric wave functions to them. Postulating the existence of a new quantum number connected with the quarks, *color*, and that only color singlet ("colorless") states can exist, the baryonic wave function is antisymmetrized. The hypothesis that quarks exist in the three color states also agreed with the relative rates of hadron to dimuon production in $e^+ + e^-$ collisions.

However, no free quarks were ever observed, only hadrons. The color hypothesis postulated that only "colorless" states exist, but did not provide an answer why. This problem is known as the "confinement" of quarks inside the hadrons and its understanding is one of the principle problems in strong interactions.

Evidence for the substructure of nucleons was first observed in the 1950's in early electron+proton (e+p) scattering experiments at Stanford University by Hofstadter and McAllister [4]. First measurements of elastic electron scattering off protons and nuclei have shown that the size of hadrons in terms of their charge distribution is finite. The RMS of

the charge distribution of the proton was measured to be $r_{ch}^{p} \approx 0.7fm$. Another important experimental result was that the nuclei do not have a sharp edge.

Later measurements in the 1960's using more powerful accelerators revealed that inelastic cross sections for higher invariant masses of the hadronic remnant system – *deep inelastic scattering* (DIS) – decreased very slowly with increasing Q^2, in a sharp contrast to elastic cross sections.

These differential inelastic cross sections can be written down in a general form, when only the scattered electron is measured in the final state:

$$\frac{\mathrm{d}\sigma}{\mathrm{d}\Omega dE'} = \frac{\alpha^2 \cos^2\frac{1}{2}\theta}{4E^2 M_p \sin^4\frac{1}{2}\theta} \left[W_2(x_{Bj}, Q^2) + 2W_1(x_{Bj}, Q^2)\tan^2\frac{1}{2}\theta\right] \tag{1.1}$$

where M_p is the proton mass, E and E' are the initial and the final state electron energies in the laboratory frame, θ is the laboratory scattering angle of the electron, and W_1 and W_2 are the proton structure functions, which depend on two variables – the electron energy loss $\nu_e = E - E'$[1] and the Q^2 of the collision, or on $x_{Bj} = Q^2/(2M_p\nu_e)$ and Q^2.

It was found that the structure functions obey scaling (i.e. independence of $\nu_e W_2$ on Q^2) predicted by Bjorken, corroborating the hypothesis of elementary constituents of hadrons. Bjorken was examining S-matrix theory using current algebra, with quarks rising from its representation. Even though Bjorken's argument was later found to be flawed, and the Bjorken scaling is only approximate, the basic formalism of structure functions, parton distribution functions and sum rules were then used by Feynman, who developed the parton model at the end of 1960s.

The parton model was an important milestone, as its basic concepts have been used since in the majority of later theoretical approaches, including QCD. These concepts can be summarized as follows: hadrons are made of point–like constituents called *partons*. The distribution of partons in hadrons is described by parton distribution functions (PDF), which depend only on the fraction of the hadron's momentum carried by the parton, the Bjorken scaling variable x_{Bj}. The observed scaling is a consequence of the fact that PDFs are in the first approximation independent of Q^2 and $\sqrt{s}$. If the e+p collision is deeply inelastic, $Q^2 \gg m_p^2$, the collision can be represented as quasi–free scattering off an individual parton. Corresponding cross sections are then sums of incoherent contributions from scattering off individual partons.

A deep inelastic interaction in the parton model is pictured in Fig. 1.1. First the electron interacts with a participating parton via a virtual photon. The parton which was hit is knocked out of the target hadron. Subsequently both of them hadronize, i.e. they dress up into hadrons, to restore color neutrality.

Assuming the interaction time τ_{int} is much shorter than the hadronization time τ_{had}, hadronization does not influence the interaction with the parton. Deep inelastic scattering (DIS) experiments discovered *asymptotic freedom*, the phenomenon that partons appear to interact as free particles in the limit of infinite momentum transfer.

DIS experiments led to the formulation of the parton model and finally to QCD. More detailed information about history of the strong force and QCD can be found in [3].

The Standard Model features Quantum Chromo–Dynamics (QCD) as the theory of the strong force. QCD is a $\mathrm{SU}_c(3)$ renormalizable gauge theory formulated in 1973 by David Gross and Frank Wilczek. "Chromo" in QCD stands for color, a quantum number

[1] The usual name ν is replaced by ν_e to avoid confusion with the mean number of intranuclear collisions ν in the later chapters.

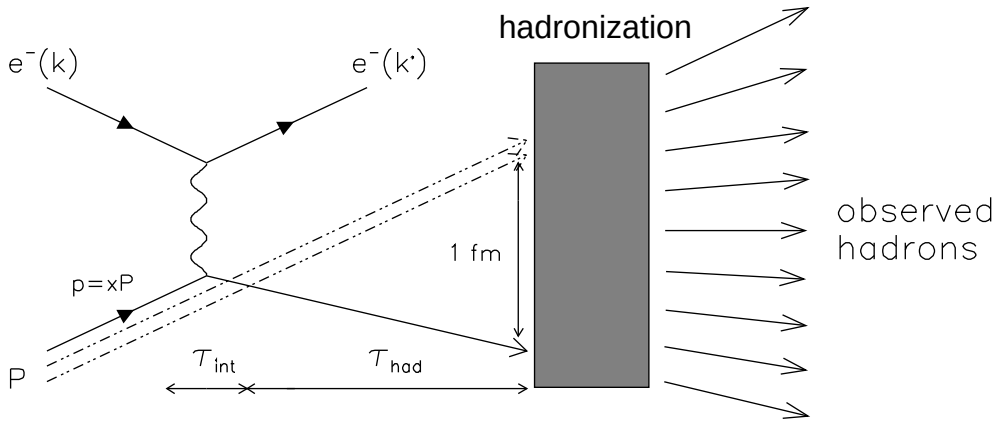

Figure 1.1: DIS interaction in the parton model, based on [3]. The electron scatters on a charged parton (quark) within τ_{int}, leaving the remaining part of the proton (diquark) intact. After the hadronization time τ_{had} the partons turn to hadrons to satisfy color neutrality.

introduced in theories preceding QCD. It was a great success for quantum field theory as a description of nature.

1.2 QCD – The theory of the strong interaction

QCD is a renormalizable[2] quantum field theory with a nonabelian gauge symmetry group $SU_c(3)$. Fermion fields q_j, quarks, interact via bosonic vector fields A^μ, gluons. The interaction is prescribed by the QCD Lagrangian:

$$L^{QCD} = -\frac{1}{4} G_{\mu\nu} G^{\mu\nu} + \sum_{j=1}^{n_f} \overline{q_j} (i\gamma_\mu D^\mu - m_{q_j}) q_j \tag{1.2}$$

where the covariant derivative $D^\mu q_j = (\partial_\mu - igA^\mu) q_j$ and n_f is 6, the number of quark flavors.

The nonabelian gauge has specific consequences for the gluon field properties. Writing the kinetic part of the Lagrangian 1.2 using the fields A^μ, $G_{\mu\nu} = \partial_\mu A_\nu - \partial_\nu A_\mu - ig[A_\mu, A_\nu]$, the terms describing *self-interaction* of the gluon field in a 3 and 4 gluon couplings are obtained.

Measurement of three–jet events in electron–positron annihilation by the JADE experiment at the PETRA collider in 1979 was one of the early experimental confirmations of QCD. In the three-jet event two jets were identified as a quark-antiquark, the third as a gluon remnant. The energy dependence of the three jet cross section was used to establish the energy dependence of the strong coupling constant α_s [5].[3]

[2]Quantities such as cross sections are calculated in quantum field theories by breaking up interactions between two particles into separate reactions, commonly represented in Feynman diagrams. Some of these terms give infinite contributions, however, the infinite terms cancel out, giving a finite solution. The process by which this is done is called renormalization.

[3][6] is a summary report on measurements of α_s in e^+e^- collisions by experiments at the PETRA machine at DESY and CERN's LEP. Interestingly, JADE has been resurrected sice 1997 and its old data reanalyzed. See [7] for details and reports.

Asymptotic freedom, a fundamental feature of QCD, is manifested as the decrease of the strong coupling α_s with increasing momentum transfer Q^2, a feature known as the running coupling strength, which may be expressed by the following formula:

$$\alpha_s(Q^2) = \frac{4\pi}{(11 - \frac{2}{3}n_f)\ln\frac{Q^2}{\Lambda^2}}, \tag{1.3}$$

where Λ is the fundamental scale introduced by the renormalization. Its numerical value has been determined experimentally to be $\Lambda \approx 200\,\mathrm{MeV}$. The confinement of partons inside hadrons is a consequence of the formula above, the antiscreening of the QCD vacuum at larger distances, corresponding to low momentum transfer.

1.2.1 Perturbative QCD

Perturbative QCD (pQCD) is usable when the coupling constant α_s is small enough to allow perturbative expansions, i.e. at high enough momentum transfer Q^2 as can be seen from equation (1.3). Then Feynman calculus analogous to QED can be used to calculate amplitudes of QCD processes. Such processes involve scattering of individual partons and are generally referred to as *hard interactions*. Hard interactions of hadrons are similar to those pictured in Fig. 1.1: first the interacting partons, having a momentum distribution according to their PDFs, scatter as free particles. Then hadronization takes place, when they turn into observed hadrons.

Examples of hard scattering are DIS, hadronic interactions with very large momentum transfer ($Q^2 \gg m_p^2$), Drell–Yan production of heavy systems, and jet structure of $e^+ + e^-$ interactions.

What the limits of pQCD applicability in hadronic interactions are is a lively topic among theorists. The present work is limited to a region of $p_T < 2\,\mathrm{GeV}$, which is generally considered out of the pQCD domain. However, there are some pQCD extrapolations into this region and explanations of some nuclear effects like the Cronin effect rely on pQCD concepts. [11]

1.2.2 Nonperturbative QCD

The vast majority of hadronic interactions occurring in nature happen at low Q^2, where the coupling constant (equation (1.3)) is large and the theory is not calculable perturbatively. These processes are known as *soft interactions*.

Facing these difficulties, other approaches have been developed. The chiral perturbation theory is an effective field theory which describes low energy phenomena such as hadron masses, magnetic moments, weak decays, near–threshold meson production etc. Lattice gauge theory is a numerical approach to solve the QCD equations on a discretized space–time lattice. The grid step a introduces naturally an inversely proportional momentum cut-off, which regularizes the theory. However these approaches are however not able to predict multiparticle final states observed in high energy hadronic collisions.

Lacking a dynamic picture calculable from QCD first principles, the understanding of particle production in the soft sector relies on phenomenological models. [4] The models

[4]Hadronic phenomenology is a wide and versatile field which has offered many different and often contradictory ideas over more than fifty years, the scope of which greatly exceeds that of this thesis, and thus is only briefly touched on. No attempt to review the subject is made. A possible way of looking at the data is suggested in later chapters. A recent attempt to summarize the key issues in hadronic physics may be found in [12].

typically investigate different dynamic scenarios underlying partonic interactions, utilize various approaches to soft hadronization, and have several parameters which are to be determined from measurements. The models usually come in the form of Monte-Carlo event generators. In the case of nuclear interactions, new dimensions open up for theoretical study. The models and their respective scenarios may be refined, falsified or corroborated by comparisons to the available measurements.

The presented work is a part of the NA49 program to create a consistent data base of precise measurements of particle production in hadronic interactions of various types of projectiles and targets using the same detector and covering a large phase space, contributing to the necessary experimental evidence. This program also attempts to contribute to the understanding of the soft sector with a data driven, and as far as possible model independent approach, using only basic principles like baryon number conservation and isospin symmetry, to shed new light on the domain of soft hadronic interactions. A summary of the previous works in this context may be found in [50, 51, 52, 53, 54, 55, 56, 57].

1.2.3 Choice of variables in a multidimensional phase space

Soft hadronic interactions at relativistic energies produce multiparticle final states with multiplicity increasing as $\sim \sqrt{s}$, representing a multidimensional phase space. Invoking energy–momentum conservation and, assuming unpolarized beams and targets, symmetry around the beam axis, there are $(3\,N$ - 5) independent coordinates in that phase space of N produced particles. In addition, the particle types, their masses and their charges, are determined to exclusively describe a soft hadronic event in an ideal case.

The reduction of this multidimensional volume to two momentum variables and one kind of the studied particle in an inclusive study as presented in this thesis represents a dramatic reduction of the available information, though necessary as the experimental information is always limited and there are obvious difficulties connected to presentation and interpretation of multidimensional structures.

To describe the momentum of produced particles, orthogonal coordinates are chosen in this thesis, namely longitudinal and transverse momentum in the center of mass system, p_L^* and p_T. This choice is based on a very basic and specific feature of soft hadronic interactions known as *longitudinal phase space* [13]. This feature means that the particle density in the longitudinal direction fills up the available phase space which grows linearly with increasing $\sqrt{s}$, whereas in the transverse direction the density is damped in roughly exponential manner, and its evolution with interaction energy is very moderate.

The longitudinal distributions of invariant cross sections of particle production were found to scale with the interaction energy, a phenomenon known as Feynman scaling [14]. For this reason in this thesis the scaling variable x_F will be used together with p_T.

$$x_F = \frac{2 \cdot p_L^*}{\sqrt{s}} \tag{1.4}$$

There were two approaches to describe this phenomenon of longitudinal phase space, dating to nearly 40 years ago. They are important from a historical perspective as the contemporary approaches are related to these pictures.

- The duality between the partonic structure of nucleons and the produced hadrons in the parton model [14, 15, 17] discussed above. For instance, this is manifested by the similarity of the valence quark structure function as a function of x_{Bj} and the x_F distribution of produced pions [16].

- The concept of limiting fragmentation [18] which assumes decay of heavy excited systems. In this approach both the longitudinal phase space and the Feynman scaling behavior can be derived in the high energy limit.

The transverse momentum originates in the first case in the hadronization process by creation of quark–antiquark pairs from the vacuum by the Schwinger mechanism [19, 20, 21] which can be naively pictured as breaking up strings pulled between the scattered partons. The transverse energy spectra are damped in Gaussian or exponential form, depending on the exact assumptions. In some approaches a transverse momentum of the partons k_T is introduced, inspired by pQCD [22, 23].

In the second case the transverse momentum originates from the cascading decay of heavy systems and the limitation of p_T originates in the low mass of the final state particles as compared to the masses the heavy systems and the low q of most of the decays [25, 61, 64].

1.2.4 Interactions of hadrons with nuclei

The main subject of this thesis is the study of interactions of hadrons with nuclei (h+A). Compared to the general questions of soft QCD introduced above, the presence of the nucleus might be considered as an additional complication. On the other hand nuclear collisions present an important laboratory which, as discussed below, allows the extension of the scope of experimental studies and therefore provide further constraints on the description of the soft hadronization process.

Compared to the size of the projectile hadron ($\sim 1\,\mathrm{fm}$) a lead nucleus ($\sim$12 fm in diameter) forms a multi-nucleon target which, depending on the impact parameter of the projectile, can lead to multiple hadronic collisions. For reactions of protons with lead (p+Pb), an average of up to about 7 such intranuclear interactions can be studied experimentally for small impact parameters. In order to sort these collisions into classes the determination of the impact parameter is necessary. The classical "minimum bias"[5] p+A experiments, which have no control over this parameter, have to use nuclei of a different size in order to obtain some range of the average number of collisions, with a wide spread around the mean, reaching maximum of about 4 intranuclear interactions. The NA49 experiment has introduced a centrality detector, discussed below, which uses the number of slow protons produced in the intranuclear cascade as a measure of the impact parameter.

An h+A interaction is by definition asymmetric as far as projectile and target fragmentation are concerned. Only the projectile sees multiple collisions, whereas each participating target nucleon interacts only once. As argued in the subsequent sections of the thesis, these two principle components of fragmentation are experimentally separable and can be scrutinized independently. It is the projectile fragmentation which is of main interest here, as a new experimental field of soft hadronization is opening and a large number of questions may be approached for the first time.

- What happens to the projectile after the first collision?

- Does it indeed split into partonic sub–systems as the loss of color neutrality in this interaction would suggest?

[5] In the context of this thesis, *minimum bias* refers to experimental conditions with the least possible bias induced by the experimental trigger on the reactions investigated. Ideally, the minimum bias experiment would capture all the inelastic events.

- What happens to the total inelastic cross section seen by the subsequent collisions? Does it decrease as expected for partonic interactions, or does it increase as expected from an excited hadron? [36]

A number of fundamental problems regarding the coherence or incoherence of subsequent collisions and the space–time evolution in the target and projectile rest systems can be addressed.

This thesis will concentrate on transverse phenomena in this wide experimental field. One of the earliest manifestations of nuclear effects is given by the "anomalous nuclear enhancement" or "Cronin effect" discovered in the early 1970's for transverse momenta above 1 GeV/c [8, 9, 10]. This phenomenon is not yet explained by theory in spite of some attempts to connect it to multiple hard parton scattering [11]. In subsequent chapters, a detailed study of the evolution of transverse pion yields up to 2 GeV/c from the projectile component, which gives new insight into this long–standing problem, will be presented.

1.2.5 Interactions of nuclei

The interaction of two large hadronic systems in nucleus+nucleus (A+A) collisions has received much interest during the past couple of decades. The reason for this interest is different from the "classical" QCD argumentation outlined above. It is incited by the hope to study a new manifestation of QCD by creating a de–confined state of matter, the "Quark–Gluon Plasma" (QGP), in relativistic heavy ion collisions [26]. This hope is founded on an assumed dramatic increase of local energy density available in such collisions [27, 28]. A sizeable number of signatures for QGP formation at SPS energies have been accumulated to date, but no decisive experimental proof [29]. This difficulty originates from the fact that all signatures are circumstantial because they have to rely on comparisons to the more elementary hadron+hadron (h+h) and h+A collisions. The unsatisfactory experimental situation in all sectors of soft hadronic interactions is one of the main reasons of this problem.

One of the expected signatures of QGP formation is given by the increased transverse momentum of particles in an A+A reaction as compared to h+h collisions, described by the radial expansion of the high–temperature partonic phase, followed by a "freezout" into the observed hadrons [30]. Available preliminary data from the NA49 experiment in Pb+Pb interactions are presented in Chapter 7.8 as a comparison of the evolution of pion yields up to 2 GeV/c transverse momentum to p+Pb collisions to shed new light on this subject.

1.3 Focus of the thesis

This thesis starts with a short discussion of the problem of centrality in h+h, h+A and A+A reactions, introducing a common scale of inelasticity, the mean number of collisions per participant nucleon ν.

The experimental aspects of detector design, centrality control, data acquisition and analysis procedures including corrections and systematic error evaluation are addressed. The resulting invariant, double–differential inclusive distributions of charged pions are then presented in data tables and corresponding plots for five bins of centrality. The phase space region covered by these data extends over the ranges $0 < x_F < 0.4$ and $0 < p_T < 2.1$ GeV/c.

In a the discussion section a detailed phenomenological analysis of the data is performed, in particular referring to the recently published results from p+p [61] and p+C [62] interactions using the same detector setup and covering the same region of phase space.

The discussion is centered on the evolution of transverse yields for comparison to p+p and Pb+Pb interactions. It allows a new inspection of the high–p_T enhancement known as the Cronin effect.

The results are then summarized.

1.4 Author's contribution

The author contributed to the overall effort of the NA49 collaboration by participation in taking data in the years 1999 – 2003. This activity included a wide variety of different experimental conditions, ranging from p+p, π+p and d+p interactions obtained by means of a fragmentation beam, through p+C, p+Pb and π+Pb reactions up to heavy ion Pb+Pb collisions.

Furthermore, the author participated in the mechanical construction and testing of a new NA49 sub-detector introduced in 2001, the "GapTPC" discussed in Section 3.7.

The author was responsible for establishing the trigger cross sections in p+p, $\pi^{\pm}$+p, p+C and p+Pb interactions using measured interaction rates and properties of the targets, as well as the evaluation of the absolute normalization of measured differential cross sections. This included the development of a trigger bias correction method and its precise evaluation for secondary particles measured in p+p, p+C and p+Pb interactions, as discussed in Section 5.4.2.

Nearly all the results contained in this thesis were obtained directly by the author by means of an individual, independent experimental analysis. For the clarity of the discussion a few other results have also been included in the thesis; each of them is referred to in the bibliography.

More specifically, the author has obtained the full set of double–differential cross sections for pion production in p+Pb reactions. The production yields of strange particles (hyperons and K mesons), which constitute the necessary input for the construction of the correction of particle yields for feed–down from weak decays (section 5.4.4) were also obtained by the author. The same is true for the problem of the precise evaluation of the empty target correction for the p+Pb data sample, Section 5.4.1.

Additionally, the author significantly participated in the analysis of pion production in Pb+Pb collisions, made within the framework of a small working sub–group of the NA49 collaboration. Selected results of this analysis are included in the present thesis.

Finally, the author participated in several other activities not contained in this thesis, namely: creating several Monte Carlo programs to study elastic and diffractive contributions to the trigger cross sections of hadronic reactions; contributing to a ROOT oriented analysis of the correlations between pion production and baryon stopping in hadronic collisions [31]; running several Monte Carlo event generators (EPOS, Pythia, Fritiof and UrQMD) in order to investigate the problem of resonance production as contained in these models [96]; creating and maintaining the web-site focusing on the p+p and p+A physics of the NA49 collaboration [97].

Chapter 2

Problem of centrality in hadronic interactions

In order to proceed with quantitative comparison between p+p, p+A and A+A interactions, a common scale needs to be defined. In this chapter some basics concepts of centrality in hadronic interactions are discussed.

2.1 h+h interactions

Collisions between two hadrons, shown in Fig. 2.1, can occur at various relative transverse coordinates, impact parameters $\mathbf{b}_{\mathrm{h+h}}$. The impact parameter is commonly used in the description of elastic [66] and diffractive scattering [67], where the measured (semi–)exclusive channels allow for impact parameter estimation and comparison with theory.

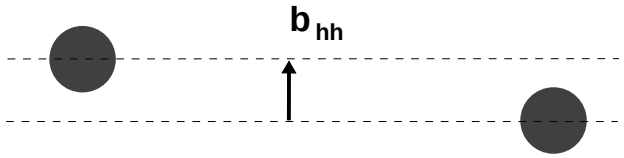

Figure 2.1: h+h interaction at impact parameter $\mathbf{b}_{\mathrm{h+h}}$.

In inelastic reactions the impact parameter is not a measurable quantity, however, the total cross section of inelastic reactions can be estimated in a geometric picture as the area of the overlap, $s = \pi R^2$, where $R = 2\mathrm{r}$ (Fig. 2.2). Assuming a diameter d of 1 fm, the total theoretic inelastic cross section corresponds to the overlap area of 31.42 mb. The measured value is 31.78 mb in p+p collisions at our energy.

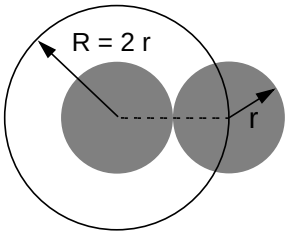

Figure 2.2: Total coss-section of h+h interactions assuming that hadrons are opaque discs.

Lacking an experimental handle on the impact parameter of an inelastic elementary hadronic interactions, other means have to be used to characterize the inelasticity or rather centrality. The amount of inelasticity can be qualitatively related to the severity of the collision, meaning the amount of projectile energy spent in a collision to create new particles.

The multiplicity N of produced particles is often used to establish the inelasticity of an event. However a collision which produces a baryon–antibaryon pair is less elastic than one which produces three low p_T pions. Besides this problem, in practice an experiment is limited to measuring charged particles within a region of phase space defined by the coverage of the detector, which weakens the correlation between the measured multiplicity and the inelasticity of the event.

Since multiplicities in both hemispheres are known to be nearly independent[1] ideally the multiplicity of both would be measured separately. This concept gets further complicated because of *feed–over*: some particles produced from projectile fragmentation find themselves in the target hemisphere (projectile feed–over) and vice versa (target feed–over), scrutinized in more detail in Section 7.6.

Particle production in a p+p interactions can be tentatively written as the sum of the particle productions from the two – "projectile" and "target" – contributions, concerning average multiplicities:

$$N^{\mathrm{p+p}} = N_{\mathrm{target}} + N_{\mathrm{projectile}} = \frac{N^{\mathrm{p+p}}}{2} + \frac{N^{\mathrm{p+p}}}{2} \tag{2.1}$$

2.2 h+A interactions

A geometric picture of a collision between a hadron and a nucleus is shown in the top panel of Fig. 2.3. In this case, the impact parameter is a better defined quantity than in the above discussed elementary case because related parameters – the thickness L of the nuclear matter traversed by the projectile and the number of hit nucleons ν – can be estimated independently.

In the projectile reference frame the target nucleus is relativistically contracted at relativistic energies. In collisions with a 158 GeV/c proton beam momentum, $\gamma^{PT} \approx 169$ between the projectile and the target system.[2] Therefore the Pb nucleus in the target, with diameter ≈ 12 fm, is contracted to ≈ 0.1 fm in the projectile frame. This makes it impossible for the projectile to resolve consecutive collisions with the target nucleons.

In the target frame, on the other hand, the projectile takes 12 fm/c to traverse a lead nucleus in a central collision, making the estimated ~ 7 consecutive collisions easily separable by hadronic time scale of ~ 1 fm/c. Since the collision occurs at the speed of light, nucleons hit in the target do not know about the preceding hits.

Centrality in h+A collisions can be estimated in various ways. In minimum bias p+A collisions the mean number of intranuclear collisions is commonly estimated [75] by the

[1] Consider single diffraction as an extreme case where particles are produced from target fragmentation and the projectile only loses a small fraction of its energy. A more thorough discussion showing the independence of projectile and target fragmentation based of bubble chamber measurements of [68] and [69] follows in Section 7.6 and can also be found in [50, 51, 56, 54, 57, 63].

[2] Note the difference between γ^{PT}, relating projectile and target coordinate systems, and γ of the CMS. In the case of a proton beam with 158 GeV/c momentum $\gamma = 9.21$, compared to $\gamma^{PT} \approx 169$.

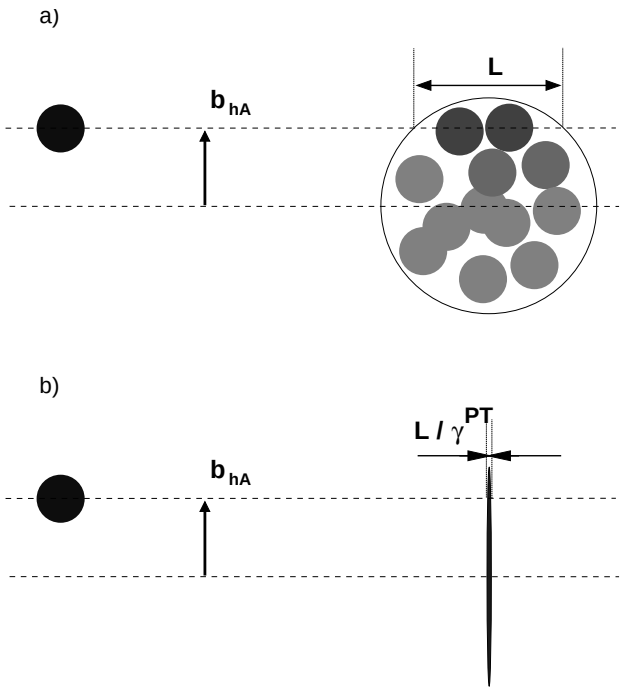

Figure 2.3: h+A interaction at impact parameter $\mathbf{b}_{\mathrm{h+A}}$. a) A projectile passes through a length L of nuclear matter hitting $\nu = 2$ target nucleons. b) In relativistic collisions, the target nucleus is contracted by $1/\gamma^{PT}$ to a thin disc in the projectile reference frame and therefore the projectile undergoes one *multiple collision* with the ν target nucleons. See discussion on page 11.

formula (2.2), where A is target nucleon number and $\sigma^{\mathrm{h+h}}$, $\sigma^{\mathrm{h+A}}$ are inelastic cross sections in hadron–proton and hadron–nucleus reactions:

$$\langle \nu \rangle = A \cdot \frac{\sigma^{\mathrm{h+h}}}{\sigma^{\mathrm{h+A}}} \tag{2.2}$$

This formula can be derived from the framework of the Glauber model [32, 33] and can be justified by the following geometrical reasoning [63]: imagine a plane covered by a random superposition of A discs each with a surface corresponding to $\sigma_{inel}^{\mathrm{p+p}}$, thus having radius of $r \approx 1\,\mathrm{fm}$, as shown above. Let the total surface covered by one layer of the discs be denoted by S_1, the area covered by two layers (area of overlap of two discs) by S_2, the area covered by three layers by S_3, ... , up to S_A. If a beam of projectile discs of the same surface $\sigma_{inel}^{\mathrm{p+p}}$ penetrates the plane, the mean number of projectile collisions with the plane discs will be:

$$\langle \nu \rangle = \frac{S_1 + 2S_2 + 3S_3 + \ldots + AS_A}{S_1 + S_2 + S_3 + \ldots + S_A} \tag{2.3}$$

The total area covered by the plane discs is $S_1 + S_2 + S_3 + \ldots + S_A$, corresponding to the total inelastic cross section $\sigma_{inel}^{\mathrm{p+A}}$. The sum of the surfaces of the discs, $A \cdot \sigma_{inel}^{\mathrm{p+p}}$, can be written as:

$$A\sigma^{\mathrm{p+p}} = S_1 + 2S_2 + 3S_3 + \ldots + AS_A \tag{2.4}$$

The last two formulae give equation (2.2). This relationship is based on the assumption that the disc surface corresponding to the inelastic cross section of interaction between

the projectile and target is constant in consecutive layers which correspond to multiple projectile collisions.

Varying the A of nuclear target can thus be used to obtain interactions with a different mean number of collisions $\langle\nu\rangle$. The mean ν does not exceed ≈ 3.8 in minimum bias interactions, as there are no nuclei large enough. The inelastic cross sections of p+A interactions along with their corresponding mean νs are shown in Table 2.1.[3]

reaction	σ_{inel} **[mb]**	$\langle\nu\rangle$
p+p	31.8 ± 0.6	1
p+C	226 ± 7	1.69
p+Pb	1806 ± 25	3.65

Table 2.1: The inelastic cross sections measured by NA49 and the corresponding mean number of projectile collisions in a minimum bias interactions using formula (2.2).

The mean number of collisions ν estimated from the inelastic cross sections using equation (2.2), presented in Table 2.1 for minimum bias p+C interactions, is higher than the number deduced from the measured yields of pions ($\nu^{\text{measured}} = 1.6$) in the target fragmentation region [63]. Such an effect was actually predicted on general grounds [34].

2.2.1 Intranuclear cascading: grey protons

The centrality of h+A interactions can be independently established by measuring the number of *grey protons* n_{grey}. These are low momentum recoil nucleons produced in the intranuclear cascade initiated by the projectile hadron traversing the target nucleus. The grey protons are defined as having a laboratory momentum between 0.15 and 1.2 GeV/c to distinguish them from nuclear fragments or produced particles. The momentum distribution of grey particles is shown in Fig. 2.4.[4]

The number of grey protons produced can be related to the number of projectile collisions ν using theory and models. This issue has been investigated in detail [35, 36]. Comparison of this theoretical prediction with later bubble chamber measurements of grey particles in p+Au at 360 GeV/c beam momentum by the EHS collaboration at CERN [76] and the Fermilab measurement at 320 GeV/c [77] are shown in Fig. 2.5, along with the NA49 measurement in minimum bias p+Pb, which has been corrected for the NA49 acceptance for grey proton counting described in the next section.

The predicted relationship between the mean number of collisions ν and the number of grey particles produced in p+Pb collisions is shown in Fig. 2.6.

Figure 2.7 shows the distribution of grey protons as measured by [38] along with the prediction from the above mentioned theory for each of the ν. Note that each value of ν corresponds to a distribution of grey particles.

[3]The concept of an inelastic interaction is clearly defined in an h+h interaction since particles are produced. However in an h+A case low-momentum transfer collisions may result in target nucleus excitation and fragmentation with no meson production – commonly called a "quasi–elastic" or "incoherent elastic" cross section. The absorption cross section refers to the total minus the "true elastic" or "coherent" cross section.

[4]The terminology comes from nuclear emulsion studies using cosmic rays or accelerator beams, which sorts the produced particle by respective track ionization density. Slow very highly ionizing nuclear fragments correspond to so called black tracks, the grey tracks are low momentum protons and light tracks are traces of produced relativistic particles close to minimum ionization. A review concerning approaches to centrality control using slow nucleons can be found in [37].

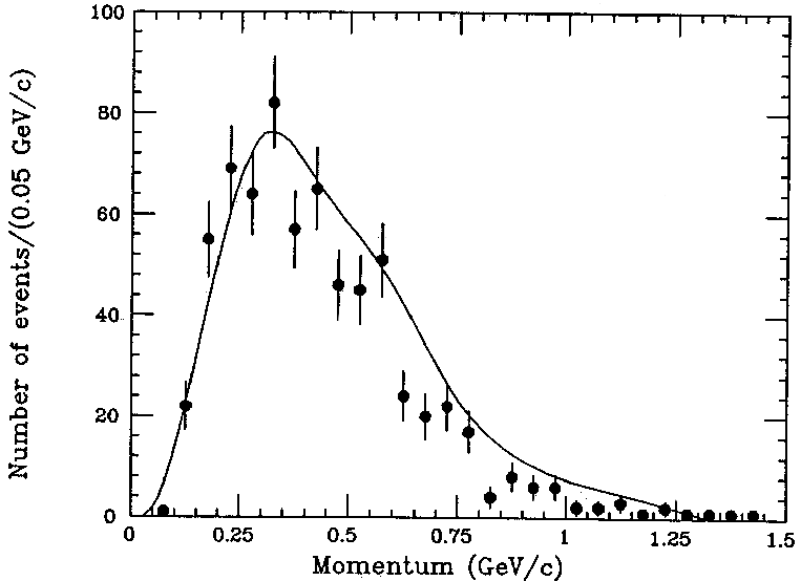

Figure 2.4: Momentum distribution of grey tracks produced in p+Al and p+Au collisions at 360 GeV/c as measured by EHS collaboration [24].

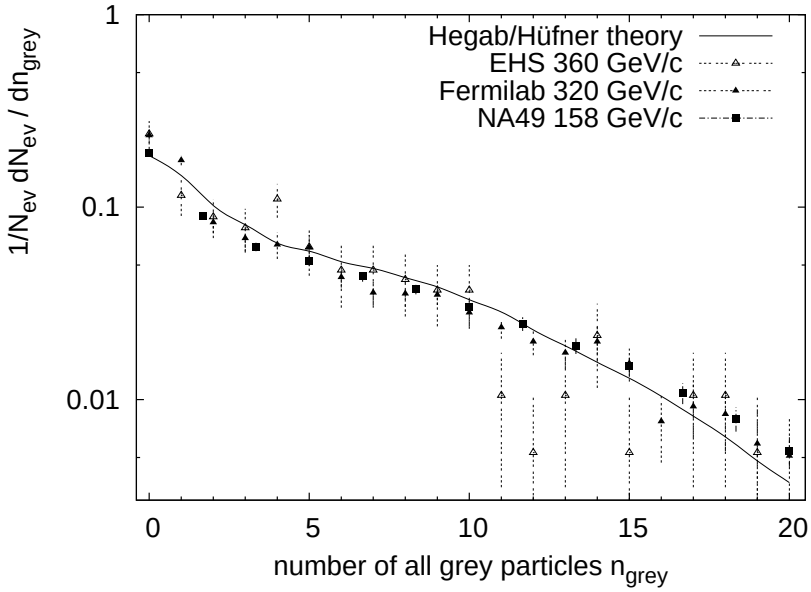

Figure 2.5: Distribution of grey particles as measured by NA49 (see text), EHS [76], and at the Fermilab 30 inch bubble chamber [77] compared to theory [36].

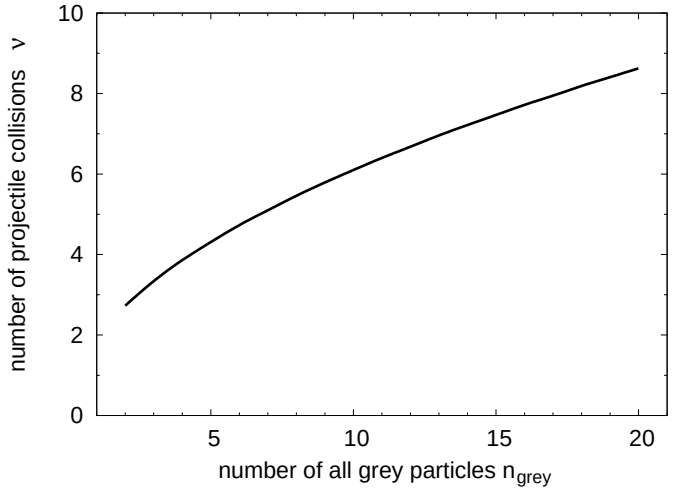

Figure 2.6: Relationship between the number of grey particles n_{grey} and the mean number of projectile collisions ν [36].

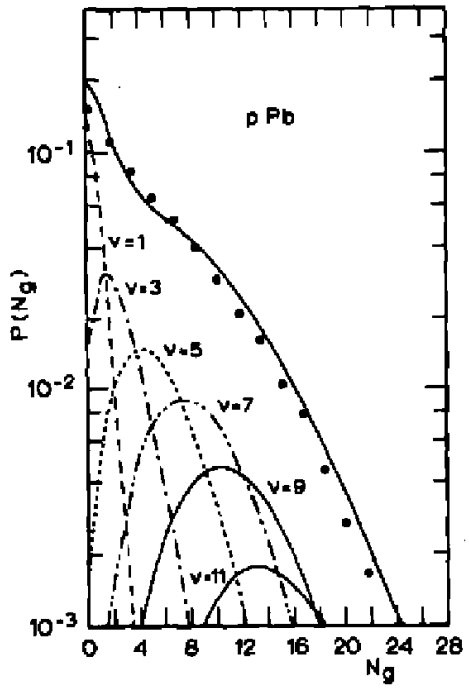

Figure 2.7: Distribution of grey particles $P(N_g)$ in minimum bias p+Pb collisions decomposed into contributions from different values of ν [36].

Most minimum bias interactions happen at low centralities due to p+A collision geometry. The strong decrease of the yield with increasing n_{grey} is evident from the figures above. There are two ways of using the information about grey protons to select more central events:

- In a minimum bias experiment, events with a higher number of grey protons can only be selected off–line. It however requires to collect a huge number of events to obtain significant sample of central collisions, see Fig. 2.8.

- An experiment that actively triggers on the number of grey protons can be designed. This way one can obtain similar statistics over a wide range in ν.

The NA49 experiment utilizes a grey proton counter, the Centrality Detector (CD) described in Section 3.5, which allows on–line triggering on the number of grey protons detected by the CD, suppressing peripheral interactions. The difference between the grey proton distribution as measured by NA49 in the minimum bias sample and in the centrality triggered sample of p+Pb events is shown in a linear scale in Fig. 2.8. Note the very large fraction of peripheral events in the minimum bias sample.

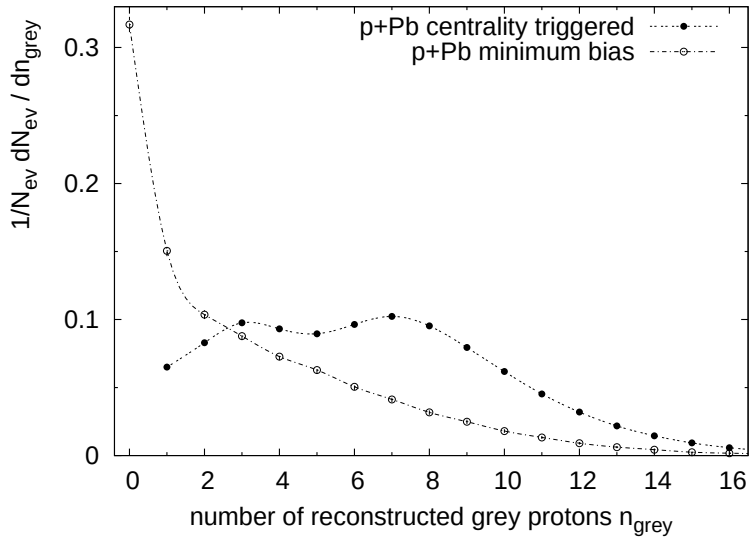

Figure 2.8: Distribution of grey protons measured in the minimum bias sample and in the sample of centrality triggered p+Pb interactions as measured by the NA49 experiment.

Using the active centrality trigger, NA49 is able to establish bins in the mean number of projectile collisions ν in p+Pb interactions ranging from 2.9 to 6.9 with comparable statistics in each bin (see Fig. 2.8 above and Tab. 5.4 on page 45).

This definition of centrality is different from the definition used in many minimum bias experiments where the only centrality measure available is the size of the nucleus A. To describe the centrality evolution of the cross sections in those cases, a $\sigma \sim A^{\alpha}$ scaling is often used. In this thesis the centrality dependence is extracted from a single large value of A, and therefore does not need to employ the A dependence.

Additionally, in the A^{α} parameterization the α depends on the size of the target nucleus A and its isospin composition, on both the projectile and the secondary particle type, and on its phase space variables such as x_F and p_T. This makes the interpretation of the α rather complicated. [39]

2.2.2 Intranuclear cascading: pions

In a p+A collision particles may also be produced due to propagation and further interactions of the participating nucleons in the target nucleus. It has been shown in [63] that pions produced in the intranuclear cascading contribute in the target hemisphere and this fraction decreases with increasing x_F. This contribution is at a few percent at $x_F = -0.1$ and consistent with zero at midrapidity.

This thesis deals with pion production at $x_F \geq 0$, therefore the cascading contribution is not considered in the data analysis.

2.2.3 Multiplicities in h+A interactions

Multiplicities of produced particles can be estimated by assuming that each of the nucleons involved in a p+A interaction – *participants* or *wounded nucleons* – contributes half of the multiplicity of a p+p interaction. At a given ν there is a contribution from ν participants from the target and one from the projectile fragmentation. This wounded nucleon model [74] predicts the following scaling for measured multiplicities N:

$$N^{\mathrm{p+A}}(\nu) = \frac{1 \cdot N^{\mathrm{p+p}}}{2} + \frac{\nu \cdot N^{\mathrm{p+p}}}{2} = (1+\nu) \cdot \frac{N^{\mathrm{p+p}}}{2} = w\frac{N^{\mathrm{p+p}}}{2} \tag{2.5}$$

where $\nu+1$ is the total number of wounded nucleons w. This simple superposition considers only the target and projectile fragmentation and disregards cascading contribution to the total multiplicity.

As seen in Fig. 2.3, target nucleons are only hit once, as in an "elementary" h+h collision, but the projectile suffered a multiple hit. Wounded nucleon scaling, as described by equation (2.5), assumes that there is no difference between particle production from fragmentation of a nucleon which was hit once and one hit multiple times.

The total multiplicities predicted by the wounded nucleon model [74] agree with the data within 20 – 30 %. In this work distributions of charged pions in the central and forward regions of phase space are studied. The effects of multiple collisions are investigated in later sections in a similar picture, allowing for enhancements due to multiple collisions.

2.3 A+A interactions

A collision of two nuclei is shown in Fig. 2.9. In A+A collisions each participating nucleon in both nuclei suffers a multiple hit, similar to the projectile in the case of p+A. The A+A collision is therefore symmetric, in contrast to an asymmetric p+A collision.

The number of participants in each nucleus n_{part} is also known as the number of participating pairs. From the point of view of each of the participating nucleons, the other nucleus is relativistically contracted, as described in the p+A case.

Considering a uniform flux of nuclei A incident on an A target, each of the participant projectiles scans the target nucleus, as in the p+A case. Therefore the distribution $\frac{\mathrm{d}N}{\mathrm{d}\nu}$ of the projectile participants in a minimum bias collision is equal in p+A and A+A configurations, as discussed in [79]. An example is shown in Fig. 2.10.

2.3.1 Spectators and intranuclear cascading

The presence of the forward spectator system is a peculiarity of A+A collisions, as compared to p+A interactions. The spectators leave the collision excited and further fragment, mostly

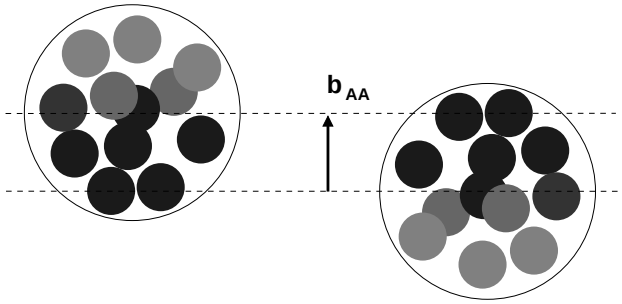

Figure 2.9: An A+A interaction at impact parameter $\mathbf{b}_{\mathrm{A+A}}$. In an A+A collision, each of interacting nucleons suffers a multiple collision. The same comment as in the p+A case applies to the relativistic contraction of the respective nuclei in the nucleon reference frame.

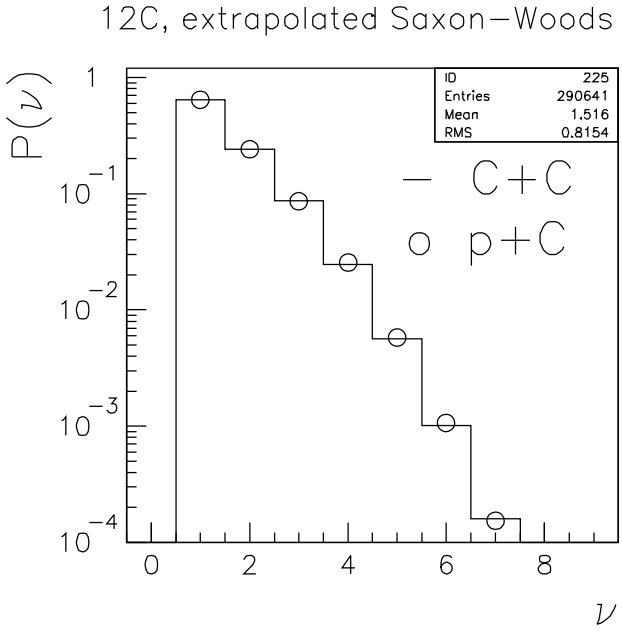

Figure 2.10: Probability distribution of the mean number of collisions ν per participant in minimum bias p+C and C+C reactions, simulated in [79] assuming Woods-Saxon density profiles.

into nucleons, deuterons and alphas. The size of this system is directly related to the centrality of the collision.

While the spectators are not deflected significantly from the path of the beam, some of them are excited slightly during the collision. The region of excitation is restricted to spectator nucleons close to participants in the edge layer of the projectile nucleus remnant, and these nucleons can be excited into low mass resonances, contributing to pion production in certain regions of phase space. This contribution decreases with increasing centrality, since the spectators turn into participants as the impact parameter decreases. For this reason, this contribution is negligible in the high centrality bin of Pb+Pb interactions which is studied in this thesis, and will not be further discussed.

2.3.2 Multiplicities in A+A interactions

Multiplicity of charged particles can also be used to characterize collision centrality, as it scales with the number of participants. There are $w = 2 \times n_{part}$ wounded nucleons in an A+A collision. The average event multiplicity $N^{\mathrm{A+A}}$ predicted by the wounded–nucleon model [74] is:

$$N^{\mathrm{A+A}} = \frac{n_{part} \cdot N^{\mathrm{p+p}}}{2} + \frac{n_{part} \cdot N^{\mathrm{p+p}}}{2} = w \cdot \frac{N^{\mathrm{p+p}}}{2} \tag{2.6}$$

The wounded–nucleon scaling does not take into account the effects of multiple collisions, nor the contribution from intranuclear cascading in the spectator system.

2.3.3 Centrality by multiplicity bins

The number of pairs of participants n_{part} in an A+A collision at a given impact parameter **b** can be estimated within a Glauber inspired geometrical picture, assuming a nuclear density profile and an "inelastic size" of a nucleon[5], [82], see Fig. 2.11.

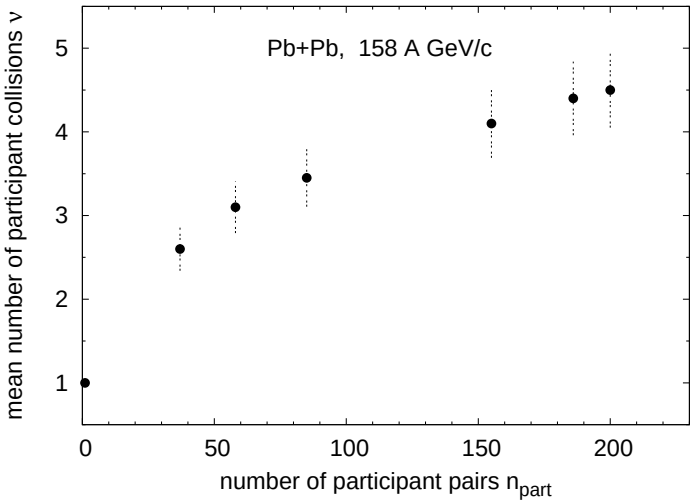

Figure 2.11: Relation between the number of participant pairs n_{part} and mean number of collisions ν. 10 % errors are indicated.

Every participant pair creates some multiplicity, which can be related to the multiplicities measured in p+p interactions in the first approximation of the wounded nucleon model (equation (2.6)). However, there is a moderate increase of multiplicity with ν which has been measured to be about 10 % of pion multiplicity in the projectile fragmentation in p+C [63] interactions and 10 – 30 % in different bins of centrality in Pb+Pb collisions [54]. This increase can be taken into account in a modified Glauber–like Monte Carlo calculation [79], and number of participant pairs n_{part} can be related to measured multiplicities in Pb+Pb interactions. This relation is shown in Fig. 2.12.

The multiplicity distribution in minimum bias Pb+Pb interactions is shown in Fig. 5.3 on page 45.

[5]As the mean number of inelastic collisions is of interest, the inelastic N+N cross section is used and the size of the nucleon is established using the black disc approximation as discussed above, see in Fig. 2.2. This "elementary" N+N cross section is typically assumed to be constant during the A+A interaction.

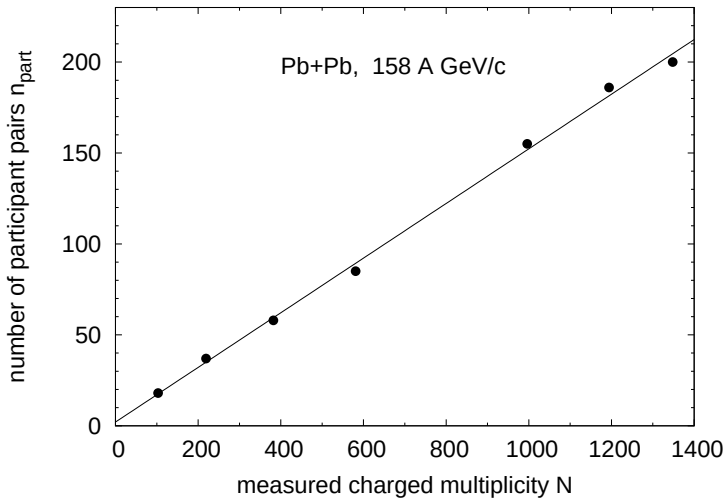

Figure 2.12: The relation between the measured multiplicity of charged tracks by NA49 and the number of participant pairs n_{part} estimated by a model [79]. The line indicates the linearity of the dependence.

Chapter 3

NA49 experiment

This chapter provides a short discussion of the NA49 experiment. A more detailed description can be found in [40].

3.1 Detector overview

The NA49 detector was built–up with the intention of studying hadron production in relativistic heavy ion collisions following the NA35 experiment. The preceding experiment investigated collisions of protons and intermediate mass ions like sulphur or oxygen with heavy ions by means of streamer chambers. The NA49 detector itself is located in the same place as its forerunner in the H2 line of the North experimental hall of the SPS accelerator in the Prevessin part of CERN.

The NA49 experiment was designed to study complex central Pb+Pb events with up to 1500 measured charged hadrons per event on an event-by-event basis. It was necessary to use a large acceptance detector with precise tracking, good track resolution and particle identification for this purpose.

These requirements have been fulfilled by means of five Time Projection Chambers (TPCs) as a primary charged particle tracking detector, the Centrality Detector (CD) for an independent estimate of h+A centrality, several Time of Flights walls, calorimeters, proportional chambers, scintillation counters and other sub-detectors. The detector diagram is shown in Fig. 3.1. It also shows the versatility of target options, which allows studies of h+p, h+A and A+A interactions using the same detector.

Due to the fixed–target geometry, particles produced from collisions at the SPS energy are emitted in a very narrow forward cone in the laboratory because of the large momentum of the center-of-mass system. This requires a strong and homogeneous magnetic field to spread the charged particles apart and to measure momentum through the curvature of the particle track in the field.

3.2 SPS accelerator

The protons and lead ions used by NA49 are accelerated in several steps by the CERN accelerator complex. The beam particles are created in ion sources. In the first step they gain energy in linear accelerators, then get injected into the Proton Synchrotron Booster where they are accelerated to 800 MeV/c for protons (94 A.MeV/c for lead ions). They are passed into the Proton Synchrotron (PS) and accelerated to 14 GeV/c (4.25 A.GeV/c). The final acceleration is done in the Super Proton Synchrotron (SPS), which is able to accelerate

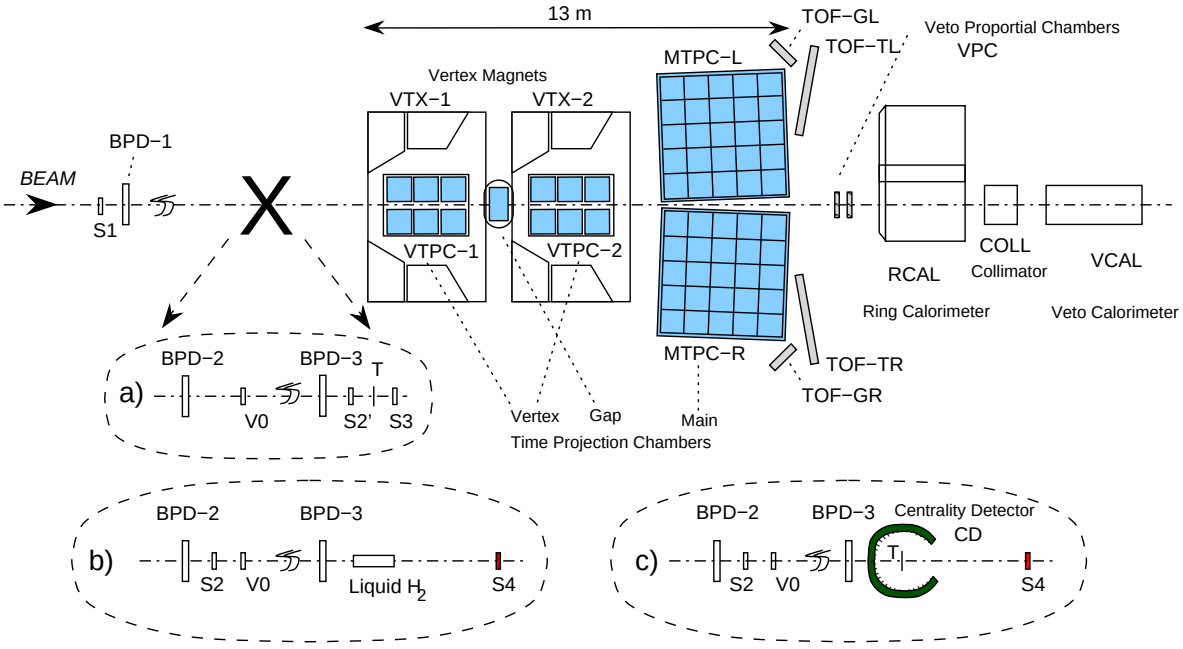

Figure 3.1: Scheme of the NA49 experimental layout, including different reaction configurations: a) A+A, b) p+p, c) p+A. The RCal is shown off center as used in the p+p and p+A runs.

protons to laboratory momenta of 400 GeV/c, intermediate mass ions of $A/Z = 2$ up to 200 GeV/c per nucleon and Pb ions up to 158 GeV/c per nucleon. The particles are delivered in short and separate spills, usually a 2.4 second spill every 14.4 seconds.

3.3 Beam particles and targets

NA49 uses two types of targets, either a foil (Pb, Si, Al, C, ...) or a cylindrical vessel filled with liquid hydrogen. Beam particles can be extracted directly from the SPS, or secondary beams can be formed from the products of an interaction of the beam with the fragmentation target – pions, kaons, or protons from a primary proton beam and deuterons and intermediate size nuclei up to phosphorus from a primary lead beam. The fragmentation target is placed about 150 m before the experimental one and the material used is 10 cm of beryllium for the proton, and 1 cm of carbon for the Pb primary beam. Figure 3.2 shows the fragment spectra of Pb ions, starting from boron.

This versatile experimental setup allows the examination of various types of hadron interactions. In this thesis pion production in p+p, p+C, p+Pb and Pb+Pb interactions is studied. Specifications of the targets used in p+p and p+A runs are shown in Table 3.1. In the case of p+Pb interactions a target very thin in terms of the interaction length was used to minimize grey proton absorption inside the target. For Pb+Pb collisions a 200 μm target of 1% interaction length was used. The A+A collisions are normalized exclusively per event, thus the target properties do not enter into the cross section determination.

In minimum bias p+p and p+A reactions the target length and density have to be determined precisely because they do enter into the absolute cross section normalization. The length of the hydrogen target was determined offline by fitting the vertex distribution of high multiplicity empty target events, separately for the different time periods when the p+p data were acquired. The resulting measurement with 0.25 % precision is shown in

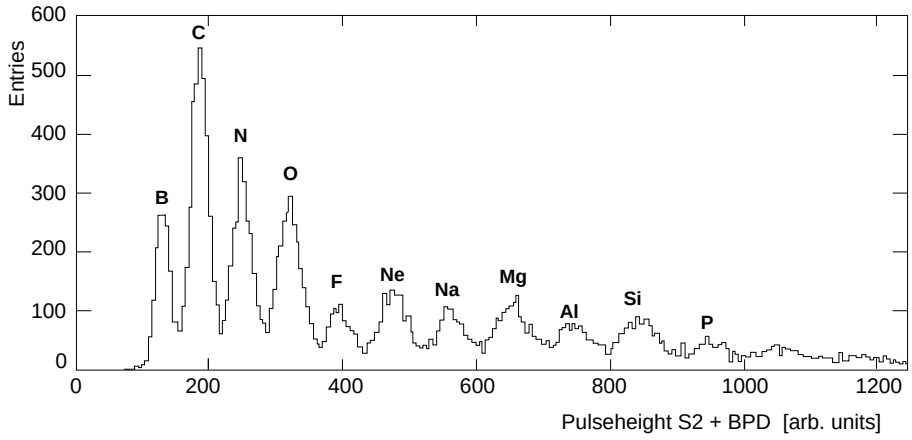

Figure 3.2: The fragmentation beams composition. Fragments lighter than boron not shown [40].

target type	proton	carbon	lead
length l [cm]	20.29	0.7	0.05
diameter d [cm]	3	0.6	0.6
density ρ [g/cm^3]	0.0707	1.83	11.35
atomic mass A [g/mol]	1.0079	12.0107	207.2
target interaction length [%]	2.8	1.5	0.28

Table 3.1: Specifications of targets used in p+p, p+C and p+Pb interactions.

Fig. 3.3. The carbon and lead targets were cut from an industrial foil with a precision of 1 μm. These targets were measured by a vernier micrometer to confirm the thickness.

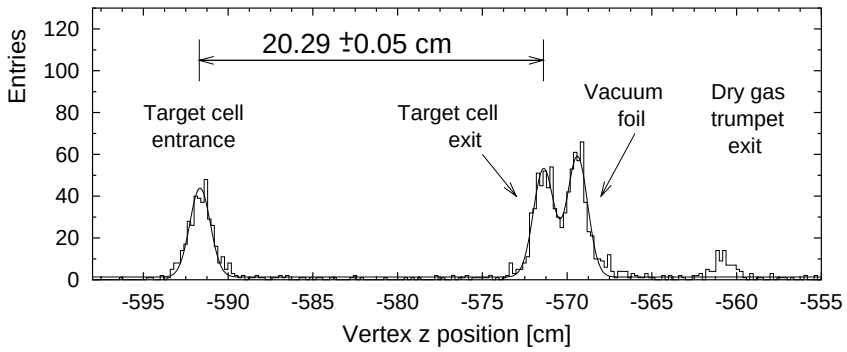

Figure 3.3: Main vertex distribution in high multiplicity empty target events measuring the length of the hydrogen target.

3.4 Beam definition and triggering

The precise measurement of the beam particle position and detection of its interaction for triggering is performed by a combination of Beam Position Detectors (BPDs), a ČErenkov Differential counter with Achromatic Ring focus, the CEDAR [42] and several scintillation detectors.

The CEDAR is about 100 m upstream of the experimental target. It measures Čerenkov rings produced in a gaseous medium by the beam particles emerging from the fragmentation beam further upstream with eight photomultipliers. Adjustable collimator and gas pressure allows selection of passing protons, kaons and pions with negligible background.

The transverse position of incoming beam particles is measured by three BPDs (BPD $1, 2, 3$ placed 33, 11 and 1 m upstream from the target). They are small ($3\times3\,\mathrm{cm}^2$) proportional wire chambers with two orthogonal cathode strip readouts. They are filled with a Ar/CH_4 80/20 gas mixture and have a resolution of $100\,\mu$m. The BPD signals are also used to select the desired fragments from the fragmentation beam by means of their specific ionization loss, $\mathrm{d}E/\mathrm{d}x$.

A system of four scintillation counters is used to provide exact timing and an interaction signal. Beam timing is defined by a coincidence between CEDAR (C), S1 and S2 scintillation detectors (34 and 10 m upstream) along with no signal in a ring shaped scintillator V0. A signal in V0 indicates an interaction of the beam particle before the target, either with air or with material from the detectors upstream. This combination of coincidences is denoted by $C \cdot S1 \cdot S2 \cdot \overline{V0}$.

A small scintillation counter S4 with a 2 cm diameter positioned 380 cm downstream from the target is used as a veto in order to trigger on interactions in the target. The beam signal along with no signal in S4 means that a valid beam particle reached the target but its track did not continue after the target, indicating that some interaction occurred. This is used for triggering. In the case of p+p interactions, about 86 % of the inelastic and 16 % of the elastic cross section gets triggered upon. More details about the contributions of the trigger cross sections for different reaction types are in Table 5.1 on page 42 in Section 5.2.2.

Each type of interaction requires slightly different trigger conditions. The Centrality Detector described below was included in the trigger during most of the p+Pb runs to increase the statistics of central collisions relative to the minimum bias trigger condition. The centrality comparison is shown in Fig. 2.8 on page 16.

The Pb+Pb data used for comparison in this thesis were obtained with a specific low intensity beam condition using a minimum bias trigger which captured 92 % of the total inelastic hadronic cross section. This trigger is based on a cut on the signal from a helium Čerenkov counter downstream of the target which eliminates non–interacting lead ions with a resolution of about 2 charge units of the total 82 in Pb.

3.5 Centrality detector

The Centrality Detector (CD) is a unique device developed by NA49 to measure the impact parameter in h+A collisions by grey proton counting, as discussed above in Section 2.2.1. It is shown in Fig. 3.4.

The CD is a cylindrical proportional chamber 12 cm in diameter and 20 cm in height surrounding the target with 256 pads each covering about 20 msterad solid angle. It has a forward window of $\pm$ 45 degrees in polar angle which corresponds to the acceptance of the TPC system. The detector is filled with a gas mixture of 80 % Ar / 20 % CH_4.

Protons below 150 MeV/c and nuclear fragments are absorbed by $200\,\mu$m copper foil between the target and proportional tubes. A threshold set in the electronics at 1.5 times the minimum ionization cuts off high momentum particles. A more detailed description of the CD can be found in [40], page 216.

Grey protons reconstructed in the TPCs in the momentum range between 0.15 and

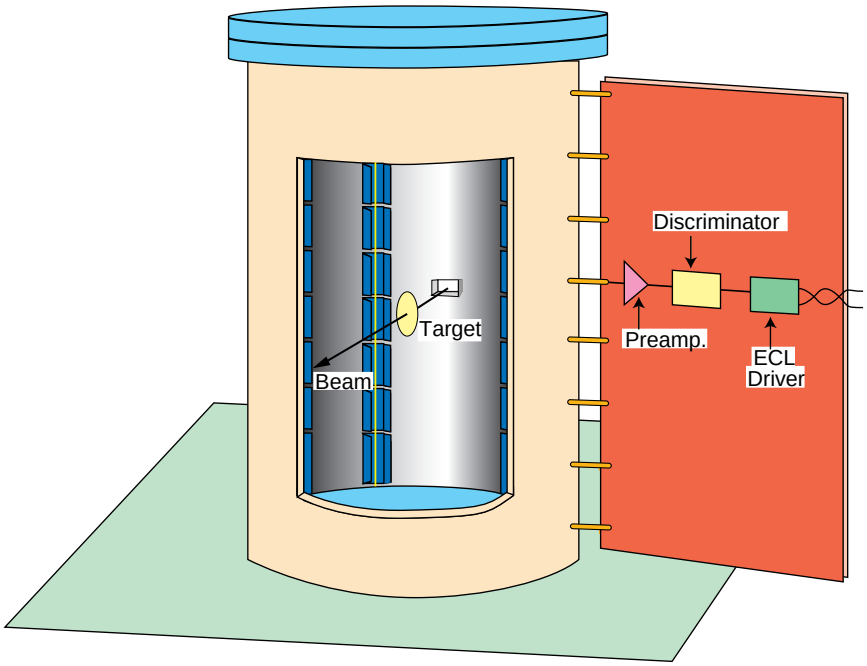

Figure 3.4: Centrality Detector

1.2 GeV/c are added to the number reconstructed in the CD during the event reconstruction. The resulting acceptance of grey protons is about 60 %.

The performance of grey proton counting using the CD is shown in Fig. 2.5 in the preceding section and in Fig. 3.6.

The number of collisions ν discussed in Section 2.2.1 can be related to n_{grey} using models. In this case a special version of VENUS 4.12 with intranuclear cascading was used [40], followed by a detailed GEANT simulation of the detector. This procedure induces some systematic uncertainty which is estimated by comparison to alternative model calculations to be about ± 10 % of the calculated value, see the shaded area in Fig. 3.5.

3.6 Magnets

There are two super-conducting Helmholtz-arranged magnets placed directly behind the target, the first with a field of 1.5 T and the second 1.1 T, generated by coil currents of 5000 A and 3500 A, respectively. The magnets are cooled by liquid helium.

The combined field provides a total bending power of 7.8 Tm giving a single charged particle a transverse kick of 2.3 GeV/c. The magnetic field maps were calculated numerically [47] and compared with a Hall probe measurement. Agreement on a 0.5 % level was found. [60]

This field allows for the determination of the particle momentum with a resolution on the order of $\Delta p/p^2 \sim 10^{-5}-10^{-4}$, which is sufficient for the inclusive cross section measurements presented in this thesis. Furthermore, adequate two track separation is achieved even for the highest centrality of Pb+Pb events.

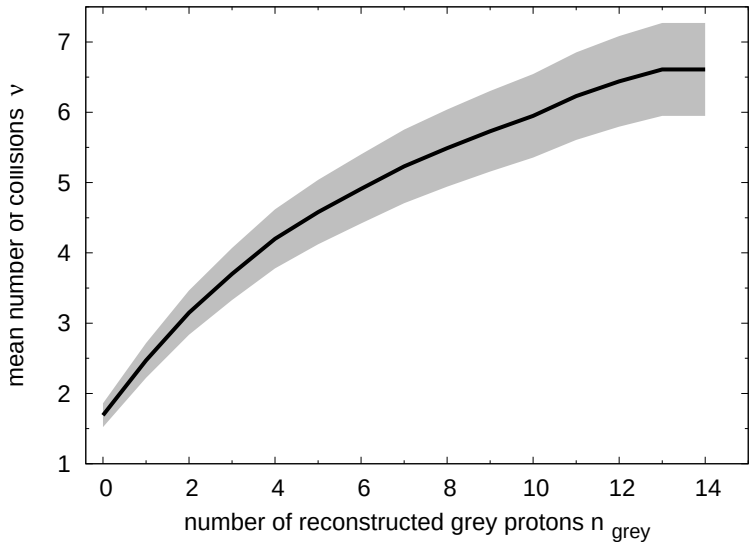

Figure 3.5: The relation between the number of grey protons n_{grey} measured in the detector and the mean number of intranuclear collisions ν in p+Pb interactions as estimated by VENUS 4.12 with intranuclear cascading in the simulation of the Centrality Detector. The shaded area corresponds to a systematic uncertainty of $\pm 10\,\%$ in the mean number of collisions.

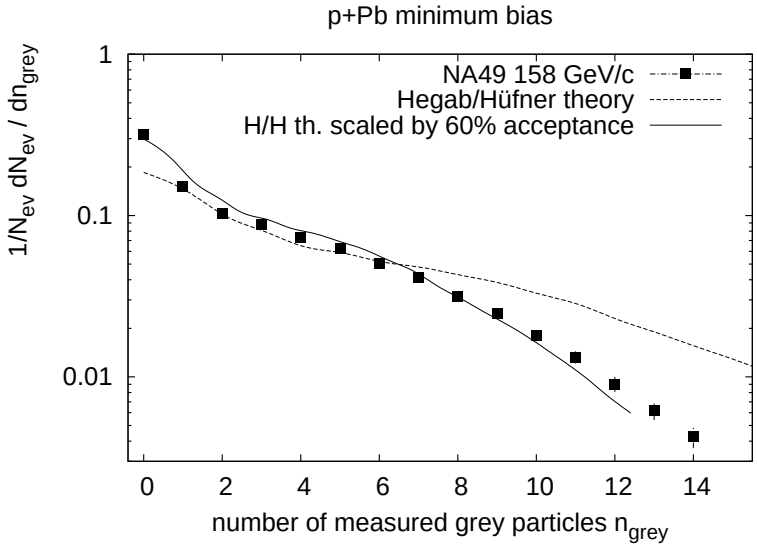

Figure 3.6: Distribution of grey protons in minimum bias p+Pb interactions measured by NA49 as compared to theory of Hegab and Hüfner [36]. To correct for the $\approx 60\,\%$ acceptance of our detector, the theoretical curve is scaled accordingly.

3.7 Time projection chambers

The Time Projection Chamber (TPC) is currently the most sophisticated detector employing gas ionization; it provides three-dimensional tracking ability and particle identification over a large volume.

The TPC consists of a large gas-filled sensitive volume and a multi-wire proportional readout section. The **sensitive volume** is surrounded by an electric field cage, which provides a constant drift velocity for electrons from ionization. On the top of the TPC there are **wire planes**, which provide multiplication of the charge from incoming electrons and gating. The **pad plane** consists of many small pads of various sizes, depending on the desired spatial resolution and expected track densities, where the charge is collected and read out.

3.7.1 Principle of operation

When a charged particle travels through the TPC volume, it ionizes gas molecules along its trajectory. Liberated electrons travel in the drift field up to the multi-wire readout chamber. In this region electrons are rapidly accelerated from the cathode plane towards the high-voltage sense wires causing an avalanche of electrons onto the wire. The charge is multiplied by the gas gain. The avalanches induce a voltage signal on the pads through their capacitive coupling. This pad signal is read out. The gating grid confines the ions in the multi-wire section after the avalanche, preventing them from drifting to the sensitive volume, distorting the drift field and reducing the signal by recombination. The principle of TPC operation is shown in Fig. 3.9.

The two horizontal coordinates are measured by the position of the pads and the vertical coordinate by the drift time, obtaining the charged track trajectory. If a TPC is placed in a magnetic field, track curvatures can be used to determine the momentum of the particle and its charge polarity. The specific ionization of a measured particle track is used to identify the particle.

3.7.2 NA49 TPCs

NA49 uses five TPCs. Two *Vertex TPCs* (VTPC1, VTPC2) are placed in the magnets, and two large *Main TPCs* (MTPCL, MTPCR) are on either side of the beam line further downstream. The fifth *Gap TPC* (GTPC) was introduced in 2001 to close the forward hemisphere by filling the acceptance hole due to the beam gap in VTPCs. The TPC system with over $45\,\mathrm{m}^3$ of sensitive volume constitutes the main part of the NA49 detector. A picture of a typical p+p event as seen from top in the TPC system is shown in Fig. 3.7.

In the center of the VTPCs there is a 20 cm wide blind region followed by a gap between the MTPCs. These gaps are necessary in heavy ion runs because of the extreme ionization of the lead beam, about $6{\cdot}10^3$ times the minimum ionizing particle, creating high energy knock-on electrons which spiral in the magnetic field and form a large background of charge deposits.

3.7.3 Field cages and construction

NA49 uses an innovative mechanical design for the field cage motivated by keeping the amount of the detector material as small as possible to minimize the probability of secondary interactions of the measured particles while maintaining mechanical and electrostatical

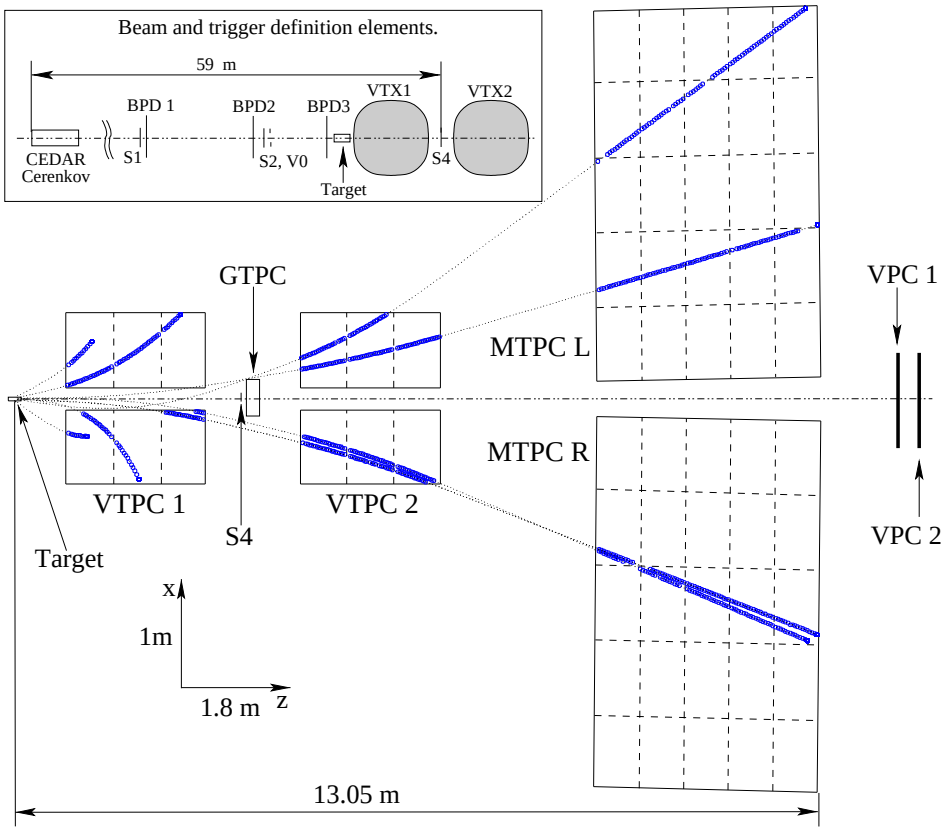

Figure 3.7: A typical p+p event measured by the NA49 TPC system. The open symbols correspond to measured points, and the dotted lines represent fit tracks. [61]

stability, homogeneity of the drift field and safe operating conditions in the presence of high voltage.

The field cage is constructed from 25 μm thick aluminized Mylar strips suspended on ceramic rods placed vertically in the cage corners. The strips are 12.7 mm wide, and 2 mm apart. They are interconnected via a resistor chain, which is grounded on the cathode plane and connected on its other end to the high voltage plane (at a potential of -13 kV – -20 kV), thus providing the homogenous electric drift field. A schematic drawing of the field cage assembly in the VTPC case is shown in Fig. 3.8.

The whole volume is enclosed by a gas envelope of double layer Mylar foil 125 μm thick. The space between the two foils is flushed by nitrogen to avoid oxygen and water vapor diffusion into the chambers. The field cages and the gas envelopes are mounted from below to massive aluminum support plates.

In the case of the GTPC the ceramic rods were replaced by glass-epoxy tubes 100 μm thick to minimize secondary interactions.

3.7.4 Readout chambers

As indicated in the detector overview figures, the NA49 TPCs are subdivided into sectors, called readout chambers. The TPC system has 62 readout chambers each with a surface of 72×72 cm. Each sector is a multiwire proportional chamber composed of a gating grid, a cathode plane, a sense and field wire plane and a segmented pad plane.

The gating grid isolates the readout chamber from the active detector volume. The drifting electrons are stopped, until there is a trigger signal. After the trigger and gas am-

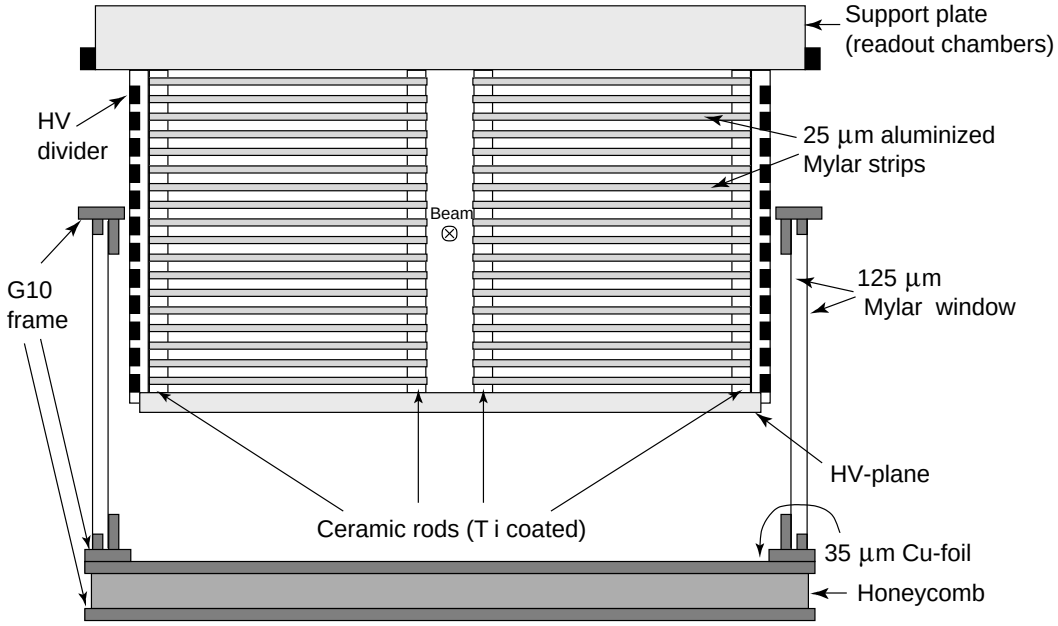

Figure 3.8: Schematic picture of a VTPC assembly, [40].

plification, it prevents ions created by the amplification from entering the sensitive volume and distorting the field. The cathode plane above the gating grid is grounded. The top wire plane consists of thin (20 μm in diameter) sense wires at 1.2 kV. The sense wires are interspaced by thicker (125 μm in diameter) grounded field wires. Electrons create avalanches in the radial electric field between the cathode and the sense wires. The avalanche charge is capacitively coupled to the pads in the pad plane. The induced signal on the pad plane is read out.

The pads are arranged in rows perpendicular to the beam direction, called padrows. There are 72 padrows for each of the VTPCs, 90 in the MTPC and 7 in the GTPC. This means the maximum number of padrows on a track passing through both VTPCs and one MTPC is 234, each padrow corresponding to one measurement of the charge deposit. The tracks analyzed in this thesis typically have hits on between 70 and 200 padrows. The pads are tilted with respect to the beam from 0^o to 55^o depending on the expected direction of the secondary tracks.

3.7.5 Alignment

The position of the NA49 TPC system with respect to the SPS beam coordinates is measured by optical methods with absolute precision better than 200 μm. This measurement is checked with multiple target runs and muon tracks accompanying the beam with magnets switched off. The vertical coordinate determined by the drift time is calibrated by measurements of the drift velocity to 10^{-4} relative precision in special drift velocity monitor detectors.

3.7.6 Gases used in the TPCs

There are different gases used in VTPCs and MTPCs. The choice of gas was made to optimize for two cluster resolution given by the diffusion coefficient and drift velocity, and for the quality of the ionization measurement influenced by electron attachment. Adding CO_2 reduces diffusion but increases electron attachment in the presence of oxygen or water

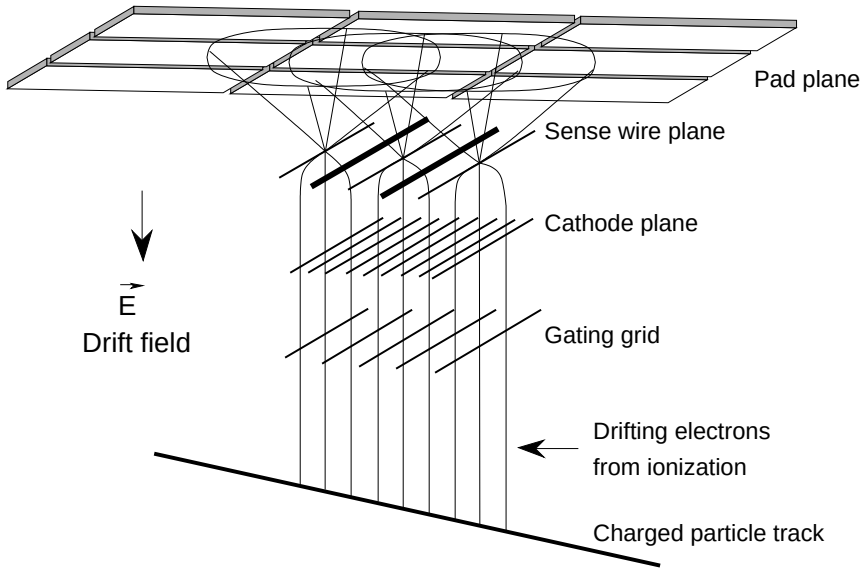

Figure 3.9: Schematic layout of the TPC readout section.

vapor. The MTPCs are filled with a mixture of 91 % Ar, 4.5 % CH_4, and 4.5 % CO_2. The VTPCs and the GTPC use 91 % Ne, and 9 % CO_2.

The gas gain factor is $2{\cdot}10^4$ in VTPCs and $5{\cdot}10^3$ in MTPCs.

	VTPC	**MTPC**	**GTPC**
Size [cm]	260 × 200 × 72	384 × 384 × 129	70 × 38.4 × 19.6
No. of pads	27 648	63 360	96
Pad size [mm]	3 × 28	3.13 × 39	4 × 28
		4.95 × 39	
Drift length [cm]	66.6	111.7	59
Drift velocity [cm/μs]	1.4	2.4	1.4
Drift field [V/cm]	200	175	200
Drift voltage [kV]	13	16.5	13

Table 3.2: NA49 TPCs parameters

A summary of the parameters of the TPCs used is shown in Table 3.2. Upper values of MTPC pad size are valid for the high-resolution sectors of the chamber, and the lower for the standard ones.

Momentum resolution $\Delta p/p^2$ of the TPCs varies from $7{\cdot}10^{-4}\,(\mathrm{GeV/c})^{-1}$ for tracks passing through VTPC1 only to $3{\cdot}10^{-5}\,(\mathrm{GeV/c})^{-1}$ for the global tracks detected in VTPCs and one MTPC.

Details about the TPC principles can be found in [43], [44]. The NA49 TPCs are covered in extensive detail in [40] and [45].

3.8 Veto proportional chambers

The Veto Proportional Chambers (VPC) were constructed in the summer of 1999, two years before the GTPC was introduced, to close the acceptance gap of the detector in the very

forward region, and to provide a charged particle information for fast proton measurement and neutron tagging in the Ring Calorimeter (RCal) described in Section 3.10.

The VPCs are two plane proportional chambers with a cathode strip readout. Each plane has two layers of crossed strips with a sensitive area of 80×160 cm. The strips are 2 cm wide with 1.6 mm spacing. They are placed in front of the RCal (Fig. 3.1).

The two–track separation efficiency of the VPC was found to be close to 100 % down to track separations of 4 mm, which is sufficient for p+p and p+A interactions. This resolution was further improved after the GTPC installation and integration. The longitudinal momentum resolution of forward protons measured by the RCal, GTPC, and VPC is $\Delta p_z/p_z \approx 0.025\,\% \times p_z[\mathrm{GeV/c}]$.

More details concerning the VPC design, construction and performance can be found in [60], and details of reconstruction software and performance with the GTPC in [98].

3.9 Time of flight detectors

NA49 uses several Time of Flight (ToF) detector systems. They were intended to improve kaon identification in momentum regions where $\mathrm{d}E/\mathrm{d}x$ information from the TPCs is limited due to the overlap of energy loss distributions.

There are two pixel scintillating walls (TOF-TL and TOF-TR in Fig. 3.1), covering 4.4 m^2 with 1782 pairs of rectangular scintillators and photo-multipliers. The detector has a 60 ps time resolution.

Detector walls TOF-GL and TOF-GR are designed differently from TOF-TL and TOF-TR. These walls are made of two plates of horizontally and vertically oriented scintillating rods, each of them with photo-multipliers at both ends. Time resolution of this detector is 85 ps.

Due to calibration problems in the low multiplicity p+p and p+A collisions, the ToF information is not used in this analysis.

3.10 Calorimeters

The NA49 experiment is equipped with two calorimeters – the Ring Calorimeter (RCal) and the "zero–degree" Veto Calorimeter (VCal). Both of them have an electromagnetic and a hadronic section. They have been used in many CERN experiments, starting with NA5 [41].

The RCal is cylindrical with an inner diameter of 56 cm and outer diameter of 3 m. It is divided into 10 radial rings and 24 azimuthal sectors, forming 240 cells. The calorimeter has an electromagnetic section in front, made of a lead and scintillator sandwich 16 radiation lengths thick, followed by a hadronic section made of iron and scintillator layers 6 interaction lengths thick. It has an energy resolution of $\sigma(\mathrm{E})/\mathrm{E} = 1.2/\sqrt{\mathrm{E[GeV]}}$.

The RCal is used to measure transverse energy in heavy ion collisions. The detector is symmetrical around the beam, which goes through the bore in its center.

In runs with a pion or a proton beam the detector is shifted transversely with respect to the beam axis, meaning its active volume is placed behind the gap between the MTPCs in order to measure particles emitted in the very forward direction. The detector is used for measuring leading baryon energy and is used with the VPC to decide if the baryon is a protons or a neutron. Combined information from the RCal sections and the VPC distinguishes pions from electrons with high momentum, $p \gtrapprox 50\,\mathrm{GeV}$.

The VCal is divided into 4 rectangular cells. Its electromagnetic lead/scintillator section 16 radiation lengths thick is followed by an iron/scintillator hadronic section 7.5 interaction lengths thick. Its resolution is $\sigma(\mathrm{E})/\mathrm{E} = 1.0/\sqrt{\mathrm{E[GeV]}}$.

The signal from the VCall 20 m downstream is used to trigger on central A+A collisions. The centrality of an event can be selected by the energy of the fragments of the beam heavy ion: the higher the centrality, the smaller is the projectile remnant and the less energy gets deposited in the VCal. To increase the resolution of the fragment's energy deposit there is an iron collimator (Coll in Fig. 3.1) in front of the VCal.

3.11 Data acquisition and readout electronics

The SPS delivers accelerated particles in spills of 2-5 seconds every 14-20 seconds, depending on the beam type. During the spill, the data are stored in temporary buffers, accumulating 20–33 events per spill. Within the pause between the spills, the data are transferred to tape. This allows $\approx$ 1 million events per week of running time. Each running period is divided into *runs*, chunks of around 10^4 of events. Information specific to the experimental conditions is recorded for each run.

3.11.1 NA49 electronics

The electronics of the NA49 experiment is composed of many units and computers. All the necessary devices in the counting house are located in about 30 standard 19" racks.

By far most of the information collected by all of the subdetectors comes from the TPCs. The raw size of one event can be estimated: 182 016 pads $\times$ 512 time slices $\times$ 1 byte = 89 MB. This amount of information is progressively reduced in the consecutive stages of readout. The TPC readout utilizes custom VLSI[1] technology to handle the complexity of the electronics and the large number of individual channels.

Signals from the pads are collected by the Frond End (FE) cards mounted directly on the readout chambers. Each pad signal is amplified, sampled and digitized into 512 time slices during the 50μs open time. The digitized information arrives to Control and Transfer (CT) cards, located close to the FE cards, which multiplex and send the information to the counting house via high speed optical links. VME based custom receiver boards perform zero suppression by rejecting signals falling below a specified threshold. Even after this reduction, a typical raw event size is about 8.5 MB for a central Pb+Pb collision and about 2 MB for lower multiplicity p+p or p+Pb interactions.

Data from the BPDs, the VPCs, the trigger system, the calorimeters and the slow controls are read out using CAMAC modules, the ToF is read out using a FASTBUS system. The information from all the sub–detectors is collected in the VME master crate which controls the data acquisition (DAQ). This crate contains a module with a master processor[2] that builds the event and writes it to a 100 GB SONY tape with a transfer rate of 16 MB/s. Events can also be sent via a FDDI link to workstations in the counting house for online monitoring. Raw data are then stored in CERN's tape library and later moved to the CASTOR[3]. A more detailed description of the NA49 readout and data acquisition can be found in [45] and [46].

[1] Very Large Scale Integration, the process of creating integrated circuits on a single chip.

[2] equipped with Motorola 68040 CPU

[3] CASTOR is CERN Advanced STORage manager that provides a transparent file-like access via a unique name space to data stored on tapes with automated temporary disc caching. This allows to easy access the terabytes of data produced by the experiments. The CASTOR replaced the old SHIFT facility

3.12 Event reconstruction

The **reconstruction chain** (RC) is a complex collection of software that analyzes the raw data to find tracks. This software evolved over ten years. The main steps are described in this section.

3.12.1 Cluster finding

The deposited ionization charge is smeared due to diffusion in the TPC drift volume and non-ideal detector response, therefore the points of the track will appear as clusters of charge values. The position of each cluster is determined by the center of the charge distribution. In the VTPCs the measured space points are corrected for distortion induced by inhomogeneities in the magnetic field and the resulting E×B effect.

3.12.2 Tracking

The reconstruction of tracks is performed in two steps. First the space points found by the cluster finder in each of the TPCs are linked together forming a local track. In the second step these pieces corresponding to the trace left by a particle are merged into one *global track*, using the precisely determined relative geometry of the TPCs.

3.12.3 Main vertex finding

The most probable position of the primary interaction, the main vertex, is found by an iterative algorithm. The point of closest approach is searched for, sequentially removing outlying tracks. Information from BPDs constrains the transverse coordinate of the main vertex.

The dependence of the longitudinal vertex resolution on the event track multiplicity is important in elementary and p+A interactions due to ordinarily lower multiplicity of events than in Pb+Pb collisions, as many low multiplicity events contain only few forward tracks with a small beam crossing angle at the vertex position. This is also true for the empty target contribution, which typically has fewer reconstructed tracks. The inevitable presence of empty target events in the analyzed samples is corrected for using the empty target correction described below.

3.12.4 V^0 finding

Although most of the tracks come from the primary interaction vertex in the target, some are traces of strange neutral[4] particle decays, mainly Λs, K^0_ss, and photon conversions. A V^0 finder is used to find such tracks, calculate the secondary vertex position and assign these V^0 decay tracks to a secondary vertex.

The tracks originating from the weak decays of both neutral and charged strange particles that remain fit to the vertex are known as feed down particles. This contamination is corrected for by the feed down correction as described in a later chapter.

---

and is being developed to meet future requirements of the LHC experiments, including integration into Tier-2 centers.

[4]The decay of a charged particle causes a kink of the track, which can be detected by the tracking routine, depending on the kink angle.

3.12.5 Momentum determination

Assuming that all reconstructed tracks originate from the determined position of the main vertex, their trajectories are fit and their momentum determined. Tracks inconsistent with the main vertex constraint are rejected.

3.13 NA49 data standards

The NA49 experiment was the largest raw data producer at CERN in the 1990's, generating about 10 TB of raw data per running period, near the order of magnitude expected from the LHC experiments. Storing huge volumes of data was a challenge. The first few years of ROOT[5] development were done using the NA49 data samples.

3.13.1 DS PACK and DSTs

The NA49 data sets are stored in an object-oriented client-server database named DS PACK. There is information about all the tracks in events, their points, secondary vertices found by the V^0 finder, and information from all the non–TPC detectors. These data are stored on Data Summary Tapes (DSTs) and the relevant files holding the information are called bigDSTs. Details about the DS PACK and the relevant object definitions can be found in [46] and [48].

The DS PACK format was used both for the raw data and for the reconstructed events. During the years 2001 and 2002, the reconstructed sets have been transformed to ROOT files, called miniDSTs.

These formats are however not suitable for all the kinds of physical analysis due to their huge size: the typical size of a sample of one million events would be a few TB for the bigDST and over ten GB for the miniDST files.

3.13.2 μDST

The μDST data format contains only well reconstructed tracks originating from the main interaction vertex, retaining only the information needed in most analyses and keeping the size manageable for analysis performed on a single computer. The typical size of a μDST is a few hundred MB.

Each μDST is a simple ASCII file that contains event–by–event information about reconstructed tracks. There is an event header containing run number, event number, vertex position and number of tracks in the event.

There is information about each track on its momentum, charge, measured $\mathrm{d}E/\mathrm{d}x$ losses, appropriate relative variance $\sigma_{\mathrm{exp}}^{\mathrm{d}E/\mathrm{d}x}$ and tags distinguishing fast forward particles, mainly protons and neutrons, using combined information from the GTPC, VPC and RCal.

[5] ROOT Object Oriented Data Analysis Framework, `http://root.cern.ch`

Chapter 4

Particle identification

The NA49 detector offers several means of particle identification. This study is focused on charged pions, which are identified via specific ionization in the TPC system over most of the forward hemisphere. A standard method developed over the years is used.

4.1 Particle identification via specific ionization

The specific energy loss of a particle at a given momentum due to ionization in a gas medium depends on its mass and thus can be used for identification. The dependence of the particle's energy loss on its $p_{lab}/(mc) = \beta\gamma$ is given by the Bethe-Bloch formula:

$$-\frac{\mathrm{d}E}{\mathrm{d}x} = 4\pi N_A r_e^2 m_e c^2 \frac{Z}{A}\rho\frac{1}{\beta^2}z^2\left(\ln\frac{\sqrt{2m_e c^2\beta^2\gamma^2 T_{max}}}{I} - \beta^2 - \delta(\beta)\right) \tag{4.1}$$

where N_A is Avogadro's number, r_e a classical electron radius, m_e an electron mass, Z and A the atomic numbers of the medium, ρ the density of the medium, z is the charge of the projectile, I the average ionization energy, T_{max} the maximum energy transfer to an electron in the ionization process, and the δ parameter describing saturation at relativistic energies.

The Bethe-Bloch formula as a function of particle $\beta\gamma$ is shown in Fig. 4.1. Its general feature is decrease as $\sim \beta^{-2}$ in the nonrelativistic area. It reaches a minimum at $\beta\gamma \approx 3$, then rises as $\sim ln(\beta\gamma)$ up to saturation at $\beta\gamma \gg 10^3$. The region of the relativistic rise is used for identification in this study.

The process of ionization has two components: primary ionization electrons resulting from random collisions of the charged particle with the gas media and secondary ionization caused by sequent processes. This second component introduces a tail into the distribution of energy loss. The sum of all the ionization contributions forms a Landau distribution, which is a wide asymmetric distribution with a long tail towards the higher values. [43].

4.2 $\mathrm{d}E/\mathrm{d}x$ measurement

The TPC system measures the charge deposits along the track trajectory, each cluster corresponding to a few centimeters of the track length, a quantity proportional to the specific energy loss $\mathrm{d}E/\mathrm{d}x$. The standard method of $\mathrm{d}E/\mathrm{d}x$ calibration and measurement is used. The method is explained in detail in [60] and [59]. Some basic principles are discussed.

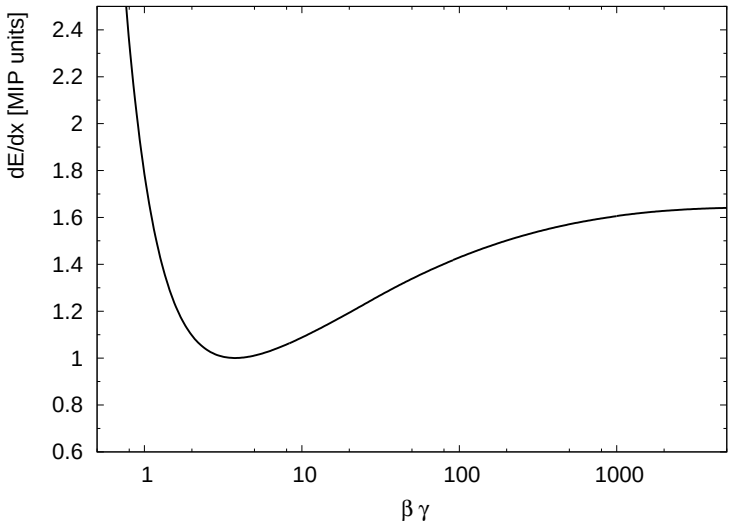

Figure 4.1: Example of the Bethe-Bloch function as a function particle velocity.

4.2.1 Truncated mean

Due to the long tails of the above mentioned Landau distribution, the use of a simple mean of the measured charge deposits is not an optimal method. To optimize resolution of the $\mathrm{d}E/\mathrm{d}x$ measurement, the method of *truncated mean* is used. A defined subsample of ionization measurements is selected to form the mean. A MC simulation proved that the optimal choice is to average the lower half of a sample ordered by increasing charge. This improves the $\mathrm{d}E/\mathrm{d}x$ resolution by about 20 %. The truncation transforms the Landau distribution into an approximate Gaussian distribution if the number of the samples is above 30. This truncation produces a non–linear transformation of the Bethe-Bloch function, which is taken into account by using a distorted approximation of the function.

4.2.2 $\mathbf{d}E/\mathbf{d}x$ calibration

The first step in the electronic channel gain calibration is done by the krypton calibration method. A small amount of radioactive ^{83}Kr is injected into the detector gas. Successive decays of the ^{83}Kr isotope produce a characteristic spectrum of energy deposits from electrons and photons, allowing for relative channel calibration. This way the dead or aging channels and electronics chips can also be detected and removed from reconstruction (and later repaired). The clusters produced by krypton decay contain higher charge deposits than clusters formed by ionizing particles in collisions. This calibration necessitates decreased voltage on the sense wires to avoid overflows in the readout, and therefore is applicable only as a relative calibration within a TPC sector, as the different readout chambers differ in details of construction and have separate high and low voltage power sources.

The next step in the calibration involves correcting the cluster charges to compensate for detector effects:

- The gas gain in a TPC system depends on gas density, and therefore on variations of temperature and pressure. The TPCs are under atmospheric pressure which is monitored while taking data and is used for offline gain correction. The TPCs are housed in an air conditioned environment stabilizing the temperature to within ± 0.1 °C. However, there are still variations in the gain corresponding to the day/night cycle, slow

gain drift possibly due to imperfect corrections of the pressure dependence and possible variations in the voltage of the readout chambers. To eliminate these effects a correction that follows the time dependence of the measured gas gain was applied.

- The charge collected at the pad plane depends on the relative angle between the track and the pad. The pads on the readout plates are tilted to follow typical expected directions of the produced particle tracks. Other tracks may differ in the crossing angle, thus the collected charge is smaller than in the optimal case. There is a geometrical correction applied to correct for this effect.

- The electrons from ionization drift up a long distance in the TPC volume (Table 3.2), until they reach the readout chamber. While drifting they can get lost due to attachment to water or oxygen molecules. The loss can reach up to 2 % in the VTPCs and 4 % in MTPCs and is corrected for.

- A more complex problem arises from combination of the above effects, diffusion of electrons as they drift upwards and losses due to threshold in the readout electronics. Diffusion of electrons increases the cluster width. Due to a fixed threshold of 5 ADC counts in the electronics implemented to suppress noise and zeros, edges of the clusters get lost. These losses can reach up to 20 % and were corrected for by a complex Monte Carlo simulation.

These corrections are applied separately in each of the 62 sectors of VTPCs and MTPCs. The GTPC is not used for the $\mathrm{d}E/\mathrm{d}x$ measurement, as it gives only up to seven measured points. To normalize the gas gain among different sectors, meaning to calculate sector constants, an iterative algorithm is used. In each iteration the preliminary particle identification is performed by sharp cuts around the Bethe-Bloch function. Corresponding clusters are found in each sector separately. Their charges are normalized by the corresponding Bethe-Bloch function. The truncated mean of these values is used as a preliminary sector constant.

The truncated means of energy deposits are calculated separately for the two gases. In order to combine samples from the VTPCs and the MTPC, the value from the MTPC is transformed using a linear function to the corresponding value of the VTPC. The mean of these two values, weighed by their respective resolutions, form a "global $\mathrm{d}E/\mathrm{d}x$".

The resulting energy loss distribution for a sample of tracks produced in p+Pb collisions is shown in Fig. 4.2 as a function of laboratory momentum. Bands for protons, kaons and πs are clearly visible. The $\mathrm{d}E/\mathrm{d}x$ resolution can be parameterized by: [61]

$$\frac{\sigma(N_c, \mathrm{d}E/\mathrm{d}x)}{\mathrm{d}E/\mathrm{d}x} = \sigma_0 \frac{1}{N_c^{\beta}} (\mathrm{d}E/\mathrm{d}x)^{\alpha} \tag{4.2}$$

where N_c is the number of clusters on a track and σ_0, α and β are the parameters which have been determined to be:

$$\begin{aligned} a &= -0.39 \pm 0.03 \\ b &= 0.50 \pm 0.01 \\ \sigma_0 &= 0.352 \end{aligned} \tag{4.3}$$

This results in a relative $\mathrm{d}E/\mathrm{d}x$ resolution of 3–4 % for the tracks used in this study.

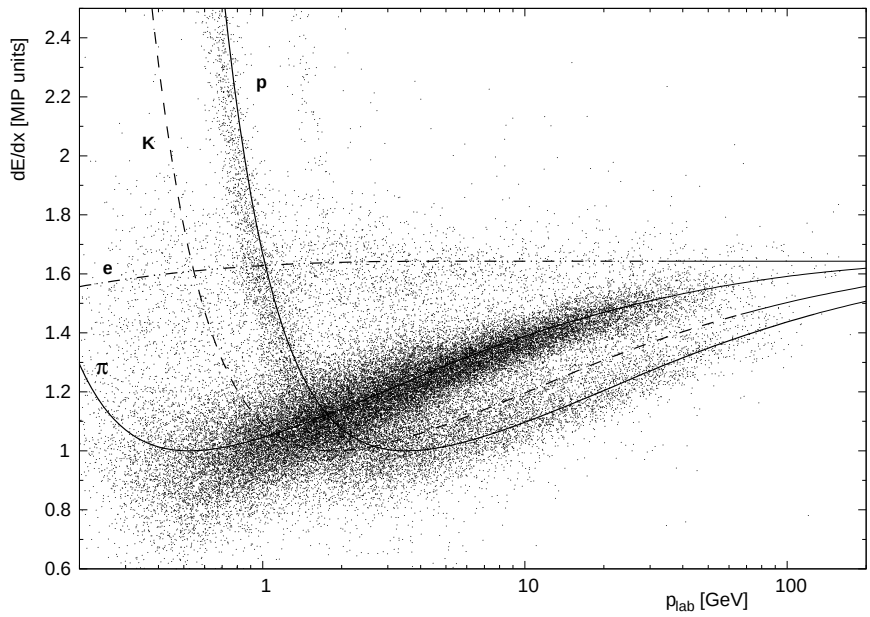

Figure 4.2: Bethe-Bloch function approximation for pions, electrons, kaons and protons as a function of total laboratory momentum along with measured ionization deposits for 50 000 tracks produced in p+Pb collisions.

4.3 dE/dx fitting

Particle identification is achieved by fitting the dE/dx distribution of tracks within a small momentum bin by a superposition of skewed Gaussians with variances determined for each track. For each particle type (protons, kaons, pions, electrons) variations are determined from the number of points left in detector by each track, thus taking proper care of resolution variation over the studied bin. Two typical examples are shown in Fig. 4.3. The skew in the Gaussians was introduced to take the distortions created by the truncation into account.

The fit has nine parameters: yields of the four particle types (p, K, π, e), shifts of the four probe functions relative to the determined Bethe-Bloch curve and the σ_{rel} parameter describing relative width of the fitting distributions. The resulting fit function is a sum of these four distributions.

Iterative fitting using the nine parameters is performed by minimizing the χ^2 of the fit to find the optimum description of the dE/dx distribution. The χ^2 as a function of the fit parameters A^k (k=(1..9)) is usually:

$$\chi^2 = \sum_i \frac{(m_i - T_i)^2}{\sigma_i^2} \tag{4.4}$$

where i denotes the bins of the dE/dx distribution, m_i is the measured number of entries in each of the bins, σ_i is the error of the bin content ($\sim \sqrt{m_i}$) and T_i is the fit function determined by the nine parameters.

The above expression is valid only if the number of entries in the bins is large enough ($m_i \gg 1$). If the bins contain only a few entries, or even zero, the following formula is valid:

$$\chi^2 = 2 \sum_i (T_i - m_i + m_i \ln(m_i/T_i)) \tag{4.5}$$

This standard procedure of dE/dx fitting is described in detail in [60, 98].

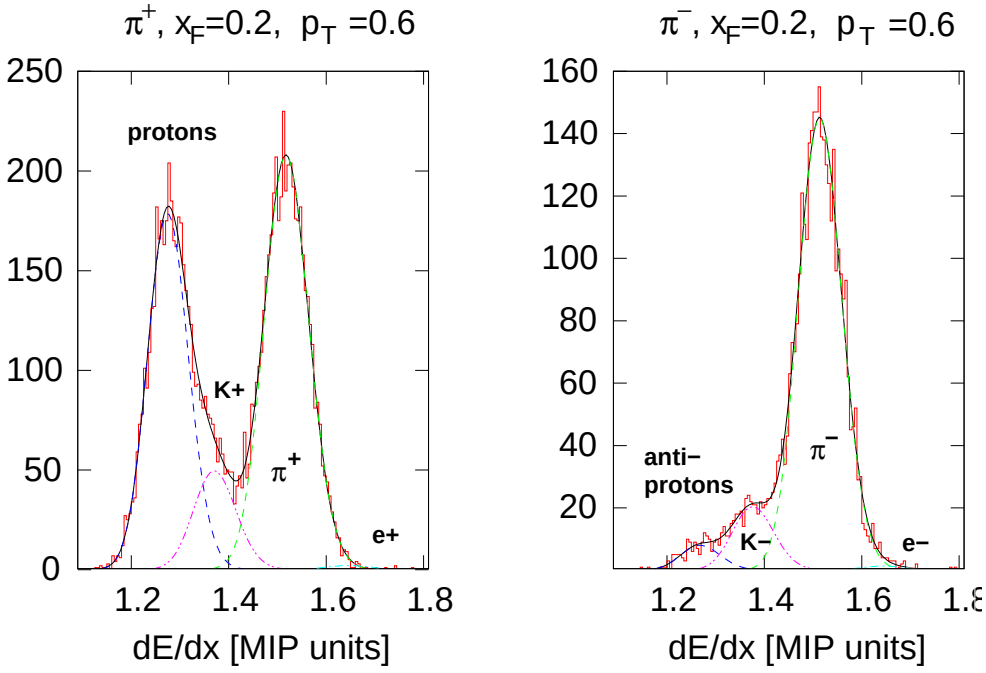

Figure 4.3: $\mathrm{d}E/\mathrm{d}x$ spectrum in a x_F/p_T bin for positive and negative secondaries. p_T is given in GeV/c.

The shifts and relative resolution are a consequence of local imperfections of the Bethe-Bloch functions discussed above, detector related imperfections in the elaboration of local calibration, magnetic field effects and pulse formation in the readout electronics. The shifts are typically on the order of 0.01 in the $\mathrm{d}E/\mathrm{d}x$ scale shown in Fig. 4.2.

The region of p_T below 300 MeV at $x_F = 0$ is difficult to analyze as this region corresponds to total lab momentum below 3 GeV, where the Bethe-Bloch functions describing specific energy loss of pions, protons and kaons approach each other, as shown in Fig. 4.2. Furthermore, the number of measured points per track reduces significantly in this region, decreasing the $\mathrm{d}E/\mathrm{d}x$ resolution. This led to a choice of a small bin size to reduce variance of the Bethe-Bloch function over the bin size.

To obtain cross sections in this region, straight forward assumptions about the behavior of K/π and p/π ratios as a function of p_T have to be made, introducing systematic uncertainties which are absorbed in the given statistical error.

Chapter 5

Cross section extraction

5.1 Total cross section of hadronic interactions

The total interaction cross section σ_{tot} is one of the basic hadronic observables. In elementary h+h interactions it is composed of elastic σ_{el} and inelastic σ_{inel} contributions, clearly distinguished by particle production in the inelastic case.

$$\sigma_{tot}^{\mathrm{h+h}} = \sigma_{el} + \sigma_{inel} \tag{5.1}$$

In h+A collisions there is a third quasi-elastic contribution $\sigma_{quasi-el}$, corresponding to collisions where a projectile elastically scatters off a target nucleon, yielding no meson production but disintegrating the nucleus.

Pure elastic (sometimes called "coherent") h+A scattering happens when the projectile interacts with the whole target nucleus, leaving it intact. The total nonelastic cross section is known as the absorption cross section σ_{abs}.

$$\sigma_{tot}^{\mathrm{h+A}} = \sigma_{el} + \sigma_{quasi-el} + \sigma_{inel} = \sigma_{el} + \sigma_{abs} \tag{5.2}$$

The situation gets further complicated in relativistic heavy ion collisions, where the strong electromagnetic interaction between the nuclei dominates the total cross section, causes dissociation of the nuclei and can even lead to particle production. [65]

The normalization of particle production cross section can be performed in two ways. Either by relating it to the total inelastic cross section in the minimum bias case, yielding millibarn values, or selecting a sample of specific events and normalizing the cross section per event.

5.2 Total inelastic cross section and event definition

The invariant inclusive cross sections of particle production is normalized per inelastic event by referring to the total inelastic cross section σ_{inel} in minimum bias p+p and p+A interactions. In triggered experiments such as NA49, an interaction trigger has to be designed so that it comes as close as possible to the total inelastic cross section. This issue and the resulting measurements of inelastic cross sections is discussed in the following sections.

In centrality selected interactions, the bulk of data discussed in this thesis, the definition of the corresponding reference cross section is problematic as it depends on details of the experimental setup such as particularities of grey proton counting, acceptance for the

charged multiplicity measurement, etc. A comparison of different experiments and theoretical predictions therefore has to rely on an independent parameter characterizing each event sample. In this case this parameter is given by the number of collisions of the projectile proton in p+A interactions and per participant nucleon in A+A reactions. In these cases, invariant particle densities (Section 5.4) per triggered event in the respective sample are given, rather than absolute millibarn cross sections.

5.2.1 Trigger cross section

Beam protons were selected by the coincidence $C \cdot S1 \cdot S2 \cdot \overline{V0}$ yielding the beam rate R_{beam}. Interactions were triggered in minimum bias runs by the coincidence $C \cdot S1 \cdot S2 \cdot \overline{V0} \cdot \overline{S4}$ or $C \cdot S1 \cdot S2 \cdot \overline{V0} \cdot \overline{S4} \cdot CD$ in centrality triggered runs as discussed in Section 3.4. The trigger conditions delivered interaction rates R_{FT} for full target and R_{ET} for empty target measurements for each interaction type and trigger setting. The corresponding cross section of the trigger is calculated by the formula:

$$\sigma_{trig} = \frac{P}{\rho \cdot l \cdot N_A/A} \tag{5.3}$$

where ρ is the target density, l the target length, N_A the Avogadro number and A the target atomic number. Numerical values for different targets are given in Table 3.1, page 23.

The interaction probability P is extracted from the measured beam and interaction rates R_{beam}, R_{FT} and R_{ET}, taking into account exponential beam attenuation when traversing the target, reduction of beam intensity due to interaction upstream of the target, reduction of the downstream interaction probability when the target is full and the content of the target when it is empty (gaseous hydrogen in the proton target case and mostly argon in the case of carbon and lead). Neglecting higher order terms, the following formula is used [61]:

$$P = \frac{R_{FT} - R_{ET}}{R_{beam}} \left(1 + \frac{R_{FT} - R_{ET}}{2R_{beam}} + \frac{R_{ET}}{R_{beam}} + \frac{\rho_{ET}}{\rho}\right) \tag{5.4}$$

Both the carbon and lead targets have a diameter of only 6 mm to minimize energy loss of the grey protons at large angles. This diameter is small enough for some beam particles to miss the target without hitting the S4. These losses were measured to be 3.3 % of the trigger cross section in these interactions and corrected for.

5.2.2 Estimation of total inelastic cross section

The measured trigger cross section can be used to establish the total inelastic cross section, providing a consistency check with earlier measurements, as discussed in [61], [62], [81].

The trigger cross section of measured interactions, after correcting for beam attenuation inside the target and projectiles barely missing the target, is shown in Table 5.1. It has to be further corrected for event losses due to an accidental hit of S4 by a secondary particle, vetoing the event. Most of these losses are caused by a diffractively scattered proton. The trigger accepts the high p_T tail of elastic scattering which has to be subtracted. Respective cross section values were calculated by Monte Carlo calculations and are summarized in the following table. The error on the trigger cross section determination is estimated to be 2 %.

interaction type	p+p	p+C	p+Pb
σ_{trig}	28.23 mb	210.1 mb	1737 mb
loss from p	3.98 mb	17.1 mb	59 mb
loss from π and K	0.33 mb	2.4 mb	5 mb
contribution from σ_{el}	-1.08 mb	-3.3 mb	neglected
predicted σ_{inel}	31.46 mb	226.3 mb	1806 mb
literature value	31.78 mb	225.8 mb	1768 mb*

Table 5.1: Measured trigger cross sections in minimum bias p+p, p+C and p+Pb interactions, estimated event losses due to produced particles, and predicted inelastic cross section and its literature value, [61], [62], [81].
*) Older data of Bellettini [84] and Ashmore [85] were removed from the average due to the large error.

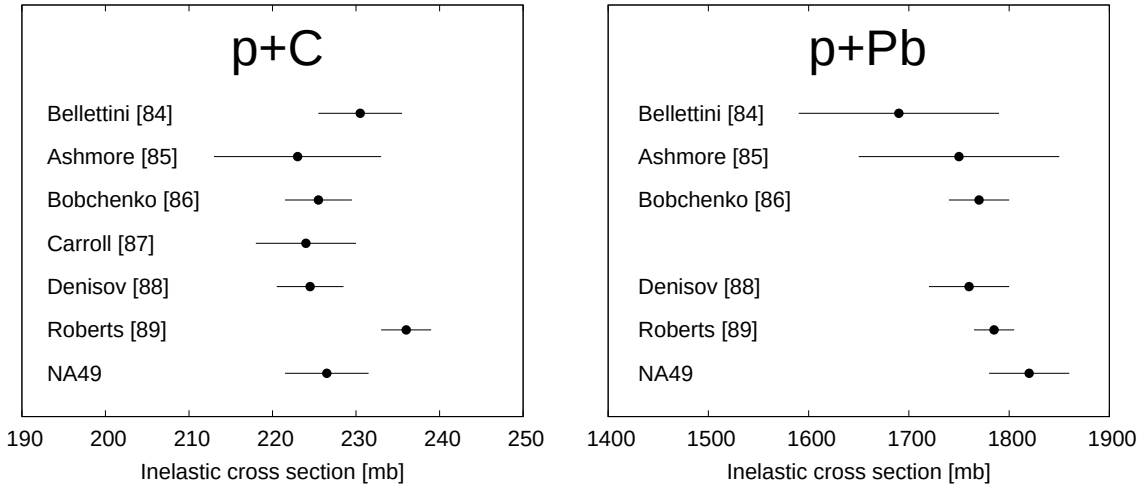

Figure 5.1: Summary of the p+C and p+Pb inelastic cross sections.

Corrected values of measured inelastic cross sections in p+C and p+Pb are compared to a compilation of earlier measurements [81] in Fig. 5.1.

5.3 Event selection

To clean up the event sample and reduce the empty target background, two cuts are applied as described in [61].

The first cut concerns the position of the beam particle upstream from the target. The beam particle transverse positions are measured over a 30 m distance by the 3 BPDs. These measurements are used to constrain collinearity of the projectile particle by requiring that the transverse coordinates of the beam measured by both BPD-1 and BPD-2, when extrapolated to BPD-3 position, match the beam position measured by the BPD-3, as shown in Fig. 5.2. The beam collinearity is achieved by accepting only the events for which the extrapolation falls between the two lines indicated in the figure. An additional less restrictive cut on the beam profile is imposed. This cut involves information from before the interaction takes place, therefore it makes no bias and needs no correction.

The second cut constrains the interaction vertex along to beam direction to the region

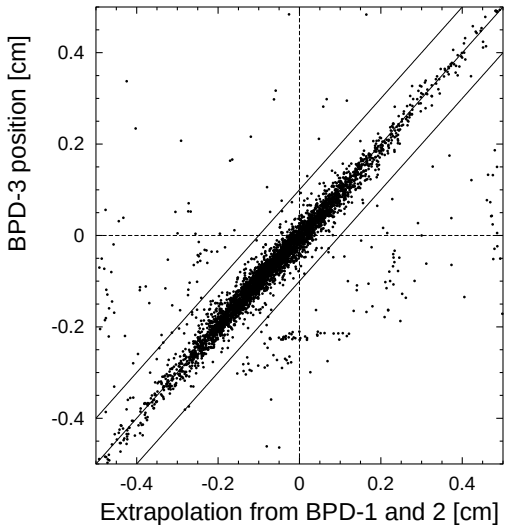

Figure 5.2: Beam position at BPD3 versus extrapolated position from BPD1 and BPD2 to BPD3.

of target, eliminating large fraction of empty target background. As the vertex resolution increases with multiplicity, the cut window narrows with multiplicity, retaining all the interactions with the target.

These cuts decrease the empty target admixture in the analyzed samples by about half: from 18 % to 9 % in p+p and from 30 % to 16 % in p+C. For p+Pb interactions this contribution varies with the CD trigger settings from about 40 % in the minimum bias trigger condition to a negligible fraction in the higher centrality trigger. The remaining empty target contribution is corrected for by the empty target correction, discussed in Section 5.4.1.

5.3.1 Track selection

A track is a collection of points (charged clusters) found in the TPC system. The TPC tracking is very reliable: local efficiency for cluster forming is almost unity with a below the per mill loss level, as determined by extensive eye scans of events. The expected number of points on each track can reliably be predicted by detector simulation, except on some edges of the VTPCs due to the $E \times B$ effect caused by field inhomogeneity.

Only the μDST tracks are used in the analysis. The tracks are selected in a phase space bin defined by perpendicular longitudinal and transverse variables: (x_F, p_T). For each bin a wedge in azimuth (φ) is chosen to ensure full detector acceptance by inspecting the distribution of the number of points per track as compared to the expected one. In some regions of phase space the φ wedge is chosen smaller than that imposed by full acceptance in order to reduce the contribution from strange particle decays discussed in Section 5.4.4.

For particle identification using $\mathrm{d}E/\mathrm{d}x$ (Section 4.3) only tracks with at least 30 measured points are considered to ensure a sufficient $\mathrm{d}E/\mathrm{d}x$ fit. This can cut pions due to their weak decay inside the detector or a hadronic interaction with the TPC gas. It was checked by eye scans and detector simulation that both of these losses are below a few per mill level [61] and therefore can be neglected (Section 5.4.6).

5.3.2 Event statistics

This study focuses on pion production, following works [61] and [62] where pions produced in p+p and p+C interactions were studied. Both concern the minimum bias trigger.

p+Pb interactions were taken in years 1997, 1999 and 2001 under different trigger conditions to enhance central collisions, as discussed in Section 2.2.1. A small sample of minimum bias collisions was also taken with the same 0.3 % thin target to facilitate precise grey proton measurement. This lead to a large empty target contribution, which combined with its low statistics severely limits precision of minimum bias analysis.

	Events taken		Events after cuts	
Year	Full target	Empty target	Full target	Empty target
1997	168740	0	87174	0
1999	1048039	19920	631284	2855
2001	1457175	57042	951496	7303
Total	2673954	76962	1669954	10158

Table 5.2: Data samples analyzed in centrality triggered p+Pb interactions.

The minimum bias sample has to be treated separately due to a large background from an empty target and small statistics. Despite of difficulties related with these shortcomings, cross section measurements using this sample are very interesting, as the minimum bias trigger setting is a well defined and repeatable condition which allows the comparison with other measurements in absolute calibration.

	Events taken		Events after cuts	
Year	Full target	Empty target	Full target	Empty target
1997	306682	12404	126751	3487
1999	119208	16467	47865	3666
2001	11946	10727	4463	2275
Total	437836	39598	179079	9428

Table 5.3: Data samples analyzed in minimum bias p+Pb interactions.

The statistics of triggered and minimum bias samples is shown in Tables 5.2 and 5.3.

5.3.3 Centrality bins

The triggered sample contains 1.7 M events, enough to make bins in centrality using the reconstructed number of grey protons. The distribution of grey protons in the triggered set is shown in Fig. 2.8 page 16 along with the minimum bias measurement. In this sample a small (0.17 %) contribution from events with no measured grey protons was eliminated due to its relatively high contamination with background. Five bins were chosen as indicated in Table 5.4. The most central bin ends at $n_{grey} = 22$, eliminating 260 events with a higher number of reconstructed grey protons.

5.3.4 Event sample for Pb+Pb collisions

Charged multiplicities in central Pb+Pb collisions can reach up to 1400 (Fig. 5.3). This poses additional problems in event reconstruction: highly ionizing heavy ions can produce

centrality bin	n_{grey} selection	events	$\langle\nu\rangle$
min. bias	all	179079	3.7
all trig.	> 0	1667072	5.1
1	1,2	249509	2.9
2	3,4,5	467234	4.1
3	6,7,8	490228	5.2
4	9 – 13	400683	6.0
5	14 – 22	62039	6.9

Table 5.4: Event samples analyzed in p+Pb studies. Estimation of mean number of projectile collisions $\langle\nu\rangle$ is discussed in Section 3.5 and Fig. 3.5.

high energy δ electrons, which can get captured by the magnetic field and then cause "spirals" in the VTPCs. These spirals induce additional ionization deposits, which complicate both tracking and ionization measurement.

To avoid this problem, for the purposes of inclusive studies a special low intensity run was performed in 2001, collecting 340 000 events under minimum bias conditions described in 3.4. After the cuts, 236 000 events were reconstructed, from which several centrality bins were selected by cuts in measured multiplicity. The Pb+Pb data sample which is used for comparison in Chapter 7.8 was obtained by selecting events with a measured charged track multiplicity between 900 and 1100 per event, as indicated in Fig. 5.3. The total number of events in this multiplicity bin used for the analysis was 21 178.

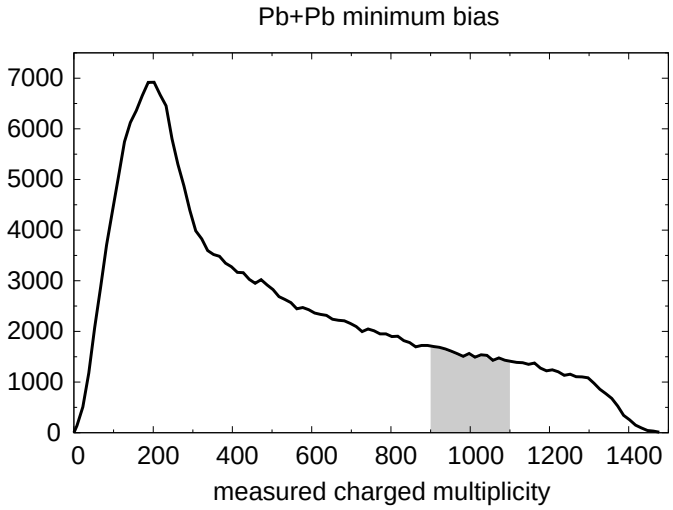

Figure 5.3: Charged multiplicity distribution measured in the minimum bias Pb+Pb event sample. The event sample selected by multiplicity cuts between 900 and 1100, used in the analysis, is indicated by the shaded area.

The average number of participant pairs was estimated to be $n_{part} = 155$ and the mean number of collisions per participant was estimated to be $\nu = 4.1$ [82, 79] as discussed in Section 2.3.3.

5.3.5 Phase space binning

A binning scheme in (x_F, p_T) phase space similar to the previous studies of p+p [61] and p+C [62] interactions was used.

All of the seven centrality sets use the same binning scheme because the pion densities are similar, with the exception of bin 5 where the cross section measurement was impossible in the region around $x_F = 0.4$ due to the small number of events in this sample combined with the decrease of particle density in the forward direction. The bins at this value of x_F were excluded.

To determine binning of the available phase space, the following aspects were considered:

- Optimum exploitation of the available phase space with respect to the studied transverse phenomena.
- Definition of bin centers at user-friendly and consistent values of x_F and p_T to ease comparison with other reactions and data sources.
- Compliance with the structure of the inclusive cross sections – in dense regions smaller bins are used.
- The bin size in total momentum should be sufficiently small to avoid smearing $\mathrm{d}E/\mathrm{d}x$ resolution due to the dependence of the mean $\mathrm{d}E/\mathrm{d}x$ on the particle's momentum.
- Avoidance of overlap.
- Optimization of bin sizes for minimum binning effects and corresponding corrections.
- To study transverse phenomena, bins in one x_F with p_T up to the highest values allowed by the statistics were used.
- In the region of $x_F = 0$ and p_T below 300 MeV very small bins were chosen. This choice was discussed in connection to the method of fitting $\mathrm{d}E/\mathrm{d}x$ in Section 4.3, page 39.

The binning schemes and an indication of the resulting statistical precision is shown in the Figures 5.4 and 5.5.

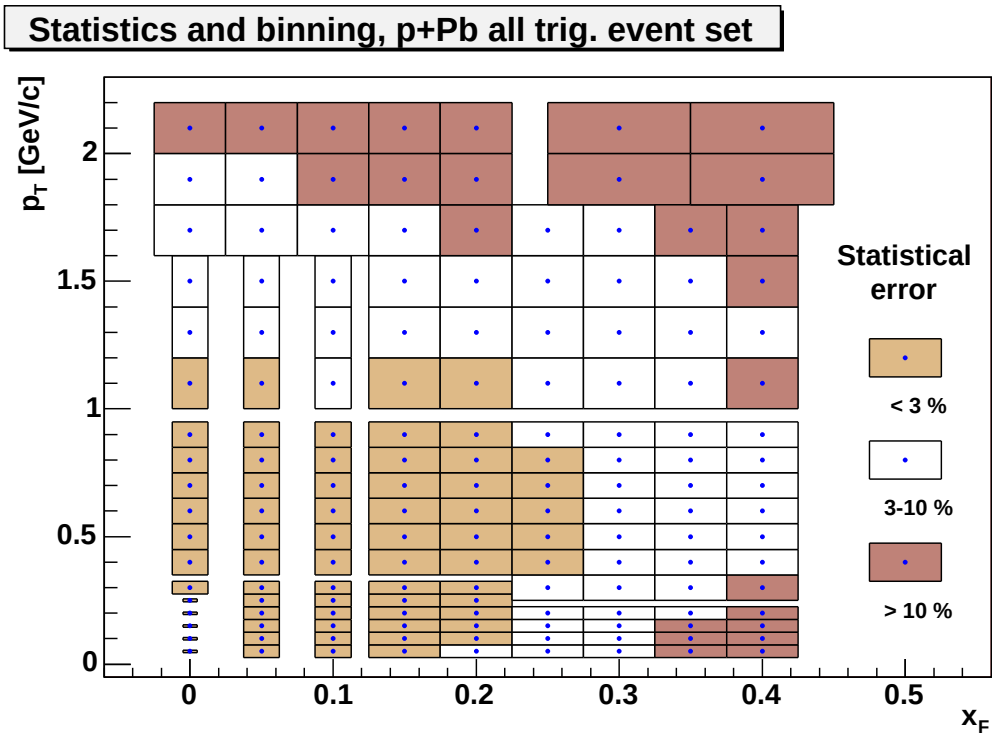

Figure 5.4: Binning scheme in (x_F, p_T) and information about the statistical error of all centrality triggered events in p+Pb.

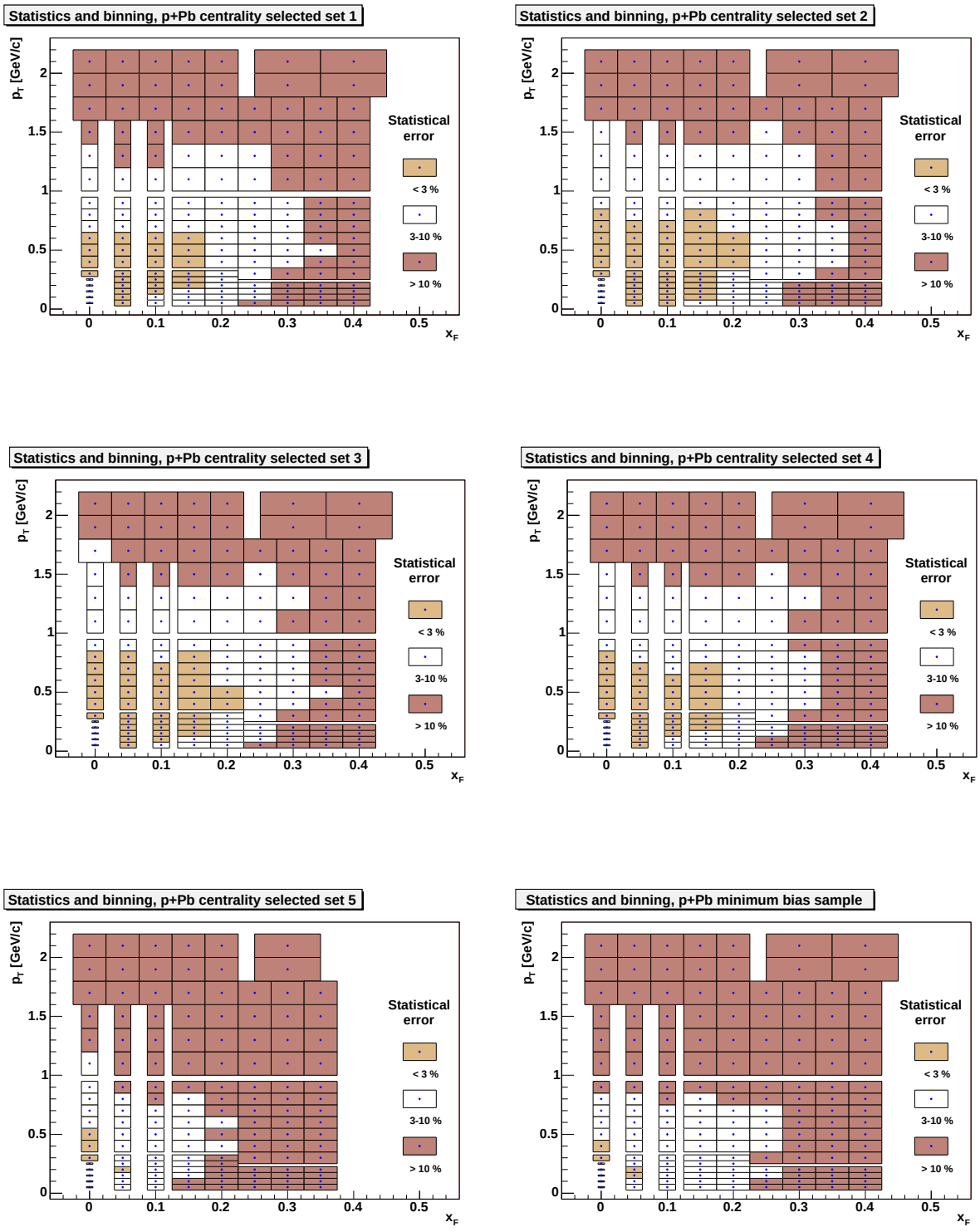

Figure 5.5: Binning scheme in (x_F, p_T) and information about statistical error in the centrality bins 1 – 5 of p+Pb interactions along with the minimum bias sample.

5.4 Cross section evaluation and corrections

As described in Section 5.2, the particle yields in the centrality selected p+Pb and Pb+Pb event sets are given as double differential inclusive invariant densities of produced particles:

$$\begin{aligned} d(x_F, p_T) &= E(x_F, p_T) \cdot \frac{\mathrm{d}^3 n}{\mathrm{d}p^3}(x_F, p_T) \\ &= \frac{E(x_F, p_T)}{\pi\sqrt{s}} \cdot \frac{1}{p_T} \cdot \frac{\mathrm{d}^2 n(x_F, p_T)}{\mathrm{d}x_F \mathrm{d}p_T} \end{aligned} \tag{5.5}$$

where σ_{inel} is the inelastic cross section, $\mathrm{d}^3n/\mathrm{d}p^3$ is the particle density at the phase space point $\mathrm{d}p^3$, E is the particle energy at that point, and x_F and p_T are the kinematic variables.

This definition is to be compared to the p+p and the minimum bias p+C and p+Pb interactions where absolute invariant cross sections normalized to σ_{inel} have been defined as:

$$\begin{aligned} f(x_F, p_T) &= E(x_F, p_T) \cdot \sigma_{inel} \cdot \frac{\mathrm{d}^3 n}{\mathrm{d}p^3}(x_F, p_T) \\ &= \frac{E(x_F, p_T)}{\pi\sqrt{s}} \cdot \frac{\sigma_{inel}}{p_T} \cdot \frac{\mathrm{d}^2 n(x_F, p_T)}{\mathrm{d}x_F \mathrm{d}p_T} \end{aligned} \tag{5.6}$$

The quantities $d(x_F, p_T)$ and $f(x_F, p_T)$ are related to the measured number of identified particles Δn in each phase space bin Δp^3 by:

$$d_{meas}(x_F, p_T, \Delta p^3) = E(x_F, p_T, \Delta p^3) \cdot \frac{1}{N_{ev}} \cdot \frac{\Delta n(x_F, p_T, \Delta p^3)}{\Delta p^3} \tag{5.7}$$

and

$$f_{meas}(x_F, p_T, \Delta p^3) = E(x_F, p_T, \Delta p^3) \cdot \frac{\sigma_{trig}}{N_{ev}} \cdot \frac{\Delta n(x_F, p_T, \Delta p^3)}{\Delta p^3} \tag{5.8}$$

where σ_{trig} is the trigger cross section and N_{ev} is the total number of events originating from the target in the analyzed set.

Several normalization steps and corrections are necessary for f_{meas} to approach $f(x_F, p_T)$:

- The number of events N_{ev} in relation to Δn has to be determined from separate measurements of full and empty target yields.
- The number of measured pions Δn has to be corrected for weak decays of pions, pion absorption in the detector material, and feed–down pions coming from weak decays of strange particles.
- The measured σ_{trig} is not equal to σ_{inel}, as discussed in Section 5.2.2 and Table 5.1, necessitating a trigger bias correction.
- Averaging over the finite volume element Δp^3 influences the measured value depending of the shape of $f(x_F, p_T)$ over the bin, necessitating a binning correction.

5.4.1 Empty target correction

The particle yield $\Delta n/N_{ev}$ may be established by separate measurements of full and empty target yields in each bin using the formula:

$$\left(\frac{\Delta n}{N_{ev}}\right)^{FT-ET} = \frac{1}{1-\epsilon}\left(\left(\frac{\Delta n}{N_{ev}}\right)^{FT} - \epsilon\left(\frac{\Delta n}{N_{ev}}\right)^{ET}\right) \tag{5.9}$$

where $\epsilon = R_{ET}/R_{FT}$.

Such an approach would require large enough empty target event sample to ensure comparable statistic errors from both ratios in equation (5.9). It would also further complicate $\mathrm{d}E/\mathrm{d}x$ fits in the regions of low cross sections. Given the time constrains on taking data and the event cuts introduced to reduce the empty target admixture in the analyzed sample, a more efficient approach to normalization developed in [61] is used.

It was found that unlike in the p+p and p+C cases the empty target correction in the p+Pb case also depends on p_T, due to the fact that the empty target background is created from nuclei which are light compared to the heavy Pb target (N, O, C). It was checked in detail that the dependence on pion charge is insignificant, as in the p+p and p+C cases.

To establish the correction a crude phase space binning was established. Instead of detailed $\mathrm{d}E/\mathrm{d}x$ fits, tracks found within 1 σ of the pion Bethe-Bloch position were counted in both full and empty target events. The correction was calculated separately for the minimum bias sample, the whole triggered sample, and for each n_{grey} value, and then interpolated as a function of (x_F, p_T). From these the correction in centrality bins 1 to 3 is established taking into account the n_{grey} composition of the bins.

This correction is decisive in the minimum bias sample due to the thinness of the lead target (Table 3.1). Its value varies between -20 and +50 %. In the first centrality selected data set the absolute value is below 10 % and decreases with centrality as it is less probable to obtain a large number of grey protons from lighter nuclei. This decrease is visible from panel e) in Figures 5.23 to 5.22. There is no empty target correction for the centrality sets 4 and 5 due to lack of empty target interactions that would produce high enough grey proton multiplicities. The correction in centrality bin 1 for two values of x_F is shown in Fig. 5.6.

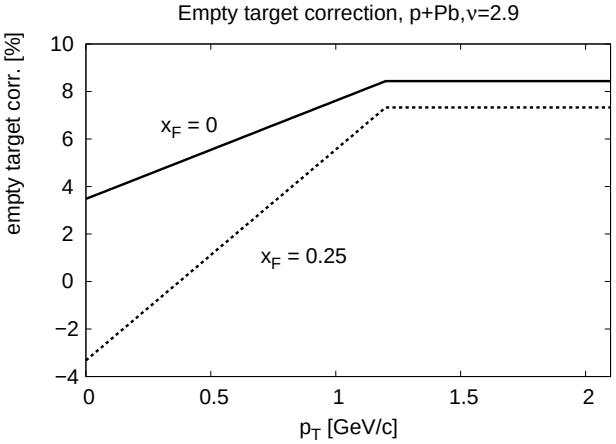

Figure 5.6: The empty target correction as a function of p_T for $x_F = 0$ and $x_F = 0.25$ for centrality bin 1 of p+Pb interactions.

5.4.2 Trigger bias correction

The trigger setup discussed in Section 3.4 excludes some inelastic events. Some events get vetoed by secondary particles hitting S4, mostly forward protons with appropriate transverse momentum to hit S4. The total fraction of such rejected events is 14 % in p+p, 9 % in p+C, and 4 % in minimum bias p+Pb collisions, corresponding to the increase of stopping with the target system size which decreases particle density at large x_F. The bias induced by the trigger will affect measured cross sections in a non–trivial way via the following expression:

$$f_{meas} \sim \sigma_{trig} \cdot \frac{\Delta n}{N_{ev}} \tag{5.10}$$

The correction depends on event topologies. If there is a fast forward particle detected, no other particle can reset the S4 counter due to energy–momentum conservation and the correction is zero. If the particle yields fully decouple between the forward and the backward hemispheres, as discussed in the next chapter, the event loss should be manifested wholly in the backward region. A smooth transition from this value to zero at $x_F = 1$ is expected.

The correction was obtained experimentally by studying the correlation of measured particles with tracks passing close to the S4 counter. This study was possible in the last year of running when the GTPC was installed. The S4 counter is placed before the GTPC and tracks passing the veto counter are reconstructed.

Three rims around the S4 counter of the same area as the S4 counter were selected offline. The ratios of particle density as a function of longitudinal laboratory momentum over the particle density going through the real S4 veto counter were established in the three rims from relevant measurements of particle production, mostly forward protons. These ratios were then used as weights relating the events lost by secondary particles hitting the three rims to describe the real event loss due to the presence of the actual S4 counter.

The trigger correction was established by investigating a fraction of events which would be vetoed by another track hitting the three rims as a function of (x_F, p_T) of the measured particle, which were identified by cuts around the nominal Bethe-Bloch position. It was checked that a comparable value for the trigger correction was established from all three rims over most of phase space. An example is shown in Fig. 5.7.

This method relies entirely on measured quantities, which was important especially in p+p and p+C collisions, where this correction (along with the feed–down correction) is the largest, and no event generator can be expected to be reliable at the level of precision required. The systematic error of this method is dominated by the statistical error of this correction, which is typically smaller by a factor of three than the statistical error of the extracted data.

The reliability of this method was independently checked by a different approach. Restricting the secondary particles that may veto the event to the tracks with longitudinal laboratory momentum below 90 GeV/c, the S4 image in (p_x, p_y) momentum space moves completely to negative p_x. Azimuthal symmetry allows reflection of the S4 image around the $p_x = 0$ line and direct estimates of the fraction of events vetoed due to secondaries with $p_z^{lab} < 90\,\mathrm{GeV}$. The same restriction on the veto tracks can be imposed in the above discussed three rim method. Both the methods agreed within errors.

In p+A interactions the trigger bias correction is reduced with respect to p+p reactions as a consequence of several phenomena:

- Most of the correction in the case of p+p interactions is caused by fast protons. In the p+A interactions, the protons are transfered to the central region progressively

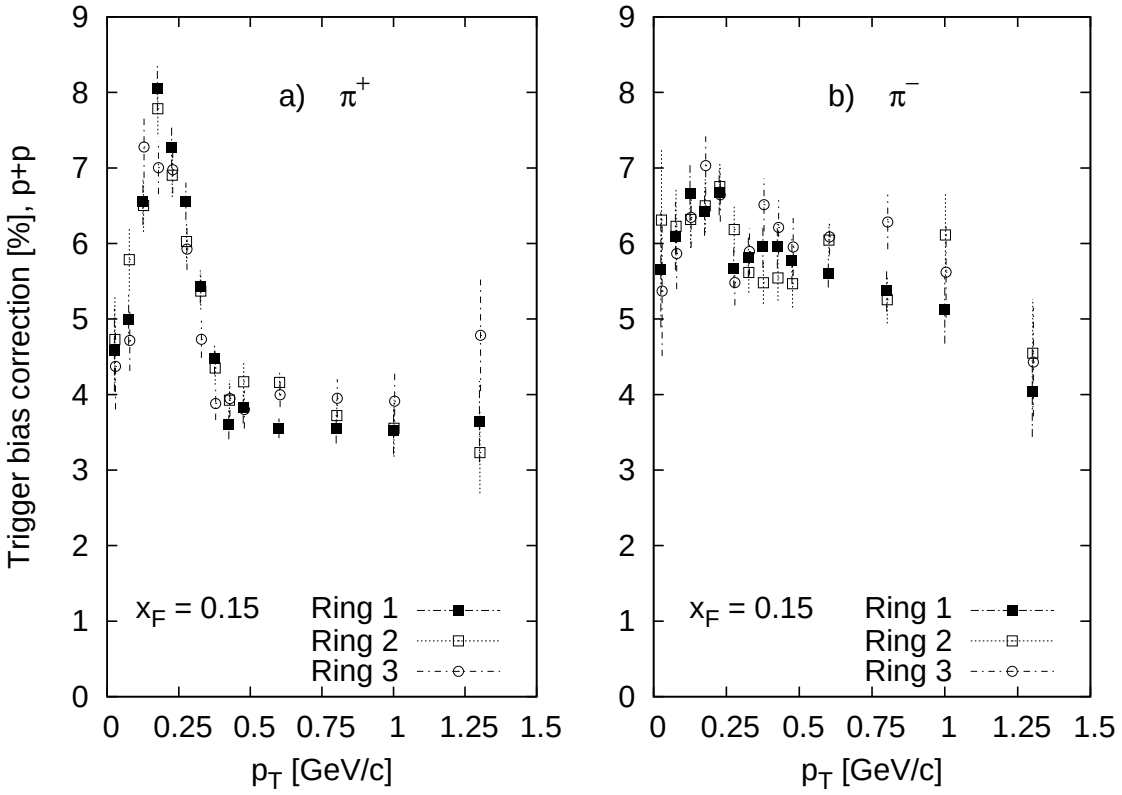

Figure 5.7: Trigger bias correction in p+p interactions for a) π^+ and b) π^- at $x_F = 0.15$ in p+p interactions at 160 GeV/c. The correction is shown as measured in the three rims around the S4 veto counter.

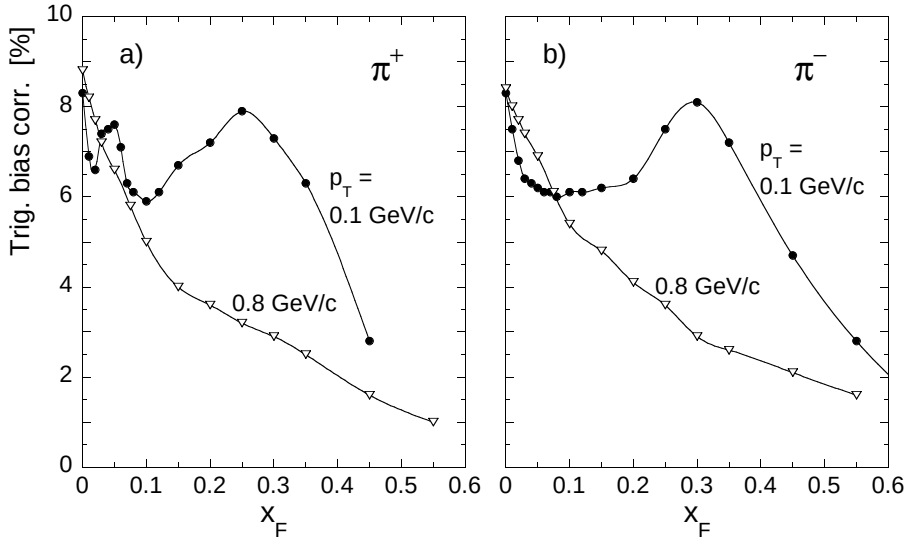

Figure 5.8: Trigger bias correction as a function of x_F for two p_T values for a) π^+ and b) π^- in minimum bias p+p interactions. The lines connecting the points in this figure and the following figures serve to guide the eye. [61]

with an increasing number of projectile collisions ν. This phenomenon is known as baryon stopping. [51, 54, 57] The fewer forward protons, the smaller the correction.

- A similar and correlated steepening of particle densities is observed for other particles. See Section 7.4 for a detailed discussion. Again the decrease of forward particle density decreases the correction value.

- Contrary to the interactions of single hadrons, there is a long–range correlation between target fragmentation and forward particle density in p+A collisions. Particles at forward x_F are correlated with single projectile collisions that result in small backward multiplicities. Central collisions with multiple projectile collisions yield large target multiplicities but low forward density. This correlation reduces the trigger bias in the target fragmentation region.

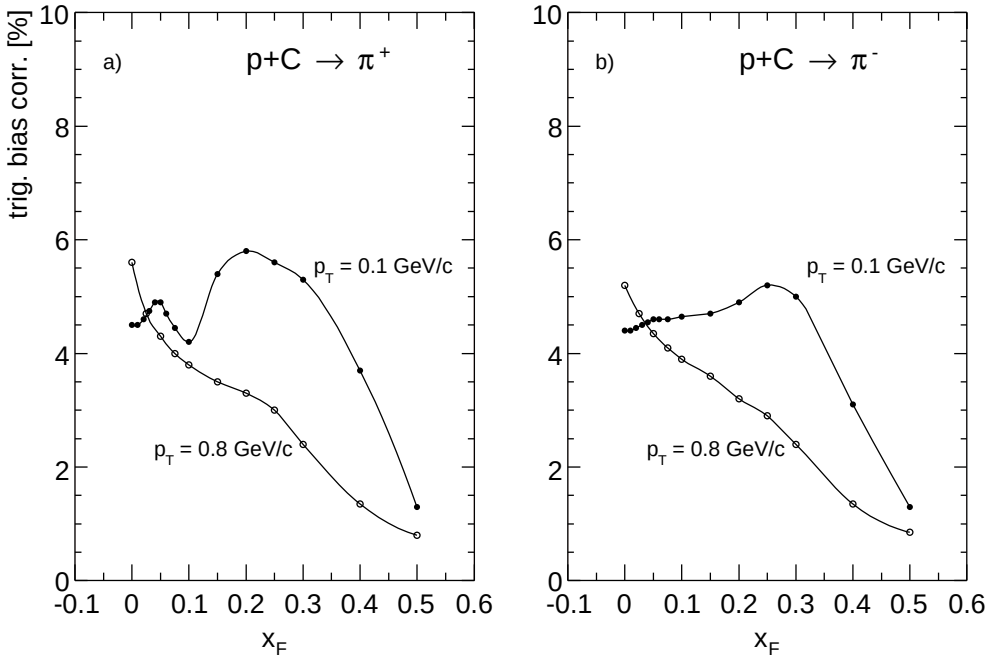

Figure 5.9: Trigger bias correction as a function of x_F for two p_T values for a) π^+ and b) π^- in minimum bias p+C interactions. [62]

In the most central centrality triggered p+Pb runs, requiring an online number of CD hits to be above 7, the interaction rate was within the precision of the online rate measurement independent of the presence of the S4 counter, thus it was removed from the trigger coincidence setup for these runs. Bins 4 and 5 however contain a contribution from interactions with proper number of reconstructed grey protons originating from runs with the S4 counter, therefore the correction was established for these bins as well. For the minimum bias sample, the correction obtained from centrality set 1 was used due to the high background contamination and low statistics of the sample. The trigger bias correction in the p+Pb events is on the level of 1 – 3 %.

The correction values for different reactions are presented in Fig. 5.8 for p+p interactions, Fig. 5.9 for p+C and Fig. 5.10 for p+Pb lowest centrality event selection of $\nu = 2.9$.

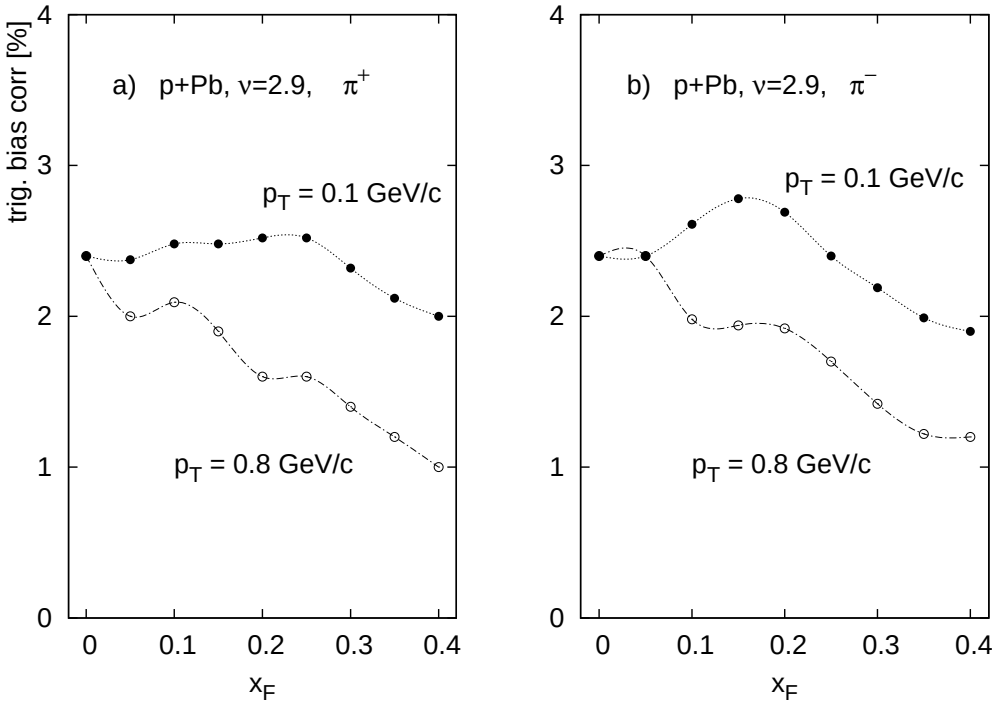

Figure 5.10: Trigger bias correction as a function of x_F for two p_T values for a) π^+ and b) π^- in p+Pb interactions in centrality bin 1, $\nu = 2.9$.

5.4.3 Absorption correction

The correction due to pions interacting with the downstream material of the detector is established using the GEANT simulation of the NA49 detector. It was concluded from eye-scans that nearly all primary pions which undergo hadronic interactions before detection are lost. This simplifies the analysis. The absorption correction as a function of x_F at two p_T values is shown in Fig. 5.11. At low p_T the x_F dependence exhibits multiple maxima which correspond to the position of the ceramic support tubes of the TPC field cages discussed in Section 3.7. This correction is independent of the projectile and target combination.

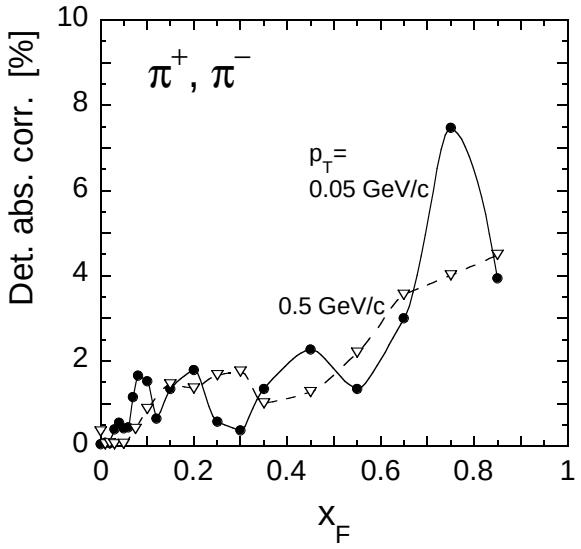

Figure 5.11: Correction due to absorption of pions in the detector material. [61]

5.4.4 Feed–down correction

Feed–down is the fraction of detected pions originating from weak decays of strange particles, where the resulting pion tracks were reconstructed as originating from the main interaction vertex. Due to the small q–value of these decays, the feed–down contribution is concentrated at low x_F and low p_T. All relevant feed–down sources were considered: $\overline{K_s^0}$, $\overline{\Lambda}$ and Σ^+ for π^+ and K_s^0, Λ and Σ^- for π^-.

The correction is determined in three steps. First the double–differential distributions of the parent particles is established from existing data. In the second step parent particles are generated corresponding to their distributions, then decayed. This way the distribution of daughter particles is obtained in the (x_F, p_T) bins of the experiment. In the third step these distributions are folded with the probabilities of being reconstructed on the main vertex, which are determined from a full GEANT simulation of the NA49 detector using VENUS to produce complete events containing the appropriate strange hadrons.

To construct the input strange particle yields in p+Pb collisions, the complete method existing for the p+p case [61] was used, using relative yields of kaons and lambdas in p+Pb interactions with respect to p+p as input for the method.

The minimum bias sample, suffering by the high background contamination and low statistics, was substituted by centrality set 1 for the purpose of the feed–down correction.

The yield of K_s^0 is determined from charged kaon measurements, $K_s^0 = (K^+ + K^-)/2$. For this purpose, $\mathrm{d}E/\mathrm{d}x$ fits of kaon yields were performed in 5 bins in x_F and 3 bins in p_T for both the charged kaons for all the 6 sets of different centrality selected p+Pb events and the p+p data set. Interpolating the bin by bin ratio of kaons produced in a particular centrality set of p+Pb over p+p collisions, and multiplying by the input kaon densities in p+p, kaon density distributions are obtained for each centrality set. Making a direct bin by bin ratio eliminates most of the corrections. To parameterize the kaon distribution outside the measured range of x_F, the two–component picture was invoked. As the measured phase space constitutes the major source of feed–down, this assumption introduces negligible bias.

The relative yields of mean kaons in the largest statistics sample are shown in Fig. 5.12 a) for the three values of transverse momentum along with the parameterization used for the correction determination.

A similar procedure is applied to estimate Λ and $\overline{\Lambda}$ densities. In this case on–vertex lambdas were measured using an event mixing and background subtraction technique [80, 58], designed for resonance production measurement. On–vertex Λs are those whose decay products are reconstructed on the main interaction vertex. It can be assumed that the efficiency of on–vertex Λ reconstruction is independent of the reaction type. This method eliminates complications associated with standard V^0 reconstruction.

For each centrality set (plus a p+p set) 5 bins in x_F were studied. The transverse distribution is less important here than for K_s^0 decays, as πs from the Λs contribute mostly to the low p_T region. Therefore the measured p_T distributions of protons were used. For Λ ($\overline{\Lambda}$) yield determination the $\pi^- + p$ ($\pi^+ + \overline{p}$) pairs were investigated by the event mixing method. The ratios of Λ ($\overline{\Lambda}$) measured in the p+A over p+p interactions were used to construct the input densities, analogous to the kaon case. The relative Λ yields in the 5 bins are shown in Fig. 5.12 b) along with the parameterization.

The $\Sigma^{\pm}$ densities were derived from the Λ parameterization, taking isospin effects and relative ratios determined in the p+p case into consideration.

The resulting feed–down correction reaches up to 5 % for positive and up to 7 % for negative pions in the low x_F and low p_T region, as shown in Figures 5.13 and 5.14 for the lowest and the highest centrality bin. Only few p_T values are shown to keep the figures

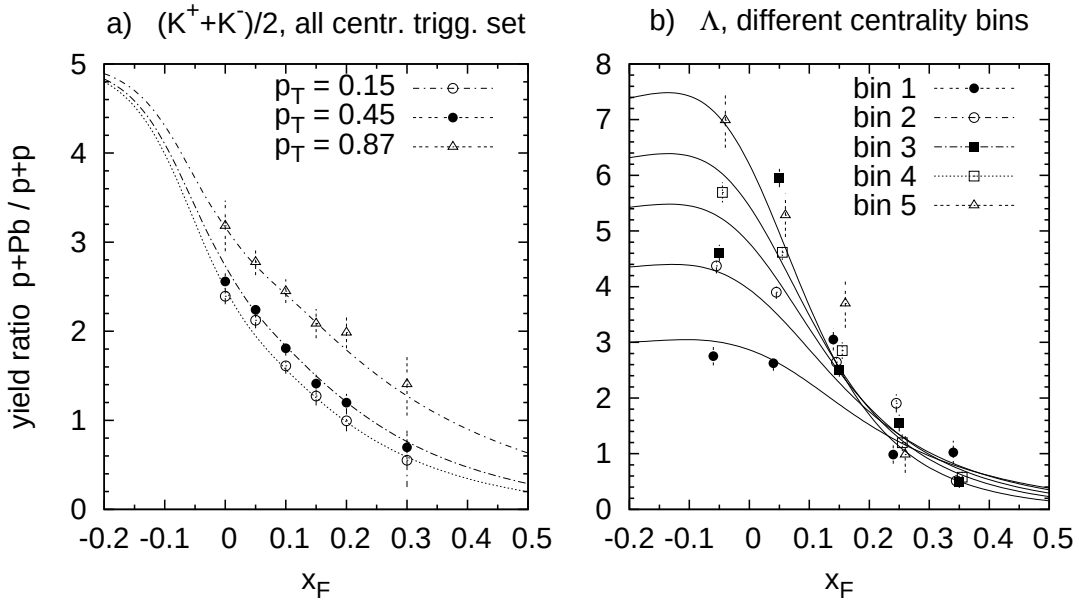

Figure 5.12: a) relative yields of charge averaged kaons as obtained from the centrality triggered sample indicating the p_T dependence; b) relative Λ yields in the 5 bins in centrality as a function of x_F. The lines show the parameterization used for calculating the feed-down correction.

comprehensible. Interestingly, the larger number of feed–down pions roughly canceled the higher pion density, making the correction similar in all the centrality sets.

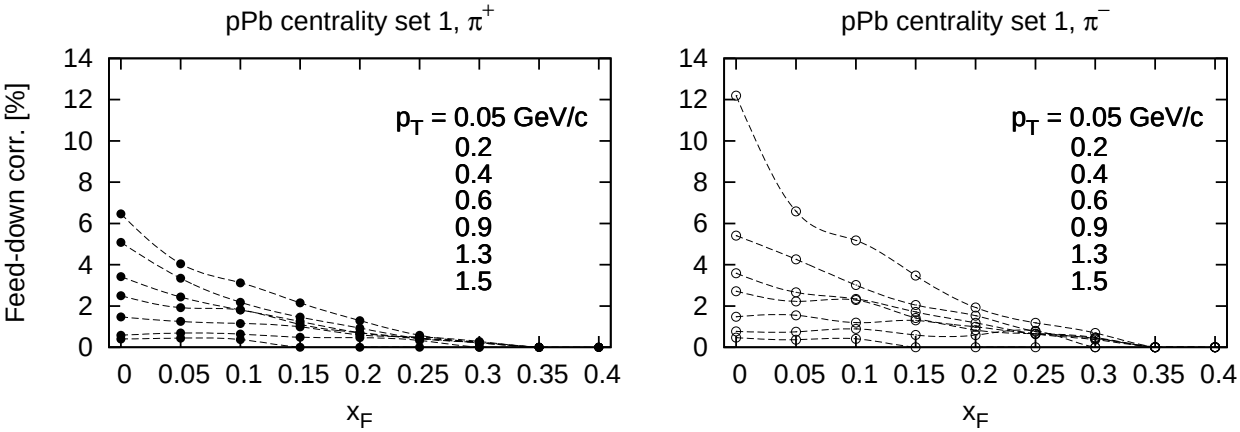

Figure 5.13: Feed–down correction for positive and negative pions measured in p+Pb centrality set 1.

The systematic uncertainties of the correction determination are dominated by the uncertainties of the strange particle yield densities in p+p interactions.

5.4.5 Binning correction

The method of extracting the invariant cross sections necessitates finite binning of the analyzed phase space. The measured yields are then integrals of the density over the

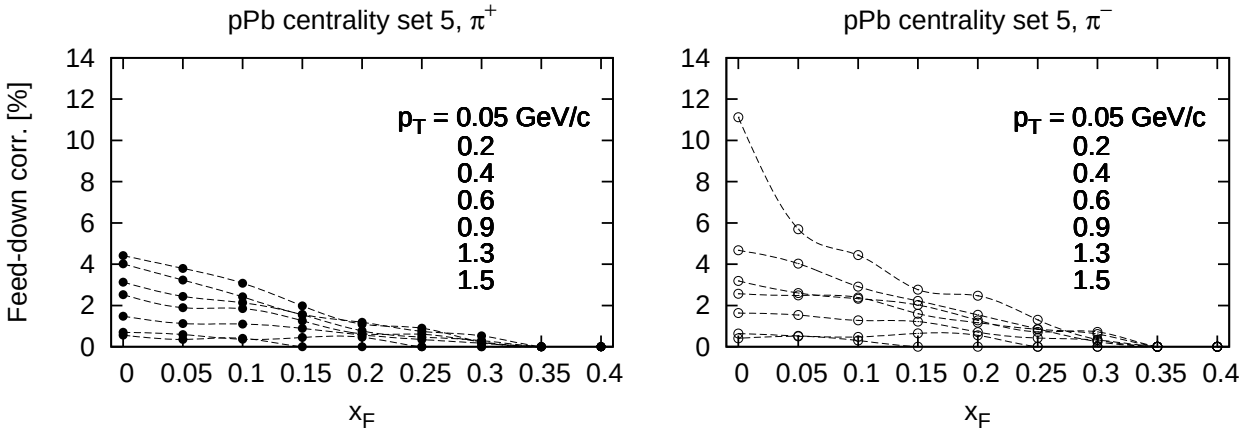

Figure 5.14: Feed–down correction for positive and negative pions measured in p+Pb centrality set 5.

respective phase space volume elements, the bins. If the studied density varies in a non–linear way, this value does not equal the yield in the bin center. The densities are flat in φ due to azimuthal symmetry, reducing the problem to the determination of binning corrections in x_F and p_T.

Assuming a particle density $\rho(t)$ as a function of the variable t over a bin of width Δ centered at t_0, the measured value is:

$$\rho_{meas}(t_0) = \frac{1}{\Delta}\int_{t_0-\Delta/2}^{t_0+\Delta/2} \rho(t)\mathrm{d}t \tag{5.11}$$

The density $\rho(t)$ can be approximated by a Taylor expansion in local derivatives to the second order term:

$$\rho(t) \approx \rho(t_0) + \rho'(t_0)(t-t_0) + \rho''(t_0)\frac{(t-t_0)^2}{2} \tag{5.12}$$

The measured value 5.11 can then be approximated as:

$$\rho_{meas}(t_0) \approx \rho(t_0) + \frac{1}{24}\rho''(t_0)\Delta^2 \tag{5.13}$$

Hence the binning correction, corresponding to the difference between the real particle density $\rho(t_0)$ and its measured value, is proportional to the second derivative of the density function and to the square of the bin width. This approximation can be used if the difference does not exceed a few percent level.

The second derivatives may be approximated from neighboring data points, assuming the sequence of bins at positions $[t_1, t_0, t_2]$:

$$\rho''(t_0) \approx \left(\left(\frac{\Delta_1\rho(t_2) + \Delta_2\rho(t_1)}{\Delta_1+\Delta_2}\right) - \rho(t_0)\right)\frac{2}{\Delta_1\Delta_2} \tag{5.14}$$

where $\Delta_1 = t_1 - t_0$ and $\Delta_2 = t_0 - t_2$, see sketch in Fig. 5.15.

The generalization of the method to the case of double differential cross sections is straightforward and it can be shown that the correction can be determined independently in the two coordinates. The binning correction was evaluated directly from the data for all data points.

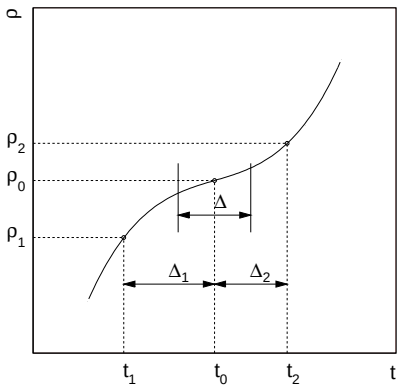

Figure 5.15: Definition of variables used in equations (5.12) and (5.14).

The statistical uncertainty introduced by the correction, determined by the error of neighboring points, is about a factor of 10 lower than the statistical error of the data point. The correction is small, below 5 % and negative in most of the bins. Figure 5.16 shows a typical example.

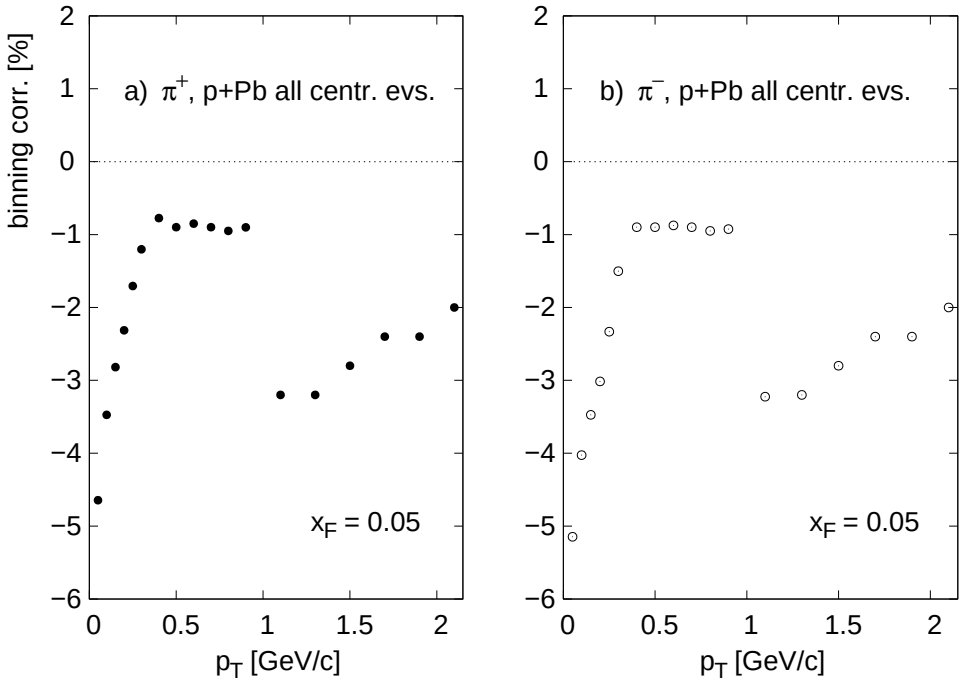

Figure 5.16: Correction due to binning effect in p+Pb all centrality triggered event sample at $x_F = 0.05$ as a function of p_T for a) π^+ and b) π^-. The steps at $p_T \approx 1\,\mathrm{GeV/c}$ are due to the increase of the transverse bin width from 0.1 to 0.2 GeV/c.

5.4.6 Neglected corrections

In the recent papers [61, 62] two other corrections, reinteraction in the target and loss from the pion weak decay, were applied. The target reinteraction correction is negligible for p+Pb interactions compared to statistical and systematic errors due to the lead target

thickness. This thickness, only 0.3 % of an interaction length, corresponds to a correction value of only few per mill.

The losses due to pion weak decay inside the detector volume are below 0.3 % everywhere in the studied phase–space.

5.5 Summary of errors

Each studied sample contains 150 measured points per charge. Distributions of the corrections discussed above, along with the resulting total correction for the 300 points per set, are shown in Figures 5.17 – 5.23. Table 5.4 on page 45 gives the set definitions.

The largest corrections are applied to the minimum bias measurements, mostly due to the thinness of the Pb target, which translated into large empty target corrections. In the other sets the total corrections decrease with centrality. The largest contributions are the feed–down and the binning corrections, which may reach values up to $\sim 6\,\%$.

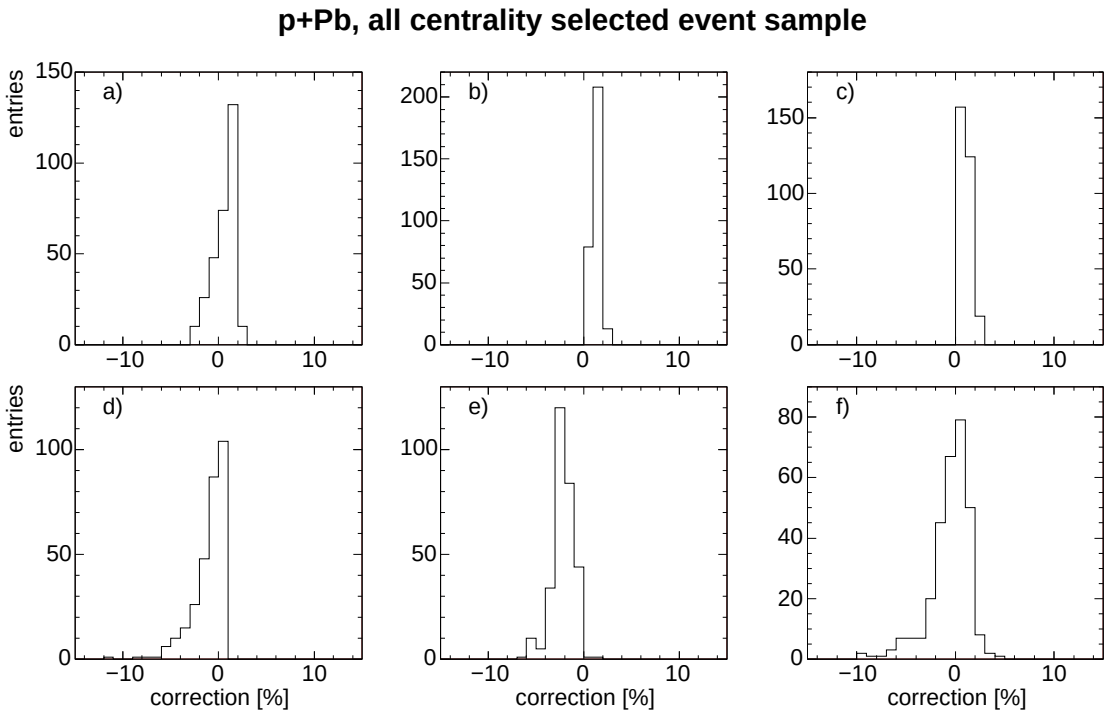

Figure 5.17: Distribution of corrections in the all centrality triggered set of p+Pb interactions for a) empty target contribution, b) trigger bias, c) absorption in detector material, d) feed–down, e) binning, f) resulting total correction.

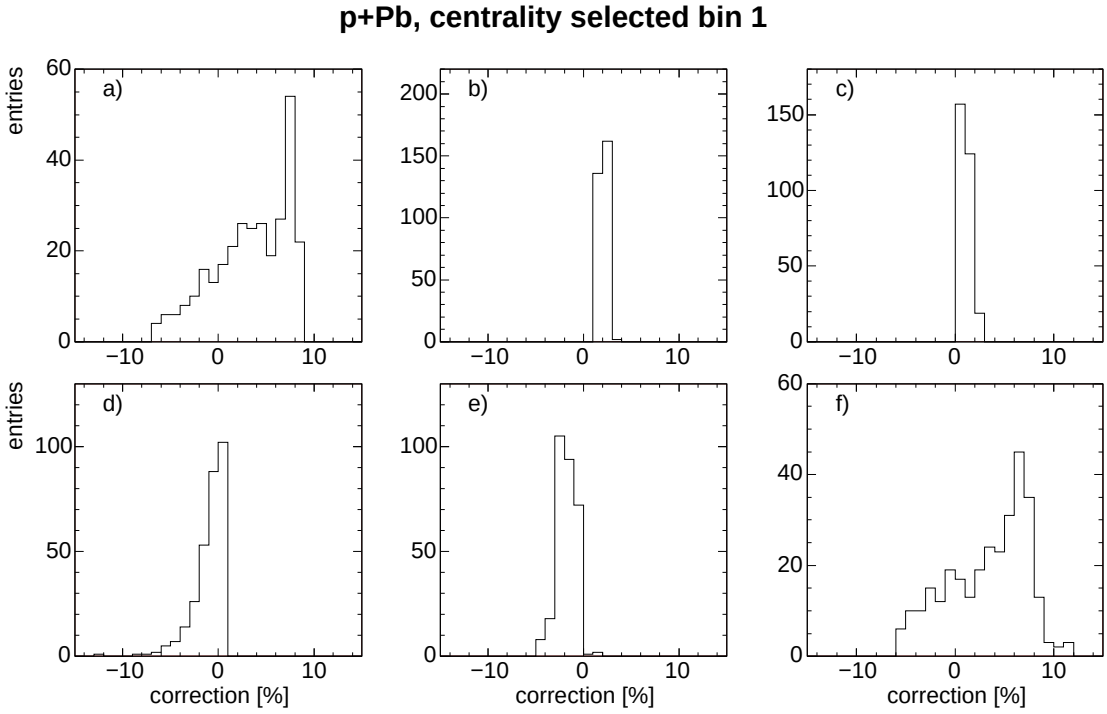

Figure 5.18: Distribution of corrections in the p+Pb centrality selected set 1 for a) empty target contribution, b) trigger bias, c) absorption in detector material, d) feed–down, e) binning, f) resulting total correction.

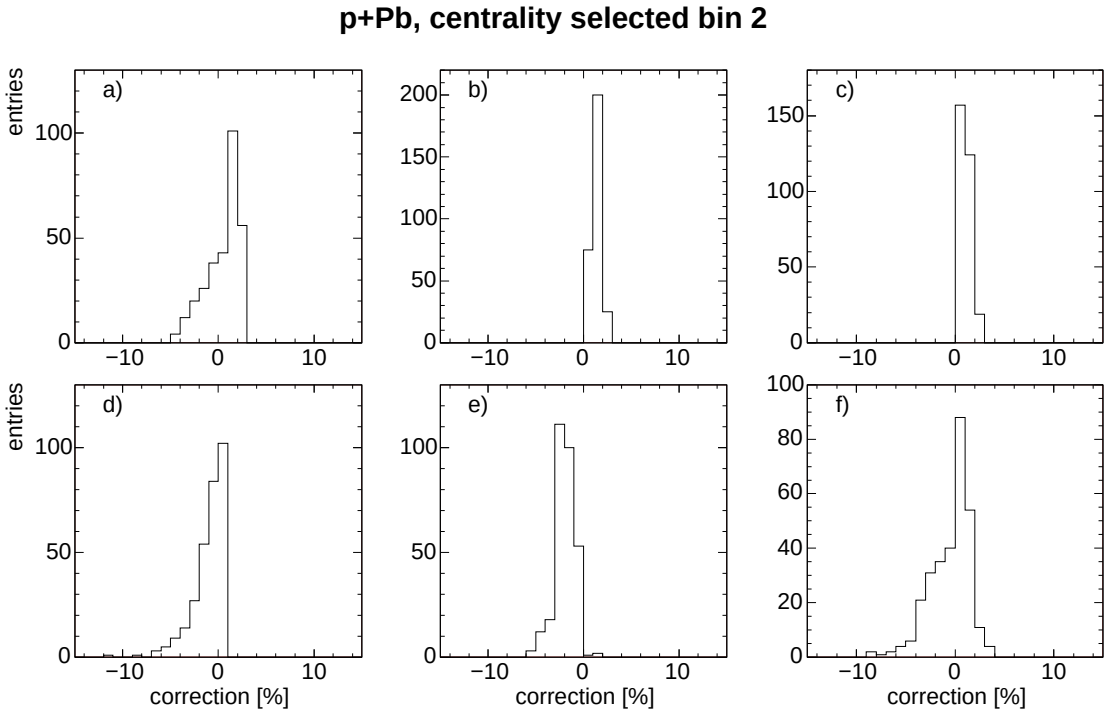

Figure 5.19: Distribution of corrections in the p+Pb centrality selected set 2 for a) empty target contribution, b) trigger bias, c) absorption in detector material, d) feed–down, e) binning, f) resulting total correction.

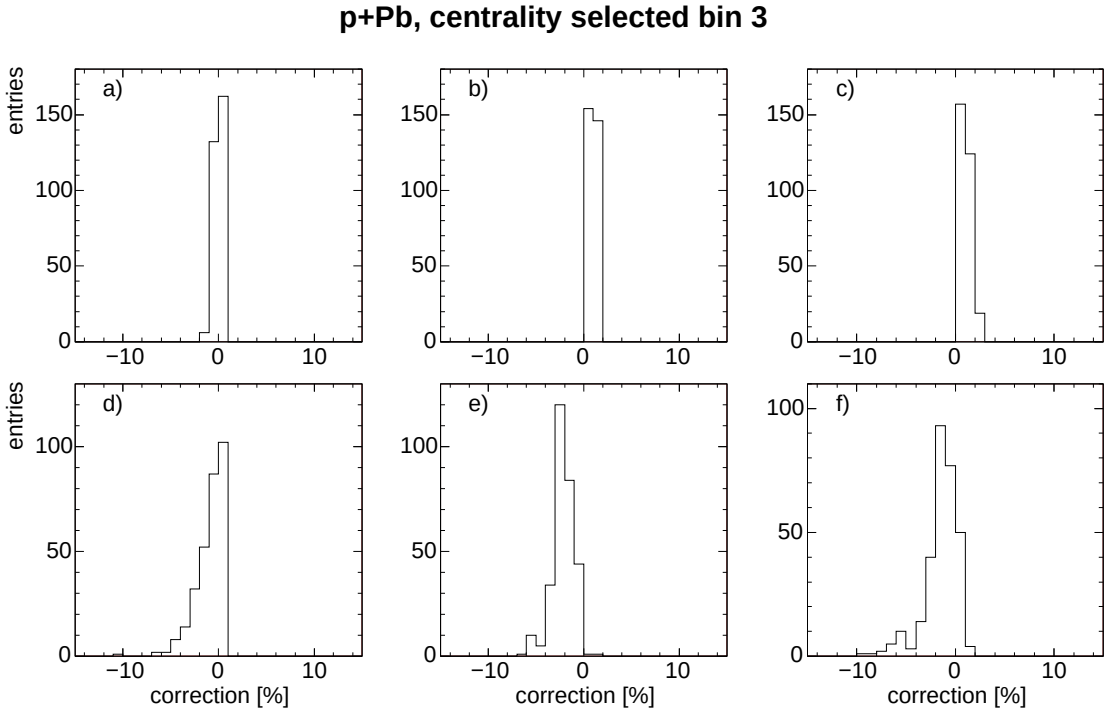

Figure 5.20: Distribution of corrections in the p+Pb centrality selected set 3 for a) empty target contribution, b) trigger bias, c) absorption in detector material, d) feed–down, e) binning, f) resulting total correction.

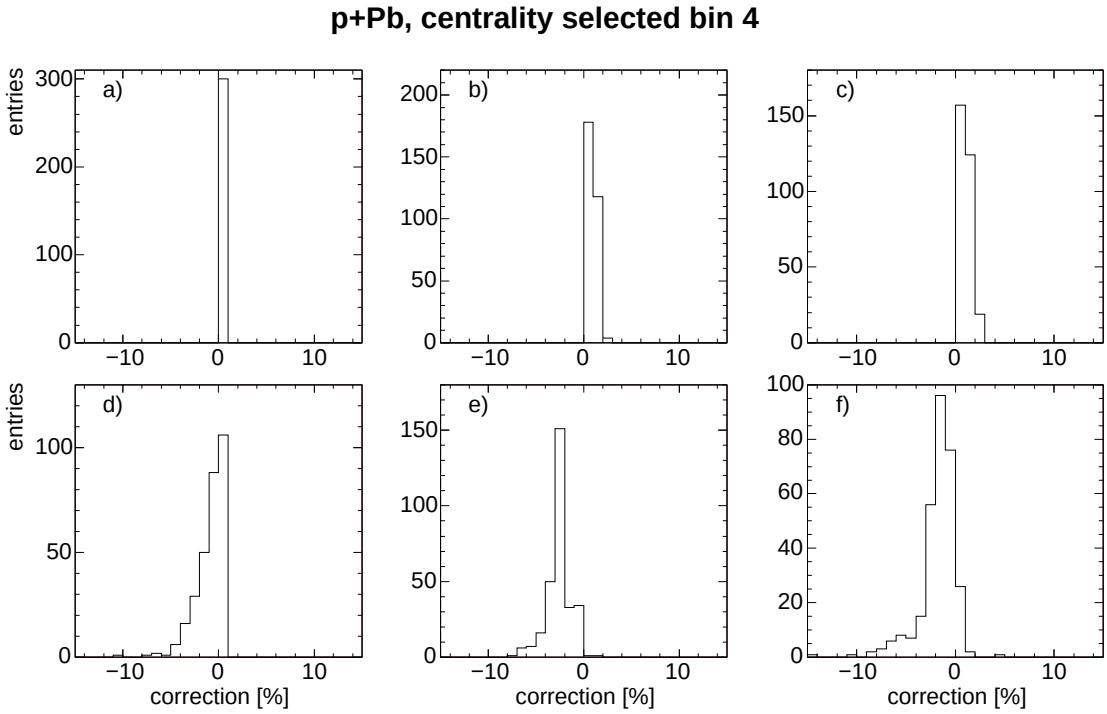

Figure 5.21: Distribution of corrections in the p+Pb centrality selected set 4 for a) empty target contribution, b) trigger bias, c) absorption in detector material, d) feed–down, e) binning, f) resulting total correction.

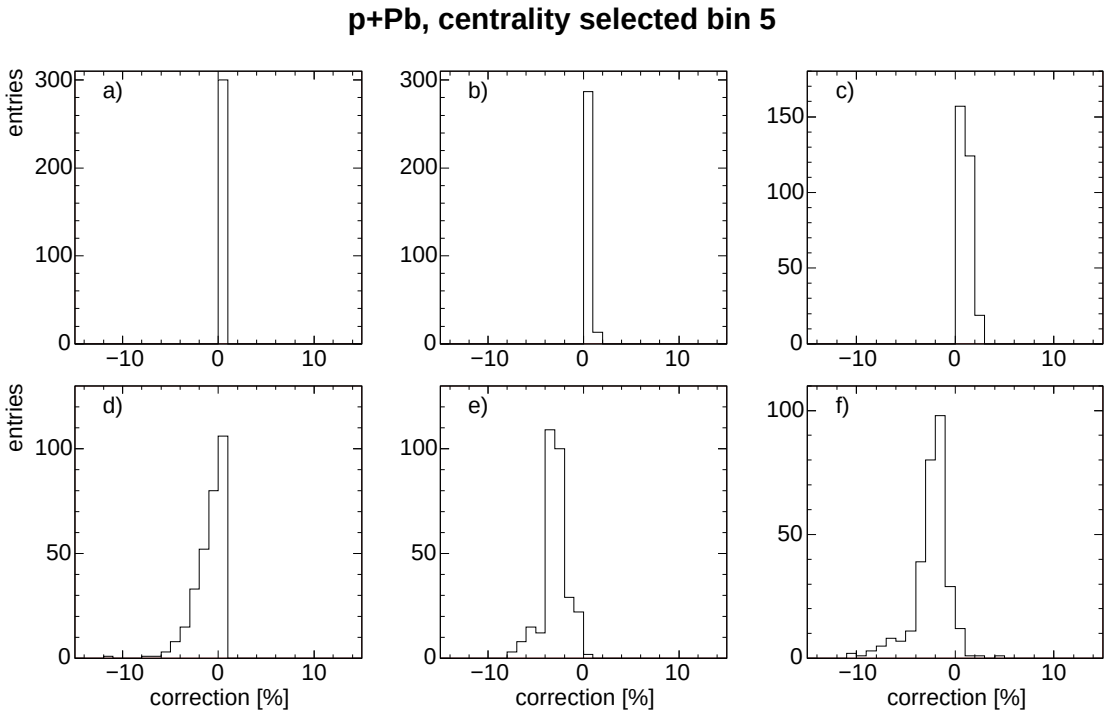

Figure 5.22: Distribution of corrections in the p+Pb centrality selected set 5 for a) empty target contribution, b) trigger bias, c) absorption in detector material, d) feed–down, e) binning, f) resulting total correction.

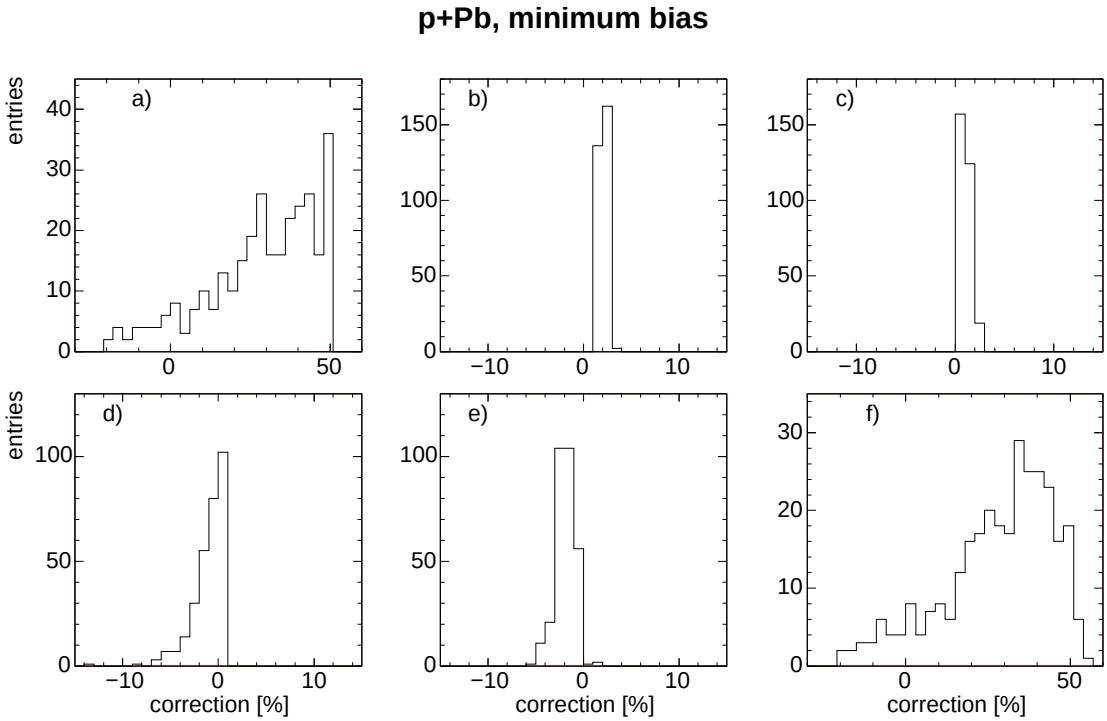

Figure 5.23: Distribution of corrections in the p+Pb minimum bias sample for a) empty target contribution, b) trigger bias, c) absorption in detector material, d) feed–down, e) binning, f) resulting total correction.

5.5.1 Systematic errors

The systematic errors of the cross section measurements are related to the size of the applied correction and to the normalization uncertainty. They can be estimated by assuming reasonable error bands around the assumptions used in the evaluation of the different contributions. These estimates are given in Table 5.5 for the seven data samples used in this thesis. They should be regarded as mean deviations averaged over the covered phase space.

Centrality set	min. bias	all trig.	1	2	3	4	5
Normalization	2 %						
Empty target contr.	5 %	0.2 %	0.7 %	0.3 %	0.2 %	0 %	0 %
Tracking efficiency	0.5 %	0.5 %	0.5 %	0.5 %	0.5 %	0.5 %	0.5 %
Trigger bias	0.2 %	0.1 %	0.2 %	0.2 %	0.1 %	0 %	0 %
Feed–down	1-2.5 %	1-2.5 %	1-2.5 %	1-2.5 %	1-2.5 %	1-2.5 %	1-2.5 %
Detector absorption	0.5 %	0.5 %	0.5 %	0.5 %	0.5 %	0.5 %	0.5 %
Binning	0.5 %	0.5 %	0.5 %	0.5 %	0.5 %	0.5 %	0.5 %
Other sources	0.5 %	0.5 %	0.5 %	0.5 %	0.5 %	0.5 %	0.5 %
Total(upper limit)	10.7 %	3.8 %	4.4 %	4.0 %	3.8 %	3.6 %	3.6 %
Total(quadratic sum)	5.7 %	1.8 %	1.9 %	1.8 %	1.8 %	1.8 %	1.8 %

Table 5.5: Systematic error sources evaluated in % for the p+Pb centrality sets. See Table 5.4 on page 45 for the set definitions.

There are a few phase space regions where additional systematic uncertainties have to be allowed, mostly connected with particle identification by $\mathrm{d}E/\mathrm{d}x$ fits:

- At $x_F = 0$ and $p_T < 0.3\,\mathrm{GeV/c}$ the K/π and p/π ratios have to be extrapolated for π^+ meson only from the measured region of p_T, due to overlap between the $\mathrm{d}E/\mathrm{d}x$ distributions of pions, kaons and protons. This may introduce yield uncertainties between 1 and 5 %.

- A similar problem arises for π^+, in the region of x_F above 0.3 where the dominating proton yield necessitates assumptions about the K/π ratio in order to stabilize the fitting procedure.

- Finally, for regions of low cross section at large p_T and in the forward region at $x_F > 0.3$, there is a systematic error again in the $\mathrm{d}E/\mathrm{d}x$ which is related to the statistics in each bin [98]. This error, however, is always below the statistical uncertainty.

Chapter 6

Measured pion cross sections

This chapter presents the measured values of the invariant cross sections respective the invariant densities of pion production in p+Pb interactions in the defined centrality sets. The data are given in tables and plots. The values were extracted as described in the preceding section using the $\mathrm{d}E/\mathrm{d}x$ fit method and applying the corrections discussed above. Similar tables and plots for the p+p and p+C reactions are available in [61] and [62].

6.1 Data tables

The double differential invariant densities for both pion charges for the centrality triggered sample are shown in Tab. 6.1; Tab. 6.2 – 6.6 cover the 5 centrality sets defined in Tab. 5.4 page 45.

The double differential invariant cross section measurements and respective statistical errors are given in Tab. 6.7 for positive and negative pions produced in minimum bias p+Pb interactions.

The statistical uncertainty Δd is given in percent to the right of the presented values in all the tables.

All centrality triggered set of p+Pb events																				
							π^+	$d(x_F, p_T)$	Δd											
$p_T \backslash x_F$	0.0		0.05		0.10		0.15		0.20		0.25		0.30		0.35		0.40			
0.05	6.17	1.3	1.654	0.7	0.701	1.6	0.380	1.9	0.2203	3.0	0.1410	5.2	0.0980	7.5	0.0548	16	0.0345	21		
0.10	5.30	1.8	1.639	0.6	0.689	1.4	0.370	1.7	0.2254	2.5	0.1415	4.5	0.0861	6.9	0.0448	13	0.0388	16		
0.15	4.48	4.3	1.552	0.6	0.672	1.1	0.366	1.3	0.2146	2.1	0.1333	3.9	0.0764	6.5	0.0474	9.6	0.0332	14		
0.20	3.17	1.8	1.363	0.5	0.638	1.0	0.338	1.2	0.1983	2.1	0.1252	3.5	0.0799	5.6	0.0422	8.8	0.0352	11		
0.25	2.365	1.6	1.168	0.6	0.573	1.0	0.3106	1.1	0.1818	1.9	0.1162	3.4								
0.30	1.784	0.5	0.953	0.6	0.500	1.0	0.2764	1.1	0.1675	1.7	0.0982	3.8	0.0654	3.8	0.0396	4.9	0.02657	7.4		
0.40	0.970	0.5	0.604	0.6	0.356	0.7	0.2093	0.8	0.1302	1.4	0.0795	2.2	0.0500	5.3	0.0324	4.8	0.02084	7.1		
0.50	0.535	0.8	0.360	0.8	0.2338	0.8	0.1483	0.9	0.0970	1.4	0.0594	2.4	0.0409	6.2	0.02510	5.1	0.01738	6.5		
0.60	0.3008	0.9	0.2228	1.0	0.1519	1.0	0.1011	1.1	0.0682	1.6	0.0445	2.4	0.02883	4.5	0.01956	6.5	0.01387	8.8		
0.70	0.1759	1.1	0.1340	1.3	0.0952	1.5	0.0667	1.3	0.0465	1.9	0.0323	2.7	0.02148	6.2	0.01495	7.0	0.01050	6.9		
0.80	0.1054	1.4	0.0797	1.6	0.0625	1.9	0.0461	1.5	0.03120	2.3	0.02332	2.8	0.01396	6.1	0.01135	6.8	0.00645	8.4		
0.90	0.0647	1.8	0.0517	2.2	0.0392	2.6	0.02991	1.8	0.02087	2.6	0.01489	3.5	0.00996	5.9	0.00750	11	0.00506	8.6		
1.10	0.02487	2.0	0.02043	2.4	0.01648	2.9	0.01291	2.1	0.00961	2.6	0.00743	3.6	0.00569	5.7	0.00402	5.9	0.002441	8.1		
1.30	0.01049	3.0	0.00915	3.6	0.00746	4.2	0.00558	3.4	0.00430	4.7	0.00326	6.3	0.002646	5.9	0.001699	8.5	0.001239	10		
1.50	0.00391	5.4	0.00367	5.7	0.00332	6.2	0.002693	5.3	0.001832	6.9	0.001559	11	0.001429	7.3	0.000817	12	0.000680	13		
1.70	0.001805	5.2	0.001820	6.0	0.001403	6.6	0.001229	8.4	0.000838	9.1	0.000733	9.4	0.000536	12	0.000494	14	0.000334	19		
1.90	0.000743	7.9	0.000939	8.0	0.000614	9.9	0.000685	11	0.000440	12			0.000247	12			0.000153	20		
2.10	0.000337	12	0.000429	12	0.000365	13	0.000295	15	0.000290	15			0.000147	15			0.000094	26		
							π^-	$d(x_F, p_T)$	Δd											
$p_T \backslash x_F$	0.0		0.05		0.10		0.15		0.20		0.25		0.30		0.35		0.40			
0.05	6.07	7.9	1.511	0.8	0.587	1.7	0.2807	2.2	0.1455	3.5	0.0874	6.1	0.0507	10	0.0358	18	0.01503	28		
0.10	5.08	2.5	1.453	0.7	0.570	1.5	0.2825	1.9	0.1451	4.7	0.0872	5.0	0.0471	9.0	0.02889	14	0.01829	18		
0.15	4.06	1.4	1.371	0.6	0.552	1.3	0.2643	1.6	0.1355	3.0	0.0774	4.4	0.0508	7.4	0.02811	11	0.01477	18		
0.20	3.157	1.5	1.216	0.5	0.500	1.2	0.2511	1.5	0.1343	2.4	0.0771	4.4	0.0414	7.2	0.02616	10	0.01689	14		
0.25	2.366	1.5	1.041	0.6	0.460	1.1	0.2247	1.4	0.1181	2.4	0.0672	3.9								
0.30	1.732	1.4	0.848	0.7	0.417	1.0	0.2036	1.3	0.1160	2.1	0.0614	4.2	0.0356	4.5	0.02161	8.2	0.01309	9.0		
0.40	0.934	0.7	0.545	0.6	0.2922	0.8	0.1549	0.9	0.0855	1.9	0.0507	2.5	0.02946	5.0	0.02024	5.8	0.01073	8.7		
0.50	0.507	0.8	0.332	0.9	0.1941	0.9	0.1111	1.0	0.0653	2.8	0.0387	2.7	0.02342	4.7	0.01426	6.2	0.00765	9.1		
0.60	0.2858	0.9	0.2010	1.1	0.1281	1.0	0.0771	1.3	0.0461	2.0	0.03001	2.8	0.01824	4.4	0.01048	6.6	0.00697	8.7		
0.70	0.1664	1.2	0.1233	1.3	0.0800	1.6	0.0512	1.5	0.0324	2.3	0.02142	3.1	0.01290	6.7	0.00889	6.7	0.00529	9.2		
0.80	0.0978	1.5	0.0761	1.6	0.0518	2.1	0.0351	1.7	0.02356	2.4	0.01473	3.4	0.00932	5.8	0.00567	8.0	0.00346	11		
0.90	0.0616	1.8	0.0464	2.3	0.0342	2.7	0.02293	2.1	0.01573	2.8	0.01020	3.9	0.00648	6.1	0.00470	8.1	0.002111	13		
1.10	0.02298	2.1	0.01878	2.5	0.01398	3.1	0.00971	2.3	0.00702	2.9	0.00482	3.9	0.00352	5.1	0.002138	7.8	0.001521	9.9		
1.30	0.01018	3.0	0.00791	3.8	0.00600	4.6	0.00453	3.7	0.003069	4.0	0.001943	8.0	0.001646	7.0	0.000921	11	0.000745	13		
1.50	0.00401	4.9	0.00352	5.8	0.002974	6.5	0.001980	6.0	0.001382	6.5	0.001136	11	0.000870	9.4	0.000512	14	0.000409	16		
1.70	0.001541	5.8	0.001471	6.3	0.001130	7.3	0.000965	8.7	0.000471	12	0.000648	9.7	0.000407	13	0.000232	21	0.000229	21		
1.90	0.000680	8.5	0.000718	8.9	0.000554	10	0.000394	13	0.000387	13			0.000155	14			0.000098	23		
2.10	0.000316	12	0.000339	14	0.000333	14	0.000172	20	0.000156	21			0.000107	18			0.000036	36		

Table 6.1: Double differential invariant density $d(x_F, p_T)$ [c^3/GeV^2] for π^+ and π^- produced in the set of all centrality triggered p+Pb interactions at 158 GeV/c. The statistical uncertainty Δd is given in %. p_T in the left column is given in GeV/c

Centrality selected set 1 of p+Pb events

π^+ $d(x_F, p_T)$ Δd

$p_T \backslash x_F$	0.0		0.05		0.10		0.15		0.20		0.25		0.30		0.35		0.40	
0.05	4.09	4.1	1.736	1.8	0.878	3.6	0.554	3.8	0.348	5.6	0.2665	8.7	0.2210	12	0.0532	43	0.0515	44
0.10	3.79	4.6	1.809	1.6	0.908	3.1	0.560	3.3	0.344	4.9	0.2736	7.1	0.1441	13	0.0674	28	0.0939	24
0.15	3.54	10	1.701	1.4	0.867	2.6	0.534	2.8	0.330	4.1	0.2278	6.4	0.1636	10.0	0.0724	20	0.0816	21
0.20	2.252	4.9	1.474	1.3	0.820	2.3	0.492	2.5	0.3067	3.7	0.2186	5.7	0.1357	9.6	0.0773	17	0.0727	18
0.25	1.827	4.6	1.231	1.5	0.729	2.2	0.435	2.4	0.2831	3.5	0.1805	6.0						
0.30	1.395	1.5	0.992	1.6	0.594	2.3	0.386	2.3	0.2562	3.3	0.1634	4.1	0.1175	6.1	0.0626	9.8	0.0496	14
0.40	0.765	1.3	0.576	1.6	0.428	1.7	0.2714	1.7	0.1847	2.8	0.1195	4.1	0.0851	6.5	0.0549	9.3	0.0442	12
0.50	0.433	1.8	0.341	2.2	0.2543	2.0	0.1819	1.9	0.1344	3.0	0.0879	4.4	0.0665	6.7	0.0362	10.0	0.0368	11
0.60	0.2397	2.3	0.2038	2.7	0.1629	2.3	0.1189	2.6	0.0888	3.4	0.0629	4.7	0.0456	7.1	0.02759	11	0.02226	13
0.70	0.1364	3.1	0.1161	3.5	0.0985	3.7	0.0763	3.0	0.0565	4.2	0.0442	5.3	0.02964	8.7	0.02193	12	0.01519	15
0.80	0.0803	4.0	0.0677	4.5	0.0611	4.9	0.0489	3.6	0.0385	4.9	0.0334	5.7	0.02145	9.3	0.01376	13	0.00872	19
0.90	0.0498	5.1	0.0439	6.2	0.0344	7.0	0.02982	4.5	0.02371	6.0	0.01720	7.7	0.01130	12	0.00890	16	0.00905	16
1.10	0.01731	6.0	0.01536	7.2	0.01449	8.0	0.01057	5.7	0.00923	6.3	0.00918	6.9	0.00616	11	0.00548	13	0.002305	22
1.30	0.00860	8.4	0.00656	11	0.00554	13	0.00537	8.9	0.00430	9.0	0.00372	10	0.002712	15	0.001870	21	0.001317	26
1.50	0.00357	14	0.002365	18	0.00317	17	0.002286	15	0.001661	16	0.001537	18	0.001468	19	0.000846	31	0.000893	31
1.70	0.001253	16	0.001821	15	0.001204	19	0.000626	29	0.000410	35	0.000892	22	0.000824	25	0.000559	34	0.000241	67
1.90	0.000463	27	0.000669	25	0.000553	28	0.000432	34	0.000322	37			0.000277	29			0.000229	44
2.10	0.000279	36	0.000380	33	0.000394	33	0.000213	48	0.000237	46			0.000100	52			0.000032	82

π^- $d(x_F, p_T)$ Δd

$p_T \backslash x_F$	0.0		0.05		0.10		0.15		0.20		0.25		0.30		0.35		0.40	
0.05	3.84	6.9	1.533	2.0	0.684	4.1	0.377	4.7	0.2227	7.0	0.1214	13	0.0689	23	0.0680	33	0.0357	46
0.10	3.45	4.6	1.494	1.7	0.693	3.5	0.391	4.0	0.2243	6.1	0.1621	9.2	0.0800	18	0.0371	32	0.0540	28
0.15	2.922	3.8	1.435	1.5	0.659	3.0	0.372	3.3	0.1909	5.4	0.0980	9.8	0.0944	13	0.0525	22	0.02225	37
0.20	2.427	4.1	1.246	1.4	0.619	2.7	0.351	3.0	0.1801	4.8	0.1180	7.6	0.0677	14	0.0348	23	0.01348	49
0.25	1.767	4.7	1.073	1.6	0.537	2.6	0.2999	2.9	0.1767	4.3	0.1073	7.7						
0.30	1.334	1.5	0.851	1.7	0.490	2.5	0.2658	2.8	0.1650	4.1	0.0938	5.3	0.0641	8.1	0.0358	13	0.02908	15
0.40	0.742	1.4	0.527	1.7	0.329	1.9	0.1965	2.1	0.1087	3.6	0.0778	5.1	0.0480	8.2	0.03158	12	0.02433	15
0.50	0.397	1.8	0.3085	2.3	0.2034	2.2	0.1311	2.3	0.0887	3.6	0.0574	5.3	0.0361	8.5	0.02371	12	0.01305	18
0.60	0.2211	2.4	0.1750	2.9	0.1282	2.6	0.0926	2.9	0.0630	4.0	0.0424	5.7	0.02584	9.3	0.01662	14	0.01016	19
0.70	0.1302	3.1	0.1055	3.7	0.0841	4.0	0.0556	3.5	0.0375	5.2	0.02916	6.4	0.01814	10	0.01332	14	0.00658	21
0.80	0.0738	4.2	0.0616	4.7	0.0478	5.6	0.0335	4.3	0.02583	5.9	0.01720	8.0	0.01304	12	0.00713	19	0.00379	27
0.90	0.0496	5.1	0.0354	6.9	0.0333	7.1	0.02264	5.1	0.01707	7.0	0.01290	8.8	0.00666	15	0.00663	18	0.00453	23
1.10	0.01806	5.9	0.01438	7.5	0.01189	8.9	0.00818	6.4	0.00648	7.4	0.00454	9.7	0.00328	14	0.002321	20	0.002236	22
1.30	0.00652	9.9	0.00604	12	0.00396	15	0.00440	9.8	0.00338	9.7	0.001529	16	0.001764	18	0.001125	27	0.000600	44
1.50	0.003064	14	0.002864	17	0.002903	17	0.001742	17	0.001271	18	0.000727	25	0.000912	24	0.000372	47	0.000267	60
1.70	0.001286	16	0.001147	19	0.000703	25	0.000771	25	0.000320	38	0.000612	26	0.000487	33	0.000279	50	0.000245	55
1.90	0.000535	25	0.000492	29	0.000353	36	0.000347	37	0.000373	35			0.000135	42			0.000029	75
2.10	0.000197	44	0.000327	36	0.000205	46	0.000142	48	0.000148	59			0.000096	52			0.000090	85

Table 6.2: Double differential invariant density $d(x_F, p_T)$ [c^3/GeV^2] for π^+ and π^- produced in centrality selected set 1 of p+Pb interactions at 158 GeV/c. The statistical uncertainty Δd is given in %. p_T in the left column is given in GeV/c

Centrality selected set 2 of p+Pb events																						
π^+ in $d(x_F, p_T)$ Δd																						
$p_T \backslash x_F$	0.0		0.05		0.10		0.15		0.20		0.25		0.30		0.35		0.40					
0.05	5.37	2.5	1.728	1.3	0.772	2.8	0.461	3.0	0.2482	4.8	0.1501	8.5	0.1014	13	0.0601	27	0.0380	37				
0.10	4.94	2.9	1.724	1.2	0.768	2.4	0.438	2.7	0.2684	4.0	0.1715	6.5	0.1104	12	0.0653	19	0.0339	32				
0.15	4.43	6.7	1.657	1.0	0.761	2.0	0.417	2.3	0.2509	3.4	0.1481	5.8	0.0903	9.9	0.0623	15	0.02407	31				
0.20	3.20	1.8	1.438	0.9	0.707	1.8	0.369	2.1	0.2368	3.1	0.1457	5.1	0.0975	8.9	0.0510	15	0.01446	69				
0.25	2.387	1.6	1.242	1.1	0.632	1.7	0.345	1.9	0.2063	3.0	0.1345	5.0										
0.30	1.729	1.0	0.990	1.1	0.545	1.7	0.317	1.8	0.1920	2.8	0.1212	3.5	0.0812	5.3	0.0488	8.0	0.03140	13				
0.40	0.932	0.9	0.627	1.1	0.388	1.3	0.2352	1.3	0.1525	2.2	0.0897	3.5	0.0573	5.7	0.0355	8.4	0.01840	18				
0.50	0.515	1.1	0.366	1.5	0.2474	1.4	0.1611	1.5	0.1122	2.3	0.0696	3.5	0.0473	5.8	0.02486	11	0.01956	11				
0.60	0.2900	1.5	0.2217	1.8	0.1606	1.7	0.1112	1.9	0.0750	2.6	0.0501	3.8	0.0333	6.1	0.02430	8.2	0.01694	11				
0.70	0.1689	2.0	0.1332	2.3	0.0960	2.7	0.0724	2.2	0.0506	3.2	0.0384	4.1	0.02350	6.9	0.01371	12	0.01239	12				
0.80	0.1020	2.5	0.0798	3.0	0.0631	3.4	0.0473	2.6	0.0354	3.6	0.02649	4.7	0.01903	7.0	0.01432	9.5	0.00875	13				
0.90	0.0590	3.3	0.0528	4.0	0.0372	4.8	0.03148	3.1	0.02277	4.3	0.01624	5.6	0.01252	8.1	0.00891	12	0.00735	14				
1.10	0.02408	3.6	0.01974	4.5	0.01629	5.4	0.01263	3.7	0.01070	4.1	0.00837	5.2	0.00604	7.4	0.00432	10	0.00319	13				
1.30	0.00964	5.6	0.00866	6.8	0.00696	8.0	0.00527	6.4	0.00424	6.5	0.00347	7.5	0.002840	11	0.002150	14	0.000924	37				
1.50	0.00384	9.1	0.00334	11	0.002903	12	0.002290	10	0.001940	10	0.002144	10	0.001457	14	0.000702	25	0.000762	23				
1.70	0.001744	9.5	0.001661	11	0.001367	12	0.001011	16	0.000877	16	0.000890	17	0.000455	24	0.000681	22	0.000325	36				
1.90	0.000640	16	0.000903	15	0.000655	18	0.000815	17	0.000465	22			0.000234	24			0.000226	31				
2.10	0.000319	23	0.000422	24	0.000287	27	0.000197	35	0.000372	24			0.000146	28			0.000098	57				
π^- $d(x_F, p_T)$ Δd																						
$p_T \backslash x_F$	0.0		0.05		0.10		0.15		0.20		0.25		0.30		0.35		0.40					
0.05	5.19	2.3	1.600	1.4	0.666	3.0	0.322	3.6	0.1669	5.9	0.1055	10	0.0558	18	0.0408	33	0.01803	52				
0.10	4.78	2.8	1.515	1.2	0.639	2.6	0.329	3.1	0.1616	5.2	0.0844	9.3	0.0581	15	0.02808	26	0.01814	36				
0.15	3.88	2.4	1.408	1.1	0.593	2.2	0.2903	2.7	0.1524	4.4	0.0864	7.5	0.0585	12	0.0329	20	0.01649	33				
0.20	2.962	2.7	1.276	1.0	0.548	2.0	0.2805	2.4	0.1532	3.8	0.0763	7.0	0.0517	11	0.0325	18	0.02118	23				
0.25	2.278	2.9	1.064	1.1	0.504	1.9	0.2532	2.3	0.1365	3.6	0.0698	6.9										
0.30	1.629	1.0	0.881	1.2	0.449	1.9	0.2312	2.2	0.1340	3.3	0.0706	4.4	0.0393	7.5	0.02427	12	0.01592	16				
0.40	0.863	0.9	0.548	1.2	0.3121	1.4	0.1712	1.6	0.0987	2.7	0.0577	4.3	0.0346	7.0	0.02061	10	0.01292	15				
0.50	0.477	1.2	0.331	1.6	0.2073	1.6	0.1186	1.7	0.0739	2.9	0.0435	4.4	0.02705	7.1	0.01714	10	0.00889	16				
0.60	0.2648	1.6	0.2065	1.9	0.1321	1.8	0.0808	2.2	0.0521	3.1	0.0328	4.7	0.01977	7.6	0.01294	11	0.00750	16				
0.70	0.1656	2.0	0.1243	2.4	0.0824	2.9	0.0549	2.5	0.0349	3.8	0.02369	5.1	0.01507	8.1	0.00971	12	0.00557	17				
0.80	0.0927	2.6	0.0754	3.0	0.0519	3.8	0.0371	2.9	0.02540	4.2	0.01569	5.9	0.01104	9.0	0.00755	13	0.00465	18				
0.90	0.0588	3.3	0.0442	4.4	0.0343	4.9	0.02250	3.6	0.01574	5.2	0.01097	6.8	0.00782	10	0.00435	16	0.002096	26				
1.10	0.02091	3.8	0.01758	4.7	0.01365	5.9	0.00973	4.1	0.00697	5.1	0.00576	6.1	0.00385	9.1	0.002321	14	0.001679	17				
1.30	0.00895	5.9	0.00772	7.1	0.00613	8.5	0.00480	6.6	0.00317	7.1	0.002256	9.1	0.001650	13	0.001146	18	0.000904	22				
1.50	0.00361	9.3	0.00355	10	0.002860	12	0.002153	11	0.001292	12	0.001126	14	0.000740	19	0.000528	27	0.000618	26				
1.70	0.001391	11	0.001500	11	0.001012	14	0.000857	17	0.000553	20	0.000742	17	0.000296	28	0.000161	49	0.000295	41				
1.90	0.000662	16	0.000640	18	0.000320	26	0.000266	30	0.000235	31			0.000138	29			0.000122	38				
2.10	0.000244	25	0.000319	26	0.000289	27	0.000241	30	0.000103	48			0.000087	37			0.000016	74				

Table 6.3: Double differential invariant density $d(x_F, p_T)$ [c^3/GeV^2] for π^+ and π^- produced in centrality selected set 2 of p+Pb interactions at 158 GeV/c. The statistical uncertainty Δd is given in %. p_T in the left column is given in GeV/c

Centrality selected set 3 of p+Pb events

π^+ $d(x_F, p_T)$ Δd

$p_T \backslash x_F$	0.0		0.05		0.10		0.15		0.20		0.25		0.30		0.35		0.40	
0.05	6.54	2.1	1.664	1.3	0.686	2.8	0.323	3.5	0.1845	5.5	0.1092	9.7	0.0546	18	0.0513	31	0.02931	42
0.10	5.87	2.8	1.632	1.1	0.645	2.5	0.3154	3.1	0.1935	4.6	0.1084	8.1	0.0795	13	0.0401	24	0.03049	31
0.15	4.18	7.6	1.548	1.0	0.628	2.1	0.335	2.4	0.1843	3.9	0.1153	6.4	0.0553	13	0.0349	20	0.02973	26
0.20	3.30	3.2	1.364	0.9	0.599	1.9	0.3090	2.2	0.1670	3.6	0.1068	5.8	0.0600	10	0.0376	17	0.02051	26
0.25	2.480	2.9	1.171	1.1	0.540	1.8	0.2869	2.1	0.1617	3.2	0.0978	5.7						
0.30	1.872	0.9	0.946	1.1	0.481	1.7	0.2492	2.0	0.1450	3.1	0.0863	4.0	0.0511	6.6	0.0327	9.6	0.02068	15
0.40	1.013	0.8	0.609	1.1	0.344	1.3	0.1963	1.4	0.1168	2.5	0.0677	3.9	0.0421	6.5	0.0317	8.6	0.01192	17
0.50	0.556	1.1	0.367	1.4	0.2334	1.4	0.1454	1.5	0.0879	2.5	0.0510	4.0	0.0352	6.5	0.02299	8.9	0.01480	13
0.60	0.317	1.4	0.2279	1.8	0.1497	1.7	0.0980	2.0	0.0642	2.8	0.0429	4.0	0.02494	6.8	0.01903	9.2	0.01107	13
0.70	0.1844	1.8	0.1402	2.2	0.0959	2.6	0.0660	2.3	0.0457	3.2	0.03033	4.4	0.01896	7.5	0.01443	9.9	0.00985	13
0.80	0.1095	2.3	0.0826	2.8	0.0645	3.3	0.0461	2.6	0.02867	3.9	0.02261	4.8	0.01111	9.0	0.01039	11	0.00660	15
0.90	0.0688	2.9	0.0508	3.9	0.0424	4.3	0.02998	3.1	0.01971	4.5	0.01397	5.9	0.00912	9.3	0.00713	13	0.003042	20
1.10	0.02762	3.2	0.02191	4.1	0.01688	5.1	0.01385	3.4	0.00910	4.3	0.00699	5.5	0.00560	7.7	0.00431	10	0.002184	15
1.30	0.01098	5.1	0.00917	6.4	0.00819	7.1	0.00563	6.0	0.00456	6.0	0.00355	7.1	0.002813	10	0.001982	14	0.001304	18
1.50	0.00387	8.9	0.00371	10.0	0.00332	11	0.003090	8.6	0.001806	10	0.001723	11	0.001287	14	0.000933	21	0.000667	24
1.70	0.001881	8.8	0.002052	9.5	0.001455	12	0.001725	11	0.000916	16	0.000524	20	0.000496	22	0.000507	26	0.000250	41
1.90	0.000887	13	0.000896	15	0.000579	18	0.000643	19	0.000406	22			0.000271	20			0.000174	34
2.10	0.000381	20	0.000496	20	0.000411	22	0.000318	26	0.000190	33			0.000113	30			0.000106	42

π^- $d(x_F, p_T)$ Δd

$p_T \backslash x_F$	0.0		0.05		0.10		0.15		0.20		0.25		0.30		0.35		0.40	
0.05	6.61	2.0	1.508	1.4	0.572	3.1	0.2518	4.0	0.1244	6.6	0.0696	12	0.0494	18	0.02523	42	0.01108	61
0.10	5.92	2.5	1.481	1.2	0.543	2.8	0.2601	3.4	0.1357	5.7	0.0687	10	0.0403	18	0.03073	25	0.01334	39
0.15	4.58	2.1	1.376	1.0	0.549	2.2	0.2480	2.8	0.1246	4.7	0.0621	8.7	0.0415	15	0.02401	22	0.01739	29
0.20	3.27	2.5	1.220	1.0	0.481	2.1	0.2261	2.6	0.1207	4.1	0.0757	6.8	0.0350	15	0.01748	22	0.01045	31
0.25	2.523	2.7	1.060	1.1	0.440	2.0	0.2058	2.4	0.0997	4.1	0.0594	7.2						
0.30	1.833	0.9	0.856	1.2	0.400	1.9	0.1869	2.3	0.1010	3.7	0.0541	4.9	0.0329	8.2	0.01685	13	0.00840	21
0.40	0.971	0.8	0.551	1.1	0.2836	1.4	0.1465	1.6	0.0810	3.0	0.0442	4.7	0.02094	8.8	0.01876	11	0.00682	20
0.50	0.532	1.1	0.339	1.5	0.1967	1.6	0.1071	1.7	0.0593	3.2	0.0338	4.8	0.02078	7.9	0.01149	12	0.00733	17
0.60	0.3054	1.4	0.2059	1.8	0.1278	1.8	0.0752	2.2	0.0430	3.4	0.02649	5.0	0.01702	7.9	0.00844	13	0.00524	18
0.70	0.1692	1.9	0.1259	2.3	0.0801	2.8	0.0496	2.6	0.03132	3.9	0.02043	5.3	0.01084	9.4	0.00829	12	0.00508	17
0.80	0.1026	2.4	0.0796	2.8	0.0529	3.6	0.0344	3.0	0.02213	4.4	0.01445	5.9	0.00885	9.6	0.00382	18	0.00354	19
0.90	0.0637	3.1	0.0485	4.0	0.0343	4.8	0.02392	3.4	0.01673	4.8	0.00972	6.9	0.00613	11	0.00398	16	0.001098	34
1.10	0.02431	3.4	0.01914	4.4	0.01444	5.5	0.01060	3.8	0.00738	4.7	0.00479	6.4	0.00339	9.4	0.002017	14	0.001397	19
1.30	0.01145	4.9	0.00827	6.6	0.00604	8.2	0.00451	6.6	0.002756	7.3	0.002126	9.1	0.001713	12	0.000611	24	0.000702	25
1.50	0.00447	8.0	0.00335	10	0.003156	11	0.002048	11	0.001472	11	0.001116	14	0.000822	17	0.000380	29	0.000236	40
1.70	0.001520	9.9	0.001524	11	0.001084	13	0.000924	16	0.000525	20	0.000631	17	0.000320	26	0.000295	33	0.000191	42
1.90	0.000643	15	0.000694	16	0.000810	15	0.000296	27	0.000529	19			0.000137	28			0.000156	32
2.10	0.000355	21	0.000358	24	0.000336	24	0.000165	37	0.000126	43			0.000090	34			0.000065	46

Table 6.4: Double differential invariant density $d(x_F, p_T)$ [c^3/GeV^2] for π^+ and π^- produced in centrality selected set 3 of p+Pb interactions at 158 GeV/c. The statistical uncertainty Δd is given in %. p_T in the left column is given in GeV/c

Centrality selected set 4 of p+Pb events																						
π^+ $d(x_F, p_T)$ Δd																						
$p_T \backslash x_F$	0.0		0.05		0.10		0.15		0.20		0.25		0.30		0.35		0.40					
0.05	6.97	2.3	1.577	1.5	0.592	3.3	0.2817	4.2	0.1678	6.3	0.1017	11	0.0641	19	0.0464	35	0.01481	73				
0.10	6.09	2.7	1.524	1.3	0.571	3.0	0.2761	3.6	0.1579	5.7	0.0748	11	0.0433	20	0.02177	38	0.02061	42				
0.15	4.85	7.0	1.405	1.1	0.546	2.5	0.2687	3.0	0.1415	4.9	0.0950	7.8	0.0419	16	0.03083	24	0.02134	33				
0.20	3.61	2.7	1.263	1.1	0.522	2.2	0.2629	2.6	0.1380	4.4	0.0730	7.8	0.0548	12	0.02071	26	0.01962	28				
0.25	2.627	3.1	1.080	1.2	0.483	2.1	0.2409	2.5	0.1277	4.0	0.0777	7.1										
0.30	1.925	1.0	0.914	1.2	0.435	2.0	0.2153	2.4	0.1232	3.7	0.0672	5.0	0.0393	8.3	0.02908	11	0.01632	19				
0.40	1.059	0.9	0.591	1.2	0.3066	1.5	0.1670	1.7	0.0928	3.1	0.0615	4.5	0.0319	8.4	0.01644	13	0.01232	19				
0.50	0.580	1.2	0.369	1.6	0.2151	1.7	0.1226	1.8	0.0727	3.1	0.0434	4.8	0.02774	8.0	0.01595	12	0.00836	19				
0.60	0.326	1.5	0.2279	1.9	0.1408	1.9	0.0864	2.3	0.0540	3.3	0.0322	5.1	0.02035	8.3	0.01206	13	0.00983	15				
0.70	0.1939	2.0	0.1361	2.5	0.0925	2.9	0.0574	2.7	0.0383	3.9	0.02334	5.6	0.01881	8.1	0.00893	14	0.00671	17				
0.80	0.1166	2.5	0.0844	3.1	0.0607	3.7	0.0441	2.9	0.02708	4.5	0.01700	6.1	0.01004	10	0.00812	14	0.00342	23				
0.90	0.0743	3.1	0.0525	4.3	0.0402	4.9	0.02866	3.5	0.01928	5.0	0.01294	6.7	0.00757	11	0.00541	16	0.00404	19				
1.10	0.02585	3.7	0.02114	4.6	0.01681	5.7	0.01331	3.8	0.00915	4.8	0.00631	6.4	0.00502	8.9	0.002919	14	0.002033	17				
1.30	0.01170	5.4	0.01075	6.5	0.00757	8.2	0.00598	6.4	0.00418	7.0	0.00339	8.0	0.002469	12	0.000813	25	0.001212	20				
1.50	0.00452	9.0	0.00448	10.0	0.00393	11	0.002985	9.7	0.001888	11	0.001459	14	0.001724	13	0.000864	23	0.000442	33				
1.70	0.001954	9.5	0.001839	11	0.001327	14	0.001275	15	0.000971	16	0.000670	20	0.000705	20	0.000336	35	0.000371	35				
1.90	0.000878	14	0.001049	15	0.000524	21	0.000818	18	0.000449	24			0.000261	23			0.000084	55				
2.10	0.000453	20	0.000392	26	0.000402	24	0.000357	27	0.000372	25			0.000245	22			0.000143	41				
π^- $d(x_F, p_T)$ Δd																						
$p_T \backslash x_F$	0.0		0.05		0.10		0.15		0.20		0.25		0.30		0.35		0.40					
0.05	7.04	4.1	1.422	1.6	0.497	3.7	0.2281	4.6	0.1072	7.9	0.0721	13	0.0379	23	0.01118	71	0.00959	74				
0.10	5.73	2.7	1.376	1.4	0.483	3.2	0.2066	4.2	0.1102	7.0	0.0599	12	0.02363	25	0.02138	33	0.00701	62				
0.15	4.40	2.4	1.302	1.2	0.467	2.7	0.2086	3.4	0.1041	5.7	0.0625	9.7	0.0346	17	0.01469	31	0.00434	78				
0.20	3.63	2.6	1.152	1.1	0.422	2.5	0.1936	3.1	0.1002	5.0	0.0492	9.4	0.02790	17	0.01604	26	0.01069	36				
0.25	2.654	2.9	0.993	1.3	0.398	2.3	0.1811	2.9	0.0868	4.9	0.0452	9.2										
0.30	1.883	1.0	0.798	1.3	0.369	2.2	0.1634	2.8	0.0879	4.4	0.0386	6.5	0.02277	11	0.01477	16	0.00550	27				
0.40	1.013	0.9	0.534	1.3	0.2612	1.6	0.1269	2.0	0.0647	3.7	0.0316	6.2	0.02030	9.9	0.01493	13	0.00469	26				
0.50	0.552	1.2	0.330	1.7	0.1705	1.8	0.0971	2.0	0.0518	3.8	0.02634	6.1	0.01384	11	0.00869	16	0.00417	24				
0.60	0.3085	1.6	0.2037	2.1	0.1248	2.0	0.0676	2.6	0.0351	4.1	0.02209	6.0	0.01362	9.7	0.00767	15	0.00506	20				
0.70	0.1812	2.0	0.1248	2.6	0.0761	3.2	0.0463	2.9	0.02852	4.5	0.01476	6.9	0.00995	11	0.00657	15	0.00442	20				
0.80	0.1064	2.6	0.0790	3.2	0.0527	4.0	0.0343	3.3	0.02099	4.9	0.01223	7.1	0.00671	12	0.00394	19	0.001593	32				
0.90	0.0670	3.3	0.0517	4.3	0.0341	5.3	0.02154	4.0	0.01388	5.8	0.00752	8.7	0.00479	14	0.00391	18	0.001492	31				
1.10	0.02632	3.6	0.02187	4.5	0.01484	6.0	0.00919	4.5	0.00702	5.3	0.00398	7.8	0.00330	10	0.001814	17	0.000988	25				
1.30	0.01064	5.7	0.00812	7.4	0.00674	8.6	0.00450	7.3	0.002792	8.0	0.001872	11	0.001324	15	0.000912	22	0.000552	31				
1.50	0.00418	9.1	0.00378	11	0.002456	14	0.001912	12	0.001281	13	0.000776	18	0.000855	18	0.000561	27	0.000212	47				
1.70	0.001816	9.9	0.001642	12	0.001475	13	0.001067	16	0.000491	22	0.000601	20	0.000444	25	0.000073	92	0.000231	43				
1.90	0.000741	16	0.000828	16	0.000721	18	0.000755	18	0.000349	26			0.000180	26			0.000081	56				
2.10	0.000454	20	0.000324	27	0.000268	31	0.000142	46	0.000107	53			0.000103	35			0.000034	76				

Table 6.5: Double differential invariant density $d(x_F, p_T)$ [c^3/GeV^2] for π^+ and π^- produced in centrality selected set 4 of p+Pb interactions at 158 GeV/c. The statistical uncertainty Δd is given in %. p_T in the left column is given in GeV/c

Centrality selected set 5 of p+Pb events																						
π^+ $d(x_F, p_T)$ Δd																						
$p_T \backslash x_F$	0.0		0.05		0.10		0.15		0.20		0.25		0.30		0.35							
0.05	7.75	5.5	1.398	3.9	0.462	9.6	0.2281	12	0.1324	18	0.0508	42	0.0535	51	0.0387	44						
0.10	5.25	1.8	1.358	3.5	0.509	8.0	0.2274	10	0.0886	20	0.0341	43	0.0421	52	0.03028	50						
0.15	4.44	4.3	1.339	2.9	0.512	6.5	0.2246	8.3	0.1367	12	0.0781	22	0.01747	64	0.01291	77						
0.20	3.42	9.3	1.195	2.8	0.446	6.1	0.2229	7.3	0.0983	13	0.0512	24	0.02294	47	0.01508	79						
0.25	2.892	7.5	0.963	3.2	0.422	5.6	0.1880	7.1	0.1120	11	0.0746	18										
0.30	1.930	2.5	0.849	3.2	0.364	5.6	0.1760	6.8	0.0933	11	0.0584	14	0.02437	27	0.01687	38						
0.40	1.087	2.2	0.555	3.2	0.2677	4.1	0.1373	4.8	0.0848	8.0	0.0469	13	0.02381	25	0.01572	34						
0.50	0.579	2.9	0.321	4.3	0.1885	4.5	0.1007	5.1	0.0614	8.6	0.03079	15	0.01824	24	0.00777	45						
0.60	0.330	3.8	0.2231	5.0	0.1326	5.0	0.0727	6.4	0.0544	8.3	0.02138	16	0.01777	22	0.00585	47						
0.70	0.2113	4.7	0.1392	6.2	0.0832	7.9	0.0528	7.1	0.0349	10	0.01483	18	0.01509	24	0.00354	61						
0.80	0.1198	6.3	0.0799	8.0	0.0684	9.0	0.0418	7.6	0.01750	14	0.01816	15	0.00526	37	0.00432	48						
0.90	0.0690	8.2	0.0571	10	0.0326	14	0.02585	9.3	0.01559	14	0.01172	18	0.00781	28	0.003064	33						
1.10	0.02985	8.7	0.02454	11	0.01919	13	0.01257	9.9	0.00964	12	0.00536	18	0.00481	23	0.000960	65						
1.30	0.01065	15	0.00949	18	0.01070	18	0.00485	18	0.00364	19	0.00320	21	0.002534	30	0.001791	39						
1.50	0.00376	26	0.00486	25	0.00367	29	0.001829	32	0.001934	28	0.001504	34	0.001131	42	0.000685	88						
1.70	0.00340	18	0.001068	39	0.001927	29	0.000780	51	0.000663	55	0.001089	39	0.000389	65	0.000220	91						
1.90	0.001237	31	0.001447	32	0.000820	45	0.000502	62	0.000416	68			0.000286	51								
2.10	0.000326	0.0	0.000787	46	0.000204	107	0.000354	74	0.000496	56			0.000124	74								
π^- $d(x_F, p_T)$ Δd																						
$p_T \backslash x_F$	0.0		0.05		0.10		0.15		0.20		0.25		0.30		0.35							
0.05	7.23	10	1.401	3.9	0.408	10	0.1819	13	0.0587	27	0.0348	53	0.0352	64								
0.10	6.20	6.6	1.120	3.9	0.390	9.2	0.1946	11	0.0983	18	0.0409	37	0.0471	46	0.01084	55						
0.15	4.33	6.2	1.191	3.1	0.414	7.2	0.1791	9.3	0.0874	16	0.0424	29	0.0426	50	0.00722	69						
0.20	3.68	6.4	1.057	2.9	0.384	6.6	0.1573	8.7	0.0746	15	0.0439	25	0.0477	31	0.01781	58						
0.25	2.581	7.4	0.865	3.4	0.333	6.4	0.1417	8.2	0.0615	15	0.02107	35										
0.30	1.906	2.5	0.769	3.4	0.3108	6.1	0.1301	7.9	0.0685	13	0.02886	19	0.00755	54	0.01489	43						
0.40	1.081	2.2	0.522	3.3	0.2468	4.2	0.1039	5.5	0.0505	11	0.03018	16	0.00980	37	0.01026	41						
0.50	0.578	2.9	0.3115	4.4	0.1584	4.9	0.0779	5.7	0.0347	12	0.02360	16	0.01402	27	0.00718	45						
0.60	0.323	3.8	0.1696	5.7	0.1024	5.7	0.0564	7.2	0.02912	11	0.01529	19	0.00671	36	0.002827	67						
0.70	0.1721	5.3	0.1191	6.6	0.0658	8.8	0.0361	8.5	0.02333	13	0.01415	18	0.00812	30	0.00354	61						
0.80	0.1075	6.6	0.0815	7.9	0.0349	13	0.03012	8.9	0.01936	13	0.01324	17	0.00388	42	0.00535	41						
0.90	0.0625	8.6	0.0418	12	0.02805	15	0.01874	11	0.01250	16	0.00968	19	0.00404	39	0.00428	42						
1.10	0.02173	10	0.01593	14	0.01137	17	0.00848	12	0.00517	16	0.00320	22	0.002919	29	0.001451	46						
1.30	0.01155	14	0.01068	16	0.00813	20	0.00333	22	0.003005	20	0.002518	24	0.001316	40	0.000512	73						
1.50	0.00518	21	0.00342	29	0.00497	25	0.001071	42	0.001206	36	0.001336	36	0.001171	41	0.001179	47						
1.70	0.002152	23	0.001147	36	0.001597	31	0.001352	36	0.000621	52	0.000415	65	0.000296	66	0.000415	72						
1.90	0.001141	32	0.001018	38			0.000295	83	0.000303	48			0.000160	75								
2.10	0.000178	91	0.000276	82	0.000819	44	0.000326	75	0.000587	50			0.000261	56								

Table 6.6: Double differential invariant density $d(x_F, p_T)$ [c^3/GeV^2] for π^+ and π^- produced in centrality selected set 5 of p+Pb interactions at 158 GeV/c. The statistical uncertainty Δd is given in %. p_T in the left column is given in GeV/c

Minimum bias p+Pb interactions																				
π^+ $f(x_F, p_T)$ Δf																				
$p_T \backslash x_F$	0.0		0.05		0.10		0.15		0.20		0.25		0.30		0.35		0.40	
0.05	8754.7	5.0	3104.5	2.5	1800.0	4.5	1116.8	4.7	759.3	6.5	630.9	9.3	368.0	16	468.6	19	158.8	37
0.10	7333.6	5.9	3022.4	2.3	1737.6	4.0	1089.9	4.1	785.5	5.5	607.6	7.8	382.9	13	219.2	21	219.8	22
0.15	4195.9	25	2950.5	1.9	1553.6	3.5	980.3	3.6	654.8	5.0	549.5	6.9	356.9	11	189.6	19	162.7	21
0.20	4023.5	8.1	2515.5	1.8	1359.4	3.2	914.1	3.2	642.8	4.5	446.2	6.7	298.2	10	252.7	13	95.7	25
0.25	2997.7	7.2	2053.6	2.1	1218.9	3.1	784.9	3.2	517.5	4.4	378.6	6.9						
0.30	2371.0	2.2	1619.3	2.2	947.0	3.2	642.2	3.2	445.2	4.3	325.7	4.9	228.7	7.1	157.3	9.8	97.0	15
0.40	1316.8	1.9	986.5	2.3	656.9	2.4	469.5	2.3	314.0	3.7	210.3	5.3	136.4	8.6	74.9	13	57.3	17
0.50	761.5	2.5	606.1	3.0	403.6	2.9	298.6	2.7	241.5	3.8	158.9	5.6	118.1	8.3	61.5	13	56.1	14
0.60	430.1	3.3	311.3	4.0	246.6	3.4	178.6	3.7	155.2	4.5	96.4	6.6	73.4	9.4	34.6	16	41.1	15
0.70	249.7	4.2	212.9	4.8	159.4	5.3	113.1	4.5	90.4	5.9	74.8	7.1	56.4	10	33.2	16	24.27	19
0.80	151.1	5.4	122.9	6.2	89.6	7.4	69.2	5.5	55.3	7.2	39.8	9.1	25.75	15	28.72	16	22.66	19
0.90	86.6	7.2	69.9	9.0	57.6	9.8	41.5	6.8	38.0	8.3	29.50	10	16.96	17	17.84	20	10.49	26
1.10	34.2	7.9	35.4	8.8	30.09	10	20.28	7.4	15.24	8.7	11.34	11	10.49	14	8.71	18	4.06	29
1.30	14.75	13	10.17	16	12.53	15	9.15	12	5.38	14	5.35	15	3.44	24	1.963	35	2.984	29
1.50	7.61	17	4.52	24	4.84	25	4.44	19	3.18	20	2.209	26	2.476	25	1.159	47	2.268	31
1.70	3.22	18	2.012	27	1.485	32	3.29	22	1.235	37	0.769	45	0.773	47	0.591	59	0.526	74
1.90	1.687	25	0.820	43	0.950	39	1.387	35	1.004	38			0.842	29			0.327	66
2.10	0.471	51	0.639	51	0.506	55	0.423	64	0.652	50			0.2944	48			0.1878	98
π^- $d(x_F, p_T)$ Δd																				
$p_T \backslash x_F$	0.0		0.05		0.10		0.15		0.20		0.25		0.30		0.35		0.40	
0.05	6437.4	12	2707.5	2.7	1252.9	5.5	655.8	6.2	356.9	9.5	184.8	18	117.2	27	123.9	36	12.83	125
0.10	6311.2	6.6	2648.9	2.4	1173.9	4.9	552.7	5.9	374.8	8.3	202.0	14	117.3	23	65.9	36	52.6	42
0.15	5496.3	5.3	2454.9	2.1	1138.1	4.1	632.2	4.5	318.3	7.3	142.1	14	115.2	22	36.9	40	38.9	44
0.20	4275.7	5.9	2097.0	2.0	1068.5	3.7	531.4	4.3	343.7	6.0	162.7	11	93.8	23	95.5	21	53.9	29
0.25	3263.5	6.5	1712.3	2.3	889.7	3.6	511.1	3.9	285.3	6.0	164.2	10						
0.30	2364.0	2.2	1408.1	2.4	755.7	3.6	436.0	3.9	248.6	5.9	140.5	7.4	65.3	15	48.4	18	34.9	21
0.40	1310.7	1.9	865.6	2.4	541.1	2.7	316.5	2.9	181.5	4.9	105.0	7.4	75.5	11	41.3	17	43.4	17
0.50	765.1	2.7	480.6	3.4	329.8	3.2	204.3	3.2	140.4	5.1	88.4	7.4	60.4	11	38.7	16	21.75	22
0.60	402.7	4.0	303.7	4.1	207.3	3.7	127.2	4.4	82.5	6.2	55.9	8.6	44.7	12	22.02	20	19.68	22
0.70	215.7	5.9	181.1	5.2	130.9	5.9	98.7	4.7	60.0	7.2	47.0	8.8	26.03	15	7.21	34	12.75	25
0.80	138.0	6.6	101.0	6.8	75.6	8.1	52.4	6.3	37.9	8.6	24.38	12	14.07	19	12.92	24	9.70	28
0.90	86.0	9.8	70.8	9.0	53.3	10	34.2	7.6	21.97	11	18.34	13	14.02	18	7.01	30	4.58	45
1.10	27.19	9.0	29.15	9.6	19.70	13	13.88	8.9	8.43	12	8.69	12	3.99	23	4.78	24	1.006	67
1.30	10.19	15	11.68	15	7.98	19	5.02	16	3.69	17	3.70	18	3.74	21	1.640	37	1.317	48
1.50	5.27	20	5.77	21	1.983	39	2.285	27	1.846	28	1.515	31	0.558	59	0.934	48	1.085	47
1.70	2.306	22	2.236	24	2.440	24	0.861	44	0.632	48	0.336	72	0.520	40	0.327	88	0.563	65
1.90	0.948	35	1.353	33	0.385	65	0.977	41	0.619	51			0.551	37			0.457	47
2.10	0.605	44	1.150	35	0.545	53			0.533	53			0.1535	60			0.2944	54

Table 6.7: Double differential invariant cross section $f(x_F, p_T)$ [mb/(GeV^2/c^3)] for π^+ and π^- produced in minimum bias p+Pb interactions at 158 GeV/c. The statistical uncertainty Δf is given in %. p_T in the left column is given in GeV/c

6.2 Plots

This Section shows p_T distributions of invariant cross sections of charged pions production in p+p [61] and p+C interactions [62] along with the lines corresponding to the interpolation which is used in the data discussion in the following section. The respective data tables may be found in [61, 62].

The invariant densities of π^+ and π^- production in the six centrality selected p+Pb event samples are shown, followed by the invariant cross sections of pion production in minimum bias p+Pb interactions. These plots correspond to the cross section data tables presented in the preceding section.

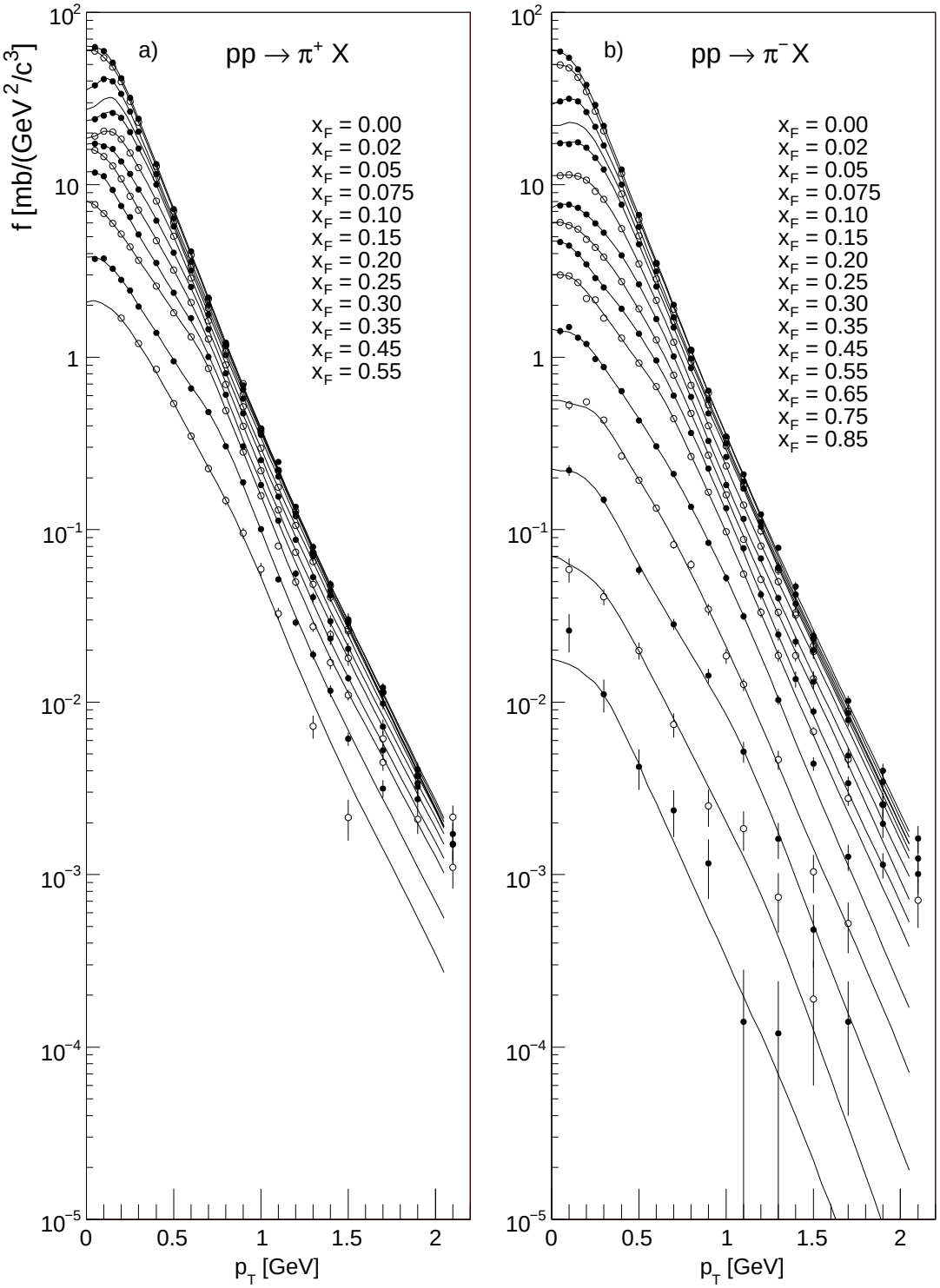

Figure 6.1: Double differential invariant cross sections of a) π^+ and b) π^- production in p+p interactions at 158 GeV/c as a function of p_T at several x_F values [61]

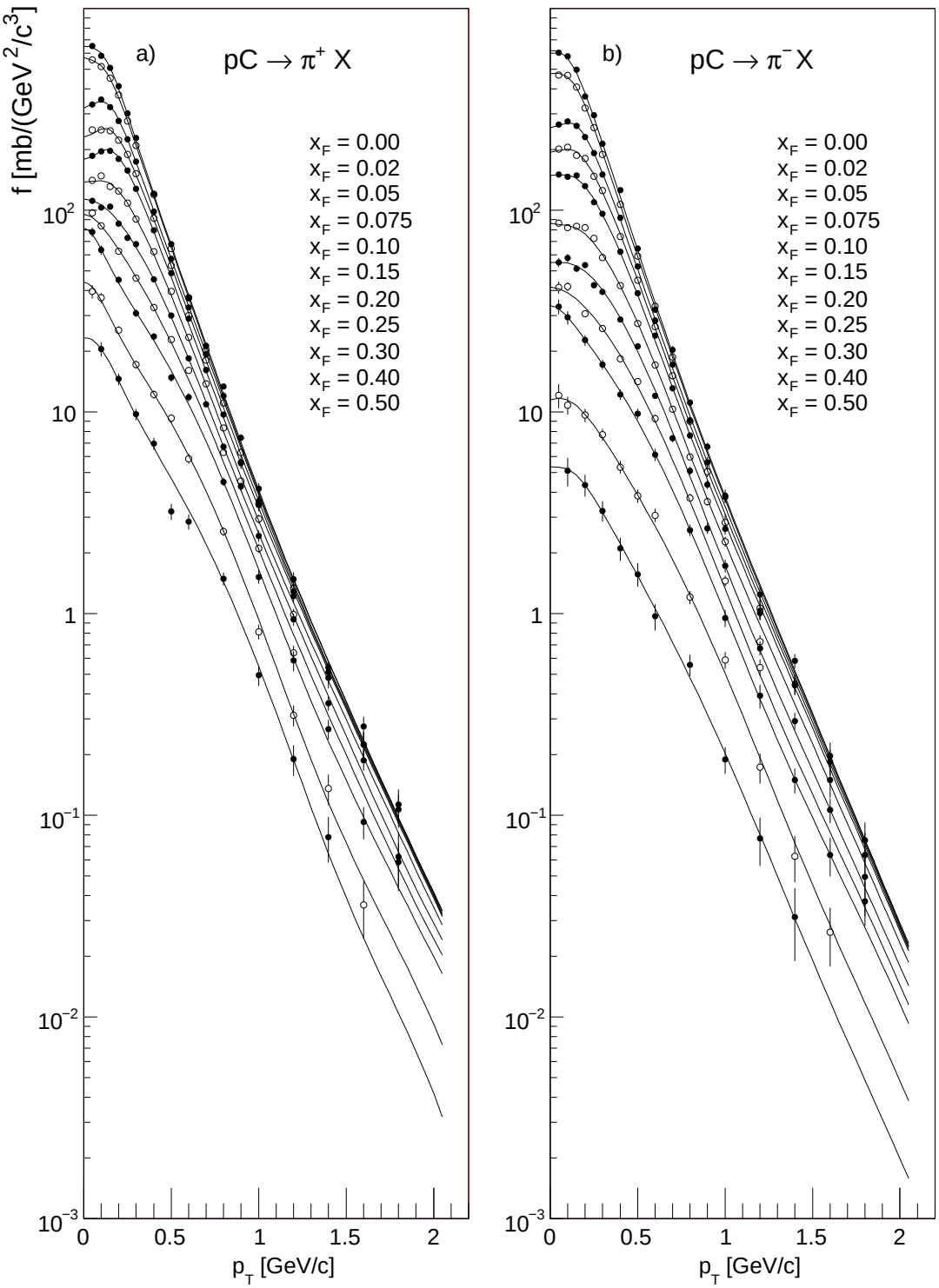

Figure 6.2: Double differential invariant cross sections of a) π^+ and b) π^- production in p+C interactions at 158 GeV/c as a function of p_T at several x_F values [62]

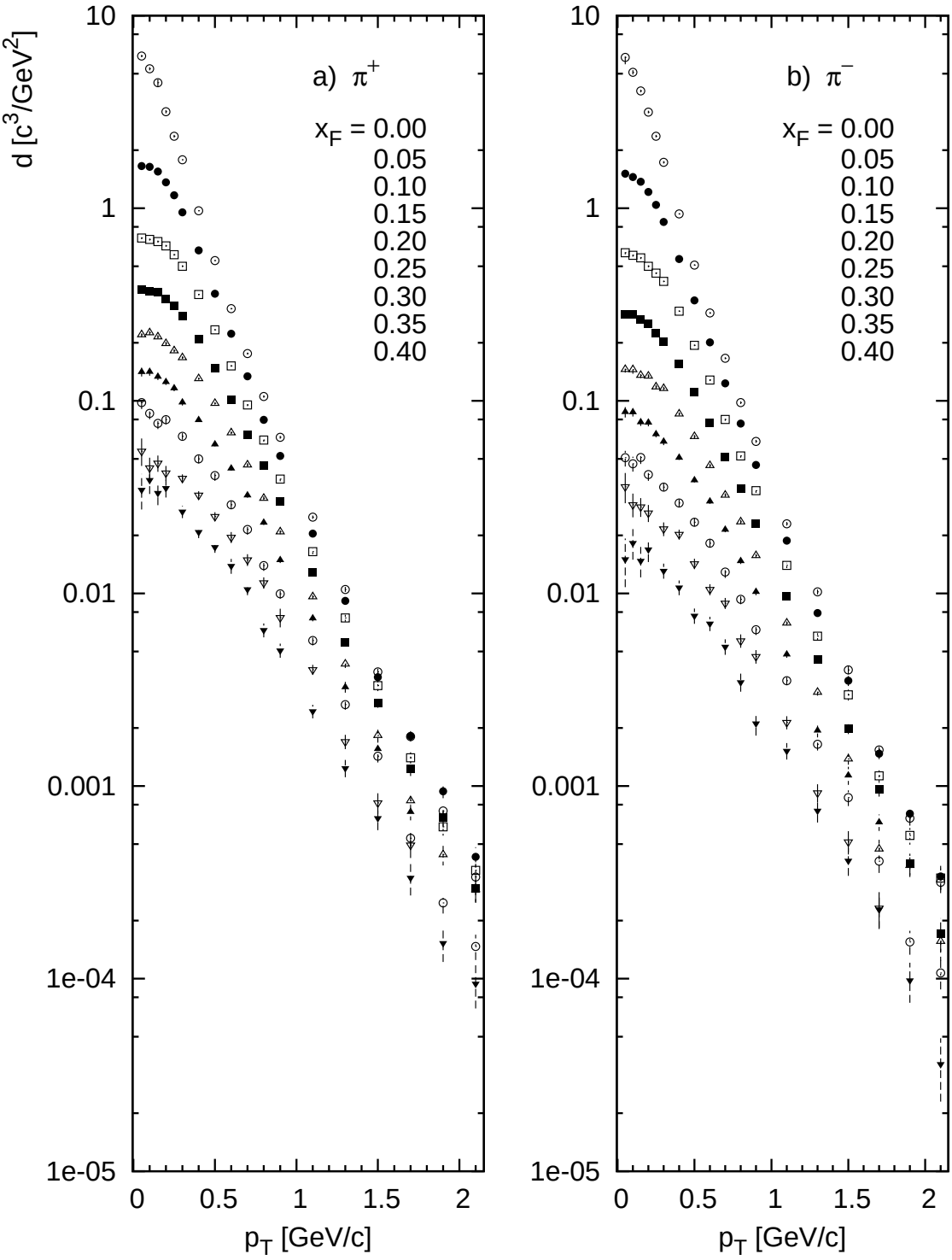

Figure 6.3: Double differential invariant cross sections of a) π^+ and b) π^- production in the set of all the centrality triggered events of p+Pb interactions at 158 GeV/c as a function of p_T at several x_F values.

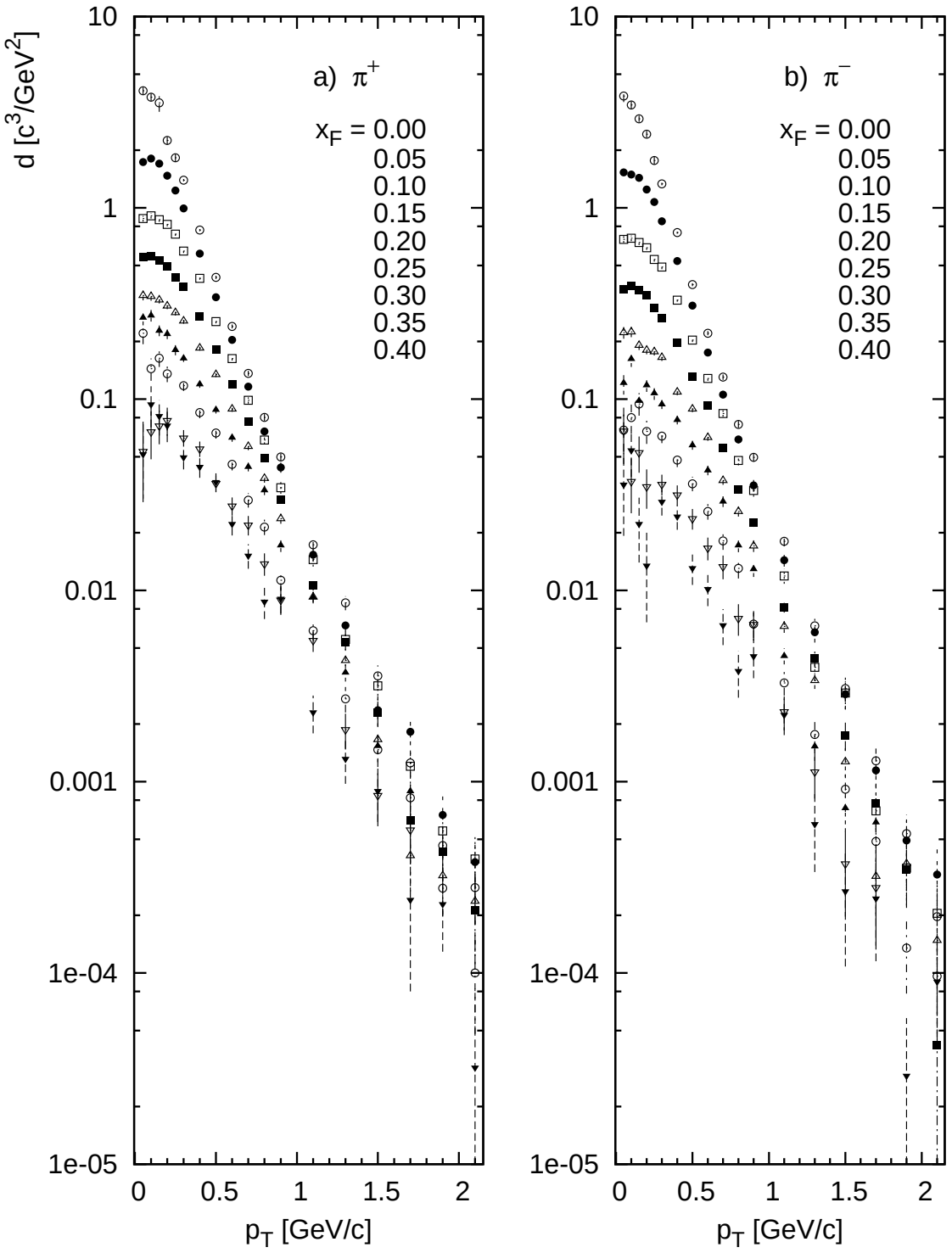

Figure 6.4: Double differential invariant cross sections of a) π^+ and b) π^- production in centrality set 1 of p+Pb interactions at 158 GeV/c as a function of p_T at several x_F values.

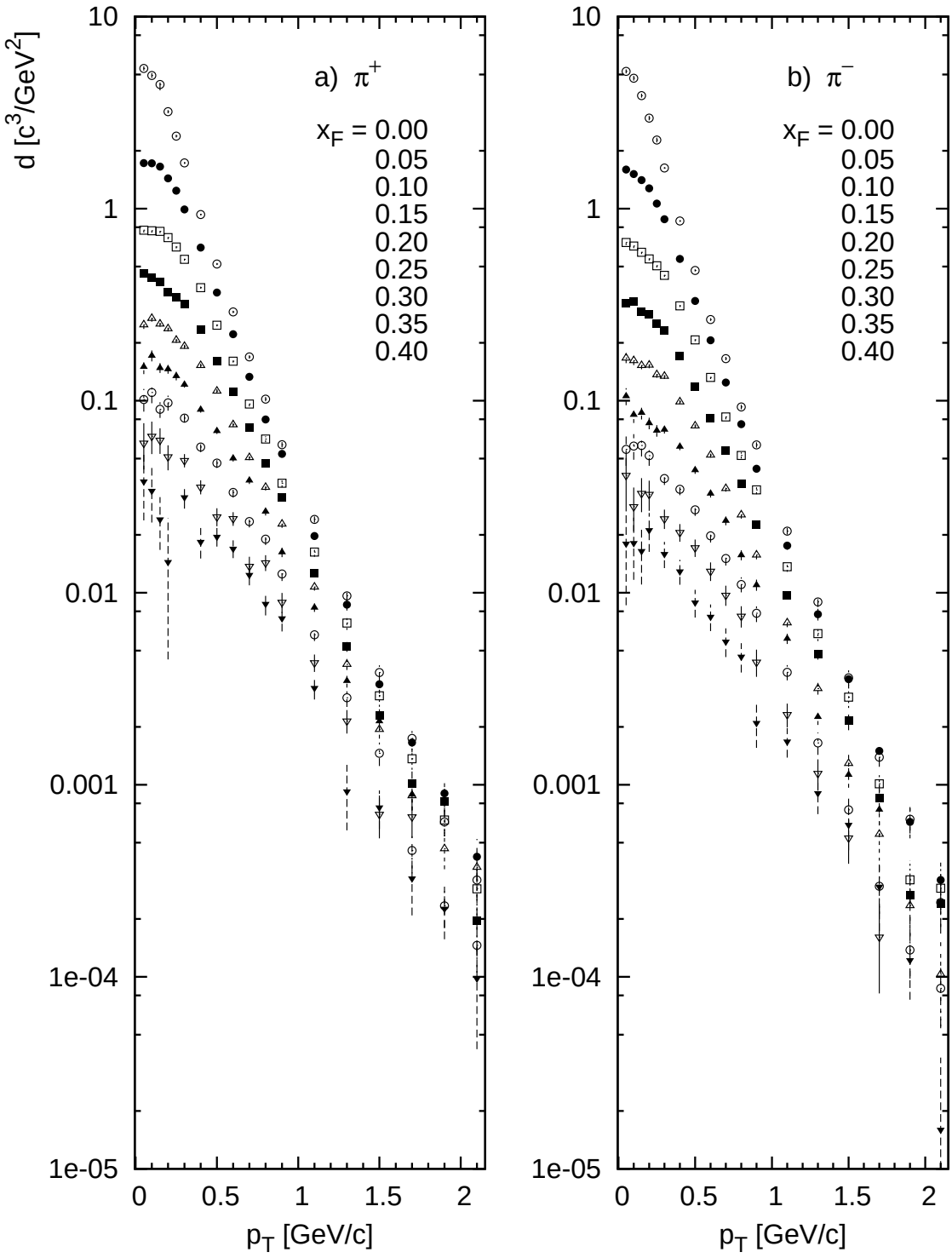

Figure 6.5: Double differential invariant cross sections of a) π^+ and b) π^- production in centrality set 2 of p+Pb interactions at 158 GeV/c as a function of p_T at several x_F values.

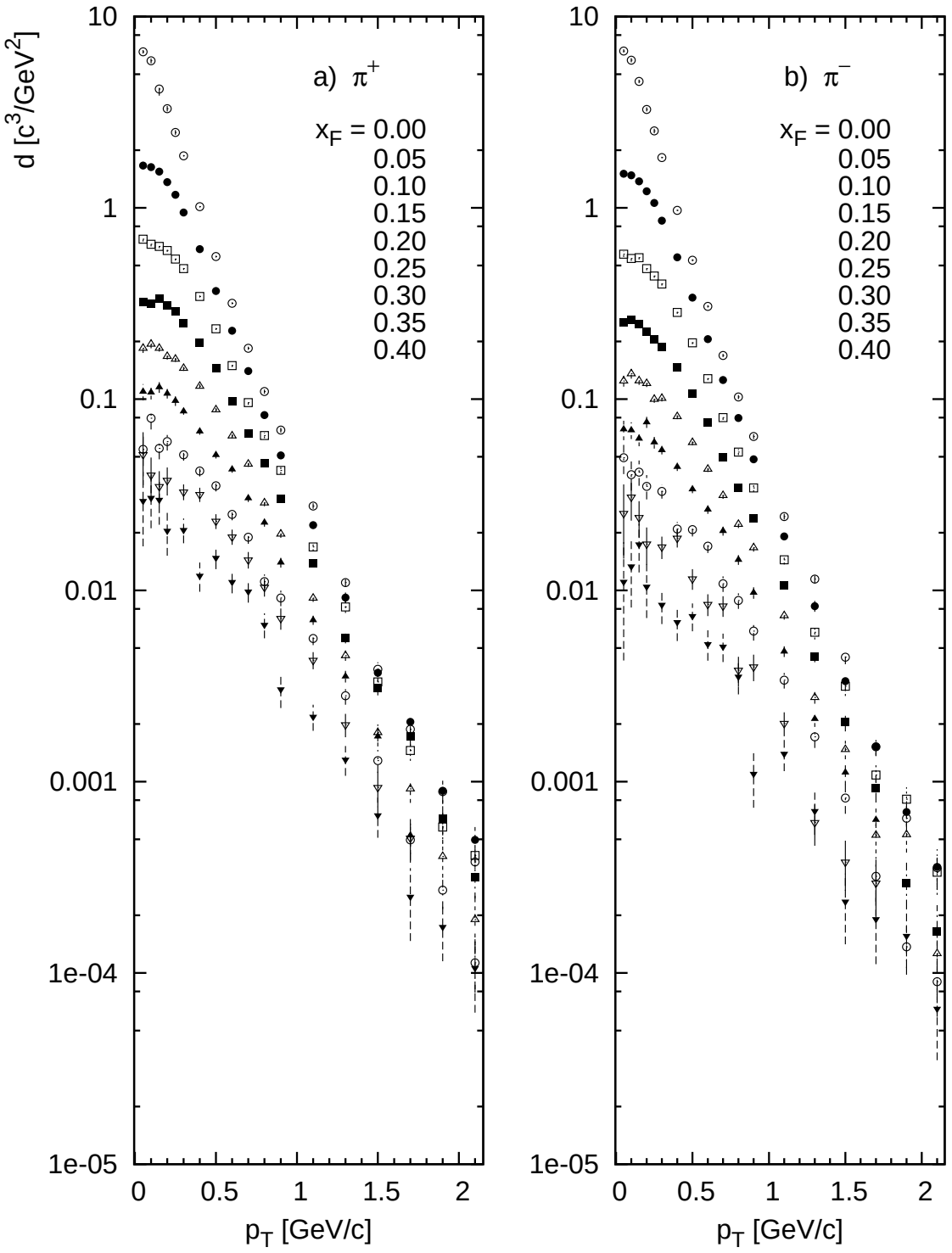

Figure 6.6: Double differential invariant cross sections of a) π^+ and b) π^- production in centrality set 3 of p+Pb interactions at 158 GeV/c as a function of p_T at several x_F values.

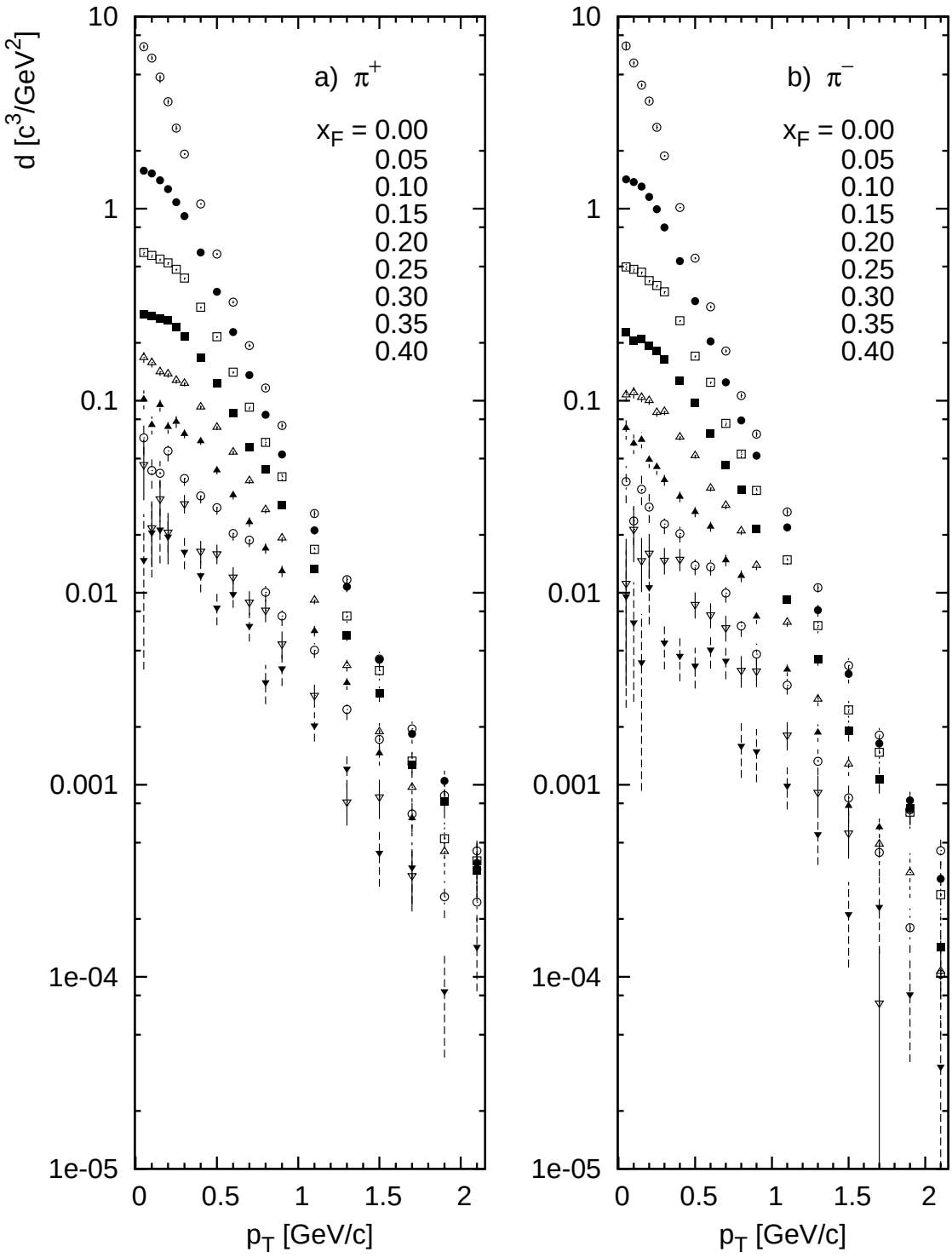

Figure 6.7: Double differential invariant cross sections of a) π^+ and b) π^- production in centrality set 4 of p+Pb interactions at 158 GeV/c as a function of p_T at several x_F values.

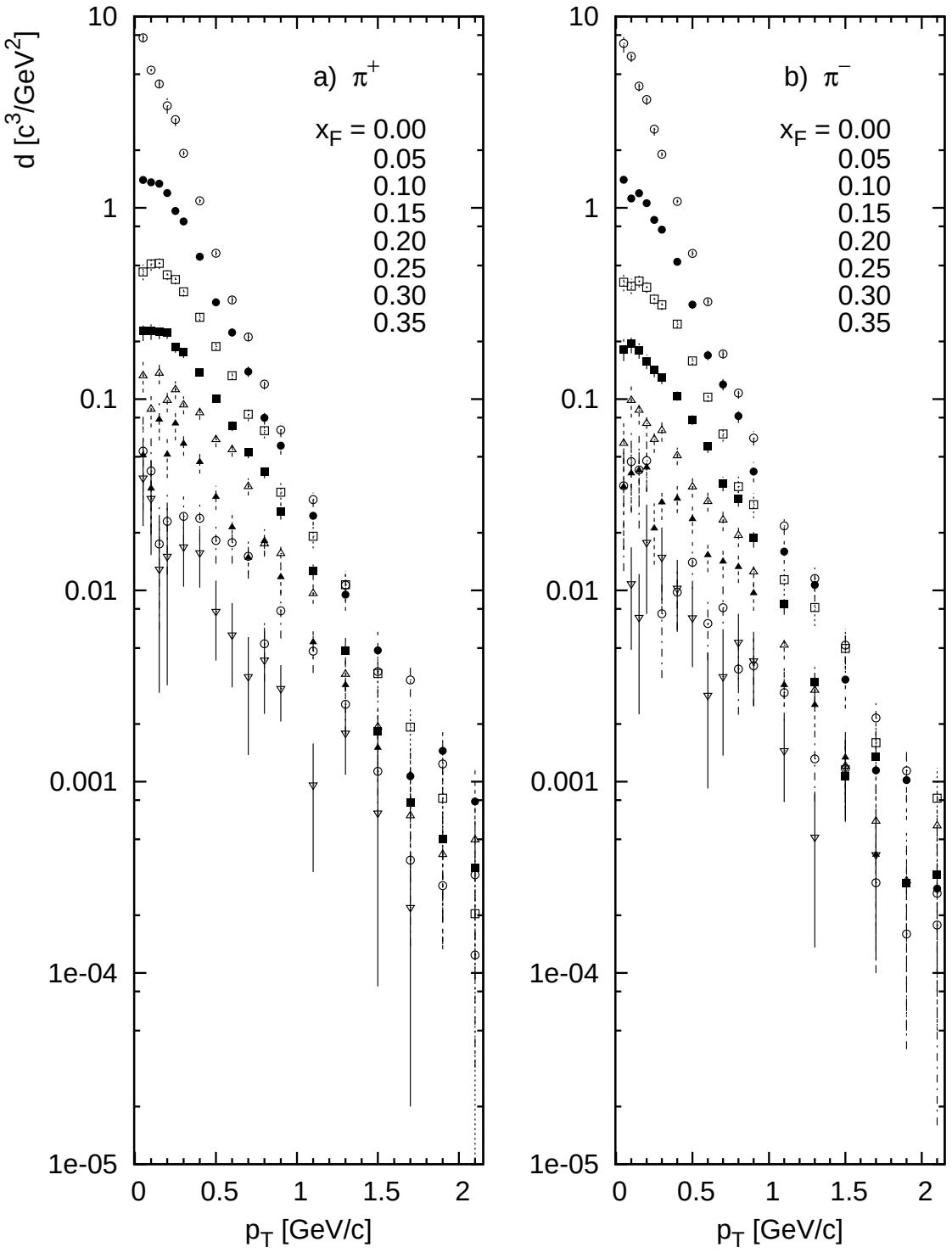

Figure 6.8: Double differential invariant cross sections of a) π^+ and b) π^- production in centrality set 5 of p+Pb interactions at 158 GeV/c as a function of p_T at several x_F values.

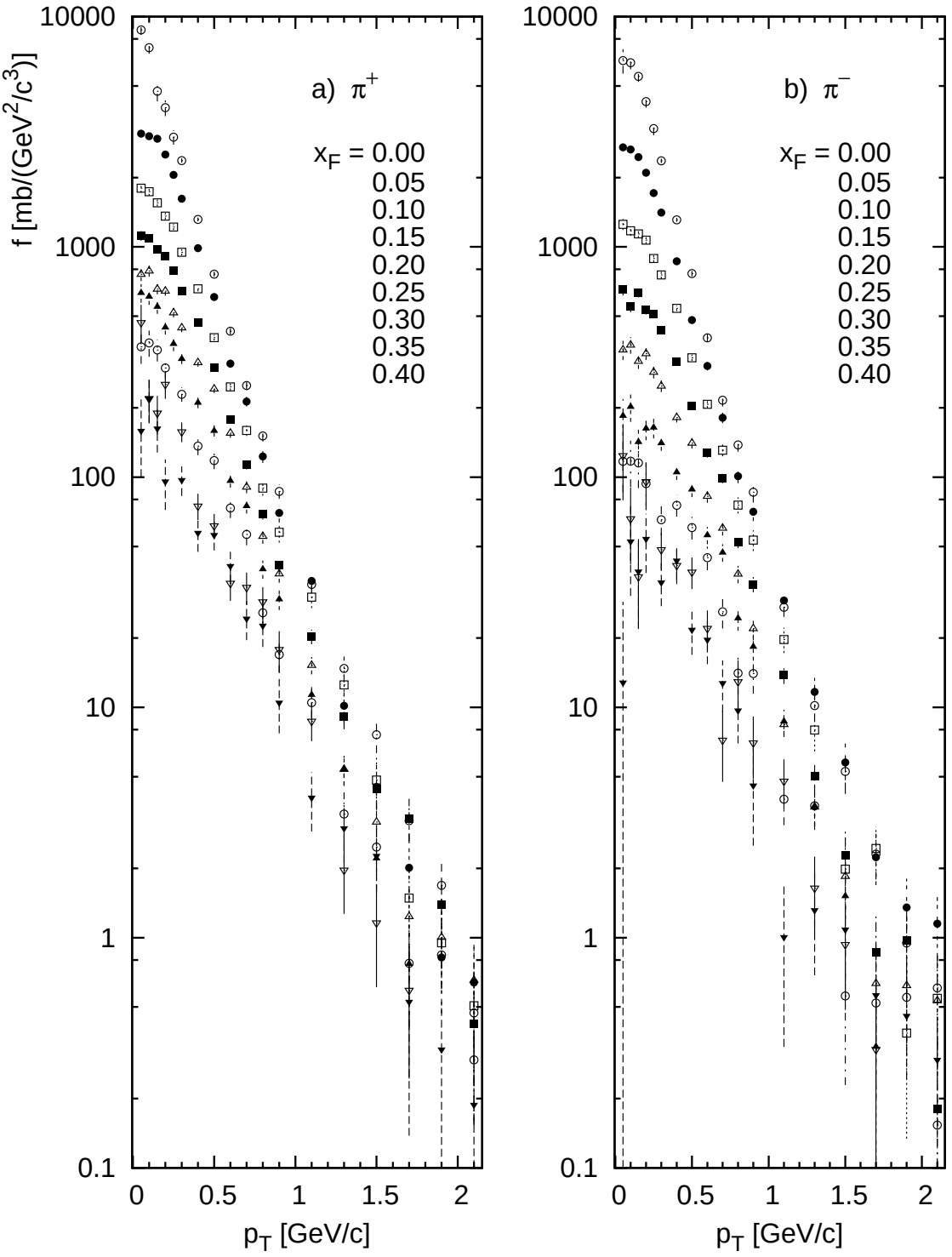

Figure 6.9: Double differential invariant cross sections of a) π^+ and b) π^- production in minimum bias p+Pb interactions at 158 GeV/c as a function of p_T at several x_F values.

6.3 p_T integrated distributions

In the following chapter, p_T integrated pion yields will be used in order to discern some important general features of p+A interactions at different ν. These integrated densities $\mathrm{d}n/\mathrm{d}x_F$ are defined as follows:

$$\begin{aligned} \mathrm{d}n/\mathrm{d}x_F &= \int \frac{\mathrm{d}^2 n}{\mathrm{d}x_F \mathrm{d}p_T} \cdot \mathrm{d}p_T \\ &= \frac{\pi \cdot \sqrt{s}}{2} \cdot \int \frac{d}{E} \cdot \mathrm{d}p_T^2 \end{aligned} \tag{6.1}$$

where d is the invariant density per event as defined by equation (5.5) and

$$\frac{\mathrm{d}^2 n}{\mathrm{d}x_F \mathrm{d}p_T} = \frac{\pi \cdot \sqrt{s} \cdot p_T}{E} \cdot d \tag{6.2}$$

is the non–invariant particle density per inelastic event.

For the minimum bias sample the corresponding quantity is given by:

$$\frac{\mathrm{d}^2 n}{\mathrm{d}x_F \mathrm{d}p_T} = \frac{\pi}{\sigma_{inel}} \cdot \frac{\sqrt{s} \cdot p_T}{E} \cdot f \tag{6.3}$$

where f is the invariant cross section as defined by equation (5.6).

The integrated quantities were established by fitting the $\mathrm{d}^2n/\mathrm{d}x_F\ \mathrm{d}p_T$ spectra as a function of p_T for various values of x_F by a fit function and then integrating this function. The following formula has been used for the fit with parameters $a_0 \ldots a_3$.

$$\frac{\mathrm{d}^2 n}{\mathrm{d}x_F \mathrm{d}p_{T\,\mathrm{fit}}}(p_T) = a_0 \cdot (p_T)^{a_1} \cdot e^{a_2 \cdot p_T} \cdot e^{a_3 \cdot (p_T)^2} \tag{6.4}$$

The errors of the integrated quantities were calculated by a Monte Carlo simulation. The measured values of the non–invariant yields were randomly varied according to a Gaussian distribution with σ corresponding to the error of the respective measurements. After each randomization the p_T distribution was fit by the function 6.4 and the integrated quantities were established from the fit function. The errors of the quantities were established from RMS values of the respective histograms.

The two missing high p_T measurements at $x_F = 0.25$ and 0.35 were calculated as the average of the neighboring x_F bins measurements at their respective p_T values. Figures 6.10 and 6.11 show the fit p_T distributions for positive and negative pions measured in the sample of all centrality selected p+Pb events.

The p_T integrated densities, along with the mean transverse momentum $\langle p_T \rangle$ and the mean transverse momentum squared $\langle p_T^2 \rangle$, are shown in Tables 6.8, 6.9 and 6.10.

All centrality triggered set of p+Pb events												
	π^+						π^-					
x_F	$\mathrm{d}n/\mathrm{d}x_F$	Δ	$\langle p_T \rangle$	Δ	$\langle p_T^2 \rangle$	Δ	$\mathrm{d}n/\mathrm{d}x_F$	Δ	$\langle p_T \rangle$	Δ	$\langle p_T^2 \rangle$	Δ
0.000	51.8	0.5	0.2543	0.7	0.1038	2.6	55.2	1.1	0.2360	3.5	0.0939	13
0.050	14.16	0.2	0.376	0.2	0.2035	0.6	12.74	0.3	0.378	0.2	0.2052	0.6
0.100	5.04	0.4	0.461	0.4	0.2951	1.2	4.17	0.4	0.465	0.5	0.2996	1.4
0.150	2.241	0.4	0.513	0.4	0.361	1.0	1.676	0.5	0.517	0.4	0.365	1.1
0.200	1.127	0.6	0.547	0.5	0.407	1.4	0.769	0.7	0.557	0.6	0.420	1.7
0.250	0.608	0.9	0.581	0.7	0.461	1.8	0.390	1.1	0.593	0.9	0.477	2.3
0.300	0.337	1.6	0.609	1.2	0.508	2.8	0.2032	1.7	0.625	1.2	0.531	2.8
0.350	0.1922	2.1	0.637	1.5	0.544	3.4	0.1104	2.3	0.627	1.6	0.532	3.8
0.400	0.1155	2.5	0.635	1.8	0.551	4.4	0.0584	3.2	0.662	2.1	0.595	4.8

Table 6.8: p_T integrated density distribution $\mathrm{d}n/\mathrm{d}x_F$, mean transverse momentum $\langle p_T \rangle$[GeV/c], and mean transverse momentum squared $\langle p_T^2 \rangle$ [(GeV/c)^2] as a function of x_F for π^+ and π^- in the all centrality triggered sample of p+Pb events at 158 GeV/c beam momentum. The statistical error Δ is given in %.

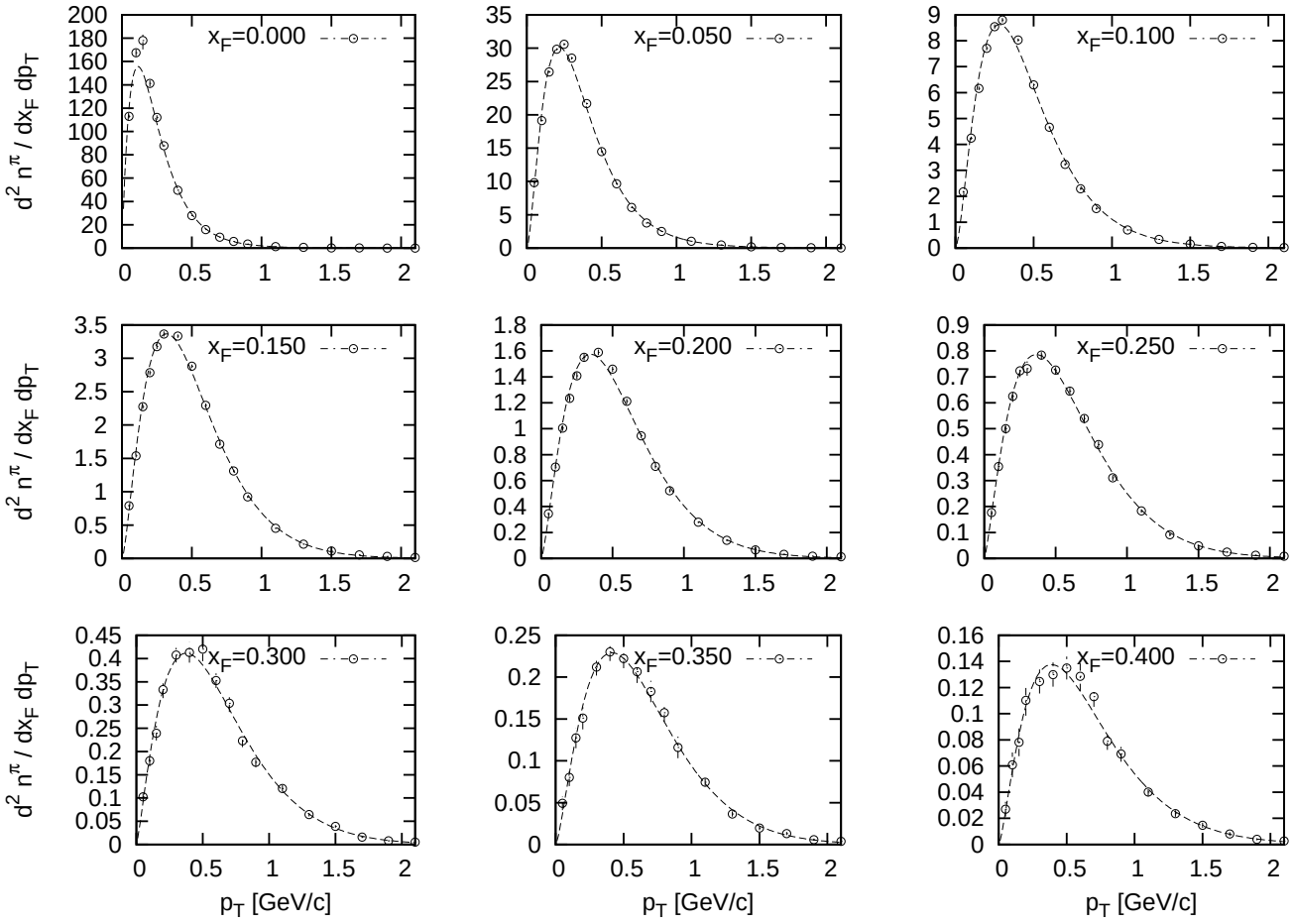

Figure 6.10: Density distributions $\mathrm{d}^2n/\mathrm{d}x_F\mathrm{d}p_T$ of positive pions measured in the set of all centrality selected p+Pb events fit by function 6.4.

Centrality selected set 1 of p+Pb events												
	π^+						π^-					
x_F	dn/dx_F	Δ	$\langle p_T \rangle$	Δ	$\langle p_T^2 \rangle$	Δ	dn/dx_F	Δ	$\langle p_T \rangle$	Δ	$\langle p_T^2 \rangle$	Δ
0.000	38.9	1.4	0.2616	2.4	0.1074	6.2	37.9	1.5	0.2574	3.6	0.1044	15
0.050	14.14	0.6	0.355	0.5	0.1814	1.3	12.33	0.7	0.360	0.6	0.1848	1.7
0.100	5.78	0.9	0.429	1.1	0.2567	3.4	4.53	1.0	0.434	1.2	0.2602	3.5
0.150	2.776	0.8	0.466	0.8	0.2970	2.4	1.999	1.0	0.475	1.0	0.3082	2.9
0.200	1.510	1.2	0.500	1.2	0.338	3.2	0.978	1.5	0.517	1.4	0.361	3.9
0.250	0.886	1.6	0.535	1.3	0.396	3.4	0.523	2.2	0.530	1.8	0.369	4.7
0.300	0.523	2.7	0.547	2.4	0.416	6.4	0.2922	3.6	0.561	3.0	0.432	7.7
0.350	0.2746	3.9	0.597	2.9	0.479	6.9	0.1596	5.2	0.584	4.1	0.456	10
0.400	0.1958	5.3	0.552	4.3	0.418	11	0.0881	7.4	0.579	6.9	0.449	15

Centrality selected set 2 of p+Pb events												
	π^+						π^-					
x_F	dn/dx_F	Δ	$\langle p_T \rangle$	Δ	$\langle p_T^2 \rangle$	Δ	dn/dx_F	Δ	$\langle p_T \rangle$	Δ	$\langle p_T^2 \rangle$	Δ
0.000	49.8	0.8	0.2557	1.3	0.1034	4.6	46.7	0.8	0.2539	1.3	0.1023	6.2
0.050	14.66	0.4	0.370	0.4	0.1969	1.0	13.01	0.5	0.374	0.4	0.2003	1.1
0.100	5.39	0.7	0.448	0.8	0.2794	2.4	4.42	0.8	0.454	0.9	0.2846	2.5
0.150	2.443	0.7	0.496	0.6	0.335	1.8	1.811	0.8	0.505	0.7	0.350	2.0
0.200	1.274	1.0	0.537	0.9	0.392	2.3	0.852	1.1	0.543	1.0	0.397	2.6
0.250	0.696	1.3	0.577	1.0	0.455	2.7	0.427	1.8	0.591	1.5	0.470	3.7
0.300	0.396	2.1	0.596	1.4	0.482	3.3	0.2301	2.7	0.609	1.8	0.498	4.3
0.350	0.2203	3.3	0.626	2.0	0.531	4.6	0.1237	4.1	0.621	2.7	0.514	6.6
0.400	0.1296	-1.0	0.668	3.5	0.585	7.8	0.0671	5.5	0.656	3.4	0.583	6.9

Centrality selected set 3 of p+Pb events												
	π^+						π^-					
x_F	dn/dx_F	Δ	$\langle p_T \rangle$	Δ	$\langle p_T^2 \rangle$	Δ	dn/dx_F	Δ	$\langle p_T \rangle$	Δ	$\langle p_T^2 \rangle$	Δ
0.000	54.5	1.0	0.2535	1.4	0.1035	6.5	54.4	0.7	0.2477	0.6	0.0988	2.7
0.050	14.27	0.4	0.379	0.3	0.2069	1.0	12.93	0.4	0.380	0.4	0.2068	1.1
0.100	4.93	0.7	0.470	0.8	0.3059	2.1	4.11	0.8	0.471	0.8	0.3070	2.4
0.150	2.146	0.7	0.530	0.7	0.384	1.8	1.607	0.8	0.529	0.7	0.380	1.9
0.200	1.026	1.1	0.560	1.0	0.425	2.5	0.719	1.2	0.571	1.0	0.438	2.4
0.250	0.545	1.4	0.599	1.0	0.482	2.6	0.354	1.8	0.611	1.3	0.503	3.2
0.300	0.2884	2.4	0.635	1.8	0.545	4.1	0.1797	3.0	0.642	1.9	0.556	4.5
0.350	0.1828	3.4	0.667	2.3	0.589	5.2	0.0896	4.7	0.632	3.6	0.543	8.5
0.400	0.0921	6.2	0.671	4.0	0.611	9.8	0.0453	7.0	0.689	5.4	0.650	13

Centrality selected set 4 of p+Pb events												
	π^+						π^-					
x_F	dn/dx_F	Δ	$\langle p_T \rangle$	Δ	$\langle p_T^2 \rangle$	Δ	dn/dx_F	Δ	$\langle p_T \rangle$	Δ	$\langle p_T^2 \rangle$	Δ
0.000	57.4	0.9	0.2519	1.3	0.1026	4.5	57.7	1.0	0.2441	3.0	0.0974	12
0.050	13.70	0.5	0.387	0.5	0.2153	1.4	12.44	0.5	0.388	0.4	0.2158	1.2
0.100	4.51	0.8	0.480	0.9	0.318	2.4	3.79	0.9	0.484	0.9	0.324	2.6
0.150	1.883	0.8	0.546	0.7	0.409	1.7	1.438	0.9	0.540	0.8	0.395	2.2
0.200	0.881	1.2	0.584	1.0	0.462	2.5	0.624	1.4	0.584	1.0	0.458	2.5
0.250	0.449	1.7	0.620	1.3	0.521	3.0	0.2769	2.3	0.616	1.6	0.512	4.0
0.300	0.2451	2.9	0.674	1.8	0.614	4.1	0.1464	3.6	0.673	2.2	0.611	4.8
0.350	0.1206	4.4	0.659	2.7	0.583	6.2	0.0783	5.3	0.665	3.2	0.584	6.9
0.400	0.0736	5.9	0.684	3.5	0.630	7.3	0.0329	9.5	0.728	7.0	0.698	16

Centrality selected set 5 of p+Pb events												
	π^+						π^-					
x_F	dn/dx_F	Δ	$\langle p_T \rangle$	Δ	$\langle p_T^2 \rangle$	Δ	dn/dx_F	Δ	$\langle p_T \rangle$	Δ	$\langle p_T^2 \rangle$	Δ
0.000	57.0	1.3	0.2561	3.6	0.1066	11	59.3	2.4	0.2441	4.6	0.0964	18
0.050	12.82	1.3	0.393	1.0	0.2217	2.8	11.40	1.3	0.388	1.3	0.2148	4.2
0.100	4.09	2.1	0.500	2.0	0.348	5.4	3.32	2.7	0.490	3.6	0.339	10
0.150	1.591	2.2	0.551	1.7	0.408	4.2	1.182	2.6	0.539	2.2	0.392	5.6
0.200	0.749	3.5	0.598	3.3	0.480	8.4	0.498	4.2	0.612	2.7	0.507	6.5
0.250	0.355	5.0	0.662	3.0	0.599	5.5	0.2415	6.0	0.677	4.0	0.604	9.1
0.300	0.1764	8.9	0.720	5.9	0.681	12	0.1052	11	0.721	8.7	0.712	12
0.350	0.0724	10	0.660	24	0.616	50	0.0605	15	0.792	21	0.873	45

Table 6.9: p_T integrated density distribution dn/dx_F, mean transverse momentum $\langle p_T \rangle$[GeV/c], and mean transverse momentum squared $\langle p_T^2 \rangle$ [(GeV/c)^2] as a function of x_F for π^+ and π^- in the centrality triggered samples of p+Pb events at 158 GeV/c beam momentum. The statistical error Δ is given in %.

Minimum bias sample of p+Pb events												
	π^+						π^-					
x_F	$\mathrm{d}n/\mathrm{d}x_F$	Δ	$\langle p_T\rangle$	Δ	$\langle p_T^2\rangle$	Δ	$\mathrm{d}n/\mathrm{d}x_F$	Δ	$\langle p_T\rangle$	Δ	$\langle p_T^2\rangle$	Δ
0.000	39.1	2.9	0.2561	4.7	0.1068	19	37.7	2.2	0.2578	3.4	0.1040	14
0.050	13.33	0.9	0.356	0.7	0.1823	1.7	11.45	1.0	0.363	0.8	0.1923	2.0
0.100	5.24	1.2	0.423	1.2	0.2551	3.6	4.11	1.4	0.429	1.6	0.2558	4.7
0.150	2.604	1.2	0.457	1.3	0.2991	4.0	1.748	1.4	0.469	1.4	0.2999	3.9
0.200	1.474	1.6	0.476	1.7	0.3144	4.6	0.833	2.1	0.493	2.1	0.330	5.7
0.250	0.866	2.1	0.485	1.6	0.335	4.4	0.431	3.1	0.554	2.7	0.410	7.1
0.300	0.510	3.3	0.511	2.8	0.378	7.5	0.2289	6.2	0.568	4.7	0.437	12
0.350	0.2818	4.7	0.516	3.6	0.387	5.6	0.1163	7.5	0.603	5.7	0.512	12
0.400	0.1865	6.1	0.562	4.9	0.451	12	0.0807	9.1	0.607	9.2	0.524	23

Table 6.10: p_T integrated density distribution $\mathrm{d}n/\mathrm{d}x_F$, mean transverse momentum $\langle p_T\rangle$[GeV/c], and mean transverse momentum squared $\langle p_T^2\rangle$ [(GeV/c)^2] as a function of x_F for π^+ and π^- in minimum bias p+Pb interactions at 158 GeV/c beam momentum. The statistical error Δ is given in %.

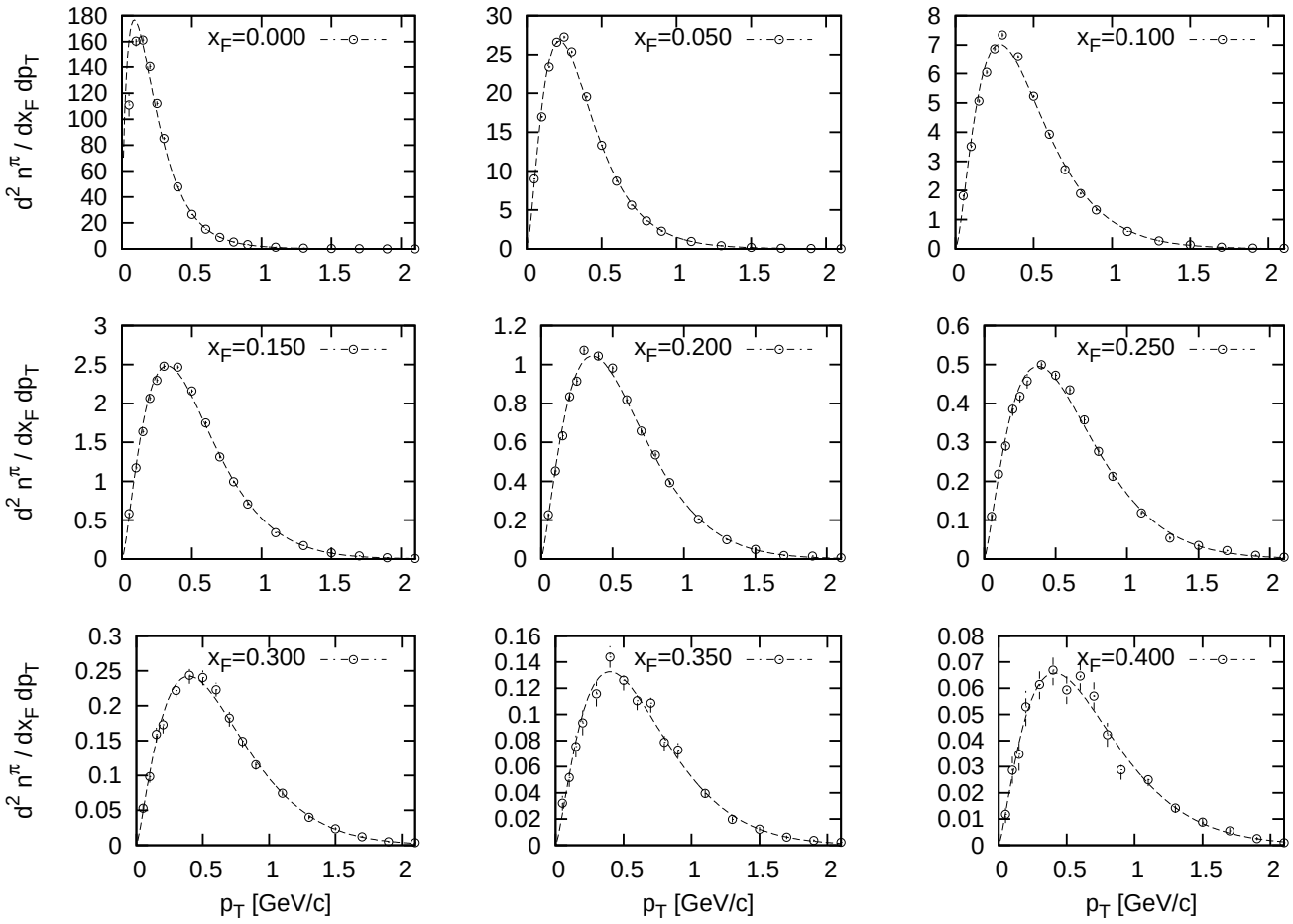

Figure 6.11: Density distributions $\mathrm{d}^2n/\mathrm{d}x_F\mathrm{d}p_T$ of negative pions measured in the set of all centrality selected p+Pb events fit by function 6.4.

6.4 Comparison to other measurements

Unfortunately there are very few measurements of double differential cross sections of identified pions in minimum bias p+Pb interactions at SPS energies that allow a direct comparison with the presented data. The only directly comparable data set comes from the Fermilab Single Arm Spectrometer (SAS) at 100 GeV/c [90]. The experiment was focused on the very forward region and the overlap is at only two values of x_F.

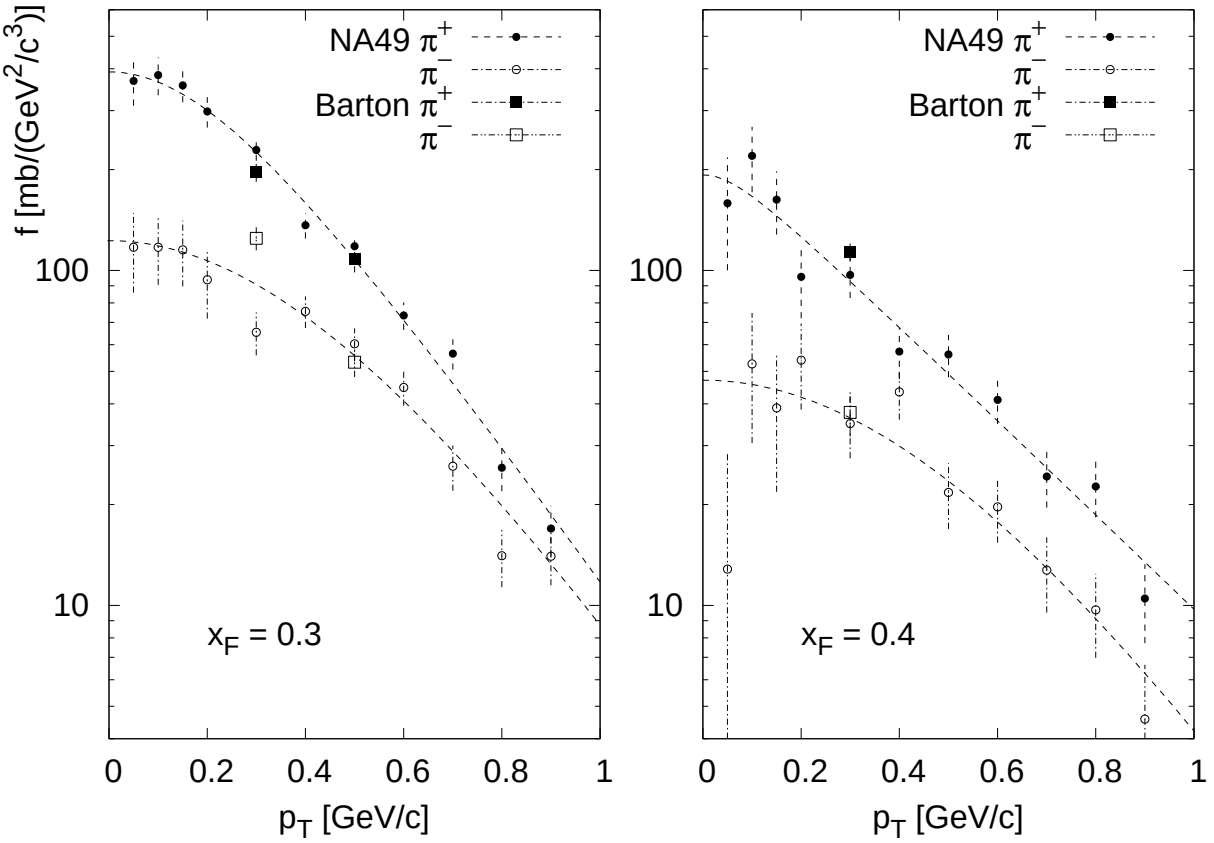

Figure 6.12: Comparison of the invariant cross sections of charged pion production in minimum bias p+Pb interactions (circles) as a function of p_T at two values of x_F with the measurements by [90] at 100 GeV/c (squares). Lines are to guide the eye.

The comparison is shown in Fig. 6.12. Five of the six common points coincide within the errors, which is a satisfying agreement. Interestingly, in a previous comparison of pion production in p+p interactions between NA49 and the SAS experiment discussed in [61], a satisfying agreement within errors was also found. Whereas in the comparison of pions produced in p+C as measured by NA49 [62] with the same data set from SAS [90], a systematic difference of +25 %, or +3.6 standard deviations, was observed with respect to the NA49 measurements

There are no other directly comparable measurements of identified pions in p+Pb collisions know to the author. This thesis deals with the transverse evolution of mean pion $\langle\pi\rangle = (\pi^+ + \pi^-)/2$ production up to 2 GeV/c of p_T, therefore it is interesting to compare the measurements with the original "Cronin" data [10] in the overlap region of p_T. That experiment used Be, Ti and W nuclear targets, therefore the cross sections have to be slightly extrapolated from W to Pb using the measured A dependence. They can then be directly compared to the presented inclusive cross sections in minimum bias p+Pb colli-

sions at $x_F = 0$. This comparison of mean pion cross sections is shown in the left panel in Fig. 6.13, along with a similar comparison for p+C interactions in the right panel. The latter was already presented in [63].

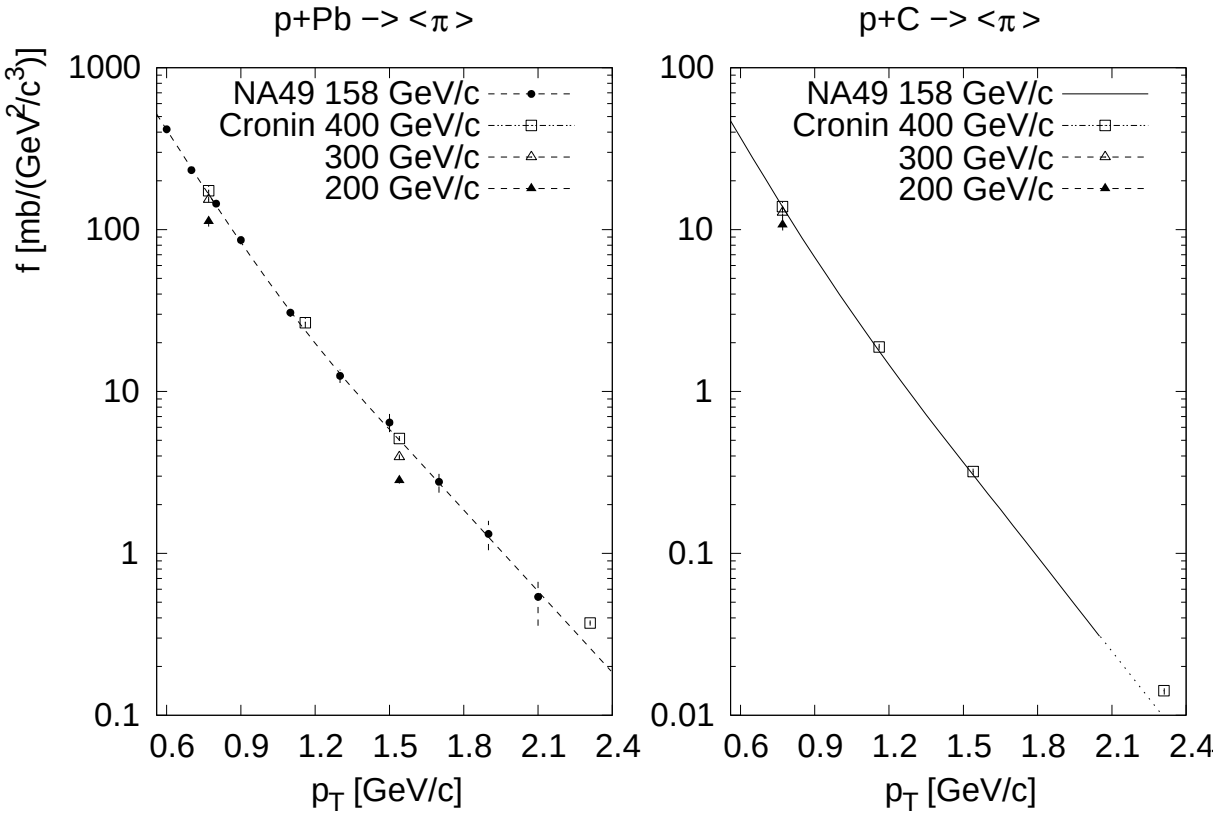

Figure 6.13: The left panel compares the presented cross section of charged average pion production, $\langle\pi\rangle = (\pi^+ + \pi^-)/2$, in minimum bias p+Pb interactions (circles) as a function of p_T at $x_F = 0$ to measurements by [10] extrapolated to Pb; the line is to guide the eye. The right panel shows the comparison of $\langle\pi\rangle$ cross sections in p+C as measured by NA49 (the full line is the cross section interpolation presented in [63] and shown in the next chapter) with measurements of [10] interpolated to carbon.

In both reactions the NA49 measurement coincides with the 400 GeV/c beam data from [10], which shows that there is no A dependent systematics between the two experiments. The agreement however is not expected due to the sizable s-dependence of the cross section at midrapidity. The data at 200 GeV beam momentum, which are closest to NA49 energy, are significantly below the NA49 measurements.

Part of this deviation can be understood as a consequence of the experimental setup, as all the data of [10] were obtained at a fixed laboratory angle of 77 mrad. This introduces a p_T and s-dependent spread of the corresponding x_F values. Considering the slope of the pion cross sections around midrapidity at fixed p_T values, downward deviations of the order of 10–20 % are expected at 200 GeV/c beam momentum. Including in addition the large relative normalization uncertainties of [10] and a possible few percent systematics involved in the A dependence of the cross section, the mutual consistency of the data may still be considered valid.

Chapter 7

Discussion

In the subsequent sections several aspects of the pion cross sections in p+Pb interactions presented in the preceding parts of the thesis are discussed in detail. In order to put these new data in perspective, they will be compared to the extensive data sets from p+p [61] and p+C [62] collisions at the same beam energy of 158 GeV/c available from NA49. Since a complete precise two-dimensional interpolation scheme has been developed in x_F and p_T for these cross sections, the interpolated values will be used for the comparison.

As described in Section 5.4 above, the invariant pion densities in centrality selected p+Pb interactions are given per event using equation (5.5). When comparing to minimum bias p+p and p+C interactions, these are normalized by their respective inelastic cross sections to obtain invariant densities per inelastic event:

$$d^{\pi} = \frac{f^{\pi}}{\sigma_{inelastic}} \tag{7.1}$$

As the thesis focuses on p_T dependencies, the charge averaged pion invariant densities

$$d^{\langle\pi\rangle} = \frac{d^{\pi^+} + d^{\pi^-}}{2} \tag{7.2}$$

will be used throughout this chapter in order to reduce the number of discussed parameters and gain in statistical precision.

The discussion will be conducted in a completely model–independent way. This is made possible by the completeness, the quality in terms of statistical and systematic errors, and the unprecedented phase space coverage of the data. The argumentation will proceed step-by-step from a straightforward phenomenological comparison to the extraction of physics quantities like a two–component fragmentation mechanism and a new assessment of the Cronin effect.

7.1 A first look at the p_T, x_F and ν dependences

The wealth of data presented in the preceding chapter has to be reduced to a few characteristic distributions in order to approach the essence of the underlying phenomena in an evident fashion. This is proposed in Fig. 7.1 which shows invariant p_T distributions in three x_F bins ($x_F = 0$, 0.15, 0.3) and for three of the five centrality bins available, characterized by the mean number of collisions at $\nu = 2.9$, 5.1 and 6.9. In addition the interpolated reference data from p+p ($\nu = 1$) and p+C ($\nu = 1.6$ [63]) interactions are presented.

This first set of distributions reveals a rich phenomenology. Several main aspects are to be noted here:

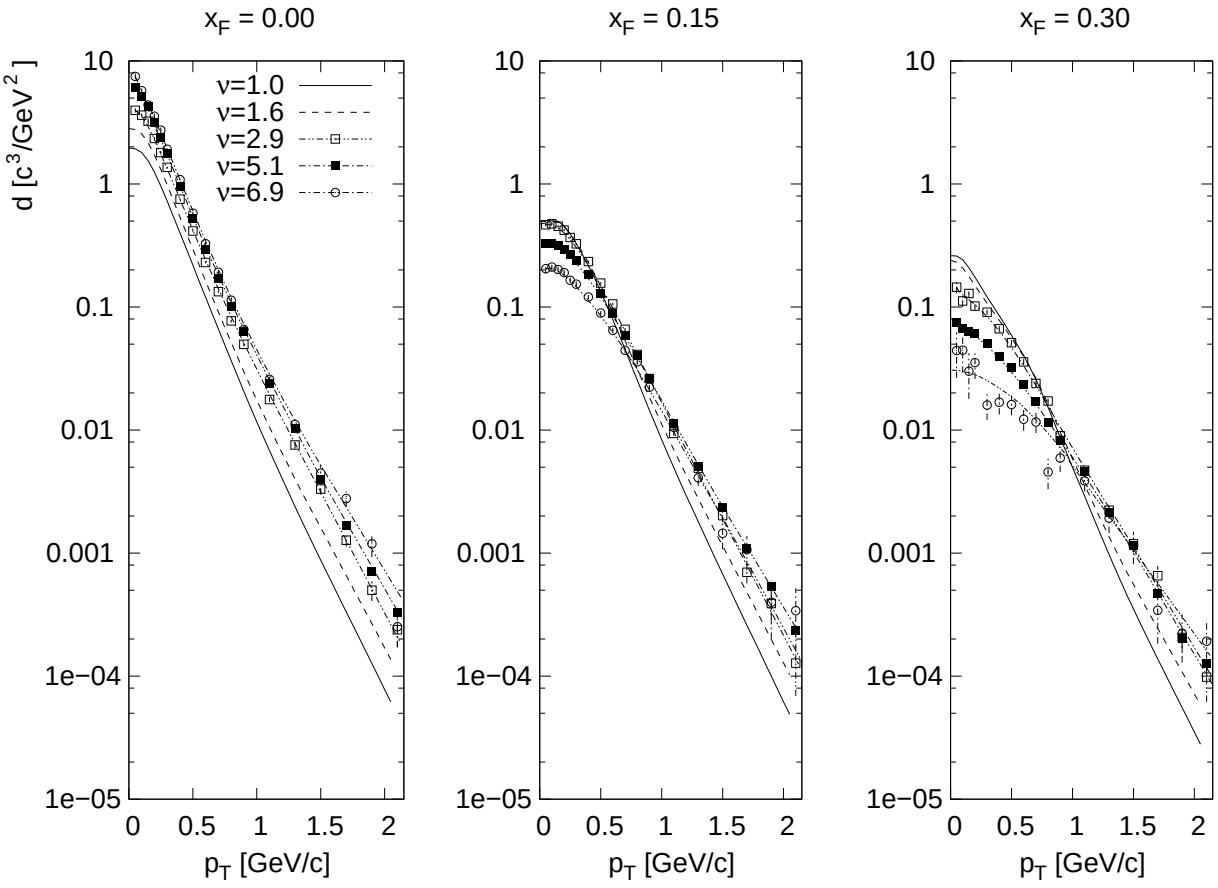

Figure 7.1: Invariant densities of $\langle\pi\rangle$ production at three x_F values as a function of p_T in different reactions: p+p ($\nu = 1$), p+C ($\nu = 1.6$) and p+Pb ($\nu = 2.9$, 5.1 and 6.9). Lines connecting the points are to guide the eye throughout this chapter unless stated otherwise.

- The steepness of all presented p_T distributions flattens out when proceeding forward from $x_F = 0$ to $x_F = 0.3$, from more than 4 orders of magnitude at $x_F = 0$ to about 2.5 orders of magnitude in cross section at $x_F = 0.3$ over the measured range of transverse momentum up to 2 GeV/c.

- At $x_F = 0$ the shape of the p_T distributions is rather similar for the elementary p+p and the p+A collisions, up to the highest centrality in p+Pb.

- On the contrary, a strong shape evolution is visible in the forward region $x_F > 0$. The slopes of the p_T distributions get smaller with increasing ν.

- In addition, the absolute invariant densities exhibit a complex pattern both as a function of x_F and of ν. At $x_F = 0$, there is a general smooth increase with ν which reaches factors between 3 and 10 for different regions of transverse momentum. In the forward direction this trend is inverted for $p_T < 1$ GeV/c where the cross sections decrease, whereas for $p_T > 1$ GeV/c they increase, with increasing collision centrality.

In the following sections this phenomenology will be investigated in more detail.

7.2 Shape of the p_T distributions

In order to clearly bring out the shape variation of the p_T distributions as a function of x_F and ν, one may normalize all distributions at small p_T. This is shown in Fig. 7.2 where the average yield between $p_T = 0$ and $p_T = 0.15\,\mathrm{GeV/c}$ as obtained for each distribution has been used as a normalization value.

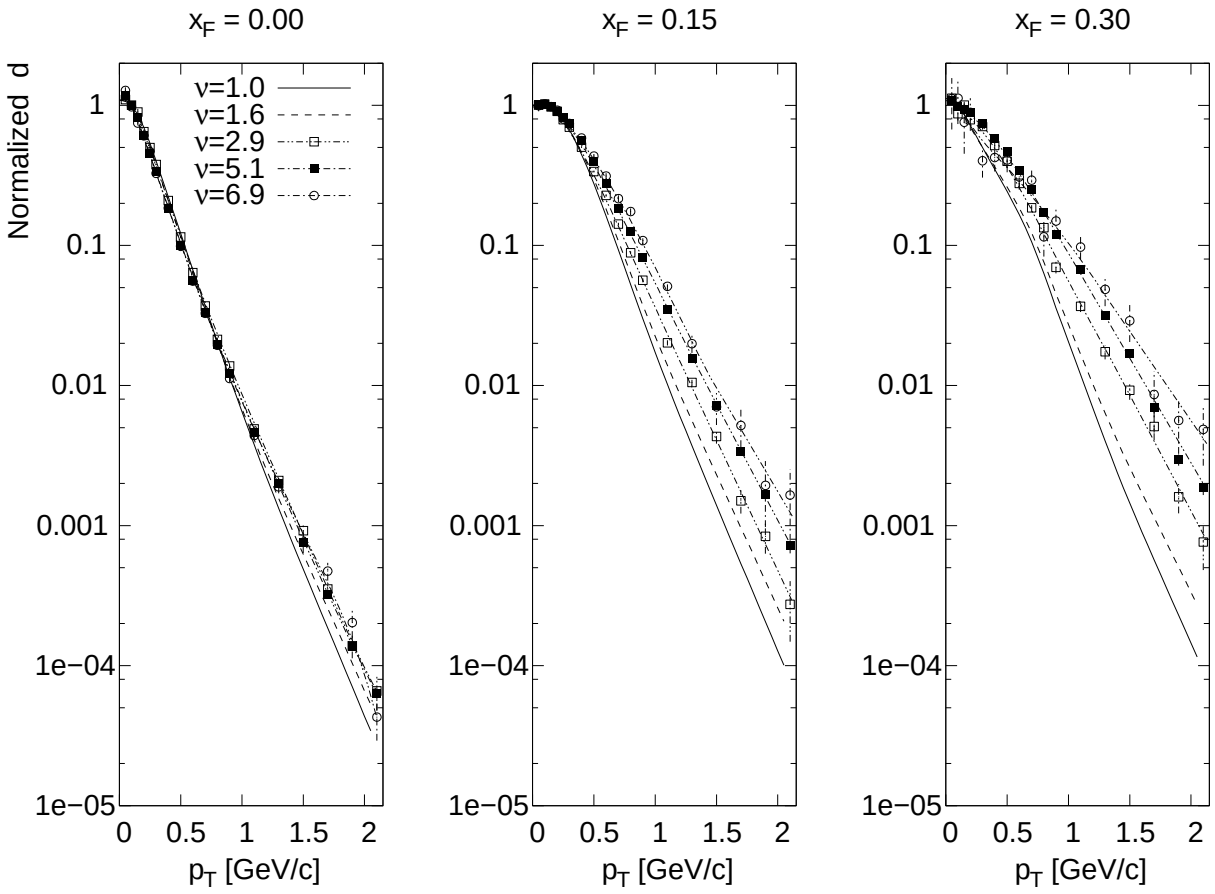

Figure 7.2: Transverse distributions of invariant densities of $\langle\pi\rangle$ production normalized at low p_T at three x_F values and at the five values of ν.

Evidently this normalization demonstrates a relative increase of cross sections with transverse momentum in p+A collisions as compared to p+p interactions. This increase is small at $x_F = 0$ but becomes very pronounced (more than an order of magnitude in the higher p_T range accessible by this experiment) in forward direction between x_F of 0.15 and 0.3. At this point it is already worth pointing out a principle feature of p+A interactions. These collisions are asymmetric between the target and projectile hemispheres. The projectile undergoes ν collisions, whereas each of the ν hit target nucleons fragments after a single collision. Both the target and the projectile fragmentation extend into the projectile and target hemispheres, respectively, within a range which has been demonstrated in [63] to extend to about 0.1 – 0.2 units of x_F. At $x_F = 0$ this superposition leads to a prevailance of the target contribution, which is roughly proportional to ν, over the projectile fragmentation which does not increase as rapidly. As the target contribution is generated from single collisions, its shape may be expected to be close to the one from p+p collisions, explaining the similarity between the different reactions at $x_F = 0$. In the forward direction, however, the target component dies out and the projectile component only will survive.

Thus the observed strong flattening of the transverse distributions is a clear feature of the multiple collision process taking place in p+A reactions.

This first and preliminary argument will be deepened and quantified in the subsequent sections.

7.3 Pion density distributions and their first moment

In order to further quantify the shape evolution of the transverse distributions, the non-invariant double inclusive densities of pion yield:

$$\frac{\mathrm{d}^2 n}{\mathrm{d}x_F dp_T} = \pi \cdot \sqrt{s} \cdot \frac{p_T}{E} \cdot d \tag{7.3}$$

are plotted in Fig. 7.3 for the same selection of ν and x_F as in the preceding figures. These distributions are normalized to a unit surface in order to give a clear picture of the pion density evolution as a function of x_F and ν.

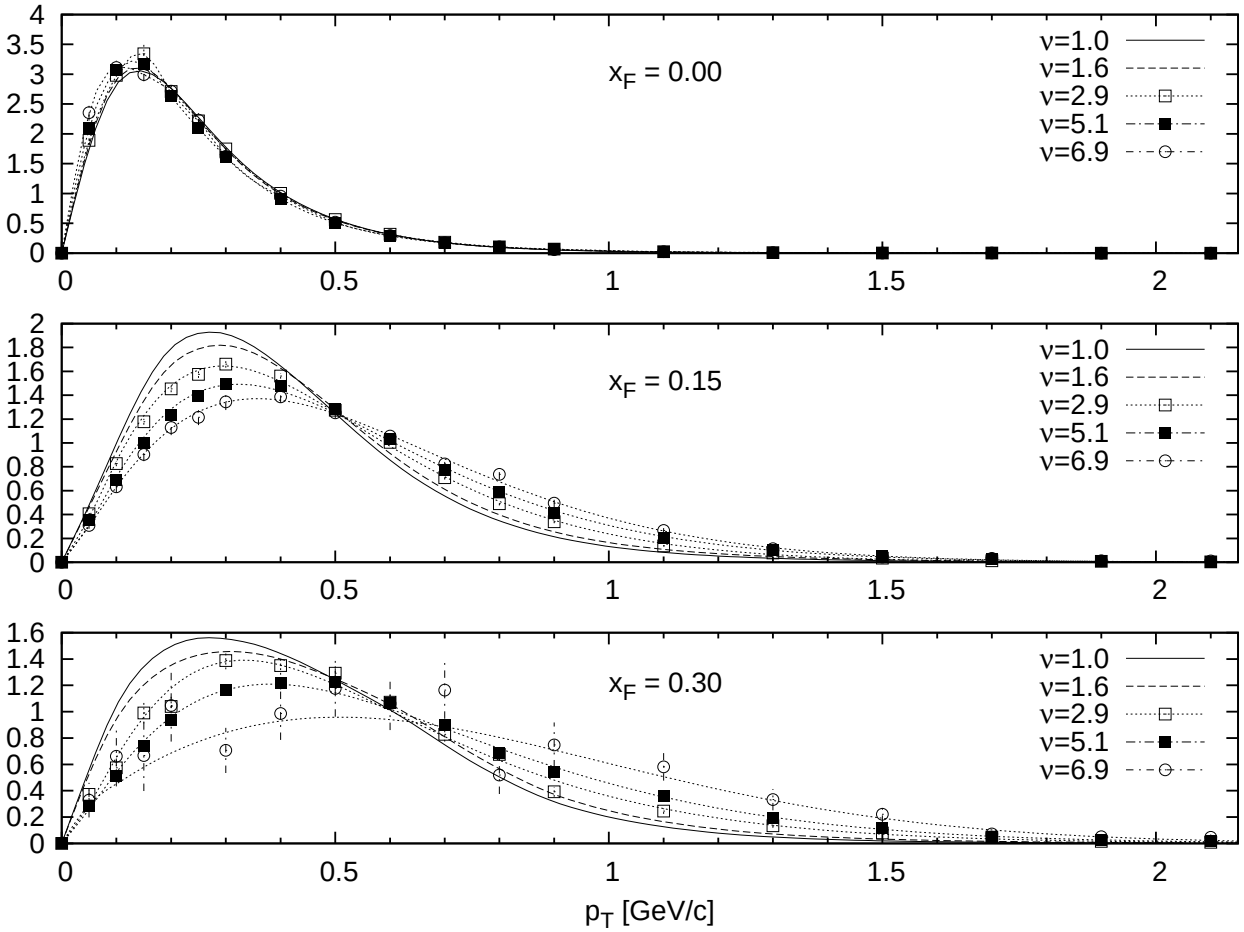

Figure 7.3: Transverse distributions of non-invariant densities of $\langle\pi\rangle$ production normalized to a unit surface at three x_F values at the five values of ν.

From these plots it becomes clear that the mean transverse momentum $\langle p_T \rangle$, which is the first moment of the presented distribution, shows a strong increase both with x_F and with ν. The extracted $\langle p_T \rangle$ values are presented in Fig. 7.4 for π^+ and π^- separately.

The smooth evolution of $\langle p_T \rangle$ over the forward hemisphere from the elementary p+p to the most central p+Pb collisions is quantified for the first time in these data. The

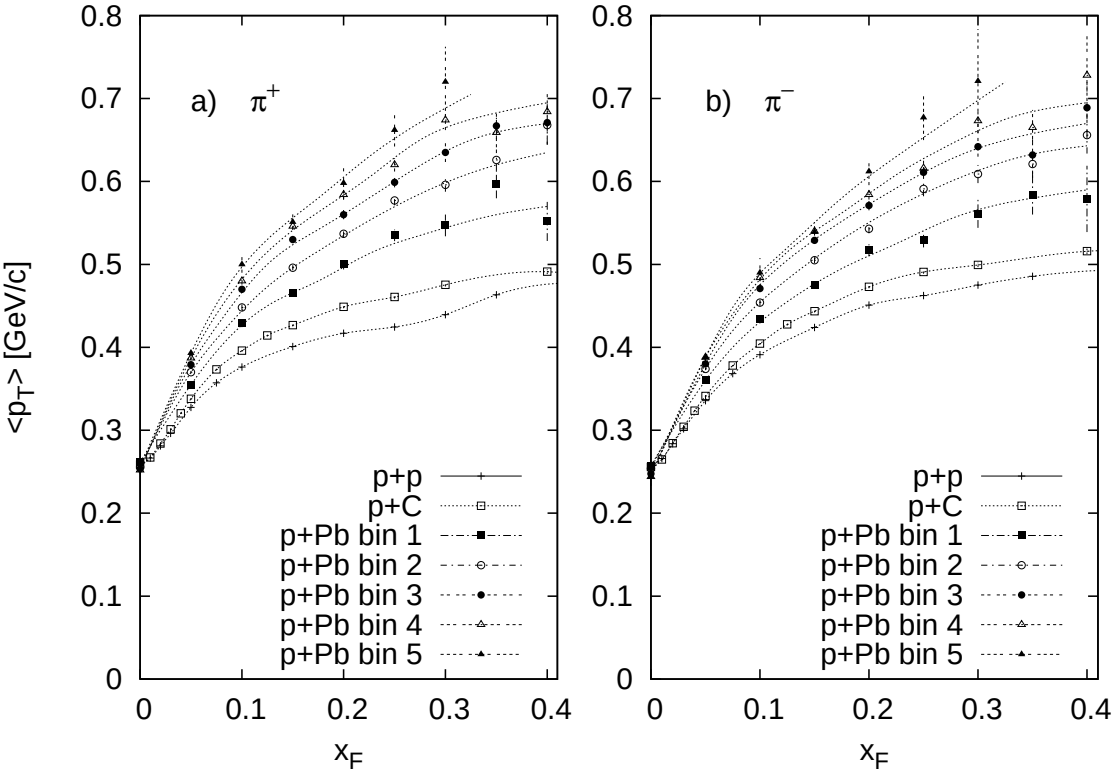

Figure 7.4: Mean transverse momentum $\langle p_T \rangle$ of $\langle \pi \rangle$ as a function of x_F for p+p, p+C and the five centrality bins of p+Pb.

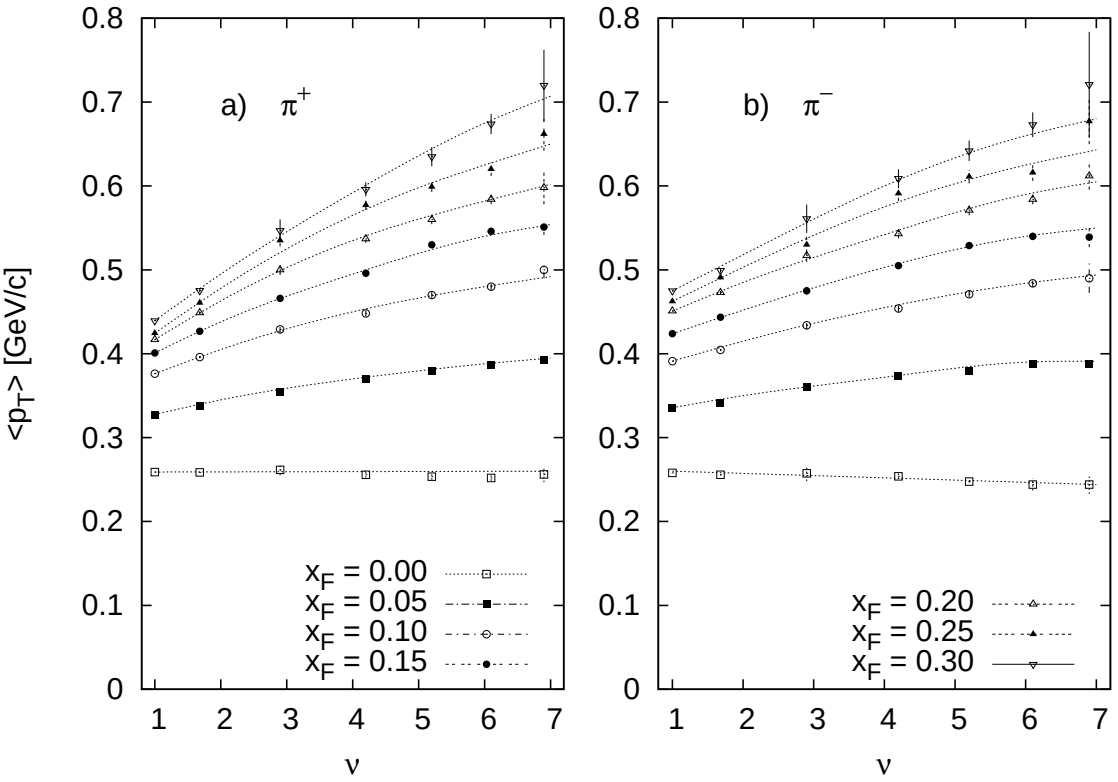

Figure 7.5: Mean transverse momentum $\langle p_T \rangle$ of $\langle \pi \rangle$ as a function of ν at different values of x_F for p+p, p+C and the five centrality bins of p+Pb. The figure legend is split between the two panels.

maximum $\langle p_T \rangle$ values are increased by almost a factor of two with respect to the "seagull" distribution in p+p interactions. The origin of the seagull effect has been shown to be due to resonance decay [61], [59]. The fact that this evolution is significantly reduced at $x_F = 0$ is partially an effect of the prevailance of the target fragmentation at this value of x_F. The mean transverse momentum is very similar for π^+ and π^- over all forward phase space, with a small but significant excess for π^- with respect to π^+ at small ν, an effect which decreases with increasing centrality.

The increase of $\langle p_T \rangle$ with ν is quantified in Fig. 7.5 for several values of x_F. Note the smooth increase up to the highest values of ν at all forward x_F.

7.4 p_T integrated yields

The pion yield densities were integrated as described in Section 6.3. The numerical values for the separate charges are tabulated in Table 6.9 and 6.10 on page 85. In this Section their charged averages will be investigated.

This integrated quantity is governed by a limited p_T region around its mean value $\langle p_T \rangle$, as seen from the shapes of the distributions in Fig. 7.3 above. A first overview of the integrated yield densities with x_F and ν is presented in Fig. 7.6, showing p+p ($\nu = 1$), p+C ($\nu = 1.6$) and three centrality bins in p+Pb interactions ($\nu = 2.9$, 5.1 and 6.9).

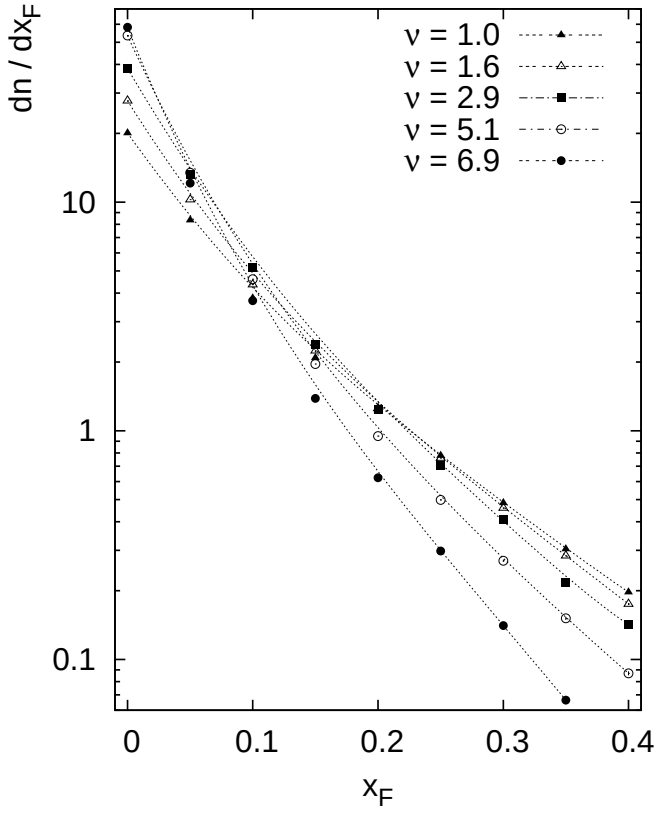

Figure 7.6: Integrated yield densities of $\langle \pi \rangle$ production as a function of x_F in the different reactions: p+p ($\nu = 1$), p+C ($\nu = 1.6$) and p+Pb ($\nu = 2.9$, 5.1 and 6.9).

The rather complex general pattern has the following noteworthy features if compared to elementary p+p interactions:

- At x_F below ≈ 0.1 there is a general increase of pion density with ν.

- This increase is followed by a cross–over region where the densities become equal. The x_F point where the $\langle\pi\rangle$ density in p+A drops below the one measured in p+p depends on ν and ranges from $x_F = 0.22$ in minimum bias p+C interactions to 0.1 in the most central p+Pb.

- Above the cross–over region there is a continuous decrease with increasing x_F, up to the highest values of x_F accessible with the NA49 data. This decrease gets stronger with increasing centrality.

These patterns show some of the features already discussed in connection with Fig. 7.1. They are presented in a linear scale by plotting the integrated density ratio in p+A over p+p:

$$R = \frac{(\mathrm{d}n/\mathrm{d}x_F)^{\mathrm{p+A}}}{(\mathrm{d}n/\mathrm{d}x_F)^{\mathrm{p+p}}} \tag{7.4}$$

This is shown in Fig. 7.7 for p+C and the five centrality bins in p+Pb interactions. The figure shows a smooth evolution of R with ν up to the highest centralities in p+Pb collisions. It is worth mentioning here that these data allow the first time a study of this phenomenology thanks to the completeness and extended phase space coverage of the NA49 data.

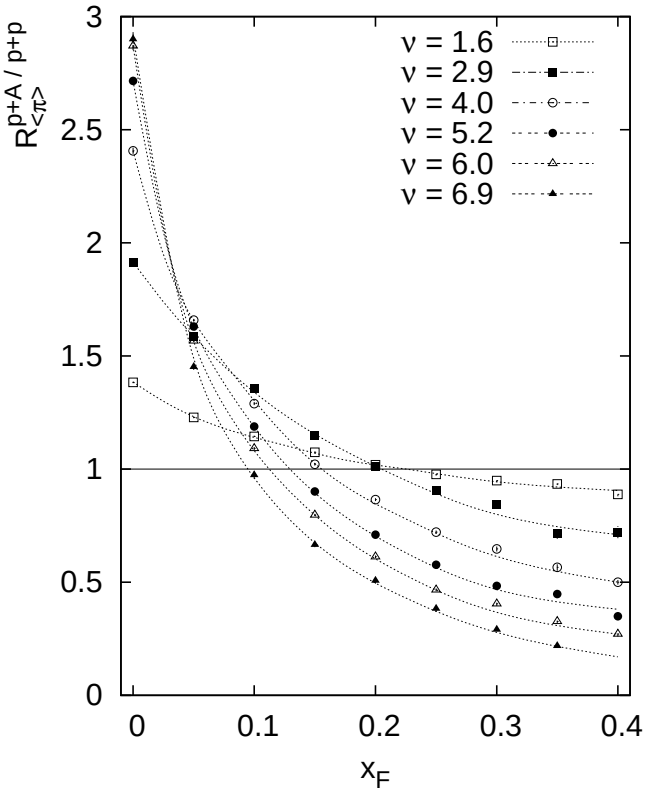

Figure 7.7: Ratio of integrated yield densities of $\langle\pi\rangle$ production as a function of x_F in p+C ($\nu = 1.6$) and the five centrality selected bins of p+Pb interactions. Lines connecting the points are to guide the eye.

Due to the steep x_F dependence of the pion yield densities show in Fig. 7.6, the strong decrease at higher x_F values relative to p+p shown in Fig. 7.7 has only a small influence on the total pion multiplicity in the projectile hemisphere. It indicates however a fundamental phenomenon of the projectile fragmentation in multiple collision processes. The

corresponding evolution of net baryon density with centrality, a phenomenon known as *baryon stopping*[1], is a well known but not well understood theoretically in p+A and A+A interactions. The crucial features of baryon stopping are manifested in Fig. 7.8, where the corresponding density ratios for proton production in p+C and p+Pb from preliminary NA49 data are presented.

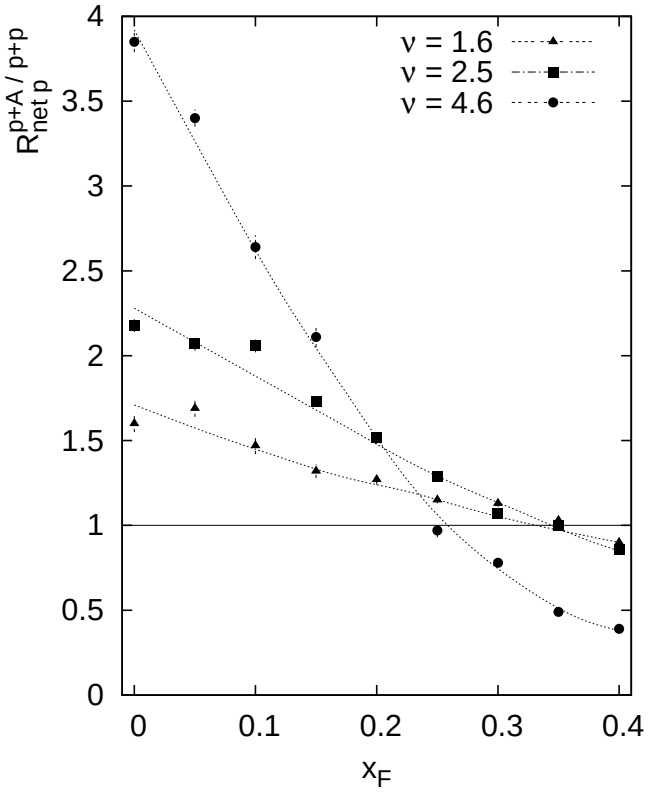

Figure 7.8: Ratio of integrated yield densities of net proton (p - $\overline{\text{p}}$) production as a function of x_F in p+C ($\nu = 1.6$) and two centrality selected bins of p+Pb ($\nu = 2.5$ and 4.6) interactions.

Baryon number conservation plays an essential role in constraining the transfer process of proton density from the forward to the central region of projectile fragmentation [51]. For pions such a constraint does not exist. However the striking similarity of the centrality dependencies of pion and proton spectra indicates that both phenomena have a common origin.

The ratio R for average pion production can also be studied as a function of ν at fixed values of x_F, as shown in Fig. 7.9.

An interesting pattern emerges. There is a nearly linear decrease of the ratio with ν starting at $x_F \sim 0.1$ towards forward values of x_F which has a ν-dependent offset. Apparently the decrease is counterbalanced by a relative density increase at small x_F.

The increase at $x_F = 0$ shows a linear dependency on ν up to $\nu \approx 4$. The linear increase is in fact expected for a two–component superposition mechanism (elaborated in detail in Section 7.6). In this mechanism at $x_F = 0$ the target nucleons contribute ν–times the pion density in p+p collisions, whereas the projectile contributes with weight 1:

$$\frac{\mathrm{d}n^{\mathrm{p+A}}}{\mathrm{d}x}(x_F = 0) = \frac{\nu + 1}{2}\frac{\mathrm{d}n^{\mathrm{p+p}}}{\mathrm{d}x}(x_F = 0) \tag{7.5}$$

[1]The phenomena of baryon stopping is beyond the scope of the presented thesis. It had been extensively studied by the NA49 and the reader is referred to [51, 54, 57] for further details.

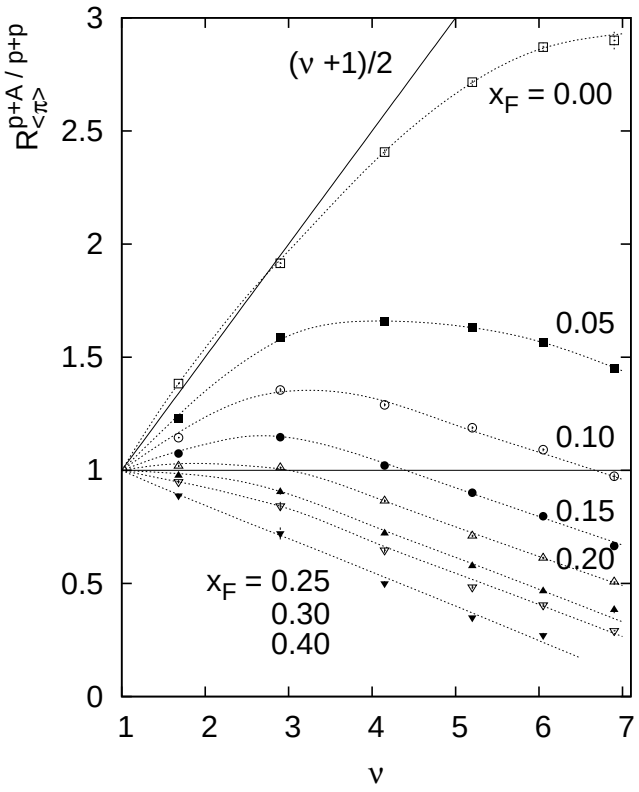

Figure 7.9: Ratio of integrated yield densities of $\langle\pi\rangle$ production as a function of ν at fixed values of x_F. Solid line of $(\nu{+}1)/2$ indicates the expected superposition in the two component mechanism at $x_F = 0$.

The linearity of the increase at $x_F = 0$ is followed by a flattening towards the highest collision centrality. The latter effect will be commented upon in Section 7.6, page 104 below.

After this excursion into p_T integrated distributions the discussion turns back to the main point of the thesis, the study of the transverse dependencies.

7.5 Cross section ratios as a function of p_T, x_F and ν

The cross section ratios R_{norm} are extracted from the invariant density distributions normalized at small p_T, already shown in Fig. 7.2.

$$R_{norm}(x_F, p_T) = \frac{d^{\mathrm{p+A}}_{norm}}{d^{\mathrm{p+p}}}(x_F, p_T) \tag{7.6}$$

These ratios are shown in Fig. 7.10 for the same x_F and ν selection as in Fig. 7.2. Due to the small increase at very low p_T visible at $x_F = 0$ in Fig. 7.10 the normalization interval was shifted to p_T between 0.2–0.3 GeV/c at this x_F value. This small increase is still under study.

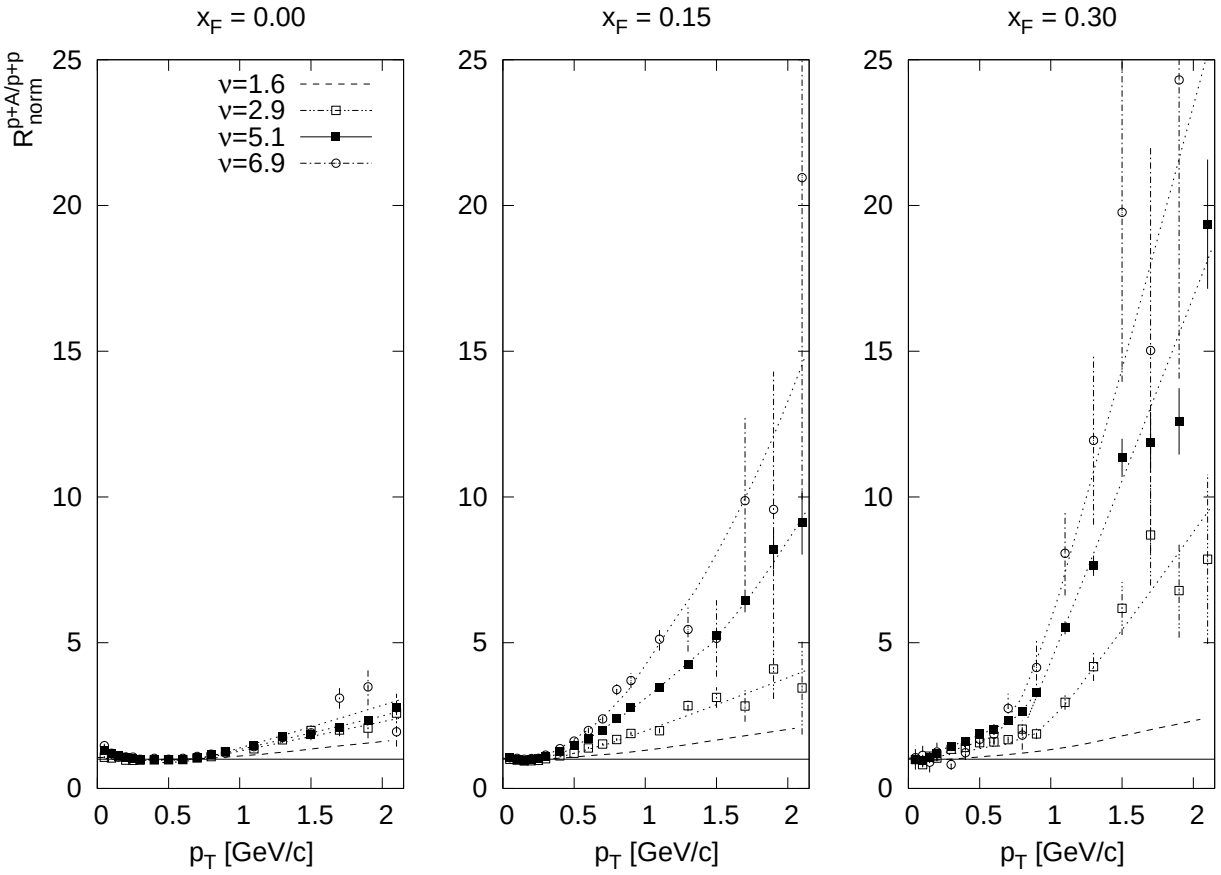

Figure 7.10: Ratio of invariant densities of $\langle\pi\rangle$ production at three x_F values as a function of p_T normalized at low p_T in different reactions: p+p ($\nu = 1$), p+C ($\nu = 1.6$) and p+Pb ($\nu = 2.9$, 5.1 and 6.9).

The general smooth increase of the ratio with transverse momentum already pointed out above is now visible on a linear scale, with factors reaching about one order of magnitude at the highest available values of p_T. This evolution can also be studied as a function of ν at fixed transverse momentum, which is presented in Fig. 7.11.

Again the systematic increase of R_{norm} with ν and x_F is evident. This phenomenon has been studied up to now only at $x_F \sim 0$ for Be, Ti and W nuclei in a minimum bias experiment [10]. This corresponds to a range of ν from 1.3 to 3.4. Compared to this earlier work both the ranges in ν and x_F are decisively extended by the new NA49 data. The p_T scale of [10], on the other hand, reaches out to much higher values, up to 6 GeV. The respective R_{norm} extrapolated from this experiment at their closest beam momentum

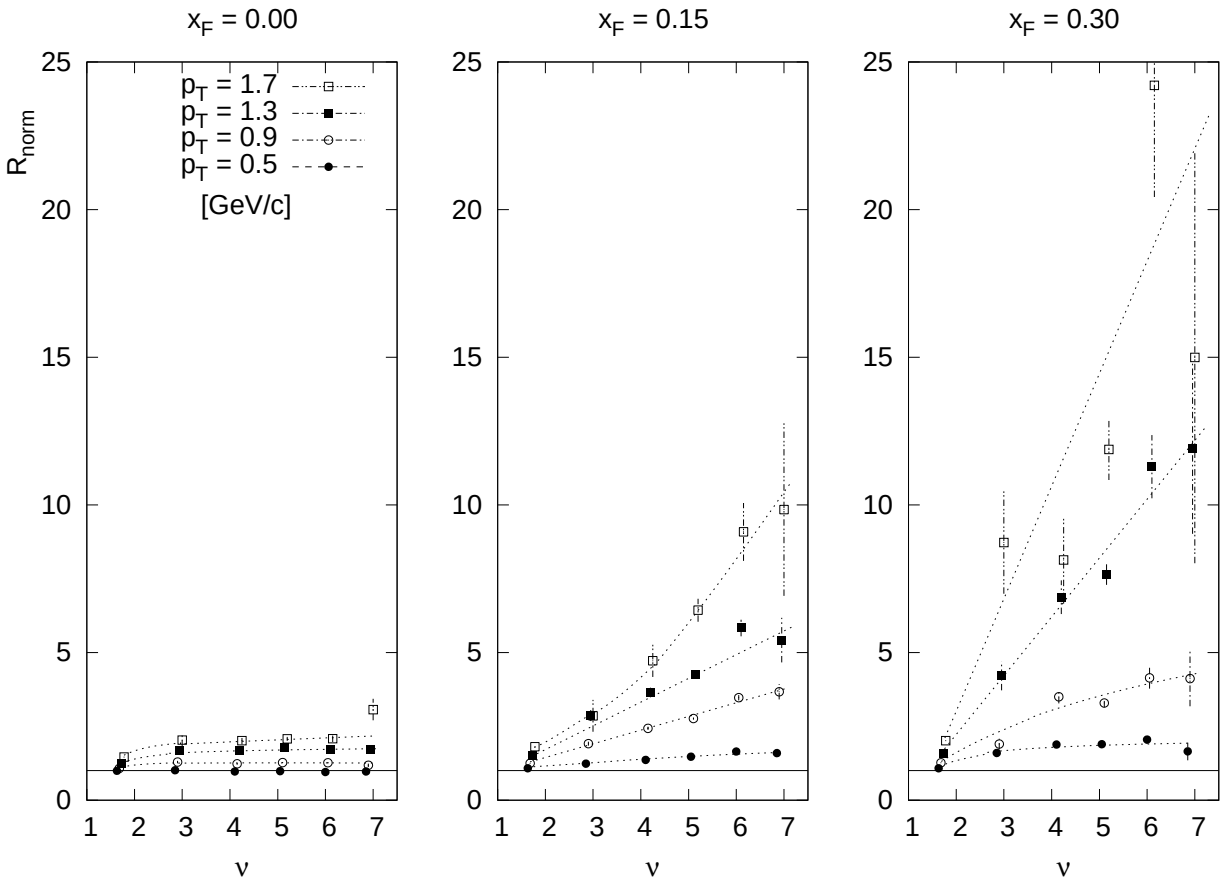

Figure 7.11: Normalized ratio of invariant densities of $\langle\pi\rangle$ production at three x_F values as a function of ν normalized for several values of transverse momentum. The points corresponding to different values of p_T are slightly displaced in ν for clarity.

of 200 GeV/c, with a slight extrapolation from W to Pb as described in Section 6.4, are presented in Fig. 7.12 in comparison with the NA49 data. As experiment [10] has not measured cross sections at low p_T the relative normalization between the data sets is fixed at their lowest p_T value of 0.77 GeV/c.

As already shown in the cross section comparison presented in Section 6.4, the results of [10] are compatible with the NA49 data in the overlap region up to 2 GeV/c transverse momentum. It is also evident from the Fig. 7.12 that the enhancement continues to increase with p_T up to the saturation at $p_T \sim 4$ GeV/c, followed by a decrease at higher values of transverse momentum. This phenomenon, if characterized by its A dependence, is known as the Cronin effect. Its origin is generally assumed [11] to be multiple hard partonic scattering in nuclear matter, although the theoretical foundation of this assumption is questionable [64]. A look at the detailed x_F dependence at fixed ν, presented in Fig. 7.13 and 7.14, may help to clarify this point.

It is evident that the enhancement at fixed values of transverse momentum has a very strong longitudinal dependence and increases smoothly from its minimum value at $x_F = 0$ towards the x_F limit of the NA49 data set at 0.4, with the exception of the p+C interactions, where a decrease at large x_F has been connected to the prevailance of single collisions in this reaction [63]. It will be shown that the longitudinal increase of the enhancement is compatible with a two–component fragmentation mechanism where the target contribution piles up with the ν sub-collisions suffered by the target nucleons, but has no enhancement as each target nucleon is only hit once. The projectile contribution is therefore only small

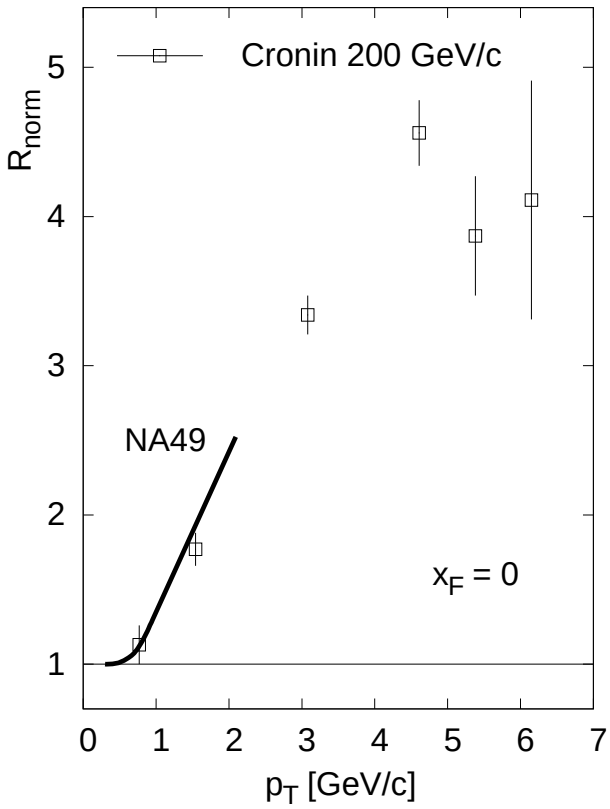

Figure 7.12: Transverse dependence of the normalized ratio of invariant densities of $\langle\pi\rangle$ production at $x_F = 0$ as measured by NA49 (line compatible with all the measured points is indicated) and by [10] at 200 GeV/c beam momentum. Relative normalization is fixed at the lowest measured p_T value of [10].

at small x_F, explaining the small resulting R_{norm} values. With growing x_F the target contribution dies out progressively and the enhancement, which is only valid for the projectile component, shows its full evolution. It remains to be seen to what extent this asymmetric situation can be explained by perturbative parton–parton scattering. A more detailed justification of this two–component hadronization scheme is given in the following Section.

A simple prediction however can be already made at this point. Since in A+A collisions all participant nucleons undergo multiple collisions in a symmetric configuration, the decrease of R_{norm} towards $x_F = 0$ should not exist in this case. This prediction will be verified in Section 7.8 below.

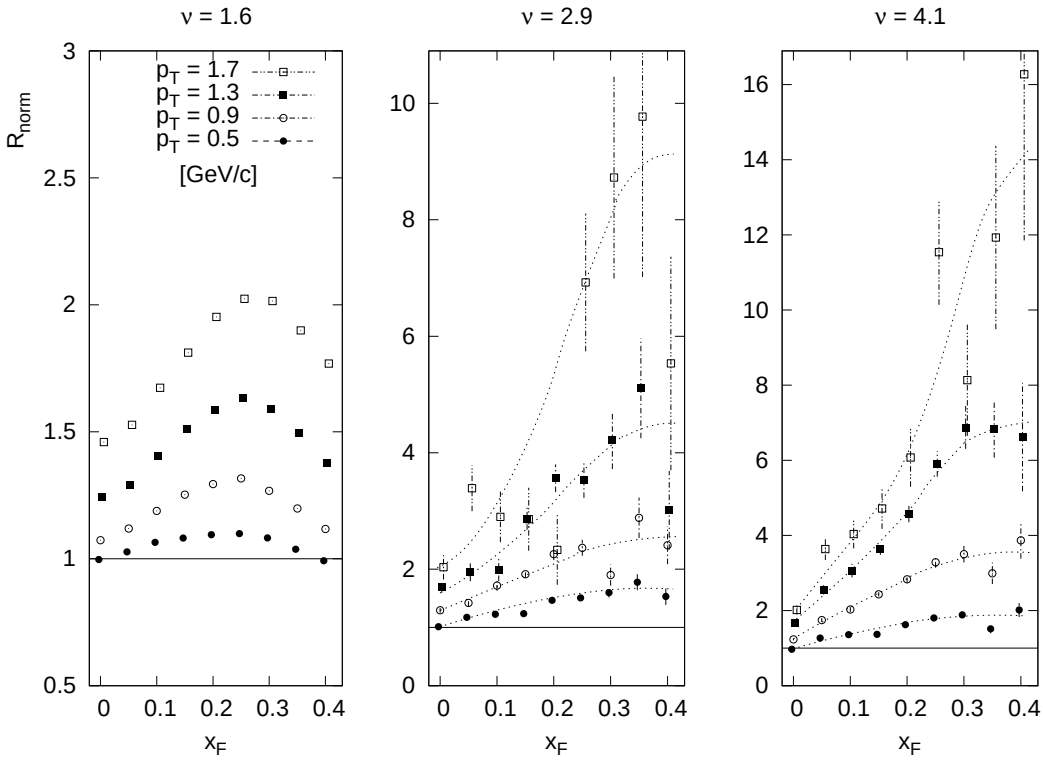

Figure 7.13: Evolution of R_{norm} with x_F for a few values of constant p_T in p+C and the first two bins in centrality of p+Pb.

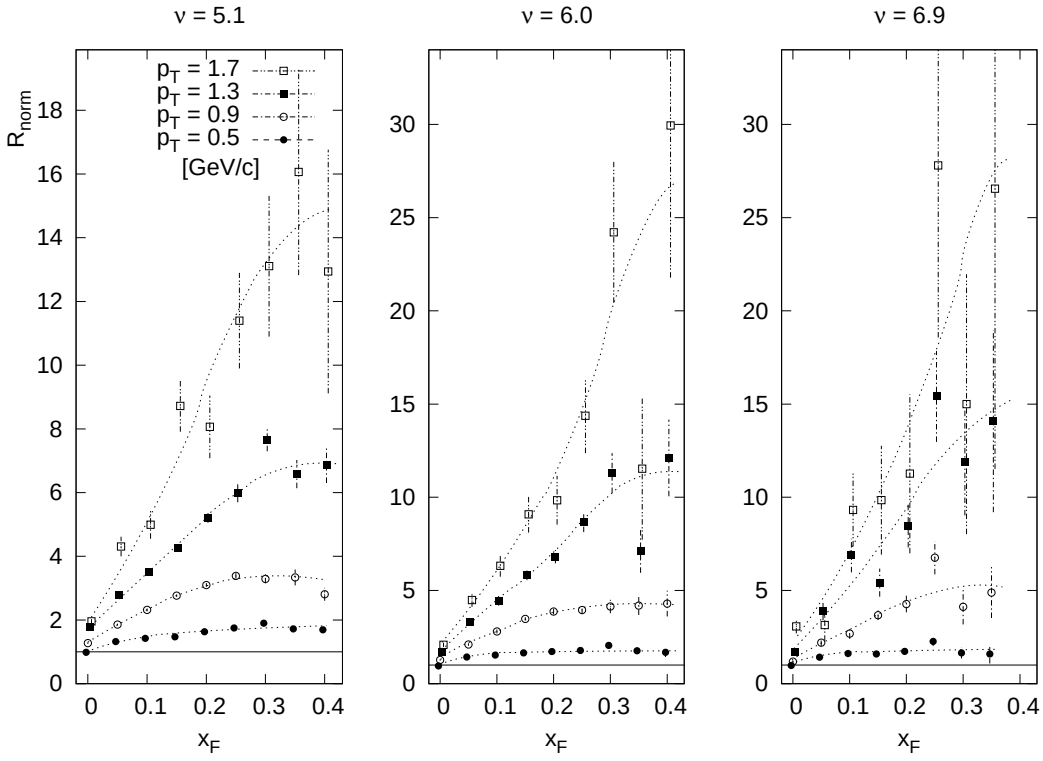

Figure 7.14: Evolution of R_{norm} with x_F for a few values of constant p_T in p+Pb with a ν of 5.1, 6.0, and 6.9. The points corresponding to different values of transverse momentum are slightly displaced in x_F for clarity.

7.6 Two–component hadronization mechanism

It has already been shown by the NA49 experiment [50, 51, 56, 54, 57] that the evolution of net baryon distributions in p+p, π+p, p+A and π+A collisions follows a two–component pattern, factorizing the measured spectra to target and projectile contributions. This argument could be conducted in a model independent way, using only the baryon conservation as underlying constraint.

For pion production, as discussed in this thesis, the situation is slightly more complicated as there is no conservation law for the number of produced pions. There is, however, isospin symmetry, which has been shown to hold for pions for double differential inclusive spectra at our energy [51, 55]. There is also beam target factorization which means that the fragmentation process of the target particle is independent of the type of the projectile hadron. This principle has been experimentally proven to hold at least in the backward hemisphere at $x_F < -0.2$ for hadron+proton collisions using a wide range of projectiles including protons, neutrons, pions, kaons and photons (see [49] and the references therein). In the argumentation of [63] essentially three experimental results related to these fundamental facts have been used:

- The absence of long range two–particle correlations between target and projectile fragmentation as it has been studied at the CERN ISR [69] for $x_F > 0.2$.
- The presence of forward–backward multiplicity correlations limited to a range of $x_F < 0.1$ as investigated at SPS and ISR energies [70, 71, 72, 73]. These measurements allow the quantification of the pion yield fed from the target to the projectile hemisphere and vice versa, the feed–over.
- The detailed behavior of the π^+/π^- ratio as a function of x_F in $\langle\pi\rangle$+p by the NA49 experiment, where $\langle\pi\rangle$ indicates the average combination of results from π^++p and π^-+p interactions. This study uses the fact that isospin symmetry results in a π^+/π^- ratio exactly equal to unity over the full range of projectile fragmentation. The approach of the charged ratio to unity in the projectile hemisphere allows the shape of the target contribution below $x_F = 0.1$ to be fixed, in addition to the integrated yield emerging from the multiplicity correlation.

The resulting two–component fragmentation mechanism for pions is presented in Fig. 7.15 both in absolute pion density $\mathrm{d}n/\mathrm{d}x_F$ and in the relative yield contribution from projectile $p(x_F) = (\mathrm{d}n/\mathrm{d}x_F)^{\mathrm{projectile}}$ / $(\mathrm{d}n/\mathrm{d}x_F)^{\mathrm{inclusive}}$ and target nucleon $t(x_F) = (\mathrm{d}n/\mathrm{d}x_F)^{\mathrm{target}}$ / $(\mathrm{d}n/\mathrm{d}x_F)^{\mathrm{inclusive}}$.

The detailed study of p+C interactions presented in [63] has demonstrated that for this light ion interaction the target contribution is proportional to the number of projectile collisions ν with target nucleons, whereas the projectile fragmentation is modified in a characteristic fashion which is in complete agreement with the phenomenology discussed above. In the first approximation this modification may be characterized by an enhancement factor $\mathrm{E}(x_F)$ which multiplies the projectile contribution:

$$\frac{\mathrm{d}n}{\mathrm{d}x_F} = \nu \cdot t(x_F) + E \cdot p(x_F) \tag{7.7}$$

The contributions from target and projectile fragmentation are schematically presented in Fig. 7.16 for $\mathrm{E} = 1$.

Two more experimental results concerning this description of the hadronization process will be used in the subsequent section:

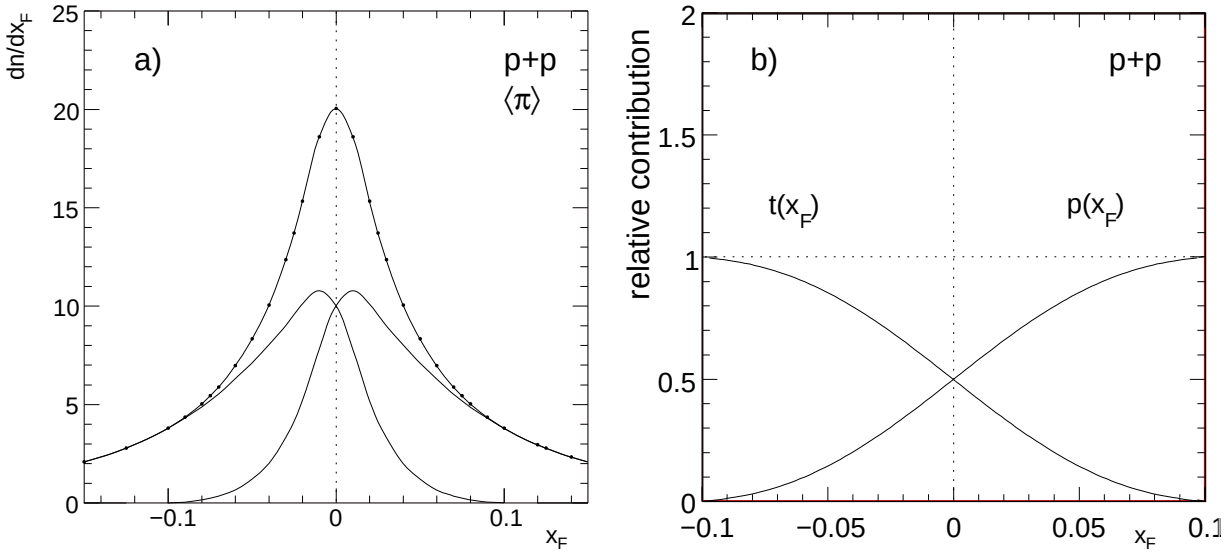

Figure 7.15: Two component decomposition of pion density in p+p interactions, in a) absolute density $\mathrm{d}n/\mathrm{d}x_F$, b) in relative densities $(\mathrm{d}n/\mathrm{d}x_F)^{\mathrm{projectile}}$ / $(\mathrm{d}n/\mathrm{d}x_F)^{\mathrm{inclusive}}$.

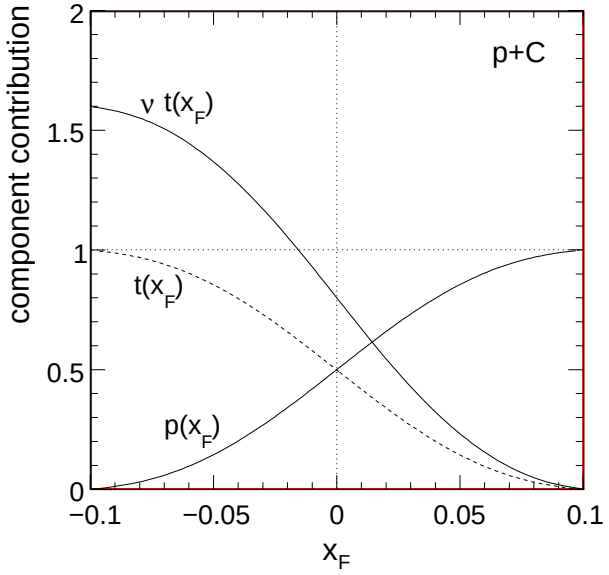

Figure 7.16: The target $t(x_F)$ and projectile $p(x_F)$ contributions to the pion yield according to the two component fragmentation scheme as extracted in p+C interactions [63]. The dashed line shows the target contribution per participant target nucleon.

- The dependence of the feed–over range on the particle mass.
- Its dependence on transverse momentum.

The first fact is quantified in Fig. 7.17 which compares the shapes and ranges of proton target fragmentation into pions and protons as they have been independently extracted from NA49 data. [63]

These distributions are obtained by using p_T integrated pion densities $\mathrm{d}n/\mathrm{d}x_F$ which are governed by the yield in the neighborhood of the mean transverse momentum (see also Section 7.3, Fig. 7.3), thus this feed-over shape corresponds to low p_T. By studying transversely integrated distributions for protons shown in Fig. 7.17, a strong mass dependence

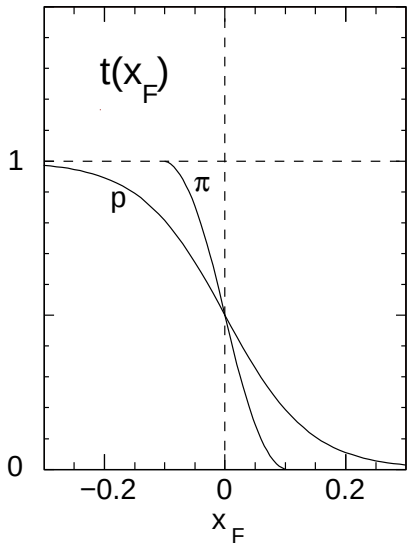

Figure 7.17: Relative contributions from target fragmentation for protons and pions in the case of proton target [62].

of the feed–over range was observed. Looking at Figures 7.13 and 7.14 in more detail, it can be concluded that the point of maxima or saturation of the R_{norm} dependence with x_F shifts forward with increasing values of transverse momentum in all the different centrality selections, indicating the p_T dependence of the feed-over.

Both the mass and the p_T dependence have been shown to be a result of resonance decay [63], which is known to contribute more than 70 % of the total yield of stable mesons [91, 92]. This process explains both the mass and the p_T dependences observed above by a straight–forward action of decay kinematics. The kinematics of a resonance decay is governed by the Lorentz transformation from the resonance rest system into the overall center of mass system:

$$p^* = \gamma_{\rm res} \cdot \left(q + \beta_{\rm res} \cdot \sqrt{q^2 + m^2} \right) \tag{7.8}$$

where m is the decay particle mass and q is the momentum of the decay products in the resonance rest system,

$$q = \frac{1}{2m_{\rm res}} \sqrt{(m_{\rm res}^2 - (m_1 + m_2)^2)(m_{\rm res}^2 - (m_1 - m_2)^2)} \tag{7.9}$$

where m_1 and m_2 are the decay product masses and $m_{\rm res}$ is the mass of the original resonance.

As a result the momentum of the decay products in the overall center of mass frame depends via q on the resonance mass $m_{\rm res}$ and via the Lorentz transformation on the particle mass m. At low q, corresponding to a low mass resonances, there will be an important dependence on particle mass because pions will receive much smaller boost than protons. For large q, $q \gg m_\pi$, this mass dependence will be diminished due to the prevailance of q in energy term. If large p_T values originate from high mass resonances or the Breit–Wigner tail of the resonance mass distribution, a strong p_T dependence of the two–component fragmentation mechanism for pions is also predicted. This is demonstrated in Fig. 7.18 [63] which gives a practical demonstration of the effects using the $\Delta^{++}(1232)$ resonance as an example.

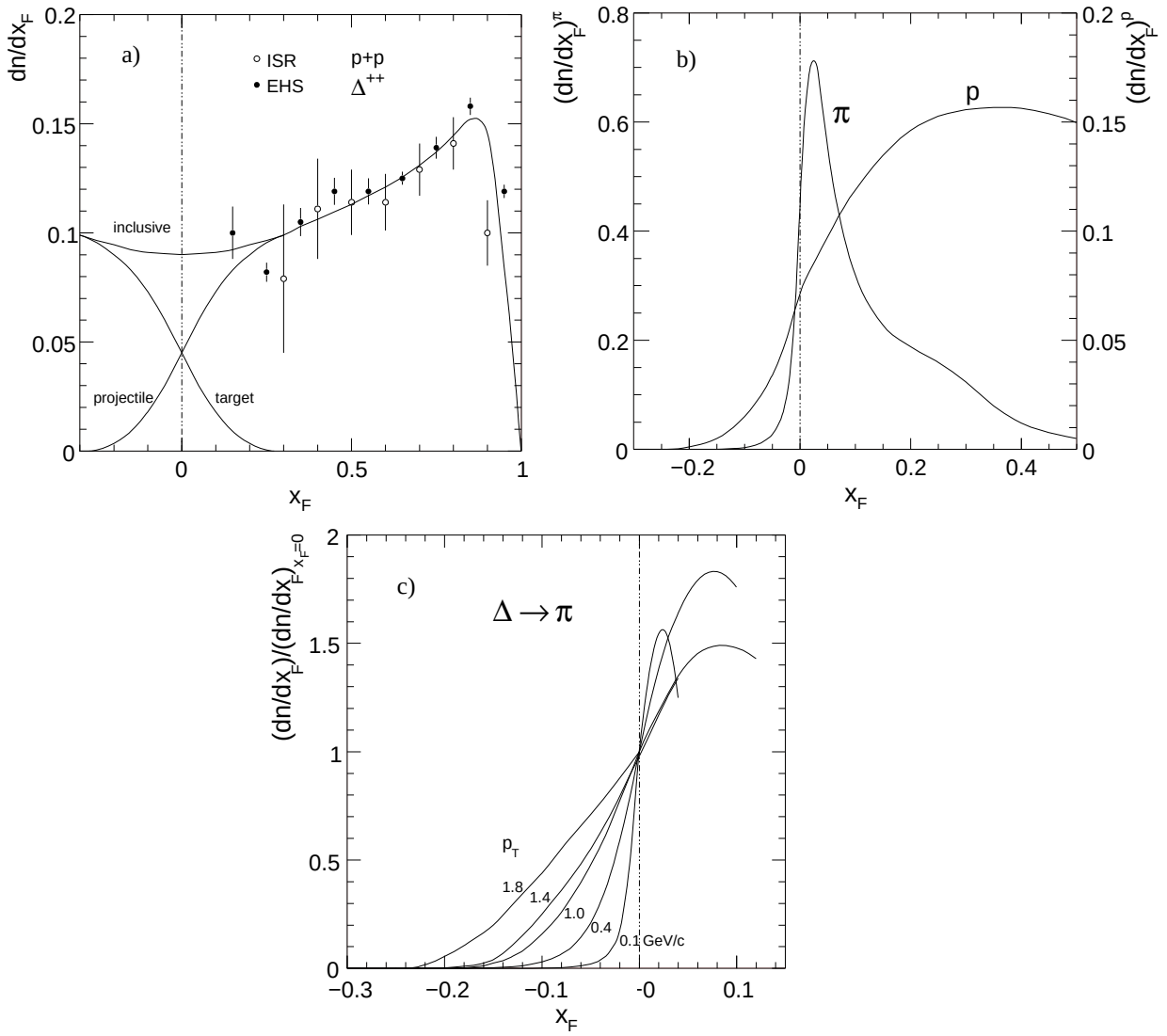

Figure 7.18: a) Two–component decomposition of $\Delta^{++}(1232)$ production, b) p_T integrated densities of pions and protons produced from Δ^{++} decay, c) Pion feed–over from Δ^{++} decay for different values of p_T normalized to one at $x_F = 0$.

Panel 7.18 a) shows the measured x_F distribution of the Δ^{++} and its decomposition into target and projectile contributions, using the measured two–component behavior for baryons (Fig. 7.17 and [98, 56]). Panel 7.18 b) gives the resulting feed–over distributions for protons and pions from the Δ^{++} decay which reproduces the observed mass dependence (Fig. 7.17). Panel 7.18 c) displays the p_T dependence of the feed-over range for pions from the same decay, verifying both the above prediction and the observed transverse dependence of R_{norm}, shown in Section 7.5 and Figures 7.13 and 7.14.

There may be energy loss in p+A collisions, meaning that the consecutive collisions with the ν target nucleons happen at reduced energy. This means that the overall center of mass system used in the definition of x_F is not the proper reference frame. In this frame the target contribution from subsequent collisions will shift to negative x_F with increasing number of projectile collisions ν. This effect might explain the observed nonlinearity of the superposition at $x_F = 0$, see Fig. 7.9. Work on this second order effect is still in progress and the subsequent sections of this thesis will not include this phenomenon.

7.7 Application of the two–component scheme to R_{norm}

The normalized ratio R_{norm} as defined in equation (7.6) relates the transverse dependence of particle densities to the p+p interaction and takes the main part of their x_F dependence into account by normalizing at low p_T. This quantity has two components:

- A target contribution R_{norm}^{target} which may be assumed to be equal to 1 in the first approximation and which contributes with the weight $t(x_F, p_T) \cdot \nu$.
- A projectile contribution $R_{norm}^{\text{projectile}}$ which has the weight $p(x_F, p_T)$ and which has a characteristic enhancement factor $\mathrm{E}(x_F, p_T)$, which is of interest here.

This can be formalized using the following relations:

$$R_{norm}(x_F, p_T) = \frac{\nu \cdot t(x_F, p_T) + E(x_F, p_T) \cdot p(x_F, p_T)}{\nu \cdot t(x_F, p_T) + p(x_F, p_T)} \tag{7.10}$$

$$E(x_F, p_T) = \frac{(\nu \cdot t(x_F, p_T) + p(x_F, p_T))) \cdot R_{norm}(x_F, p_T) - \nu \cdot t(x_F, p_T)}{p(x_F, p_T)} \tag{7.11}$$

This formulation demonstrates that in the far forward direction where the target contribution vanishes, $t(x_F, p_T) = 0$ and $p(x_F, p_T) = 1$, the projectile enhancement factor is directly given by the measured quantity R_{norm}. At $x_F = 0$, where $t = p$, R_{norm} is suppressed with respect to E according to the following formula:

$$R_{norm}(0, p_T) = \frac{E(0, p_T) + \nu}{\nu + 1} \tag{7.12}$$

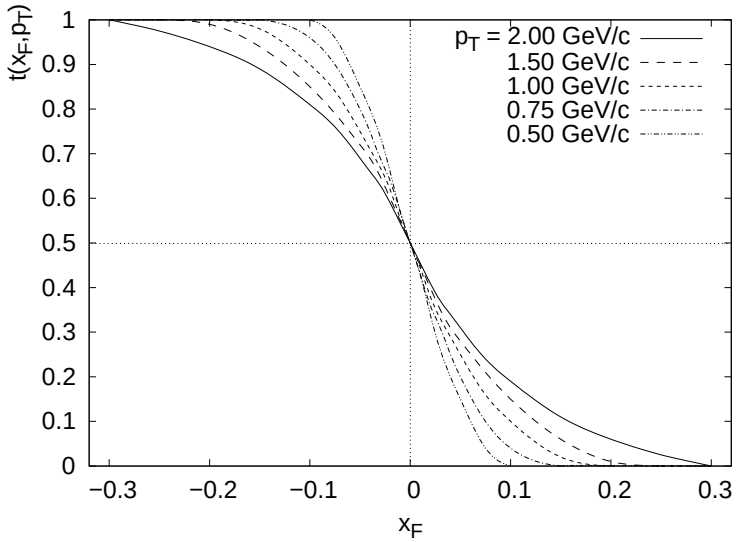

Figure 7.19: The target weight functions t as a function of x_F for several values of p_T. The projectile weight functions are symmetric: $p(x_F, p_T) = t(-x_F, p_T)$.

Finally in the far backward direction where $p(x_F, p_T)$ vanishes, E is undefined but $R_{norm}(x_F, p_T)$ approaches one.

The target weight function $t(x_F, p_T)$, used in subsequent analysis, is given in Fig. 7.19. The projectile weight function $p(x_F, p_T)$ is obtained by reflection around $x_F = 0$, meaning

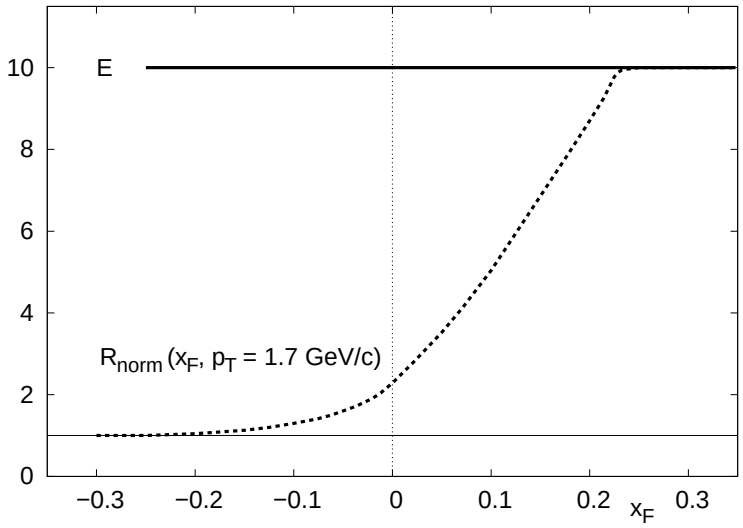

Figure 7.20: Schematic demonstration of the target feed-over effect on the measured R_{norm} (dashed line) assuming constant E = 10 (full line) in the two–component mechanism for hypothetical p+A collisions with $\nu = 6$ at $p_T = 1.7\,\mathrm{GeV/c}$.

$p(x_F, p_T) = t(-x_F, p_T)$. These weight functions correspond to the x_F and p_T dependencies discussed in the preceding Section.

The difference between the measured quantity R_{norm} and the projectile enhancement E is schematically demonstrated in Fig. 7.20 for the assumed case of constant $E(x_F, p_T) = 10$ and $\nu = 6$. The strong suppression of the measured ratio R_{norm} with respect to the true enhancement value at small x_F, where most of the existing experiments perform their measurement, is striking. A careful extraction of the projectile properties is therefore absolutely mandatory in this region for p+A interactions. This also applies to other measured quantities such as strangeness enhancement, as discussed in [52, 53].

The weight functions $t(x_F, p_T)$ and $p(x_F, p_T)$ can be applied to p_T and x_F dependence of the measured $R_{norm}(x_F, p_T)$ shown in Figures 7.13 and 7.14. The resulting projectile enhancement factor $E(x_F, p_T)$ is presented in Fig. 7.21 as a function of x_F for different values of p_T for the highest statistics sample of all centrality triggered p+Pb events, $\nu = 5.1$.

The strong decrease of R_{norm} from the forward direction towards $x_F = 0$ as observed in Figures 7.13 and 7.14 is replaced by a moderate, smooth x_F dependence.

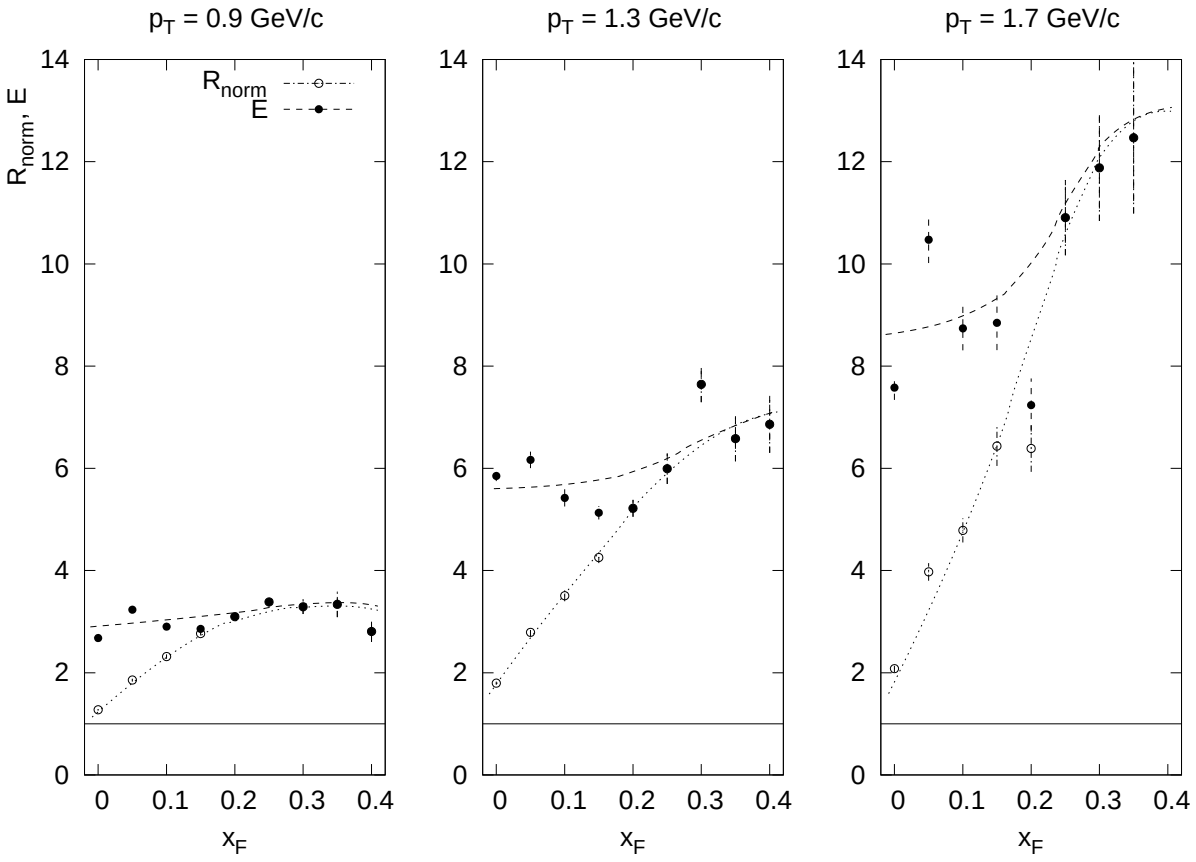

Figure 7.21: R_{norm} and E for the highest statistics centrality selected sample $\nu = 5.1$.

7.8 Comparison to Pb+Pb interactions

In this Section, the similarities and differences between the transverse evolution of pion densities in Pb+Pb and p+Pb are investigated, using the phenomenological framework developed in the preceding sections.

The superposition of target and projectile components in the symmetric case of Pb+Pb interactions is expected to differ from p+Pb reactions, since all participating nucleons undergo multiple collisions both in the target and the projectile nucleus, as discussed in the Section 2.3. The measured density ratio normalized at low p_T:

$$R_{norm}^{\mathrm{Pb+Pb}}(x_F, p_T) = \frac{d_{norm}^{\mathrm{Pb+Pb}}}{d^{\mathrm{p+p}}}(x_F, p_T) \tag{7.13}$$

is not dominated by single collisions suffered by the ν target nucleons anymore in the region with a significant target contribution, since both target and projectile contributions carry an equal imprint of the multiple collision process. Equation (7.10) can therefore be reformulated as:

$$R_{norm}^{\mathrm{Pb+Pb}}(x_F, p_T) = \frac{E(-x_F, p_T) \cdot t(x_F, p_T) + E(x_F, p_T) \cdot p(x_F, p_T)}{t(x_F, p_T) + p(x_F, p_T)} \tag{7.14}$$

where the factors $E(-x_F, p_T)$ and $E(x_F, p_T)$ represent the target and the projectile enhancements respectively. The relative weights of the contributions add up to unity, $t(x_F, p_T) + p(x_F, p_T) = 1$. The equation (7.14) says that the projectile weight function $p(x_F, p_T)$ cuts off the enhancement $E(x_F, p_T)$ at $x_F < 0$, and that the target weight function $t(x_F, p_T)$ cuts off $E(-x_F, p_T)$ at $x_F > 0$. What remains is approximately $E(|x_F|, p_T)$.

The only region where some of the asymmetry may be manifested is the region of $x_F \approx 0$. However, even if the enhancement factors are asymmetric around $x_F = 0$, due to the overall shape of the projectile and target contributions the difference between $R_{norm}^{\mathrm{Pb+Pb}}$ and E is small at all positive x_F. This is valid even when very different shapes of $E(x_F, p_T)$ at negative values of x_F are assumed, as illustrated in Fig. 7.22.

Therefore, it is assumed that E in the case of A+A interactions can be approximated by $R_{norm}^{\mathrm{Pb+Pb}}$ for the purposes of the following discussion.

$$E(|x_F|, p_T) \approx R_{norm}^{\mathrm{Pb+Pb}}(x_F, p_T) \tag{7.15}$$

Preliminary data on x_F and p_T distributions of pions produced in Pb+Pb interactions in different centrality bins are available from the NA49 experiment [93, 94, 95]. For a comparison between the Pb+Pb and p+Pb reactions, a centrality bin with total measured multiplicity between 900 and 1100 charged particles has been chosen, which corresponds to a mean number of collisions $\nu = 4.1$ per participant nucleon, as discussed in Section 5.3.4. The ratio $R_{norm}^{\mathrm{Pb+Pb}}(x_F, p_T)$ is shown for this bin in Fig. 7.23 for $x_F = 0$, 0.15 and 0.3 as a function of transverse momentum.

The enhancement of the pion yield with increasing transverse momentum is similar in Pb+Pb and p+Pb collisions (Fig. 7.10). The sharp decrease of R_{norm} towards $x_F = 0$ in p+Pb reactions (Fig. 7.10) is absent in the case of Pb+Pb interactions (Fig. 7.23). This apparent difference can be explained by the different superposition of target and projectile contributions in the different types of reactions, as discussed above.

This is exemplified in Fig. 7.24[2]. Panel a) shows the ratio R_{norm} measured in p+Pb

[2]The values at $p_T = 1.7\,\mathrm{GeV/c}$ for p+Pb reaction shown in panel a were obtained using interpolation of the relative pion densities along the transverse direction for fixed values of x_F to smooth statistical fluctuations evident in Fig. 7.13. The enhancements shown in panel b) were calculated from these values.

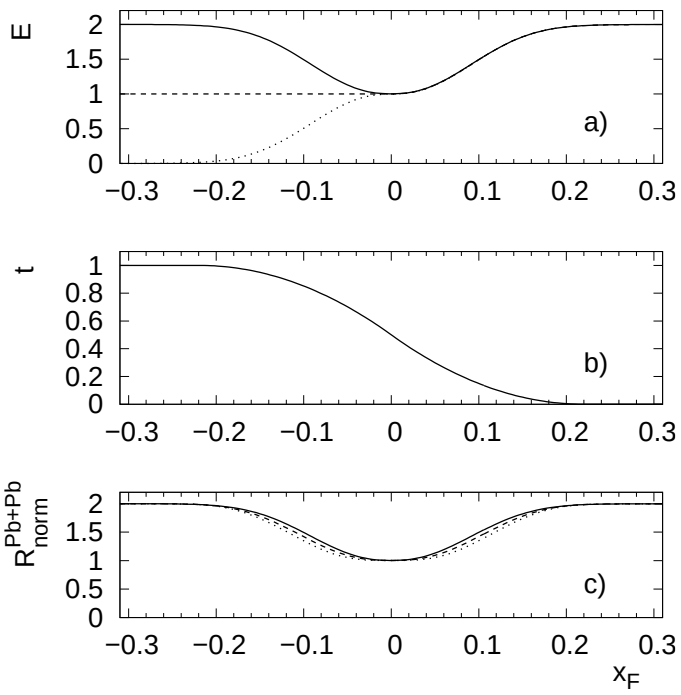

Figure 7.22: Relation between $R_{norm}^{\mathrm{Pb+Pb}}$ and E, sketched at a fixed value of p_T. a) Different possible shapes assumed for $E(x_F, p_T)$, b) the target component $t(x_F, p_T)$, c) the ratio $R_{norm}^{\mathrm{Pb+Pb}}$ as obtained from equation (7.14) assuming the E shapes shown in panel a). Note that the solid curves in panel a) and c) are identical due to symmetry around $x_F = 0$.

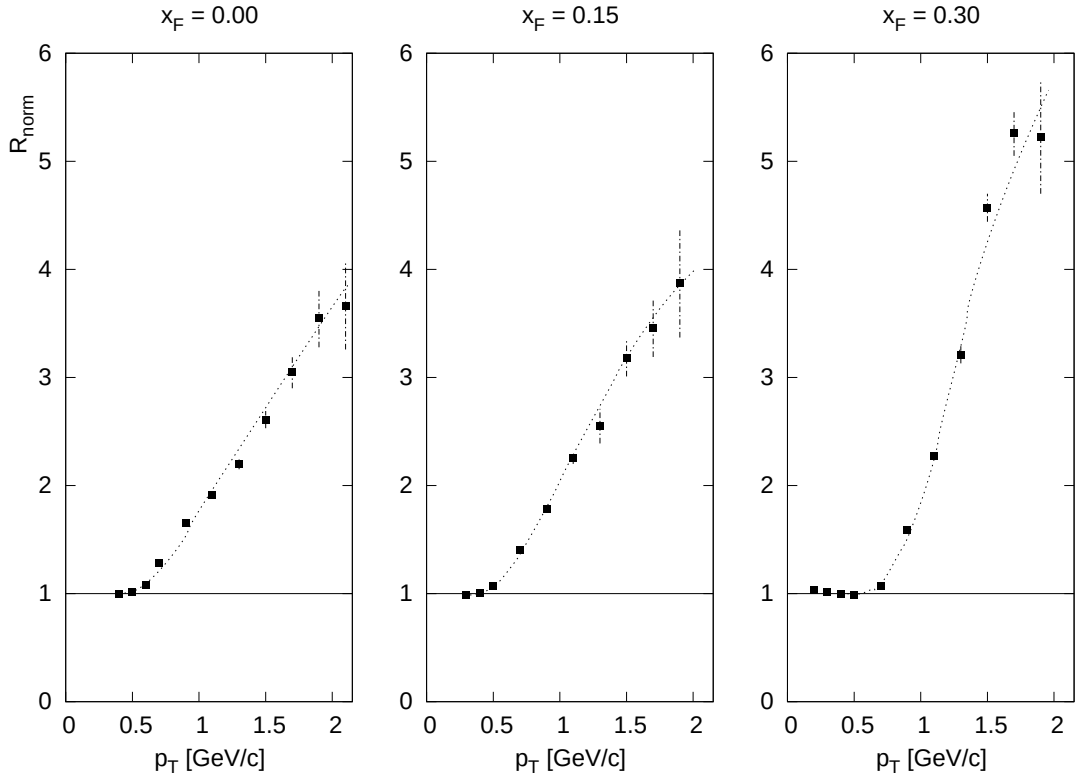

Figure 7.23: R_{norm} for Pb+Pb interactions with an average number of collisions $\nu = 4.1$ per participant as a function of p_T for three values of x_F.

interactions at three values of transverse momentum (p_T = 0.9, 1.3 and 1.7 GeV/c), presented as a function of x_F. The corresponding values of projectile enhancement factors E are shown in the panel b). Apparently the sharp decrease of the measured ratio towards $x_F = 0$ vanishes after the contribution from the target part in p+Pb collisions has been corrected for. The ratios $R_{norm} \approx E$ measured in Pb+Pb interactions are presented in panel c). Both in the shapes of their x_F evolution and in the sequence of pion enhancements with increasing p_T, the Pb+Pb reaction shows a striking similarity to the dependencies seen in the panel b) for the projectile enhancements in the p+Pb reaction. This clearly points to a similar phenomenon which appears as a consequence of the multiple collision process in p+Pb and Pb+Pb reactions.

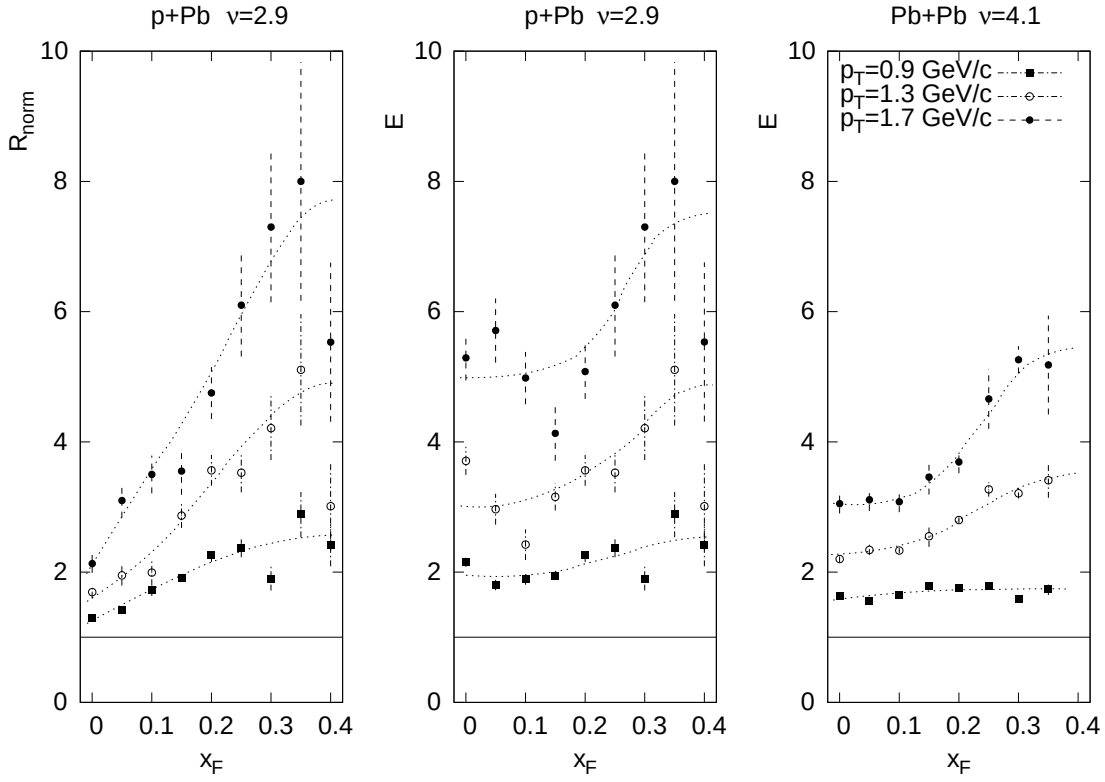

Figure 7.24: a) R_{norm} for p+Pb interactions of $\nu = 2.9$ for several values of p_T as a function of x_F, b) E for the same p+Pb reaction, c) $R_{norm}^{\mathrm{Pb+Pb}}$ for Pb+Pb interactions at $\nu = 4.1$.

This is neither the first nor the only example of similarities between the two types of nuclear reactions. Other phenomena like strangeness enhancement [52], in particular Ξ hyperon production [53], baryon number transfer [54], and the evolution of baryon transverse momentum in connection with "transverse expansion" [51] have been already discussed using NA49 data. In all these cases, proper treatment of the asymmetric nature of the p+A interactions by separating out the projectile component has been necessary for a quantitative understanding of these phenomena.

Moreover, by comparing Fig. 7.24 b) and c), the midrapidity region at $x_F = 0$ does not seem to be significant in the observed evolution of p_T dependent enhancement. The observed pattern is more pronounced at forward x_F values in both the reaction types.

Finally, on top of the similarities discussed, quantitative differences are shown in Fig. 7.24 b) and c): for each of the considered values of transverse momentum the enhancement is higher in p+Pb than in Pb+Pb collisions and similar absolute values of the p_T enhancement do not quite correspond to the same number of mean collisions per participant nucleon, since

ν has to be larger in Pb+Pb collisions in order to produce the same effect. Part of this difference may be understood as a consequence of a definite systematic uncertainty in the determination of ν of $\sim \pm 10\,\%$ because for both reactions one has to rely on Monte Carlo calculations, which are model dependent.

Also, the distribution of ν about a given mean value is not the same in centrality triggered p+A reactions and in A+A interactions with a comparable mean ν. In the A+A case there is a certain fraction of single collisions present at each impact parameter. For centrality selection by grey proton counting in the p+A interactions, there is no tail towards $\nu = 1$. If the studied phenomena are non–linear in ν such as the ones discussed in this chapter, convoluting with different distributions of ν gives different results for the same mean value of the number of projectile collisions.

The interpretation of this phenomenon, including a detailed study of the difference of energy loss (Section 7.6) in the two cases of asymmetric p+A and symmetric A+A reactions, is still in progress.

Chapter 8

Summary and conclusions

This thesis is concerned with pion production in a wide range of soft hadronic interactions. It is centered on p+Pb collisions but contains in addition a detailed comparison with elementary p+p, minimum–bias p+C and central Pb+Pb reactions. The thesis comprises two parts: the experimental part and the data discussion.

The part describing the experiment and the experimental procedures can be summarized as follows:

- It describes the extraction of invariant inclusive pion cross sections from a set of about 2 million p+Pb measured events obtained in the years from 1997 to 2001 at the CERN SPS using the NA49 detector setup. This extraction includes the reduction of a raw data volume of several Terabytes into DSTs and μDSTs after event selection, track reconstruction and particle identification.

- A number of corrections applied to the extracted data are presented in detail. This includes a method of correction for trigger induced bias developed by the author.

- The thesis presents measurements of the total inelastic cross section in minimum bias p+C and p+Pb interactions. The values agree within errors with previous dedicated measurements.

- The sample of minimum bias p+Pb interactions was analyzed. Charged pions were extracted in the ranges of $0 < x_F < 0.4$ and $0 < p_T < 2.1\,\mathrm{GeV/c}$ in 155 bins per charge and compared to the small available set of existing measurements. A satisfactory agreement was found.

- An important peculiarity of the data set is given by the on-line centrality control of the p+Pb interactions via grey proton counting in a special centrality detector. This allows sorting of the collisions into 5 centrality bins which are characterized by the number of projectile collisions ν in the range from 2.9 to 6.9, as compared to a minimum bias sample with only 3.7 collisions. Due to the tight control of all systematic error sources the systematic uncertainty of the obtained cross sections could be kept below the 3 % level on average.

- The resulting roughly 2 000 data points cover the forward hemisphere in a dense set of 155 bins per centrality set per charge over the ranges of $0 < x_F < 0.4$ and $0 < p_T < 2.1\,\mathrm{GeV/c}$, offering a sample of cross section which is unprecedented in p+A collisions.

In its physics discussion part the thesis uses the extracted data for a detailed comparison with other hadronic interactions, making full use of the other high precision results also available from the NA49 experiment. The discussion is centered on the evolution of the pion yields in transverse momentum but contains also new results on the x_F dependence of p_T integrated quantities like the pion density $\mathrm{d}n/\mathrm{d}x_F$ and the mean transverse momentum, $\langle p_T \rangle$. Several physics aspects emerge from these new data:

- The integrated yields $\mathrm{d}n/\mathrm{d}x_F$ show a distinct pattern as a function of x_F. At $x_F = 0$ there is a strong increase with the number of collisions up to a factor of ~ 3 for the highest centrality. This corresponds to an approximately linear increase with the quantity $(\nu+1)/2$ which in turn indicates the expected superposition of the fragmentation of ν target nucleons and of the single projectile.

- For $x_F > 0.2$ there is a strong suppression of the pion yield which reaches a suppression factor of 0.2 for the highest centrality at $x_F = 0.4$. This effect is shown to correspond to the observed baryon transfer in p+A collisions, the "stopping".

- The mean transverse momentum of produced pions increases smoothly with the number of collisions and x_F. It reaches values of $\langle p_T \rangle \sim 0.7\,\mathrm{GeV/c}$ for the highest centrality at $x_F = 0.4$.

- A general flattening of the measured invariant p_T distribution with increasing ν is observed as a function of transverse momentum.

- If normalized to the corresponding distributions for p+p collisions at low p_T, the cross section ratio increases smoothly with transverse momentum and reaches values of about 20 for the most central collisions at $p_T = 2\,\mathrm{GeV/c}$ and $x_F = 0.4$.

- The increase shows a strong x_F dependence: It is strongly reduced when approaching $x_F = 0$. This reduction is related to the target–projectile superposition already evident in the integrated yields at $x_F = 0$, invoking a fragmentation of the target part, which is expected to be equal to the elementary nucleon+nucleon collision, since the target part experiences a single collision per participant.

- In this two–component target–projectile superposition scheme the p_T enhancement of the projectile component is extracted and compared to Pb+Pb collisions where all participants undergo multiple collisions.

- A similarity of the p_T enhancement between p+Pb and Pb+Pb interactions is shown. This means that A+A collisions are not unique with respect to this phenomenon.

- A comparison of the minimum bias sample with the anomalous nuclear enhancement, the Cronin effect, is conducted. It is shown that these data, obtained at $x_F \sim 0$, have to be corrected in order to extract the projectile part of the observed enhancement. It is argued that only this projectile enhancement, which is bigger than the measured increase, should be compared to A+A data.

Acknowledgments

I would like to thank my Supervisor Dr. Jiří Dolejší for his incredible support, patience and help throughout the time of my graduate study, for patient and friendly encouragements, and last but not least for the opportunity to participate in an international collaboration and work in CERN.

I would like to express my deep gratitude to Dr. Hans Gerhard Fischer, initiator of the hadron beam program within the NA49 experiment, for his inspiring guidance, continuous support and challenging discussions during my studies. He introduced me to the field of experimental high energy physics and taught me how to conduct experimental research.

I am thankful to my close collaborators from NA49, Andrzej Rybicki, Dezso Varga, Martin Makariev, Michal Kreps, Bozena Boimska and Gabor Veres, for their hard work necessary for the success of our experiment and their support and helpful discussions during all the stages of my work. I am also thankful to Latchezar Betev for maintaining our server farm, Zoltan Fodor, Siegfried Wenig, Helena Bialkowska and Vladimír Černý for their contributions to the success of NA49 and for valuable discussions, and to all other NA49 collaborators.

I wish to thank Christine Nattrass for careful reading of the manuscript and correcting many errors and typos.

I enjoyed hospitality of the Institute of Nuclear and Particle Physics in Prague under the leadership of prof. Jiří Hořejší to whom I am very thankful. I express my gratitude to my colleagues from Prague, Dalibor Nosek, Karel Soustružník, Vít Vorobel and Martin Spousta for helping with various questions and useful discussion.

Finally I wish to thank my family and my friends, especially my parents for their moral support and patience.

Bibliography

[1] W. Noel Cottingham, Derek A. Greenwood: *An Introduction to the Standard Model of Particle Physics*, Cambridge University Press, ISBN 0-521-58832-4

[2] E. Rutherford: *The Scattering of α and β Particles by Matter and the Structure of the Atom* Phil. Mag. **21** (1911) 669

[3] J. Chýla: *Quarks, partons and Quantum Chromodynamics* `http://www-hep.fzu.cz/Theory/notes/text.pdf`

[4] R. Hofstadter: *Electron Scattering and Nuclear Structure* Rev. Mod. Phys. 28 (1956) 214

[5] JADE Collaboration: *Experimental investigation of the energy dependence of the strong coupling strength* Phys. Lett. B 213 (1988) 235

[6] S. Bethke: *Jet Physics at LEP and World Summary of α_s*, arXiv:hep-ex/9812026

[7] JADE Resurrection Homepage `http://wwwjade.mppmu.mpg.de/`

[8] J. W. Cronin et al.: *Production of hadrons at large transverse momentum at 200, 300, and 400 GeV*, Phys. Rev. **D** 11, (1975) 3105

[9] D. Antreasyan et al.: *Production of pi+ and pi- at Large Transverse Momentum in p-p and p-d Collisions at 200, 300, and 400 GeV*, Phys. Rev. Lett. 38, (1977) 112

[10] D. Antreasyan et al.: *Production of hadrons at large transverse momentum in 200-, 300-, and 400-GeV p-p and p-nucleus collisions*, Phys. Rev. **D** 19, (1979) 764

[11] A. Accardi: *Cronin effect in proton-nucleus collisions: a survey of theoretical models*, arXiv:hep-ph/0212148

[12] S. Capstick et al.: *Key Issues in Hadronic Physics*, arXiv:hep-ph/0012238

[13] L. Van Hove, *Longitudinal phase-space plots of multiparticle hadron collisions at high energy*, Nucl. Phys. B **9** (1969) 331

[14] R. P. Feynman, *Very high-energy collisions of hadrons*, Phys. Rev. Lett. **23** (1969) 1415

[15] J. D. Bjorken, *Asymptotic Sum Rules At Infinite Momentum*, Phys. Rev. **179**, 1547 (1969)

[16] W. Ochs, *Hadron Fragmentation At High-Energies And Quark Constituents*, Nucl. Phys. B **118** (1977) 397

[17] E. D. Bloom and F. J. Gilman, *Scaling And The Behavior Of Nucleon Resonances In Inelastic Electron - Nucleon Scattering*, Phys. Rev. D **4** (1971) 2901

[18] J. Benecke, T. T. Chou, C. N. Yang and E. Yen, *Hypothesis Of Limiting Fragmentation In High-Energy Collisions*, Phys. Rev. **188** (1969) 2159

[19] A. Casher, H. Neuberger and S. Nussinov, *Chromoelectric Flux Tube Model Of Particle Production*, Phys. Rev. D **20** (1979) 179.

[20] A. Bialas, *Fluctuations of string tension and transverse mass distribution*, Phys. Lett. B **466** (1999) 301, arXiv:hep-ph/9909417

[21] A. Baran, W. Broniowski and W. Florkowski, *Description of the particle ratios and transverse-momentum spectra for various centralities at RHIC in a single-freeze-out model*, Acta Phys. Polon. B **35** (2004) 779, arXiv:nucl-th/0305075

[22] R. P. Feynman, R. D. Field and G. C. Fox, *Quantum-chromodynamic approach for the large-transverse-momentum production of particles and jets*, Phys. Rev. D **18** (1978) 3320

[23] L. V. Gribov, E. M. Levin and M. G. Ryskin, *Semihard Processes In QCD*, Phys. Rept. **100** (1983) 1

[24] J. L. Bailly *et al.* [EHS-RCBC Collaboration], *Multiparticle Production In Proton–Nucleus Collisions At 360 GeV/c Using The European Hybrid Spectrometer*, Z. Phys. C **35** (1987) 301 [Erratum-ibid. C **36** (1987) 512]

[25] E. Yen and E. L. Berger, *Distributions in transverse momentum for deeply inelastic hadron collisions*, Phys. Rev. Lett. **24** (1970) 695.

[26] J. W. Harris and B. Muller, *The search for the quark-gluon plasma*, Ann. Rev. Nucl. Part. Sci. **46** (1996) 71, arXiv:hep-ph/9602235

[27] C. Y. Wong, *Initial Energy Density Of Quark Gluon Plasma In Relativistic Heavy Ion Collisions*, Phys. Rev. D **30** (1984) 961

[28] M. Gyulassy and T. Matsui, *Quark Gluon Plasma Evolution In Scaling Hydrodynamics*, Phys. Rev. D **29** (1984) 419

[29] S. A. Bass, M. Gyulassy, H. Stoecker and W. Greiner, *Signatures of quark-gluon-plasma formation in high energy heavy-ion colisions: A critical review*, J. Phys. G **25** (1999) R1, arXiv:hep-ph/9810281

[30] R. Stock, *Quark Matter 99 summary: Hadronic signals*, Nucl. Phys. A **661** (1999) 282, arXiv:hep-ph/9911408

[31] The ROOT oriented analysis framework has been designed and developed by Michal Kreps, Comenius University, Slovakia (unpublished)

[32] R. J. Glauber In: W.E. Brittin et al., *Lectures in theoretical physics Vol. 1*, Interscience Publishers Inc., New York (1959) 315

[33] R. J. Glauber and G. Matthiae, *High-energy scattering of protons by nuclei*, Nucl. Phys. B **21** (1970) 135

[34] J. Formanek, *Glauber Model And Unitarity Condition*, Czech. J. Phys. B **26** (1976) 843

[35] M. K. Hegab and J. Hufner, *How Often Does A High-Energy Hadron Collide Inside A Nucleus?*, Phys. Lett. B **105** (1981) 103

[36] M. K. Hegab and J. Hufner, *The Distribution Of Gray Particles In Very High-Energy Hadron Nucleus Collisions*, Nucl. Phys. A **384** (1982) 353

[37] F. Sikler, *Centrality control of hadron-nucleus interactions by detection of slow nucleons*, arXiv:hep-ph/0304065

[38] K. Braune *et al.*, *The Nuclear Response In High Energy Hadron - Nucleus Interactions*, Z. Phys. C **13** (1982) 191

[39] W. M. Geist, *Atomic mass dependence in soft and hard pA collisions*, Nucl. Phys. A **525** (1991) 149C

[40] NA49 Collaboration: *The NA49 Large Acceptance Hadron Detector*, Nucl. Instrum. Methods Phys. Res., A430 (1999) 210

[41] C. De Marzo *et al.* [NA5 Collaboration], *A Segmented Photon - Hadron Calorimeter Using A Two Colored Wavelength Shifter Optical Readout System*, Nucl. Instrum. Meth. **217** (1983) 405

[42] C. Bovet, R. Maleyran, L. Piemontese, A. Placci and M. Placidi, *The Cedar Counters For Particle Identification In The SPS Secondary Beams: A Description And An Operation Manual*, CERN-82-13

[43] W. Blum, L. Rolandi, *Particle Detection with Drift Chambers*, Springler–Verlag Berlin Heidelberg 1993

[44] W. R. Leo, *Techniques for Nuclear and Particle Physics Experiments*, second edition, Springler–Verlag Berlin Heidelberg

[45] F. Beiser et al., *Design and performance of TPC readout electronics for the NA49 experiment*, Nucl. Instrum. Methods Phys. Res., A 385 (1997) [535–546]

[46] C. Bormann et al, *A Software Environment for the NA49 TPCs*, Nucl. Instrum. Methods Phys. Res., A 374 (1996) [227–234]

[47] Ch. Roland, *Flavor Fluctuations in Central Pb+Pb Collisions at 158 GeV/A*, PhD. thesis

[48] Application Software Group, CN Division, CERN, *DS PACK – Data Manager*, CERN, Geneva (1993)

[49] V. Bakken, F. o. Breivik, T. Jacobsen and A. l. Rudjord [Scandinavian Bubble Chamber Collaboration], *Inclusive Production Of Delta++ (1232) In P N Interactions At 19 GeV/c* Nuovo Cim. A **72** (1982) 377

[50] NA49 Collaboration, *Addendum-10 to Proposal SPSLC/P264*, CERN/SPSC 2002-008 (2002)

[51] H. G. Fischer et al. [NA49 Collaboration], *Elementary hadronic interactions at the CERN SPS*, Nucl. Phys. A **715** (2003) 118, arXiv:hep-ex/0209043

[52] H. G. Fischer et al. [NA49 Collaboration], *Baryon Yields, Isospin Effects and Strangeness Production in Elementary Hadronic Interactions*, Heavy Ion Phys. **17** (2003) 369

[53] M. Kreps et al. [NA49 Collaboration], *Baryon and antibaryon production in hadron-hadron and hadron-nucleus interactions*, Nucl. Phys. A **715** (2003) 502, arXiv:nucl-ex/0209003

[54] D. Varga et al. [NA49 Collaboration], *Baryon Number Transfer in Hadron+Nucleus and Nucleus+Nucleus Collisions: A Link between Elementary and Complex Interactions* Heavy Ion Phys. **17** (2003) 387, arXiv:hep-ph/0303030

[55] O. Chvala et al. [NA49 Collaboration], *On the importance of isospin effects for the interpretation of nuclear collisions*, Eur. Phys. J. C **33** (2004) 615, arXiv:hep-ex/0405053

[56] D. Varga et al. [NA49 Collaboration], *Baryon number transfer and baryon pair production in soft hadronic interactions at the CERN SPS*, Eur. Phys. J. C **33** (2004) 515

[57] A. Rybicki, *Comments on particle production in p+p, p+A and A+A reactions*, J. Phys G: Nucl Part. Phys. **30** (2004) 743

[58] M. Kreps, *Produkcia nestabilných častíc v hadrón-protoónový srážkach pri 185 GeV/c*, PhD. thesis

[59] A. Rybicki, *Charged hadron production in elementary and nuclear collisions at 158 GeV/c*, PhD. thesis

[60] G. Veres, *Baryon Momentum Transfer in Hadronic and Nuclear Collisions at the CERN NA49 Experiment*, PhD. thesis

[61] C. Alt et al. [NA49 Collaboration], *Inclusive Production of Charged Pions in p+p Collisions at 158 GeV/c Beam Momentum*, Eur. Phys. J. C **46** 2006 343, arXiv:hep-ex/0510009

[62] C. Alt et al. [NA49 Collaboration], *Inclusive Production of Charged Pions in p+C Collisions at 158 GeV/c Beam Momentum*, accepted for publication in Eur. Phys. J. C, arXiv:hep-ex/0606028

[63] G. Barr et al [NA49 Collaboration], *Charged Pion Production in p+C Collisions at 158 GeV/c Beam Momentum: Discussion*, accepted for publication in Eur. Phys. J. C, arXiv:hep-ex/0606029

[64] H. G.Fischer et at., CERN/SPSC 2005-035

[65] W. J. Llope and P. Braun- Munzinger, *Electromagnetic dissociation of relativistic heavy ions*, Phys. Rev. C **41** (1990) 2644

[66] U. Amaldi, K.R. Schubert, *Impact parameter interpretation of proton–proton scattering from critical review of all ISR data*, Nucl. Phys. B **166** (1980) 443

[67] C. Conta et al, *Analysis of double diffraction dissociation in nucleon-nucleon collisions at the CERN ISR*, Nucl. Phys. B **175** (1980) 97

[68] J. Whitmore, *Experimental results on strong interactions in he NAL hydrogen bubble chamber* Phys. Rept. (Phys. Lett. C) **10** (1974) 273

[69] G. J. Bobbink et al., *Correlations between high-momentum secondaries in pp collisions at* $\sqrt{s} = 44.7$ *and 62.3 GeV* Nucl. Phys. B **204** (1982) 173

[70] C. Bromberg et al., *Pion production in pp collisions at 102 GeV/c* Phys. Rev. D **9** (1974) 1864

[71] T. Kafka et al., *Charge and Multiplicity Fluctuations in 205-GeV/c pp Interactions* Phys. Rev. Lett. **34** (1975) 687

[72] V. V. Aivazian et al. [NA22 Collaboration], *Forward-backward multiplicity correlations in pi+ p, K+ p and p p collisions at 250-GeV/c*, Z. Phys. C **42** (1989) 533

[73] S. Uhlig, I. Derado, R. Meinke and H. Preissner, *Observation of charged particle correlations between the forward and backward hemispheres in pp collisions at ISR energies*, Nucl. Phys. B **132** (1978) 15

[74] A. Bialas et al, *Multiplicity distributions in nucleus-nucleus collisions at high energies* Nucl. Phys. B **111** (1976) 461

[75] W. Busza et al, *Charged-Particle Multiplicity in* pi^-*–Nucleus Interactions at 100 and 175 GeV/c* Phys. Rev. Lett. **34** (1975) 836

[76] J. L. Bailly et at, *Multiplicity production in proton–nucleus collisions at 360 GeV/c using European Hybrid Spectrometer* Z. Phys. C **35** (1987) 301

[77] J. J. Whitmore at al, *Inclusive charged production in hadron—nucleus interactions at 100 and 320 GeV/c* Z. Phys. C **62** (1994) 199

[78] Ferenc Sikler, *Centrality control of hadron-nucleus interactions by detection of slow nucleons*, arXiv:hep-ph/0304065

[79] A. Rybicki, *Centrality in hadron-carbon, hadron-lead, and lead-lead Reactions at 158 GeV/c*, H. Niewodniczanski Institute of Nuclear Physics, Report No. 1976/PH `http://www.ifj.edu.pl/publ/reports/2006/`

[80] D. Drijard, H.G. Fischer, T. Nakada, *Study Of Event Mixing And Its Application To The Extraction Of Resonance Signals* Nucl. Instrum. Meth. A **225** (1984) 367

[81] D. Varga, *p+C and p+Pb total inelastic cross section: compilation of earlier measurements and consistency with the NA49 values*, NA49 note

[82] G. E. Cooper, *Baryon stopping and hadronic spectra in lead - lead collisions at 158 GeV/nucleon*, Ph.D. Thesis

[83] J. B. Bowlin, A. S. Goldhaber, *Simple model for nuclear stopping power*, Phys. Rev. D **34** (1986) 778

[84] G. Bellettini et al, *Proton–nuclei cross sections at 20 GeV*, Nucl.Phys.**79** (1966) 609

[85] A. Ashmore et al, *Total cross sections of protons with momentum between 10 and 28 GeV*, Phys. Rev. Lett. **5** (1960) 576

[86] B. M. Bobchenko et al, *Measurement Of Total Inelastic Cross Sections From Proton Interactions With Nuclei In The Momentum Range From 5 GeV/c To 9 GeV/c*, Sov. J. Nucl. Phys. **30** (1979) 805

[87] A. S. Carroll et al, *Absorption Cross Sections Of Pi+-, K+-, P And Anti-P On Nuclei Between 60 GeV/c And 280 GeV/c*, Phys. Lett. B **80** (1979) 319

[88] S. P. Denisov et al, *Absorption Cross Sections For Pions, Kaons, Protons And Anti-Protons On Complex Nuclei In The 6 GeV/c To 60 GeV/c Momentum Range*, Nucl. Phys. B **61** (1973) 62

[89] T. J. Roberts et al, *Neutron Nucleus Inelastic Cross Sections From 160 GeV/c To 375 GeV/c*, Nucl. Phys. B **159** (1979) 56

[90] D. S. Barton et al., *Experimental Study Of The A-Dependence Of Inclusive Hadron Fragmentation*, Phys. Rev. D **27** (1983) 2580

[91] G. Jancso et al., *Evidence for dominant vector-meson production in inelastic proton-proton collisions at 53 GeV c.m. energy* Nucl. Phys. B **124** (1977) 1

[92] W. M. Geist, D. Drijard, A. Putzer, R. Sosnowski and D. Wegener, *Hadronic production of particles at large transverse momentum: Its relevance to hadron structure, parton fragmentation and scattering*, Phys. Rept. **197** (1990) 263

[93] Andrzej Rybicki, *Comments on particle production in p+p, p+A and A+A reactions*, J. Phys. G: Nucl. Part. Phys. **30** (2004) S743-S750

[94] O. Chvala et al. [NA49 Collaboration], *Pion Production In Pb+Pb Collisions At The SPS*, Nucl. Phys. A **749** (2005) 304

[95] A. Rybicki, *Meson Production at SPS Energies*, in Proc. 9th International Workshop on Meson Production, Properties and Interaction, Kraków, Poland, June 9-13, 2006, to appear in Int. J. Mod. Phys. A.

[96] O. Chvala, *Mass Distributions of Hadronic Resonances Produced by Some of MC Event Generators*, NA49 internal note

[97] *Detailed analysis of soft hadrons at the SPS*,
`http://cern.ch/spshadrons`

[98] D. Varga, *Study of Inclusive and Correlated Particle Production in Elementary Hadronic Interactions*, PhD. thesis

List of Figures

List of Tables